Stirling Dish System Performance Prediction Model

By

PAUL R. FRASER

A thesis submitted in partial fulfillment of the requirements for the degree of

MASTER OF SCIENCE
(MECHANICAL ENGINEERING)

at the

UNIVERSITY OF WISCONSIN-MADISON

2008

Approved by

Professor Sanford A. Klein
January 14, 2008

Abstract

An energy prediction model was created for solar Stirling dish systems to predict the location dependent long term performance of these systems. The model analyzes the performance of the parabolic mirror, receiver, Stirling engine, and the parasitic power consumption to predict the net power produced. The performance prediction models were implemented in TRNSYS and include location dependent properties that affect the performance based on the direct normal insolation, ambient temperature, density of air (altitude), sun elevation angle, and the wind speed.

This thesis outlines the theory and models for the collector, receiver, Stirling engine, and the parasitic power including the cooling system pump, fan, and cooling tower. Several detailed Stirling dish system component models were compared with three years of data from the Wilkinson, Goldberg, and Associates, Inc. (WGA) Mod 2-2 system to determine which model most accurately replicated the data. The best detailed component model has separate components for the collector, receiver, Stirling engine, and parasitic power consumption. The model uses theory from Stine and Harrigan (1985) for the collector, Stine and McDonald (1989) for natural convection from the receiver, Ma (1993) for forced convection from the receiver, a performance curve fit using data for the Stirling engine by correcting the Beale number (Urieli and Berchowitz, 1984) with a temperature correction term (McMahan, 2007), and the parasitic power model uses performance theory from the fan laws and dimensionless pump performance correlations.

The best detailed component model determined during this research predicted the net performance of the WGA Stirling dish system more accurately than existing Stirling dish system models when using one day of data to generate the performance curves. The standard deviation predicting the total energy over a three year period of WGA data for the proposed model compared was 4.0 %, whereas the most accurate existing model was 6.5 %, and another model was 6.9 %. The average difference in power with the current model was 575 W, the most accurate existing model was 640 W, and another model was 680 W. Scatter in the data contributed to 490 W for the average difference in power, which may be mostly due to mirror soiling daily variation. The proposed model is also expected to show a greater improvement in accuracy over the existing models when predicting the system performance in different locations due to the additional location dependent properties of the wind velocity, sun elevation angle, and altitude. The proposed model is capable of accurately predicting the Stirling dish system performance over a long period of time using only one day of data.

The detailed component model was implemented in TRNSYS and requires hourly data of the direct normal insolation, atmospheric pressure, ambient temperature, wind speed, and sun elevation angle to calculate the net electrical power produced. The user can automatically specify characteristic parameters for any the four Stirling dish systems manufactured by WGA, Stirling Energy Systems Inc. (SES), Schlaich-Bergermann und Partner (SBP), and Science Applications International Corp. (SAIC). It is also possible for the user to vary the parameters of the collector, receiver, Stirling engine, and parasitic power model for values not characteristic of these systems.

The TRNSYS Stirling dish system model is flexible enough to predict the system performance by changing several parameters or components. A sample of the system parameters includes the receiver aperture diameter, heater head operating temperature, operating speed of the cooling fan and pump, cooling fluid, and the receiver geometry,. The system components can also be modified in the TRNSYS model to determine how the system performance changes by replacing a direct illumination receiver (DIR) with a reflux receiver, running the system in a hybrid mode with a quartz cover over the receiver aperture, or replacing the fan and radiator with a central cooling tower. A summary of various TRNSYS simulation results can be found in this thesis using different design scenarios and operating parameters for the WGA system in specific locations.

Acknowledgements

I have greatly appreciated the technical support, freedom, and detailed advice offered by my advisors Sandy Klein and Doug Reindl. They both contributed much more time and effort to my research and reports than I expected. My technical skills have been greatly improved as a result of working and learning with them.

I have also been grateful for the flexibility offered by Nate Blair and Mark Mehos from the National Renewable Energy Laboratory (NREL) who provided the financial support for this research. I was able to research a large variety of topics related to Stirling dish systems with their continued support and interest.

Chuck Andraka from Sandia National Laboratories provided crucial data for validating the models in this research. His knowledge of Stirling dish systems and technical papers also allowed for a much better understanding of factors that affected the performance of these systems.

This project was financially supported by the National Renewable Energy Laboratory (NREL) under contract number ADC-5-55027-01.

Table of Contents

List of Tables

List of Figures

Nomenclature

A	Area
A_a	Cavity aperture area
A_i	Inner surface area of the cavity
$Beale$	Beale number
C	Thermal capacitance
DNI	Direct normal insolation
d	Diameter of the collector
e	Regeneration effectiveness
f	Engine operating frequency
f_f	Friction factor
g	Gravitational constant
h	Convection coefficient
I_b	Beam radiation incident on the receiver surface
$I_{bm,corr}$	Corrected beam radiation
k	Thermal conductivity
K	Term for minor pumping losses
L	Length
m	Mass of working fluid
M	Molar mass
n	Number of standard deviations for the receiver model
n_r	Engine speed
N	Pump or fan speed
Nu	Nusselt number
P	Pressure
P_{gross}	Gross engine power
P_{net}	Net engine power
P_{head}	Pump pressure head
Pr	Prandtl number
p	Distance from the concentrator surface to the focal point of the aperture
P_{mean}	Mean engine pressure
Q,q	Heat transfer
R	Resistance
R	Ideal gas constant
Ra	Rayleigh number
Re	Reynold's number
S	Stroke of the engine piston
Sc	Schmidt number
T	Temperature
v	Velocity
V	Volume
V_{max}	Maximum swept volume
V_{min}	Minimum swept volume (V_{max} subtracted by the displacement volume)
Vsw	Swept volume
V_{swc}	Swept volume of the compression space
V_{swe}	Swept volumes of the expansion spaces

w_n	Beam spread projected onto the focal plane of the receiver
W	Work
$West$	West number

Greek Letters

α	Receiver absorptance
α_{eff}	Effective absorptance
α_{i}	Inner surface absorptance of the cavity
β	Thermal expansion coefficient
Γ	Flux capture fraction which equals the intercept factor
$\Delta\dot{Q}$	Power intercepted for a specific ring
Δr	Total beam spread in the plane perpendicular to the centerline of the reflected light
ε_{s}	Emissivity of a surface
ε	Angular size of the sun
ε_{v}	Volumetric ratio
η	Efficiency
η_{Carnot}	Carnot efficiency
η_{SE}	Stirling engine efficiency
θ	Receiver aperture angle (0 is horizontal, 90 is vertically down)
$\Theta_{\text{T,cw}}$	Normalized cooling water inlet temperature
μ	Dynamic viscosity
υ	Kinematic viscosity
ρ	Mirror specular reflectance
σ_{slope}	Spread of the collector beam due to error in the mirror slope
σ_{sensor}	Spread of the collector beam due to sensor error
σ_{drive}	Spread of the collector beam due to the tracking drive error
σ_{align}	Spread of the collector beam due to mirror alignment
$\sigma_{reflect}$	Spread of the collector beam caused by mirror reflection discrepencies
σ_{sun}	Spread of the collector beam caused by the width of the sun
σ	Stefan Boltzmann's constant
τ_c	Transmittance of the hybrid receiver cover
τ_d	Transmittance of the hybrid receiver cover for isotropic diffuse radiation
$d\Phi/d\psi$	Change in the radiant flux with respect to the change in the angle in the collector
Φ_{R}	Normalized mirror reflectance
Ψ	Angle between the line between the collector vertex and focus, and the line for the location on the collector where light is reflecting from
ψ_{rim}	Collector rim angle

Subscripts

amb	Ambient
ap	Receiver aperture
C, c	Compression space
cav	Receiver cavity

cond	Conduction
conv	Convection
cw	Cooling water
E, e	Expansion space
eff	Effective
forced	Forced convection
g	Working fluid (gas)
h	Heater
k	Cooler
m	Mean
min	Minimum
max	Maximum
natural	Natural convection
r	Regenerator
SE	Stirling engine
SW	Swept (volume)
w	Wall of cavity
wall	Wall of cavity

Acronyms

EES	Engineering Equation Solver
NREL	National Renewable Energy Laboratory
SAIC	Science Applications International Corp
SBP	Schlaich–Bergermann und Partner
SES	Stirling Energy Systems
WGA	Wilkinson, Goldberg, and Associates, Inc

1 Introduction

A Stirling dish system recorded a world record in solar-to-electric energy conversion efficiency of 29.4 % in 1984 (Andraka et al, 1996). Since then, there has been interest in the potential for these systems to produce inexpensive and reliable renewable electric power to the market in the near future. Stirling Energy Systems is expected to install the largest solar-electric power plant in the world over the next several years after initial testing of a 40 dish 1 MW test pilot project (SES, 2007). Parabolic troughs have dominated the concentrating solar power market thus far, but Stirling dish systems are anticipated to surpass parabolic troughs by producing power at more economical rates and higher efficiencies.

Stirling dish systems have not been researched as extensively as other solar technologies such as photovoltaics or solar hot water heaters, and literature on these systems is difficult to find and rarely organized in one cohesive report. Data on the performance of Stirling dish systems have typically not been accessible to the public, and few Stirling dish systems have been constructed to date. Despite these limitations, data were obtained from Sandia National Laboratory for the WGA Mod 2-2 Stirling dish system in order to validate models of Stirling dish power systems developed during the course of the present study.

1.1 Objectives

The goal of this research was to develop a semi-theoretical component-based model of Stirling dish systems in TRNSYS capable of predicting the location-dependent system performance. The model developed is suitable for location dependent system studies and comparisons with alternative solar electric power generation systems. The model is also capable of predicting how the performance of Stirling dish systems will change based on various parameters. A sample of these parameters includes varying the receiver aperture diameter, engine heater head operating temperature, the fan operating speed, or using a cooling tower instead of a radiator and fan. Location dependent parameters include the ambient temperature, density of air (altitude), direct normal insolation, wind speed, and the sun elevation angle.

This thesis presents background information on the location dependent performance of Stirling dish systems, but does not focus on economical analyses of various designs. A summary of Stirling dish system background information and a brief summary of economics can be found in Chapter 2, component models to predict the system performance are provided in Chapter 3, an analysis of data for the WGA Stirling dish system is given in Chapter 4, performance prediction results comparing the accuracy of various Stirling dish system models to data in Chapter 5, and an analysis of how the TRNSYS model predicts the system performance will change based on location in Chapter 6. Concluding remarks and suggestions for further research can be found in Chapter 7.

1.2 Concentrating Solar Power Overview

Concentrating Solar Power (CSP) energy systems convert sunlight into electricity using parabolic mirrors capable of concentrating the solar radiation by a factor of over 13,000 for Stirling dish systems (Mancini et al, 2003). The concentrated solar energy is either focused on a photovoltaic module, or a receiver that absorbs the solar energy and transfers it to a working fluid such as a high temperature oil, molten salt, or hydrogen. The working fluid is then directly or indirectly used as the thermal source in a power cycle. Many of these technologies can operate with thermodynamic cycles similar to conventional power plants fueled by coal or natural gas; however, they have been modified to run off of solar energy as the primary fuel.

Electricity produced from concentrating solar power has become more economical and its influence in the electricity market is expected to significantly increase in the near future as these technologies mature. The most widely used CSP technology is the parabolic trough with over 350 MW of installed capacity in the U.S. at a cost of about 10 cents per kilowatt hour (Teagan, 2001). Power towers are another CSP technology that could become more economical than parabolic troughs by using a field of mirrors to focus on a central receiver that boils water for a standard steam cycle. The most recent technology that may surpass all other CSP technologies in total installed capacity is the Stirling dish systems, which is the focus of this thesis.

1.2.1 Parabolic Trough

The trough systems use parabolic mirrors that are extended for long distances in rows. A receiver pipe at the focal point of the parabolic troughs absorbs the concentrated solar energy as shown in Figure 1-1. The collector fields are aligned in parallel rows on a north-south axis and pivot on a single axis to track the sun throughout the day (DOE, 2006). Trough systems have been designed to provide up to 80 MW, and there is currently 354 MW of installed capacity in California (Teagan, 2001). The working fluid can be an organic fluid or water with a maximum operating temperature around 400°C. A steam turbine is used as the prime mover for power generation (McMahan, 2006). The parabolic trough plants often are hybridized up to 25 % with natural gas to enable dispatchable power when solar resources are unavailable. They operate at a maximum solar to electric efficiency of 20 % (Teagan, 2001).

Thermal storage can be used in these systems to provide electricity during peak hours or when the sun intensity is low. Thermal energy has been stored in a two tank system with one hot and one cold tank, or in a stratified tank where cold fluid naturally sinks below the less dense hot fluid. The storage tanks use rocks or concrete tubes to store energy for water or oil systems, or molten salts for indirect heat exchange systems (McMahan, 2006). The molten salt storage tanks offer an inexpensive means of storing solar energy in comparison to other storage media such as batteries as shown in Table 1.1. Parabolic troughs are currently the most economical CSP capable of electric production at costs around 10 cents per kW-hr. Electricity from these systems is expected to cost less than six cents per kW-hr in the near future (DOE, 2006).

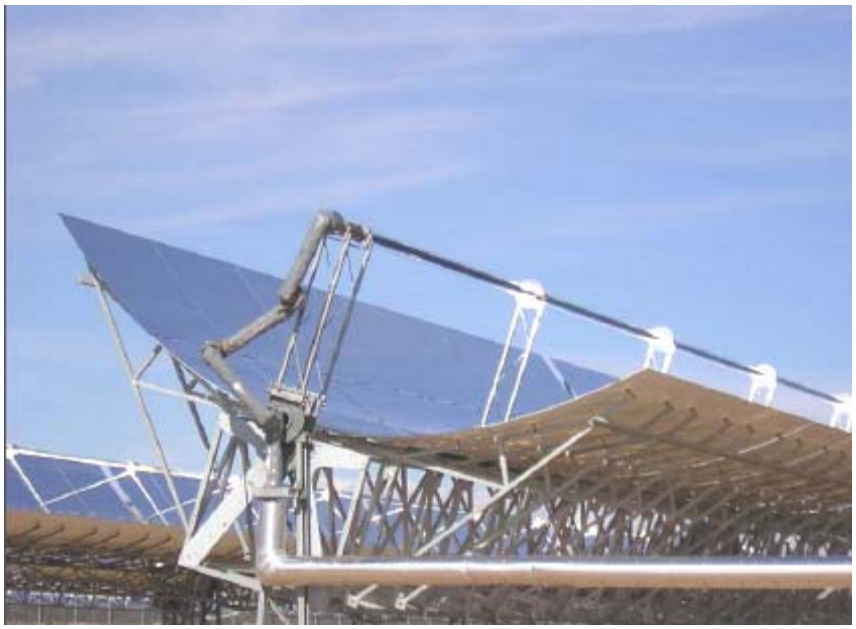

Figure 1-1 Parabolic trough assembly (Patnode, 2006)

1.2.2 Power Tower

A Power tower is a CSP technology that uses a large field of mirrors (heliostats) to concentrate solar energy onto a tower-mounted receiver as seen in Figure 1-2. The heliostats have dual-axis tracking for the sun, which enables an overall solar to electric efficiency of around 23 % due to a higher maximum operating temperature of over 550°C (McMahan, 2006). Energy storage is achieved by pumping molten salt in an indirect heat exchanger that powers a conventional steam turbine in a similar fashion to parabolic trough energy storage systems.

Solar Two is a 10 MW power tower test plant that uses molten salt for thermal storage and can produce power for up to 12 hours after there is no solar radiation (DOE, 2006). The Solar One and Two plants were a collaboration between U.S. utilities and the Department of Energy (DOE) to promote and advance the technology of power towers. With advances in technology, power towers are expected to be the most economical solar energy technology with estimates of less than four cents per kW-hour (DOE, 2006).

Figure 1-2 Solar Two power tower (DOE, 2006)

Renewable energy from solar and wind energy have had economic limitations for storing energy and therefore has not been able to produce dispatchable power during peak demand. These limitations may prevent renewable energy sources from representing a large fraction of the energy market and will reduce the return on investing in these technologies. Parabolic troughs and power towers, however, have been able to use a cost effective means of storing thermal energy in thermo-cline or two-tank storage systems. A molten salt is pumped into these tanks for storage and pumped back into a heat exchanger to transfer the thermal energy to a steam turbine when the demand increases (McMahan, 2006). The cost of these thermal storage systems and their efficiency are much more advantageous than producing electricity and storing the energy in batteries as depicted in Table 1.1 below. Stirling dish systems have not been able to take advantage of the thermal storage systems due to integration issues.

Table 1.1 Comparison of energy storage for solar thermal systems for a 200 MW plant (Teagan, 2001)

Energy Storage Medium	Installed cost for 200 MW plant $/kW-hr(e)	Lifetime (years)	Round-Trip Efficiency (%)
Molten Salt	30	30	99
Synthetic Oil	200	30	95
Battery storage (grid connect)	500-800	5-10	76

1.2.3 Concentrating Photovoltaics

High concentrating photovoltaics (HCPV) have recently become the most energy efficient technology to convert solar energy into electricity. The Spectrolab (owned by Boeing) achieved an efficiency of 32 % in 1999 and has continued to improve the solar to electric efficiency up to 37.3 % in 2004 and 40.7 % in 2006 (Spectrolab, 2006). Researchers at the University of Delaware have improved the solar to electric efficiency record to 42.8 % in 2007 (UDEL, 2007). The DOE is anticipating increasing the HCPV efficiency to 50 %.

Amonix is a company that installed over 500 kW of HCPV systems as of 2004 (Stone, 2004). They use a 7x7 inch Fresnel lens to achieve a solar concentration ratio of 250:1 in their 5 kW modules. Amonix has typically connected the units together to produce 25 kW to 35 kW and they mount the modules on a dual-axis tower as shown in Figure 1-3. The system has an overall efficiency of about 18 % with a life of 20 years. The efficiency of these systems should increase as the cost comes down for the more advanced HCPV technologies.

Figure 1-3 Amonix HCPV system and details (Stone, 2006)

2 Stirling Dish System Overview

The Stirling dish system shown in Figure 2-1, produces electricity using concentrated solar thermal energy to drive a Stirling engine. The system utilizes a parabolic mirror equipped with dual-axis tracking to concentrate solar radiation onto a thermal receiver integrated in the Stirling engine. The receiver consists of a heat exchanger designed to transfer the absorbed solar energy to the working fluid, typically, hydrogen. The Stirling engine then converts the absorbed thermal energy to mechanical power by expanding the gas in a piston-cylinder in a manner similar to a gas or diesel engine. The linear motion is converted to a rotary motion to turn a generator to produce electricity. The Stirling dish systems can produce electricity from the sun with efficiencies up to 29 % (Teagan, 2001).

Figure 2-1 Stirling dish systems at Sandia National Labs (SES website, 2006)

2.1 Parabolic Concentrator

The concentrator for the Stirling dish systems uses parabolic mirrors mounted on a structure that tracks the sun by pivoting on two axes. The parabolic concentrator must be sized to deliver about four times more thermal energy than the rated electrical output due to an average net system efficiency of around 25 % (Diver et al, 2001). Existing Stirling dish systems have been built to provide 10 kW and 25 kW electric with an approximate diameter of the parabolic dish being 7.5 and 11 meters respectively (WGAssociates, 2006).

The solar reflectance of the silvered mirrors ranges between 91-95 % for current Stirling dish systems fabricated by four manufacturers (Mancini et al, 2003). The most durable mirror surfaces employ silver/glass mirrors. Attempts to produce low cost reflective polymer films have had limited success in the past (Teagan, 2001). ReflecTech has recently developed a polymer reflective film (ReflecTech™) that has excellent optical properties with a 94.5 % mirror reflectivity and costs $1.30 per square foot in large volume (ReflecTech, 2007). The most innovative parabolic mirrors use stretched-membranes where the reflective membrane is stretched across a hoop or rim and a second membrane is placed behind the first. A partial vacuum then pulls the first membrane into a parabolic shape.

The dual-axis solar tracking is accomplished through azimuth-elevation tracking or polar tracking. Azimuth-elevation tracking rotates the concentrator in a plane parallel to the earth (azimuth) and in another plane perpendicular to the earth (elevation) (Teagan, 2001). For polar tracking, the concentrator rotates in a plane parallel to the rotation of the earth at a constant rate of 15 degrees per hour, and the declination axis rotates perpendicular to the polar axis by slowly varying between plus and minus 23.5 degrees over the year. Larger Stirling dishes have used azimuth-elevation tracking and smaller Stirling dish systems have used polar tracking.

2.1.1 Collector Design Criteria

The parabolic concentrator reflects direct normal solar radiation into the aperture of the receiver where it is concentrated on the absorber. The aperture must be designed to be large enough to enable a significant fraction of reflected radiation from the concentrator to be transmitted onto the absorber, although there is a drawback with designing it too large. Increasing the aperture size will increase the amount of solar radiation intercepted by the receiver, but also increase the losses due to convection and radiation out of the aperture. Convection and radiation decrease the effective radiative energy absorbed in the receiver. An analysis is necessary to determine the impact of receiver loss mechanisms resulting from errors in the collector system, aperture diameter, and the temperature of the absorber.

2.1.1.1 Intercept Factor

The intercept factor is the fraction of solar radiation reflected from the parabolic collector that enters the aperture. It is influenced by the size of the aperture, errors in the collector system, the collector rim angle (defined below), and nonparallel sunlight (Stine and Harrigan, 1985). Increasing the intercept factor will increase the fraction of the energy entering the receiver, although this may not always be beneficial. If there is an increase in the intercept factor as a result of reducing errors in the parabolic reflecting collector surface, then an increase in the intercept factor will improve the system performance. If the increase in the intercept factor is accomplished by increasing the size of the aperture, there are competing effects; an analysis is required to determine if the increase in energy intercepted by the receiver will be greater than the energy lost due to thermal losses.

2.1.1.2 Beam Spread

The beam spread is the distance light spreads perpendicular to its direction of propagation after it has reflected off of the collector surface. Reducing the spread of the beam between the point where it reflects off of the collector and to where it enters the focal plane of the receiver will allow for the aperture to be designed smaller leading to an increase in system performance. Ray tracing can be used to determine how far the beam of sunlight will spread, and the parameters to solve for the beam spread include the collector rim angle, nonparallel rays, collector errors, and focal length (Stine and Harrigan, 1985).

2.1.1.3 Collector Rim Angle and Concentration Ratio

The rim angle is an indicator of the curvature for the parabolic receiver. A collector with a larger rim angle has a steeper slope. The rim angle can be determined using either Equations (2.1) or (2.2) knowing the focal length and collector diameter.

$$A_c = 4\pi \cdot f^2 \cdot \frac{\sin^2(\psi_{rim})}{\left[1+\cos(\psi_{rim})\right]^2} \tag{2.1}$$

$$\psi_{rim} = \tan^{-1}\left(\frac{f/d}{2\cdot(f/d)^2 - 1/8}\right) \tag{2.2}$$

where f is the focal length of the collector, d is the diameter of the collector, and ψ_{rim} is the rim angle (Stine and Harrigan, 1985). The rim angle must be determined before sizing the aperture since it has an influence on the maximum concentration ratio, the intercept factor, collector slope error, and losses due to convection and radiation (Stine and Harrigan, 1985). Using known dimensions for several collectors, Equation (2.2) was applied to find the rim angle for several systems, and a summary of the rim angle for specific systems is shown in Table 2.1. A depiction of the rim angle is given in Figure 2-2 with the curved lines representing the outline of the parabolic collector.

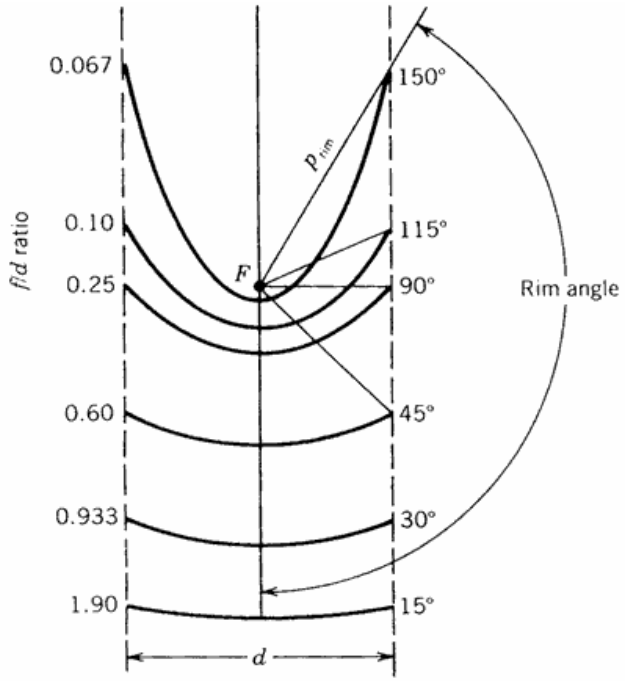

Figure 2-2 Rim angle for a common focus (Stine and Harrigan, 1985)

It is beneficial to obtain a high concentration ratio in the concentrator system since the aperture can then be designed smaller resulting in reduced thermal losses, and the intercept factor will be larger for a specified aperture diameter. The concentration ratio (Peak CR) defined in Table 2.1 is the peak concentration of the system normalized by 1000 W/m^2. The largest concentration ratio is 45,000 (Duffie and Beckman, 2007), and the theoretical maximum can be obtained with a rim angle of 45 degrees (Stine and Harrigan, 1985). Many of the manufacturer's have designs near this value for the rim angle.

Table 2.1 Concentrator system specifics for several manufacturers (Mancini et al, 2003)

Concentrator	SAIC	SBP	SES	WGA (Mod 2)
Glass area [m^2]	117.2	60	91	42.9
Projected area [m^2]	113.5	56.7	87.7	41.2
Reflectivity	0.95	0.94	0.91	0.94
Focal Length [m]	12.0	4.5	7.45	5.45
Rim angle [degrees]	29	52	40	37
Peak CR (suns)	2500	12730	7500	>13000

2.1.2 Collector System Imperfections

There are several imperfections in the collector system that contributes to the spread of the beam. These include imperfections from the slope of the parabolic mirror created during manufacturing, receiver alignment discrepancies, variations in the mirror specular reflectance, tracking error from the tracking sensors, and the tracking drives not being in a uniform position (Stine and Harrigan, 1985). These errors can significantly contribute to a reduction in the intercept factor and must be considered for an accurate collector model. Error values are all represented at one standard deviation in the collector system, and approximate values for collector errors are provided in Table 2.2 below (Stine and Harrigan, 1985).

Table 2.2 Typical error values for a Stirling dish collector system

Type of Error	*One standard deviation of error (1 σ)*
Structure (slope)	(2.5 mrad) x 2
Tracking-Sensor	2 mrad
Tracking-Drive	2 mrad
Receiver Alignment	2 mrad
Specular Reflectance	(0.25mrad) x 2
Sun's Width	2.8mrad

The total error in the Stirling dish collector is given by Equation (2.3), and for the values given in Table 2.2, the total collector system error is approximately 6.7 mille-radians (Stine and Harrigan, 1985). The WGA collector system has a high degree of accuracy with an intercept factor over 99 %, which correlates to a total collector error of just under 4.0 mille-radians (Mancini et al, 2003).

$$\sigma_{tot} = \sqrt{\left(2 \cdot \sigma_{slope}\right)^2 + \sigma_{sensor}^2 + \sigma_{drive}^2 + \sigma_{align}^2 + \left(2 \cdot \sigma_{reflect}\right)^2 + \sigma_{sun}^2} \quad (2.3)$$

2.1.2.1 Nonparallel Sun Rays

Nonparallel sun rays contribute significantly to solar radiation spreading after reflecting off the parabolic mirror, which contributes to a lower fraction of intercepted solar energy in the receiver. The beam spread resulting from nonparallel rays can be determined by Equation (2.4)

$$\Delta r = 2p * \tan\left(\frac{\varepsilon}{2}\right) \quad (2.4)$$

where ε is the angular size of the sun's disc, p is the distance from the concentrator surface to the focal point of the aperture, and Δr is the total beam spread in the plane perpendicular to the centerline of the reflected light as shown in Figure 2-3 (Stine and Harrigan, 1985). The distance from the collector surface to the focus of the aperture, p, is given by Equation (2.5)

$$p = \frac{2f}{1 + \cos(\psi)} \quad (2.5)$$

where f is the focal length of the collector, and Ψ is the angle between the line between the collector vertex and focus, and the line for the location of interest on the collector where the light is reflecting from (Stine and Harrigan, 1985). These angles are depicted in Figure 2-3.

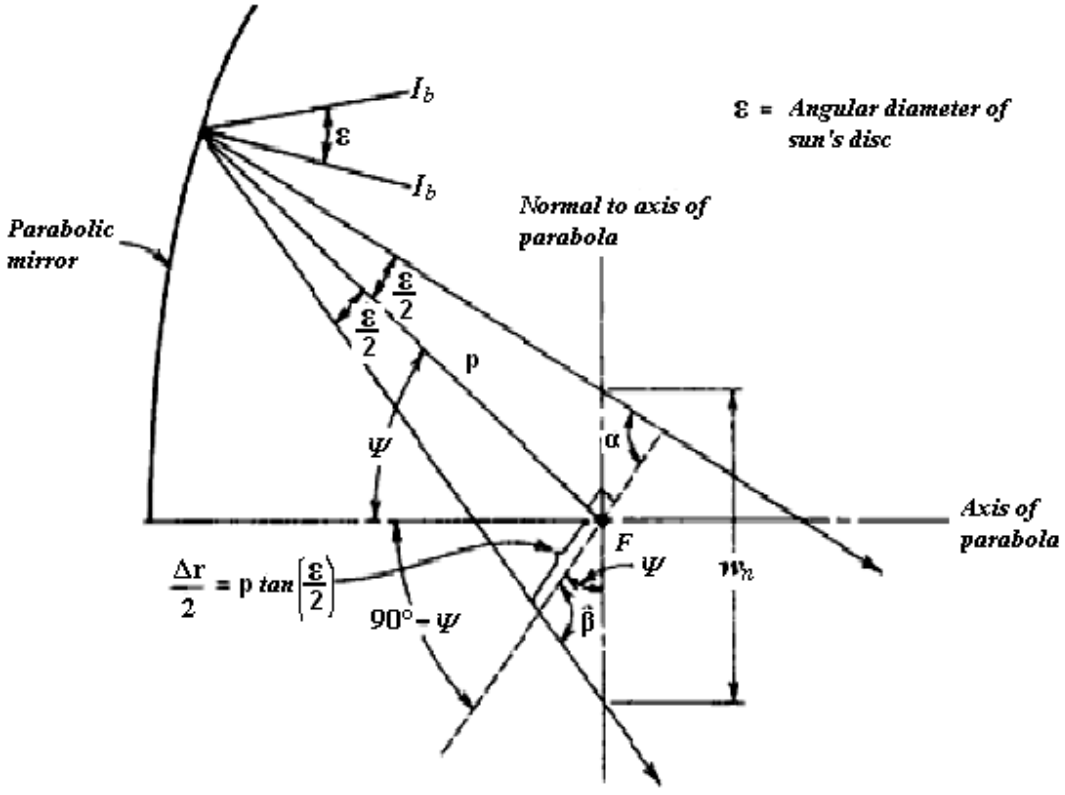

Figure 2-3 Nonparallel rays reflected from a parabolic concentrator (Stine and Harrigan, 1985)

Equations (2.4) and (2.5) indicate that the beam spread will be the least when the sunlight is reflected from the mirror vertex and the beam spread will be the greatest when light is reflected from the outer edges of the collector at the rim angle. Beam spread will result in a reduction of the intercept factor and intercepted power as the location on the parabolic mirror approaches the perimeter as shown in Figure 2-4 and Figure 2-5 respectively. The perimeter of the collector has a larger surface area in comparison to the surface area near the mirror vertex, so a larger area receiving solar power will have a smaller fraction intercepted by the receiver aperture.

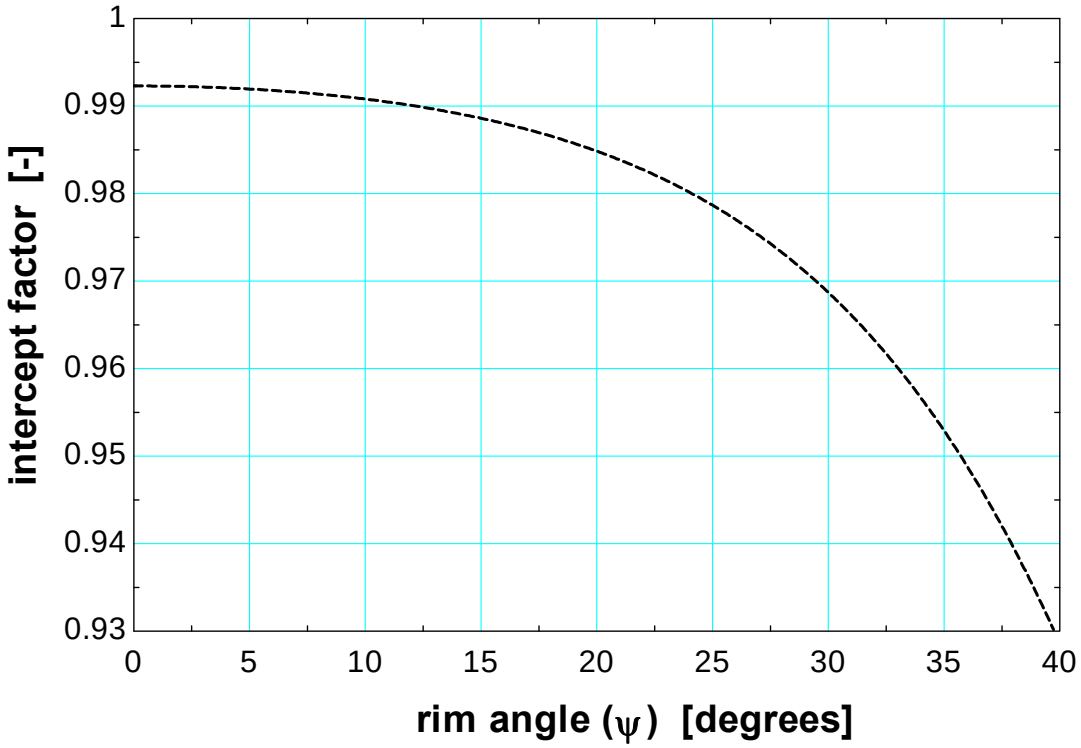

Figure 2-4 Degradation of the intercept factor for the SES system while approaching the collector perimeter

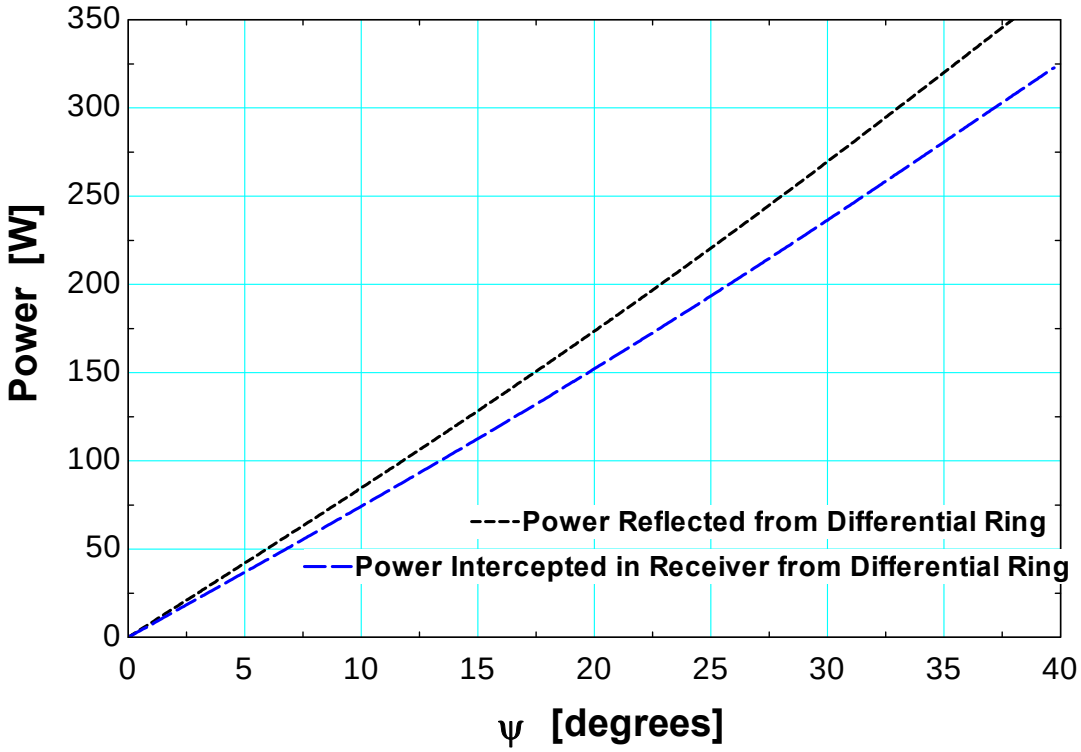

Figure 2-5 Reduction in the intercepted power by the receiver as the location on the parabolic mirror approaches the perimeter for the SES collector using 0.08 degree differential rim angle increments

2.1.2.2 Beam Spread Including Collector Errors

Errors in the collector system contribute significantly to the beam spread in addition to the spread resulting from nonparallel rays. The relation for the total beam spread with these errors included is given by Equation (2.6) with n equal to the number of standard deviations for energy entering the aperture based on the aperture diameter. A value of $n = 4$ will be equivalent to plus or minus two standard deviations and will predict about 95 % of the energy reflected from the collector to be within the total width of the beam spread given by Δr (Stine and Harrigan, 1985).

$$\Delta r = 2p * \tan\left(n\frac{\sigma_{tot}}{2}\right) \tag{2.6}$$

The projection of the beam spread onto the focal plane of the receiver is given in Equation (2.7) with ψ ranging from zero at the parabolic mirror vertex until the rim angle at the collector perimeter (~40˚ for SES).

$$w_n = \frac{\Delta r}{\cos(\psi)} \tag{2.7}$$

Figure 2-6 provides a visual representation of the beam spread (w_n) projected onto the focal plane of the receiver.

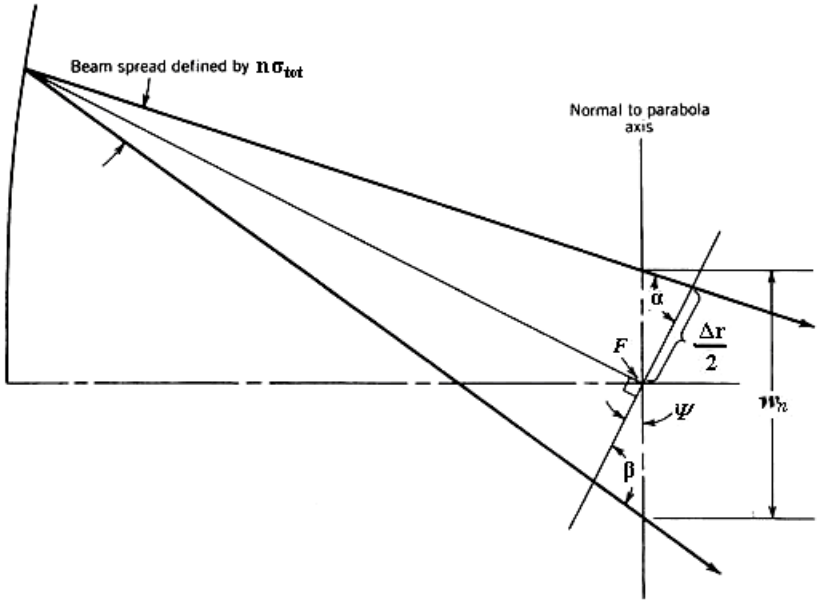

Figure 2-6 Beam spread projected onto the focal plane of the receiver (Stine and Harrigan, 1985)

2.1.3 Total Power Intercepted by Receiver

The total power intercepted by the aperture in a Stirling dish receiver can be approximated by breaking the parabolic mirror into a series of discrete circumferential rings that start from the vertex and move out to the perimeter of the collector. The power from each differential ring is then summed to obtain the net power intercepted by the aperture. Errors are assumed to be uniformly distributed in the circumferential direction. This procedure can be accomplished using Equation (2.8) where $\Delta\dot{Q}$ is the power intercepted for a specific ring, ρ is the mirror specular reflectance, α is the receiver absorptance, Γ is the flux capture fraction (intercept factor), $d\Phi/d\psi$ is the change in the radiant flux with respect to the change in the angle in the collector, and $\Delta\psi$ is the width of the ring in radians used for the integration (Stine and Harrigan, 1985).

$$\Delta\dot{Q} = \rho \cdot \alpha \cdot \Gamma \cdot \left(\frac{d\Phi}{d\psi}\right) \cdot \Delta\psi \tag{2.8}$$

A relation for $d\Phi/d\psi$ for a parabolic collector is given by Equation (2.9) where I_b is the beam normal radiation incident on the receiver surface, f is the focal length, and ψ is the specific rim angle used for integration between 0° and the total rim angle (Stine and Harrigan, 1985).

$$\frac{d\Phi}{d\psi} = \frac{8\pi \cdot I_b \cdot f^2 \cdot \sin(\psi)}{(1+\cos(\psi))^2} \tag{2.9}$$

The flux capture fraction Γ is the fraction of energy reflected from the parabolic collector with a beam having a width of n standard deviations for the specific differential ring. The flux is assumed to be normally distributed and equal to the area under the normal distribution curve when integrated between plus and minus $n/2$. A relation for the flux capture fraction is provided

in Equation (2.10) and Equation (2.11) (Stine and Harrigan, 1985). The flux capture fraction is used in Equation (2.8) to determine the power intercepted by the receiver for each differential ring from the collector. Since the number of standard deviations varies with each differential ring, so does the flux capture fraction. The flux capture fraction (intercept factor) is the greatest near the collector focus, and becomes lower moving out towards the collector perimeter (Figure 2-4).

$$\Gamma = 1 - 2 \cdot Q(x) \tag{2.10}$$

where

$$Q(x) = f(x) \cdot \left(b_1 t + b_2 t^2 + b_3 t^3 + b_4 t^4 + b_5 t^5 \right) \tag{2.11}$$

$$x = n/2 \quad ; \quad f(x) = \frac{1}{\sqrt{2\pi}} \cdot e^{-\frac{x^2}{2}} \quad ; \quad t = \frac{1}{1 + r \cdot x}$$

$r = 0.2316419$

$b_1 = 0.319381530$

$b_2 = -0.356563782$

$b_3 = 1.781477937$

$b_4 = -1.82125978$

$b_5 = 1.330274429$

2.2 Receiver

The Stirling dish receiver absorbs thermal energy from the parabolic concentrator and transfers the absorbed thermal energy to the working fluid in the Stirling engine. The receiver must accommodate a large thermal input as well as a solar flux over a thousand times greater than the direct solar radiation from the sun. A Stirling receiver consists of an aperture and an absorber. The aperture in a Stirling receiver is located at the focal point of the parabolic concentrator to reduce radiation and convection losses, and can have concentration ratios of over 13,000 (Teagan, 2001, Mancini et al, 2003). The size of the aperture has diameters ranging from about 14 to 20 centimeters to ensure an appropriate fraction of the concentrated solar energy is intercepted by the aperture (Mancini et al, 2003). The intercept factor, which is the fraction of the energy from the collector that enters the aperture and is not blocked due to the receiver housing, is often between 94 and 99 percent.

The absorber in the Stirling receiver absorbs solar radiation and transfers the thermal energy to the Stirling engine. The flux intensity in the receiver ranges between 100-110 W/cm^2 (CR of ~1,000) to both prevent absorber material degradation and to allow the working fluid to effectively absorb the energy (Diver, 2001). Current Stirling absorbers are typically direct-illumination receivers (DIR) although some heat pipe absorbers have been tested. Volumetric receivers are implemented in hybrid Stirling dish systems where natural gas is used to supplement solar energy.

Direct-illumination receivers use a bank of tubes to directly heat the working fluid in the Stirling engine using the solar radiation that is absorbed on the external surface of the tubes as shown in Figure 2-7. The working fluid is either hydrogen or helium, which can absorb a solar flux of about 75 W/cm² due to the high heat transfer capabilities of these gases at high velocities and pressures up to 20 MPa (Teagan, 2001). Drawbacks of the DIR include difficulty with balancing thermal input between the multiple Stirling cylinders, and the heater tubes will incur more thermal hot spots as compared with heat pipe absorbers. The flux can be more uniformly distributed across the DIR tubes by increasing the reflectivity of the receiver cavity walls.

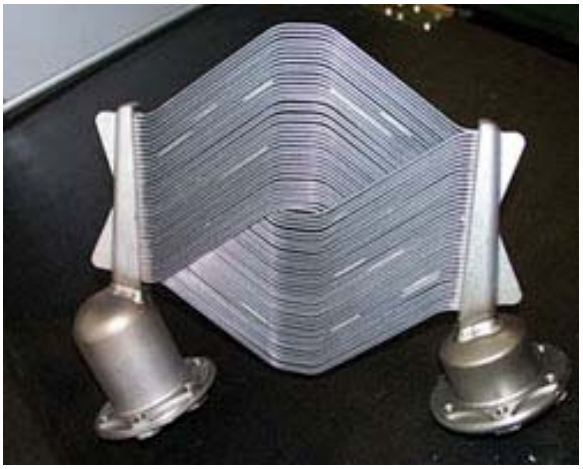

Figure 2-7 Stirling DIR cavity receiver (Ministerio De Educación Y Ciencia, 2006)

The heat pipe absorbers vaporize a liquid metal such as sodium on the absorber surface and condense it on the Stirling engine heater tubes to transfer the energy to the working fluid as in Figure 2-8. Heat pipe receivers yield more uniform temperature distributions on the heater tubes; thereby, resulting in longer life for the absorbers and engine heater heads in comparison to the DIR absorbers. The heat pipe absorbers are also more efficient as demonstrated by a performance improvement of over 10 % for the STM-4-120 Stirling engine compared with the DIR (Teagan, 2001). A Stirling receiver is typically about 90 % efficient at transferring the thermal energy from the concentrator to the Stirling engine.

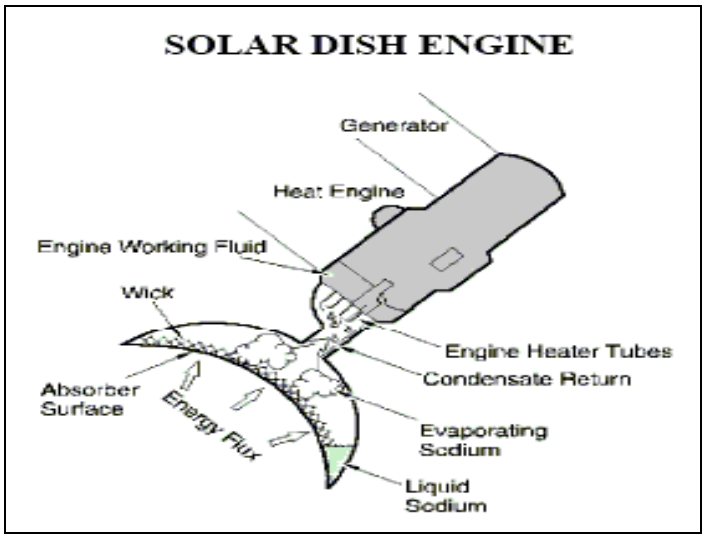

Figure 2-8 Heat pipe absorber for a Stirling dish receiver (Teagan, 2001)

Volumetric receivers have the potential to be more cost effective and reliable than the heat pipe absorbers and are used in hybrid natural gas Stirling dish systems (Mancini et al, 2003). Volumetric receivers transmit solar energy through a fused silica quartz window, and absorb the energy onto porous ceramic foams as shown in Figure 2-9 (Teagan, 2001**,** Mancini et al, 2003). These receivers have the potential to operate at a higher temperature, have larger heat transfer areas, reduce engine dead volumes, and reduce the amount of expensive high temperature alloys in current Stirling engines (Teagan, 2001). One drawback to volumetric receivers is that the quartz window prevents approximately ten percent of the solar radiation from entering the receiver. Convection and radiation losses from the receiver are reduced, however, so the net effect of a reduction in radiation entering the receiver may be minimal.

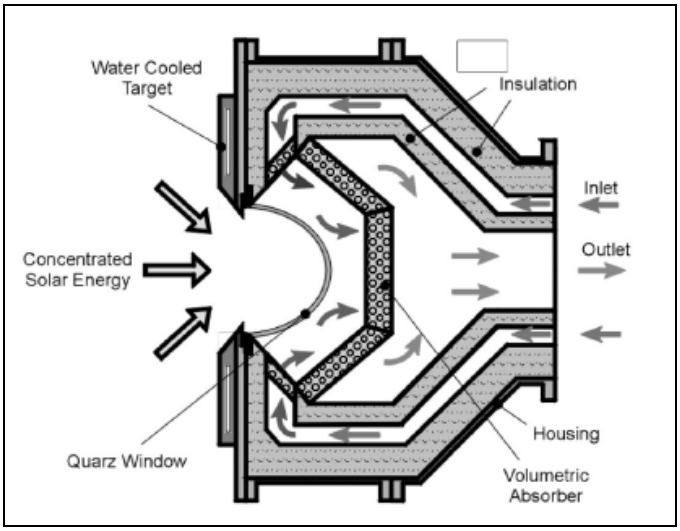

Figure 2-9 Volumetric Stirling receiver design (Diver, 2001)

2.2.1 Receiver Losses

The receiver of a Stirling dish system is responsible for the majority of the thermal losses that occur before the energy is converted into electricity in the Stirling engine. The collector losses due to the mirror reflectivity comprise of 37 % and 24 % of the thermal losses for the SES and WGA collectors respectively, the receiver intercept losses represent 12 % and 0 % of the total thermal losses for the SES and WGA systems, and the receiver thermal losses (conduction, convection, radiation) consist of 51 % and 76 % of the total thermal losses for the SES and WGA systems respectively (Mancini et al, 2003). A breakdown of the losses in a Stirling dish system is presented in Figure 2-10.

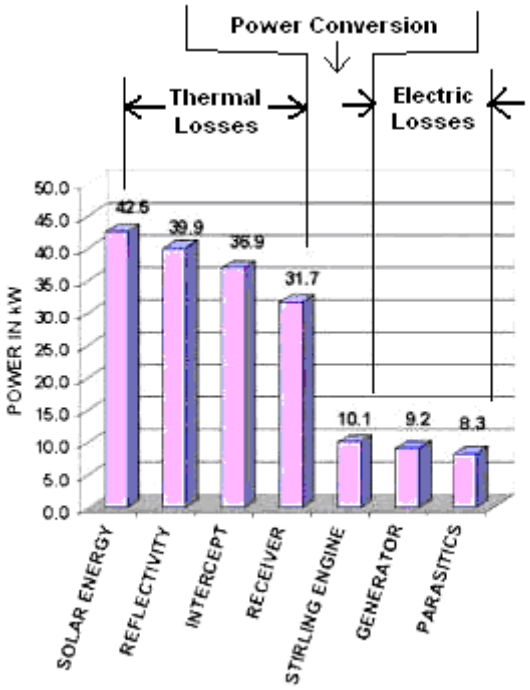

Figure 2-10 Energy waterfall chart for the SBP system at 1000 [W/m^2] insolation level (Mancini et al, 2003)

It is clear that losses in the receiver represent a significant fraction of the total system losses, and an accurate representation of these losses is necessary for a long term energy prediction model. Mechanisms that contribute to the total receiver thermal loss include conduction through the receiver housing, convection from the cavity, and radiation through the aperture opening to the ambient environment. A receiver energy balance with the loss mechanisms can be viewed in Figure 2-11.

Conduction losses through the receiver housing represent a small fraction of the total receiver loss, natural convection losses represent about 40 % of the receiver losses, and radiation is the primary receiver loss mechanism. Radiation represents the largest fraction of receiver losses during mid-day periods when the receiver orientation reduces the convection losses, but convection can represent the majority of losses during the morning or evening when the aperture is oriented horizontally (Hogan, 1991). A literature review was performed to understand the state-of-the-art in predicting each receiver loss mechanism.

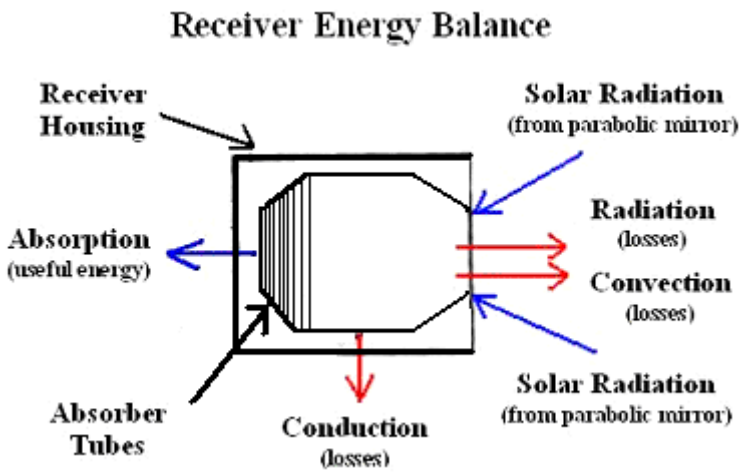

Figure 2-11 Receiver energy balance for a Stirling dish system

2.2.2 Conduction Losses

The receiver conduction losses represent a small fraction of the receiver thermal losses. As the temperature of the absorber and receiver walls increases, conduction through the receiver housing to the ambient air occurs at a more rapid rate. Fourier's law describes conduction in Equation (2.12) (Incropera and DeWitt, 2002).

$$\dot{q}_{conduction} = -k \cdot A \frac{dT}{dx} \tag{2.12}$$

where k is the thermal conductivity of a material, A is the surface area perpendicular to the temperature gradient, and dT/dx is the change in temperature over the distance parallel to thermal flow. The losses due to conduction through the receiver housing are also dependent on the convective heat transfer on the exterior of the receiver housing, so a series resistance model can be used to obtain the total conductive losses. The total losses resulting from conduction is given by Equation (2.13).

$$\dot{q}_{conduction} = \frac{T_w - T_{amb}}{R_{cond} + R_{conv}} \tag{2.13}$$

For planar geometries:

$$R_{cond} = \frac{L}{k \cdot A_{cond}} \tag{2.14}$$

$$R_{conv} = \frac{1}{h \cdot A_{conv}} \tag{2.15}$$

where T_w is the interior wall temperature of the receiver, T_{amb} is the ambient temperature, R_{cond} and R_{conv} are the conduction and convection resistances respectively, L is the width of the receiver insulation, h is the convective heat transfer coefficient of the exterior of the receiver housing, and A_{cond} and A_{conv} are the areas associated for conduction and convection correspondingly.

Conduction losses are minimal in the Stirling dish receiver since they can be easily controlled by adding insulation without appreciable losses in other components in the Stirling dish system. There is a drawback to increasing the insulation thickness, however. As the insulation thickness increases, there will be an increase in the shaded area in the center of the parabolic mirror. Mirror shading represents a significant loss since the approximate cost of the collector surface is about $390 per square meter for 2005 estimates, and mirror shading also represents a reduction in power generation (Teagan, 2001).

This shading limitation can be overcome by removing the parabolic mirror from the center of the parabola on downwards where the support structure or receiver housing tends to shade the mirror as can be seen in Figure 2-12. The shading caused by the receiver housing, Stirling engine, and support structure will still negatively impact the efficient use of land even if it does not shade the mirror surface. Stirling dish systems currently have the highest net efficiency for CSP technologies, and should therefore use land more effectively to produce power.

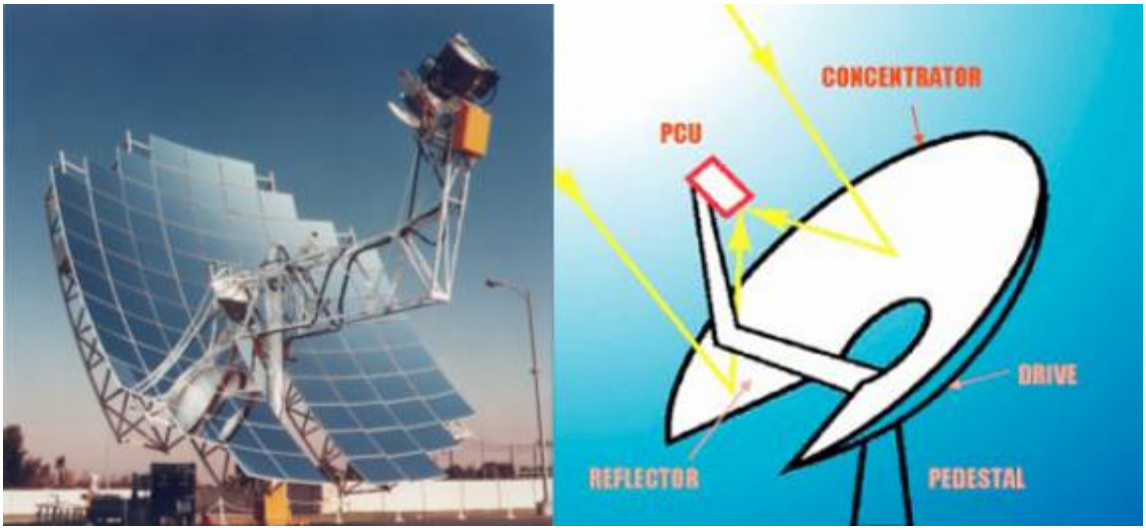

Figure 2-12 Removal of parabolic mirrors in the shaded center and lower portion (SES, 2006), (Mancini et al, 2003)

To minimize conduction in the receiver housing, an insulation thickness of 75 mm has been suggested as an effective width (Harris, 1985). This thickness was selected primarily as a means to minimize conduction through the receiver housing, while at the same time, minimizing the shading of the Stirling dish mirror. High temperature ceramic fiber insulation has been used in receiver housings and one type has a temperature dependent thermal conductivity ranging from 0.061 W/m-K at 550°C to 0.094 W/m-K at 900°C (Harris, 1985). With an effective insulator, conduction losses should represent less than 2 % of the total receiver losses and only a fractional amount of the losses in the total Stirling dish system (Hogan, 1991).

2.2.3 Natural Convection Losses

The convective losses in the receiver represent a significant fraction of the total losses in a Stirling dish system. Experimental tests performed at Sandia National Labs indicate that convection losses may represent about 25 % of receiver losses during noon, and about 40 % during the morning and evening hours in the middle of October in Albuquerque, New Mexico (Hogan, 1991). In one parabolic collector and receiver system tested (Stine and McDonald, 1988), the receiver losses were determined to be 11 % of the total solar radiation entering the receiver on a clear day at noon; this percent increased in the morning, evening, winter and at lower insolation levels due to an increase in convection losses. It is apparent that convective losses represent a large fraction of the total Stirling dish system losses and the receiver losses, and are very dependent on aperture orientation.

Convective losses are a function of cavity temperature and geometry, aperture orientation and diameter, wind velocity, and the effectiveness of the wind skirt. Convection losses are greatest in the morning and evening, and become less significant during the middle of the day with a dependence on the latitude of the systems. This dependence of convection losses with time of day results from the orientation of the receiver while tracking the sun. At noon, the receiver is pointed more vertically (with the receiver aperture facing down towards the ground) than during the early morning and late afternoon, in which orientation is more horizontal; thereby, creating a more stable convective situation. These losses are also dependent on the time of year and location since the angle between the sun and a horizontal surface changes with respect to these, and therefore affects the orientation of the receiver aperture.

A controlled experiment conducted by Stine and McDonald aimed to measure the receiver convection losses in the absence of wind based on different elevation angles (Stine and McDonald, 1988). A hot fluid was passed through the receiver to obtain a steady-state temperature in the absorber. The radiation losses were measured using a windowless HyCal radiometer; the conduction was obtained by measuring the power required to keep the absorber at a constant temperature after placing an insulating plug in the aperture opening; and the convection losses were obtained by subtracting the radiation and conduction losses from the total losses (Stine and McDonald, 1988).

Stine and McDonald found that the total receiver losses more than doubled from 1.5 kW to 3.5 kW (at 600˚F) as the aperture orientation changed from 90 degrees (downward) to 0 degrees (horizontal) as a result of increased convection. The influence of aperture orientation can be seen in Figure 2-13 from an experiment using variations in salt concentration to represent the variances in warm and cold air densities. As the aperture becomes oriented towards 90 degrees downward, the stagnation zone fills the entire cavity and does not allow for the more buoyant hot air to escape.

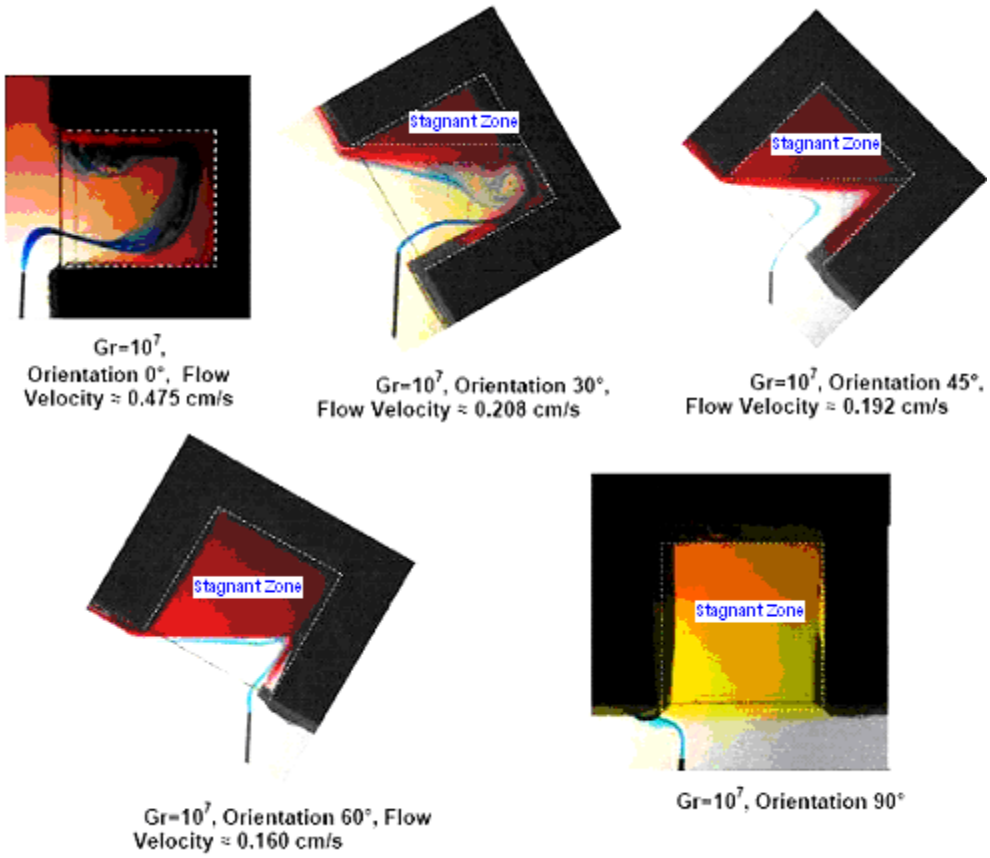

Figure 2-13 Larger stagnation zones occur as the aperture faces downwards indicating lower convection losses (Yeh et al, 2005)

The cavity geometry also has an influence on the convective losses. The three most important features of the receiver geometry include the aperture diameter, cavity average diameter, and the cavity surface area. Increasing the internal cavity diameter with respect to the aperture diameter will reduce convective losses since the smaller aperture opening will impede the motion of hot air escaping. Increasing the cavity surface area will also have an effect on reducing air currents out of the aperture and will therefore also reduce convective losses. The influence of the cavity shape such as elliptical or spherical has been shown to not have a large impact on convection or receiver losses (Harris, 1985). There is also convection from the receiver housing, but this contribution results from conduction through the walls, which was already determined to be small. A summary of the various natural convection correlations can be found in Appendix D.

2.2.4 Forced Convection Losses

The convective losses are a function of the aperture orientation and density of air, but are also highly dependent on the velocity of the wind. If the wind is directed towards the aperture opening, the convection losses will increase significantly, whereas the convection losses will not be as large if the wind is not oriented towards the aperture (Harris, 1985). Total convection losses have been measured to be up to four times that of natural convection with a 4.5 m/s wind directly facing the aperture opening (Harris, 1985). A wind skirt is often used to minimize the

convective losses resulting from the wind and can reduce forced convection losses from four times to twice that of natural convection (Harris, 1985). The best experimental data and forced convection correlation appears to be from Ma (1993).

An experimental setup to test the effect of forced convection using a receiver from the Shanandoah Project was constructed by Ma (1993). These receivers had an aperture diameter of 46 cm which is larger than the 20 cm and 14 cm aperture diameters in the SES and WGA systems respectively. Data were measured with the receiver aperture oriented at 15 or 30 degree intervals between facing horizontal until vertically down. A 4'x4'x14' wind machine generated wind speeds at 6, 8, and 20 miles per hour for side-on tests (wind parallel to the aperture opening plane) and additional speeds of 15 and 24 miles per hour were tested for head-on tests (wind perpendicular to the aperture opening) (Ma, 1993). An organic fluid was passed through the heater tubes to measure the temperature drop and corresponding convective losses with a nominal receiver temperature of 530ºF.

Ma conducted tests to determine the natural convection losses from the receiver for six alternative setups, and the data were consistent with Stine and McDonald's natural convection correlation (Ma, 1993). It is assumed that forced convection is independent of natural convection in the receiver, so the total convection losses can be represented as the sum of the natural and forced convection losses given by Equation (2.16) with the total convection coefficient expressed in Equation (2.17). (Ma, 1993).

$$q_{total,convection} = q_{natural} + q_{forced} \tag{2.16}$$

$$h_{total,convection} = h_{natural} + h_{forced} \tag{2.17}$$

2.2.4.1 Side-on Wind Forced Convection Losses

Side-on wind is defined as wind blowing parallel to the receiver aperture opening. Ma performed side-on wind tests to determine the forced convection heat transfer coefficient (h_{forced}) as a function of wind speed. To estimate the proportion of heat loss attributable to forced convection, Ma subtracted the estimated natural convection losses from the total convective losses and the resulting data were curve fit to obtain the forced convection heat loss coefficient given by Equation (2.18) where $h_{forced,side\text{-}on}$ (W/m^2-K) is the convection heat transfer coefficient and v is the wind speed (m/s) (Ma, 1993). Side-on wind convection losses are independent of the aperture orientation.

$$h_{forced,side-on} = 0.1967 \cdot v^{1.849} \tag{2.18}$$

2.2.4.2 Head-on Wind

Ma also performed head-on wind tests to characterize the convective loss under this regime (Ma, 1993). A head-on wind condition occurs when the wind blows perpendicular to the receiver's aperture opening. Head-on convection is dependent on the aperture orientation, unlike side-on convection, and Ma created a curve fit from data to determine the convection heat transfer coefficient given in Equation (2.19) (Ma, 1993).

$$h_{forced,head-on} = f(\theta) \cdot v^{1.401} \quad (2.19)$$

$$f(\theta) = 0.1634 + 0.7498 \cdot \sin(\theta) - 0.5026 \cdot \sin(2\theta) + 0.3278 \cdot \sin(3\theta) \quad (2.20)$$

where θ is the receiver aperture angle (0º is horizontal , 90º is vertically down).

2.2.5 Concentrator Dish Effect on Reducing Receiver Convection Losses

The forced convection analysis described before did not include an analysis on the effect of the receiver housing or the parabolic dish on the wind speed near the receiver aperture. The forced convection tests were performed with a wind machine, and the receiver was mounted on a test stand without a collector dish. It is reasonable to assume that the collector dish would significantly reduce the forced convection losses depending on the orientation of the collector, receiver aperture, and the wind direction.

Researchers at the Australian National University (ANU) used Fluent software to predict the reduction in wind speed near the receiver aperture for their 20 m^2 parabolic dish system (Paitoonsurikarn and Lovegrove, 2006). A virtual wind tunnel was created with a 30 m width and height, a 75 m tunnel inlet to the parabolic dish, and a 105 m wind tunnel outlet after the dish. The incidence angle was then adjusted between -90 and 90 degrees, and the free stream wind speed was varied between zero and 20 meters per second to determine the reduction in wind near the receiver aperture. A visual of the Fluent model is shown in Figure 2-14.

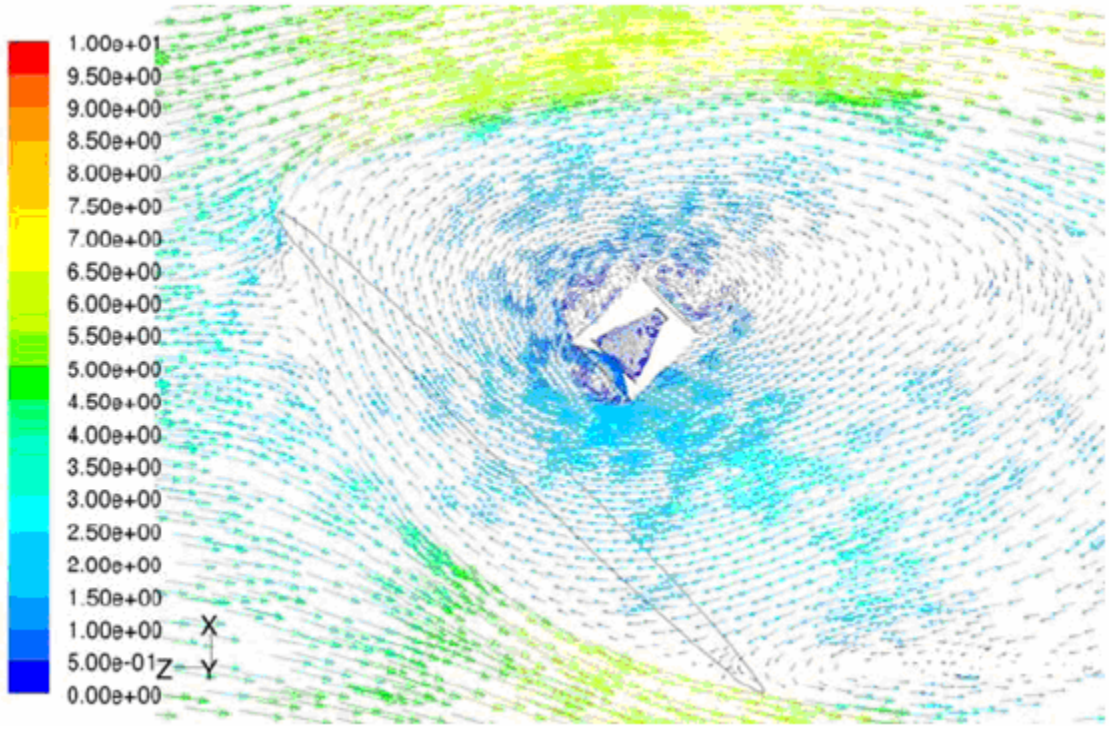

Figure 2-14 Wind velocity determination at the aperture opening for an incidence angle of 45 degrees for a 5 m/s free stream velocity (Paitoonsurikarn and Lovegrove, 2006)

The results of the simulation for the reduction in the wind speed near the aperture opening are given in Figure 2-15. An incidence angle of -90 degrees represents wind from the back of the receiver, an incidence angle of +90 degrees represents wind directed towards the aperture opening (from behind the dish), while an incidence angle of 0 degrees represents side-on wind blowing parallel to the aperture opening. Both a normal and tangential velocity component were determined for each simulation with the velocity tangent to the aperture plane representing only 40 percent of the free stream velocity at a 0 degree incidence angle as shown in Figure 2-15. A correlation of the wind speed normal to the aperture plane is given in Equation (2.21)

$$v_n = c_n \cdot v_\infty \tag{2.21}$$

$$c_n = 0.006934\text{-}0.0003546 \cdot \mathrm{i} + 0.06806 \cdot \cos(\mathrm{i})^4 \tag{2.22}$$

where v_n is the normal velocity and c_n is the fraction of the free stream wind velocity v_∞ for a specific incidence angle i.

The tangential wind component correlation v_t is expressed in Equation (2.23)

$$v_t = c_t \cdot v_\infty \tag{2.23}$$

$$c_t = 0.01581 + 0.002784 \cdot \mathrm{i}\ 0.3771 \cdot \cos(\mathrm{i})^4 \tag{2.24}$$

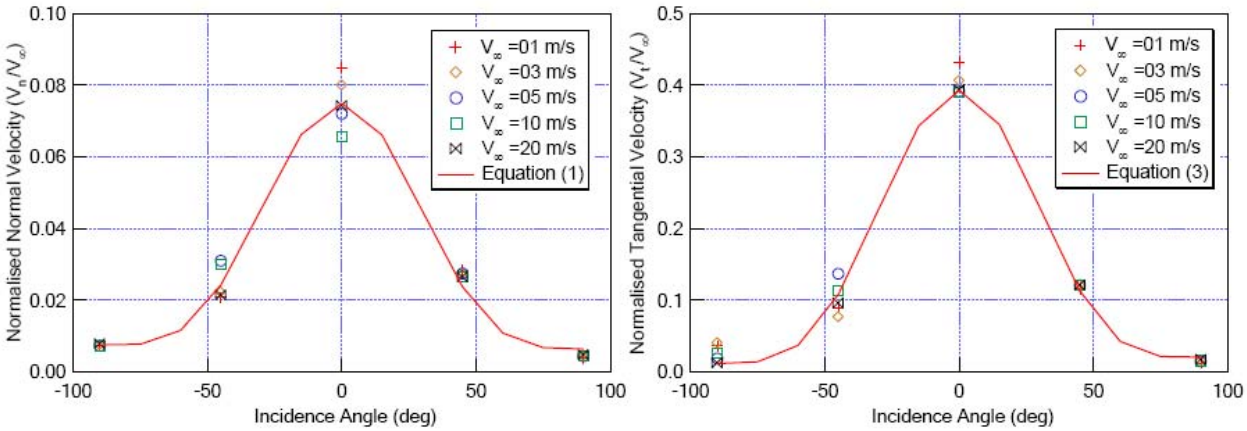

Figure 2-15 Fraction of the free stream velocity for the normal and tangential velocity components at various incidence angles (Paitoonsurikarn and Lovegrove, 2006)

It is important to note that the rim angle of the ANU dish is 70 degrees, which is much greater than the rim angle of the WGA or SES collectors which have rim angles around 40 degrees. The 70 degree rim angle would have a greater shielding impact on the wind as can be viewed in Figure 2-16. The ANU simulation primarily only used Fluent to predict the reduction of wind speed near the aperture. The results of the physical experiment evaluated by ANU only indicated that the wind speed rarely exceeded 2 m/s while the maximum wind speed recorded at the ANU site was 6 m/s (Paitoonsurikarn and Lovegrove, 2006). A more detailed experiment should be used to validate the Fluent model. The model suggested by ANU is not used in the TRNSYS

receiver model due to the differences in collector design and the insufficient quantity of validated experimental data.

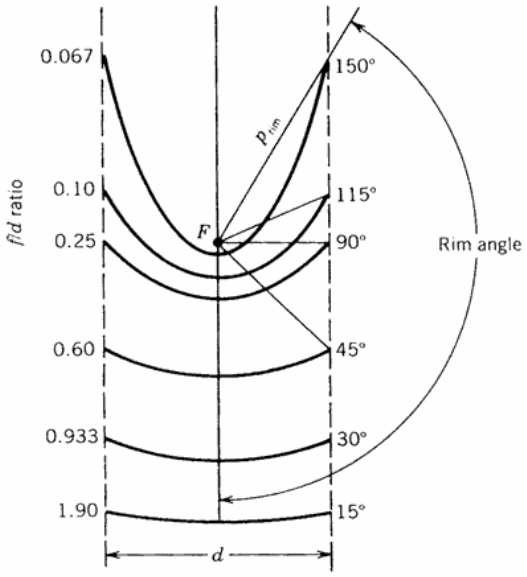

Figure 2-16 Rim angle for a common focus (Stine and Harrigan 1985)

2.2.6 Radiation Losses

The radiation losses in the receiver contribute to a significant fraction of the total losses in the receiver and in the total Stirling dish system. Experimental data obtained at Sandia National Labs indicate that radiation losses may represent about 60 % of receiver losses during the morning and evening, and about 75 % at noon in the middle of October in Albuquerque, New Mexico since convective losses vary throughout the day (Hogan, 1991). Unlike convection losses, radiation losses are relatively constant throughout the day once a steady state temperature has been reached for the heater head temperature.

Radiation due to Emission

There are two ways solar radiation contributes to losses from the receiver. The first results from thermal radiation being emitted from the aperture due to the large temperature difference between the cavity walls and the parabolic mirror. The second results from solar radiation being reflected off from the cavity walls and back through the aperture. The general equation for net radiation exchange due to emission is given by Equation (2.25) (Incropera and DeWitt, 2002). The view factor was assumed to be one since the aperture opening views most of the entire cavity interior.

$$\dot{q}_{radiation} = \varepsilon_{cav} \cdot \sigma \cdot A_{ap} \cdot \left(T_{cav}^4 - T_{amb}^4 \right) \tag{2.25}$$

ε_{cav} is the effective emissivity of the cavity aperture which can be approximated to be equivalent to the effective absorptance of the cavity (or simplified to 1.0 for a blackbody), σ is Stefan Boltzmann's constant, A_{ap} is the surface area emitting radiation (simplified to be the aperture

area), T_{cav} is the temperature of the surface losing net energy due to radiation (cavity interior), and T_{amb} is the temperature of the surface that is receiving net energy (ambient conditions). An estimate for the emissivity of an existing Stirling dish receiver measured at Sandia National Laboratories was about 0.85 (Hogan, 1991). It is important to note in Equation (2.25) that the cavity walls are at a higher temperature than the absorber since thermal energy is not actively removed from the walls as it is from the absorber, so an average internal cavity temperature should be used for T_{cav} in Equation (2.25).

A view factor analysis was also performed and compared with Equation (2.25) and found to have similar results. The view factor from the aperture opening to the cylinder side wall is given in Equation (2.26) (Howell, 2006)

$$F_{1-2} = 1/2 \left(1 - R^2 - H^2 + \sqrt{\left(1 - R^2 - H^2\right)^2 - 4R^2} \right) \tag{2.26}$$

where $H = L_{cav} / r_{ap}$ and $R = r_{cav} / r_{ap}$. The terms L_{cav} is the depth of the cavity, r_{ap} is the radius of the receiver aperture, and r_{cav} is the radius of the internal cavity walls shown in Figure 2-17.

The view factor from the cylinder side wall to the aperture and from the absorber surface to the aperture as shown in Figure 2-17 was found using the reciprocity rule and the summation rule respectively given by Equations (2.27) and (2.28) (Incropera and DeWitt, 2002) where A_1 is the area of surface one, and $F_{1\text{-}2}$ is the view factor from surface one to two and j is the total number of surfaces.

$$A_1 \cdot F_{1-2} = A_2 \cdot F_{2-1} \tag{2.27}$$

$$\sum_{j=1}^{N} F_{1-j} = 1 \tag{2.28}$$

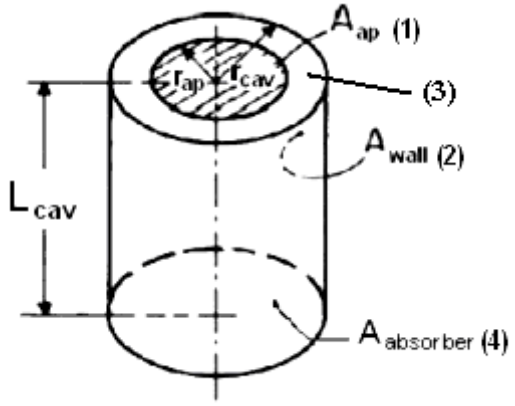

Figure 2-17 Radiation view factors based on these areas

The total thermal losses using view factors is given by equation (2.29)

$$\dot{q}_{radiation,VF} = \varepsilon \cdot F_{2-1} \cdot \sigma \cdot A_{wall} \cdot \left(T_{wall}^4 - T_{mirror}^4\right) + \varepsilon \cdot F_{4-1} \cdot \sigma \cdot A_{absorber} \cdot \left(T_{absorber}^4 - T_{mirror}^4\right) \qquad (2.29)$$

where $F_{2\text{-}1}$ is the view factor between the wall surface and the aperture and $F_{4\text{-}1}$ is the view factor between the absorber surface and the aperture. Equation (2.29) resulted in slightly lower radiation losses than Equation (2.25) but they were within about five percent of each other.

Radiation Reflection without an Aperture Cover

To determine the radiation losses due to reflection off of the cavity surfaces, the effective absorptance of a cavity receiver is required to determine the fraction of energy reflected out of the receiver. The effective absorptance of a cavity receiver without a receiver aperture cover is a function of the inner surface absorptance and the area ratio of the cavity aperture to the inner surface area. The effective absorptance is given by Equation (2.30) where α_{cav} is the cavity surface absorptance, A_a is the cavity aperture area, and $A_{cav,tot}$ is the total inner surface area of the cavity (Duffie and Beckman, 2006). The smaller the ratio is between the aperture area and the cavity surface area, the greater the effective absorptance will be in the cavity receiver. An estimate for the absorptance of the cavity surface (α_{cav}) of an existing Stirling dish receiver measured at Sandia National Laboratories was about 0.87 (Hogan, 1991). The total reflected radiation out of the cavity is given by Equation (2.31) where $\dot{q}_{in,receiver}$ is the total energy intercepted by the receiver aperture.

$$\alpha_{eff} = \frac{\alpha_{cav}}{\alpha_{cav} + \left(1 - \alpha_{cav}\right) * \left(A_{ap} \,/\, A_{cav,tot}\right)} \qquad (2.30)$$

$$\dot{q}_{rad,reflect} = \left(1 - \alpha_{eff}\right) \cdot \dot{q}_{in,receiver} \qquad (2.31)$$

Reflection With an Aperture Cover

The absorptance of a cavity receiver with an aperture cover is similar to the absorptance of a cavity receiver without a cover with the exception that transmittance terms are introduced for the cover material. The receivers used in Stirling dish systems have not typically utilized a cover unless they are operating in hybrid mode where a volumetric receiver with a fuel such as natural gas is used to power the Stirling engine in addition to solar energy. The effective absorptance for a cavity receiver with a cover is given by Equation (2.32) (Duffie and Beckman, 2006).

$$\tau_c \cdot \alpha_{eff} = \tau_c \left[\frac{\alpha_{cav}}{\alpha_{cav} + \left(1 - \alpha_{cav}\right) \tau_d \left(A_{ap} \,/\, A_{cav,tot}\right)} \right] \qquad (2.32)$$

$$\dot{q}_{rad,reflect} = \left(1 - \tau_c \cdot \alpha_{eff}\right) \cdot \dot{q}_{in,receiver} \qquad (2.33)$$

The term τ_c is the transmittance of the cover, and τ_d is the transmittance of the cover for isotropic diffuse radiation, which is the solar radiation reflected by the walls of the inner cavity. For a single glazed glass cover with a KL value of 0.0125, the value for τ_d can be estimated to be 0.82 (Duffie and Beckman, 2006).

Cavity Geometry Influence on Radiation

It would be beneficial to determine how the cavity geometry affects radiation losses in the receiver. Several geometries have been used for the receiver cavity in Stirling dish systems. Five receiver cavity geometries were analyzed, including elliptical, cylindrical, spherical, heteroconical, and conical designs as shown in Figure 2-18 (Harris, 1985). It has been found that the geometry of a receiver cavity has less than a three percent impact on the yearly thermal receiver performance (much less than one percent net power), and primarily just modifies the flux distribution on the absorber (Harris, 1985). Mapping the flux distribution was simulated with AEETES software developed by Sandia National Laboratory, which can be used to design a receiver geometry that minimizes hot spots in the receiver (Hogan, 1991). Flux mapping was not deemed necessary for the long term energy production model since it has ramifications on economics due to receiver degradation, and not much significance for energy production.

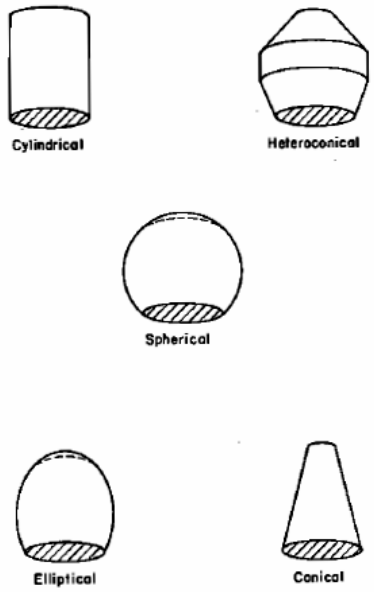

Figure 2-18 Cavity geometries analyzed to find geometry has less than a 3 % variation in receiver losses (Harris, 1985)

2.2.7 Receiver Thermal Loss Summary

Conduction, convection, and radiation from the receiver contribute to a large fraction of the total energy lost in the Stirling dish system. The conduction losses are a small proportion of the total system losses and are effectively controlled by modifying the receiver's insulation thickness. Natural convection losses contribute to about forty percent of the total receiver losses and increase with an increase in wind velocity, with a horizontal facing aperture and convection

losses can be significantly reduced by placing a glass or quartz window over the aperture opening; however, the cover will diminish the available radiation to the absorber. Long-wave radiation losses contribute to approximately sixty percent of the total losses in a Stirling dish system and are minimized by increasing the absorptance of the cavity, increasing the surface area of the cavity, adding an aperture cover, or by decreasing the aperture diameter. A balance must be made between sizing the receiver aperture diameter that will optimize the net system power taking into account the intercept factor and receiver losses.

2.3 Stirling Engine Design

The Stirling engine is an external heat (or combustion) engine that converts heat from the absorber to mechanical power in a manner similar to internal combustion engines. Unlike internal combustion engines, however, heat is applied externally to the piston heater head in a Stirling engine. Because the Stirling engine relies on an external source for heat input, the cycle itself operates as a closed system since the working fluid is contained within the cylinders and not vented to atmosphere like exhaust gases from internal combustion engines. The addition of a regenerator into a Stirling engine improves the efficiency of the engine by pre-cooling the working fluid as it moves from the expansion space to the compression space, and pre-heating the working fluid as it moves from the compression space into the expansion space. The working fluid is often hydrogen which is heated to over 700°C with a maximum pressure around 20 MPa yielding a thermal-to-mechanical efficiency of approximately 40 % (Teagan, 2001). The compression space is cooled by a refrigerant loop that circulates a secondary fluid through a common automotive radiator with forced air cooling provided by a fan.

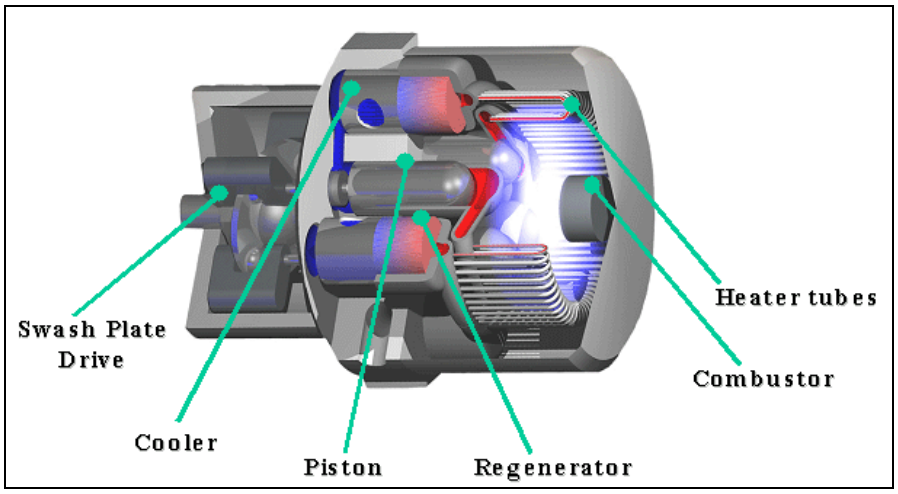

Figure 2-19 Stirling engine components (STM website, 2006)

The Stirling engines applied in dish systems include the SOLO 161 11 kW engine from Germany, the Kockums (previously United Stirling) 4-95 25 kW engine from Sweden, and the Stirling Thermal Motors STM4-120 25 kW engine from the United States (Teagan, 2001). The SOLO engine has been used for cogeneration projects and the Euro/Enviro dish research. The Kockums 4-95 engine is the power unit for the Stirling Energy Systems (SES). The STM4-120

was developed by General Motors and the Department of Energy as part of the Next Generation (Hybrid) Vehicle Program (SolarPACES, 2007).

Advantages of Stirling Engines (Urieli and Berchowitz, 1984)

1. Maximum potential efficiency for a heat engine operating between the same temperatures
2. Flexible fuel usage such as biomass, solar, geothermal, waste heat, and fossil fuels
3. Lower nitrogen oxides compared to internal combustion engines
4. Quiet and minimal vibration
5. Free-piston Stirling engines have very high reliability
6. Stirling engines allow for operation as a refrigerator or a heat pump
7. Have the highest specific work output for any closed regenerative cycle

Disadvantages of Stirling Engines (Urieli and Berchowitz, 1984)

1. Stirling engines often have a slower response to an increase or decrease in load
2. Lower specific power output so added weight and volume would be less practical for automotive purposes
3. Hydrogen or helium seals can be problematic for kinematic Stirling engines

2.3.1 Stirling Engine Types

There are two common types of Stirling engines that have been used for power production: the kinematic and the free-piston engine. Kinematic engines have the power piston connected to the crankshaft by a connecting rod, which is attached to a cross-head to eliminate lateral forces against the cylinder walls (Stine, 1999). A linear seal is used between the cross-head and piston to seal the region between high and lower pressures to allow the bearing surfaces to remain lubricated in the low-pressure area while preventing fouling of the heat exchanger surface in the high-pressure region (Stine, 1999). Kinematic Stirling engines are currently being used in the Stirling dish systems by all of the major manufacturers.

An alternative design to the crankshaft with the cross-head is to use a swash plate or wobble-plate drive. A slanted drive surface is connected to the drive shaft at an angle and moves the fixed piston push rods up or down while the drive surface rotates (Stine, 1999). The stroke length can be controlled by varying the drive surface angle with respect to the axis of rotation (Stine, 1999). The STM 4-120 engine uses a variable-angle swash plate to control the power of the engine by using a variable stroke as previously stated.

Free-piston Stirling engines do not have the power piston connected to a crankshaft, but rather cycle back and forth between the working fluid and a spring which is often another gas (Stine, 1999). The displacer is allowed to bounce on gas or mechanical springs, which are incorporated into the Beale free-piston design. The spring and mass system control the frequency, piston stroke, and timing between the two pistons. Power is generated by attaching a magnet to the power piston and moving it past stationary coils that act as a linear alternator, or the engine can be used to drive a hydraulic pump. Free piston Stirling engines only have two moving parts, no dynamic seals are required to seal the high and low pressure region since electricity is generated internally, and oil lubrication is not required (Stine, 1999). This enables the free-piston engines to have a lower cost, longer life, and minimal maintenance with respect to kinematic Stirling engines. A 6 kW free piston Stirling engine system was tested by Cummins Power Generation

and Sunpower to have a 28 % demonstrated efficiency operating with a 629°C expansion space temperature (Stine and Diver, 1994). The free-piston Stirling dish system by Sunpower had a comparable net efficiency to the SBP kinematic engine system (Stine and Diver, 1994), but no free-piston Stirling dish systems are currently planned for direct solar dish applications.

2.3.2 Stirling Engine Configurations

There are three basic engine design configurations that have been used for Stirling engines. These include alpha, beta, and gamma configurations. The alpha configuration uses a separate cylinder for the expansion and compression space while the beta and gamma configurations use a displacer piston to move the working fluid between the expansion and compression spaces. Variations on the alpha and beta engine configurations are shown in Figure 2-20

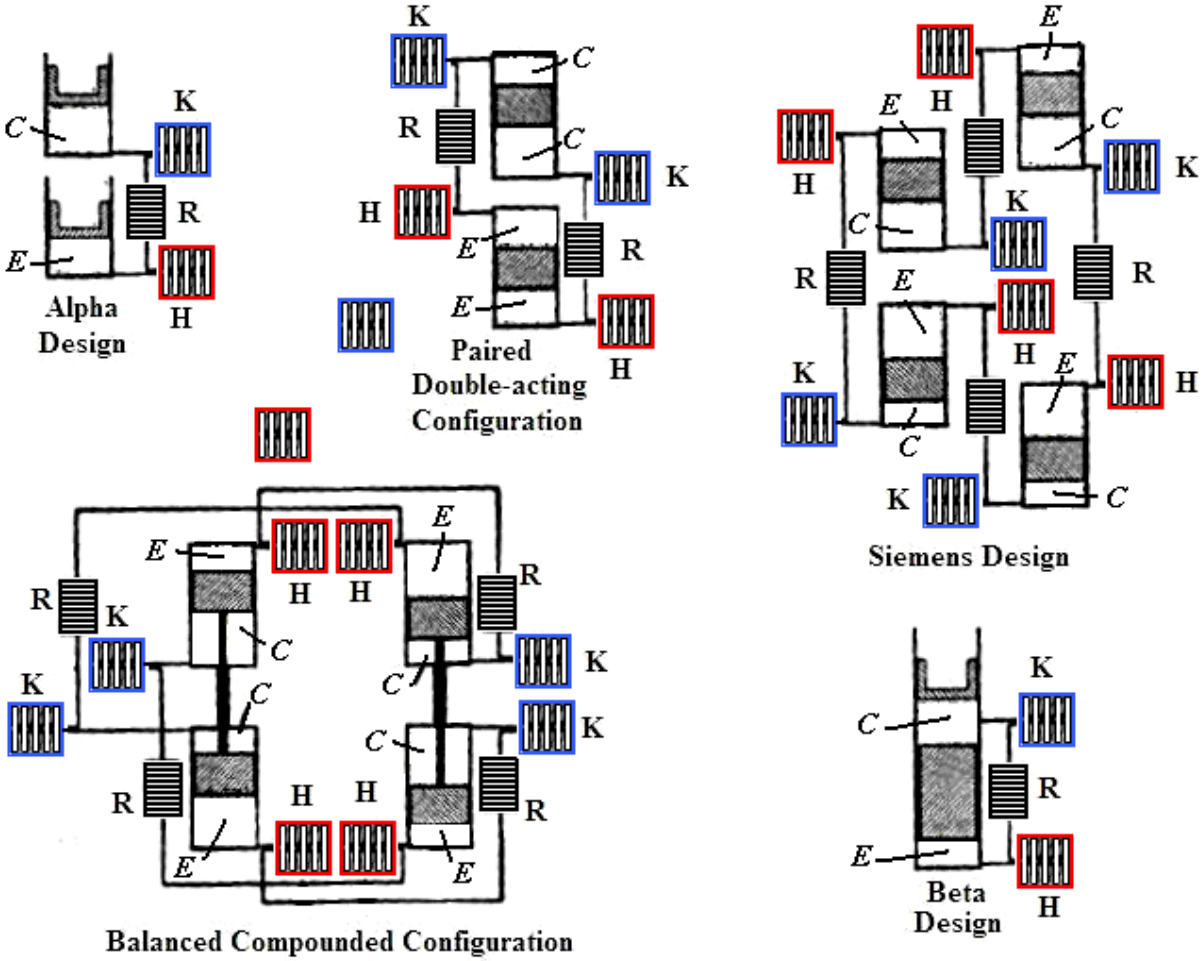

Figure 2-20 Stirling engine configurations redrawn from Finkelstein, 1998. E=expansion C=compression H=heater K=cooler R=regenerator

2.3.2.1 Alpha Configuration

An alpha configuration Stirling engine uses a separate cylinder for the expansion and compression space and has two pistons moving out of phase (Stine, 1999). Alpha arrangements

have the advantage of being arranged with multiple cylinder configurations to enable a high specific power output (Urieli and Berchowitz, 1984). There are four processes in the Stirling cycle which will be described for the alpha configuration below.

Process 1-2: **Compression**
The majority of the expanded gas is in the compression cylinder and the gas cools as it transfers heat to the external sink. The working fluid contracts as it cools and pulls both pistons away from the crankshaft as shown in Figure 2-21.

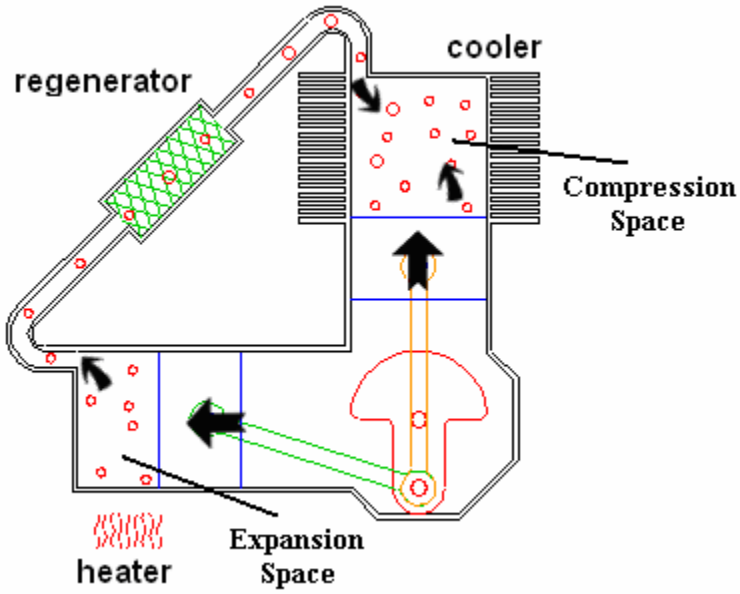

Figure 2-21 Alpha engine compression phase (Keveney, 2001)

Process 2-3: **Transfer of heat from the regenerator to the working fluid**
Most of the contracted gas is still in the compression cylinder as shown in Figure 2-22. The momentum of the flywheel continues to turn the crankshaft an additional 90 degrees as the working fluid is transferred back into the expansion cylinder. While the gas moves through the regenerator, it absorbs thermal energy.

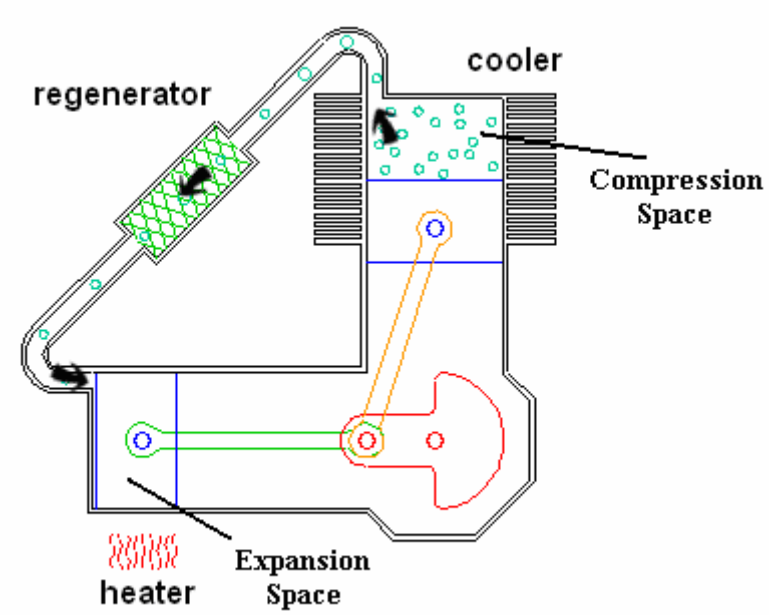

Figure 2-22 Alpha engine heat transfer from the regenerator to the working fluid (Keveney, 2001)

Process 3-4: Expansion

Most of the working fluid is in the expansion space where it is heated from an external source such as solar energy or biomass. The gas expands in the expansion space and through the regenerator while driving both of the pistons inward as shown in Figure 2-23.

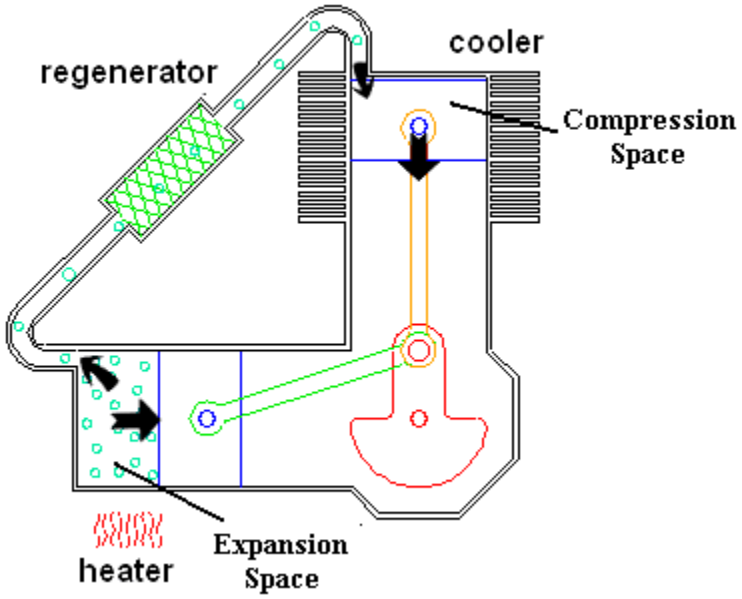

Figure 2-23 Alpha engine expansion phase (Keveney, 2001)

Process 4-1: **Heat transfer from the working fluid to the regenerator**

Most of the gas is still in the expansion space as the flywheel momentum turns the crankshaft an additional 90 degrees. This causes the remaining gas to be pushed through the regenerator into

the compression space as shown in Figure 2-24. Heat is transferred from the working fluid to the regenerator in this step.

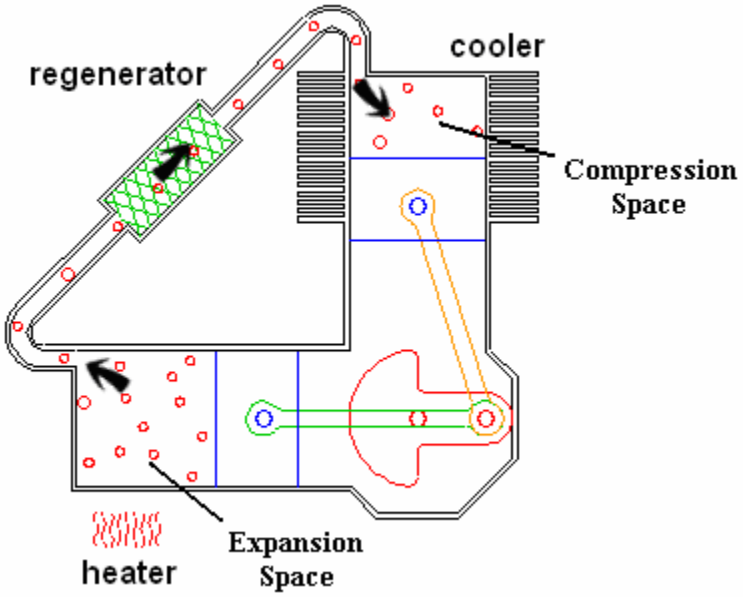

Figure 2-24 Alpha engine heat transfer from the working fluid to the regenerator (Keveney, 2001)

Most of the Stirling engine manufacturer's produce an alpha type Stirling engine for the Stirling dish systems. The Schlaich Bergermann und Partner V-160 has a typical alpha configuration engine with just one cylinder for the expansion space and one for the compression space. The SES (United Stirling/Kockums) 4-95 and the Stirling Thermal Motors STM 4-120 both use an alpha type Siemens (or Rinia) configuration (Stine, 1985). The Siemens configuration does not use two separate pistons, but rather uses the front and back side of one piston called a double-acting piston (Stine, 1999). With a double-acting piston, the volume of the front side of one piston is connected to the volume of the back side of another piston through the heater, regenerator, and cooler as shown in Figure 2-25 (Stine, 1999). The Siemens arrangement involves four cylinders each with a double-acting piston 90 degrees out of phase with the next cylinder. The alpha Rinia arrangement greatly improves the engine efficiency over the common alpha arrangement.

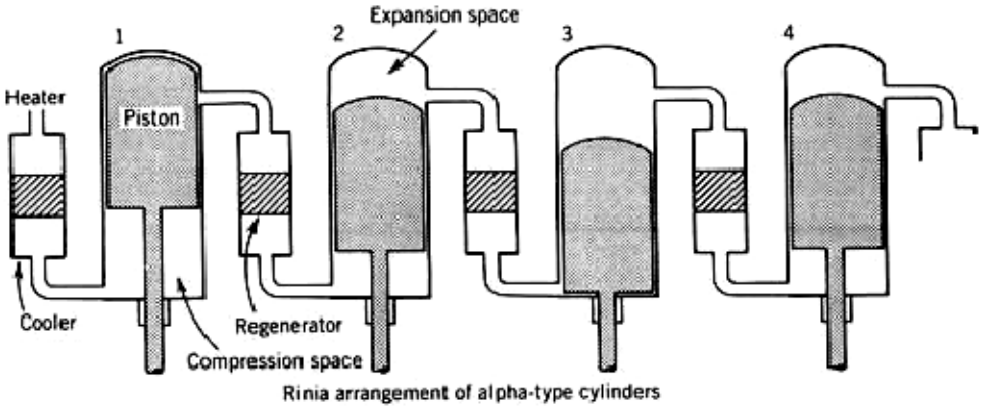

Figure 2-25 Alpha type Rinia-Siemens arrangement (Stine, 1999)

2.3.3 Power Control

For most Stirling engines, the engine power is controlled by varying the mean pressure within the expansion and compression space by varying the mass of the working fluid. This is accomplished by pumping gas in or out of the engine from an external tank (Walker, 1980). To increase the power from the Stirling engine, a system of valves is used to move high pressure gas from an external tank to the engine, and to decrease power, the working fluid is compressed back into the external tank (Stine, 1999).

Another method to control the Stirling engine power is to vary the volume within the piston cylinders with a variable stroke engine such as the SAIC (STM 4-120) Stirling engine (Walker, 1980). This method for power control can be accomplished by using a variable angle swash plate drive which enables the stroke to be controlled (Stine, 1999). This method effectively alters the displaced volume during each cycle and therefore changes the output power.

2.3.4 Regenerator

A regenerator consisting of many metal mesh disks is often used in Stirling engines to improve the efficiency of the engine (Stine, 1994). Thermal energy is absorbed by the regenerator when working fluid passes from the expansion space to the compression space, and therefore cools the working fluid before entering the compression space. Thermal energy is transferred from the regenerator to the working fluid and it is therefore pre-heated when the working fluid moves from the compression to the expansion space. The regenerator in a Stirling engine can obtain efficiencies of greater than 98 %, which indicates the working fluid will leave the regenerator close to the temperature of the space it occupies (Urieli and Berchowitz, 1984). A regenerator does not improve the output power of a specific engine design, but rather contributes to a minor reduction in output power due to the pressure losses across the regenerator. A large improvement in engine efficiency by using a regenerator far outweighs the minor reduction in specific power.

2.3.5 Stirling Engine Working Fluids

Working fluids commonly used in Stirling engines consist of air, helium, or hydrogen. The selection of a specific working fluid is based on the following fluid properties: thermal conductivity, specific heat, density, and viscosity. A working fluid with a higher thermal conductivity, density and higher specific heat will improve the heat transfer capabilities of the gas and improve the efficiency of the heat exchangers. A working fluid with a lower density and viscosity will reduce the pressure drop through the regenerator, working space, and dead space and consequently improve the engine efficiency. Two dimensionless numbers related to heat transfer are the Prandtl and Grashof numbers given by Equation (2.34) and (2.35) where g is the gravitational constant, β is the thermal expansion coefficient, T_s is the source temperature, T_∞ is the ambient temperature, L is the characteristic length, μ is the dynamic viscosity, k is the thermal conductivity, and υ is the kinematic viscosity. Increasing both of these numbers would improve the heat transfer capabilities of the heater and cooler and therefore improve the efficiency of the engine.

$$G_r = g \cdot \beta \cdot (T_s - T_\infty) \cdot L^3 / \upsilon \cdot \alpha \quad (2.34)$$

$$P_r = C_p \cdot \mu / k \quad (2.35)$$

Air can be used as a working fluid since it has a higher density than hydrogen or helium, and there will be less seal losses (Stine, 1999). The temperature of internal components is limited when using air in the engine since the materials will degrade due to the presence of oxygen, so the system efficiency can be negatively affected. Using air as a working fluid is not a good choice for high performance Stirling engines because air has a low thermal conductivity and therefore cannot maintain an increase in the engine efficiency at higher engine speeds. Estimates for the performance of the three working fluids can be observed in Figure 2-26 at various operating speeds.

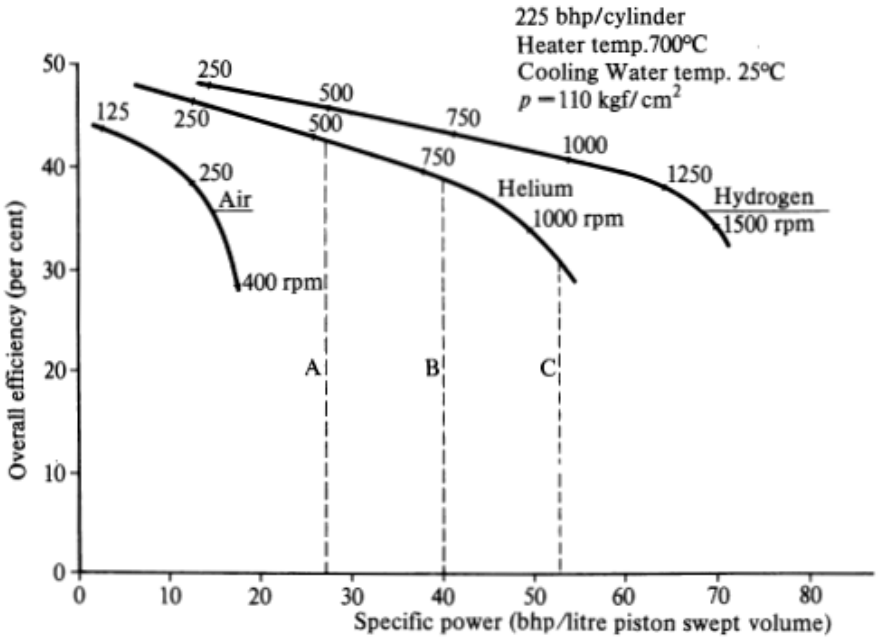

Figure 2-26 Calculated performances for Stirling engines with several working fluids (Walker, 1980)

The working fluid for high performance Stirling engines is often hydrogen or helium since they have a larger thermal conductivity and thermal capacitance than air as shown in Figure 2-27 and Figure 2-28 respectively. Each of the four Stirling cycle processes last less than 10 ms in an engine, so the choice of the working fluid depends highly on the thermal conductivity of the gas (Stine and Harrigan, 1985). A higher specific heat for the working fluid also improves the effectiveness of transferring energy to the regenerator. The heat transfer capability of the working fluid has been shown to be related to the density and specific heat with the following correlation (Walker, 1980):

$$Q \propto \sqrt{\rho^2 \cdot C^3} \propto \sqrt{M^2 \cdot C^3} \quad (2.36)$$

Hydrogen has the highest factor for the heat transfer in equation (2.36) with a value of 104 $kJ^{1.5}/(kg^{0.5}\text{-}K^{1.5}\text{-}kmol)$, then helium with 44, and finally air at 29 (Walker, 1980). Hydrogen should be the most effective working fluid at transferring heat, which is supported with a performance comparison with helium. Sandia labs tested the STM 4-120 engine with helium and hydrogen in the same engine and found that the average efficiency with helium was around 24 % and the average with hydrogen was 26 % (Andraka, 1996). The power output of the engine also increased about 1.5 kW from about 17.0 kW using helium to 18.5 kW using hydrogen.

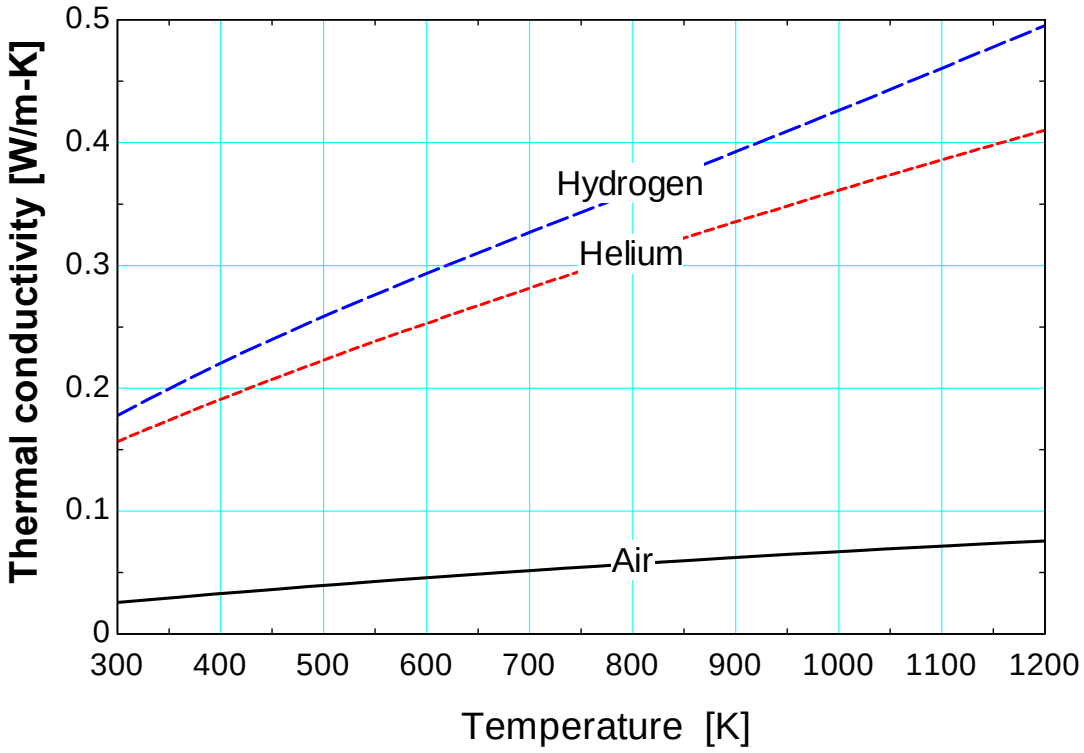

Figure 2-27 Thermal conductivities of working fluids as a function of temperature (Klein, 2007)

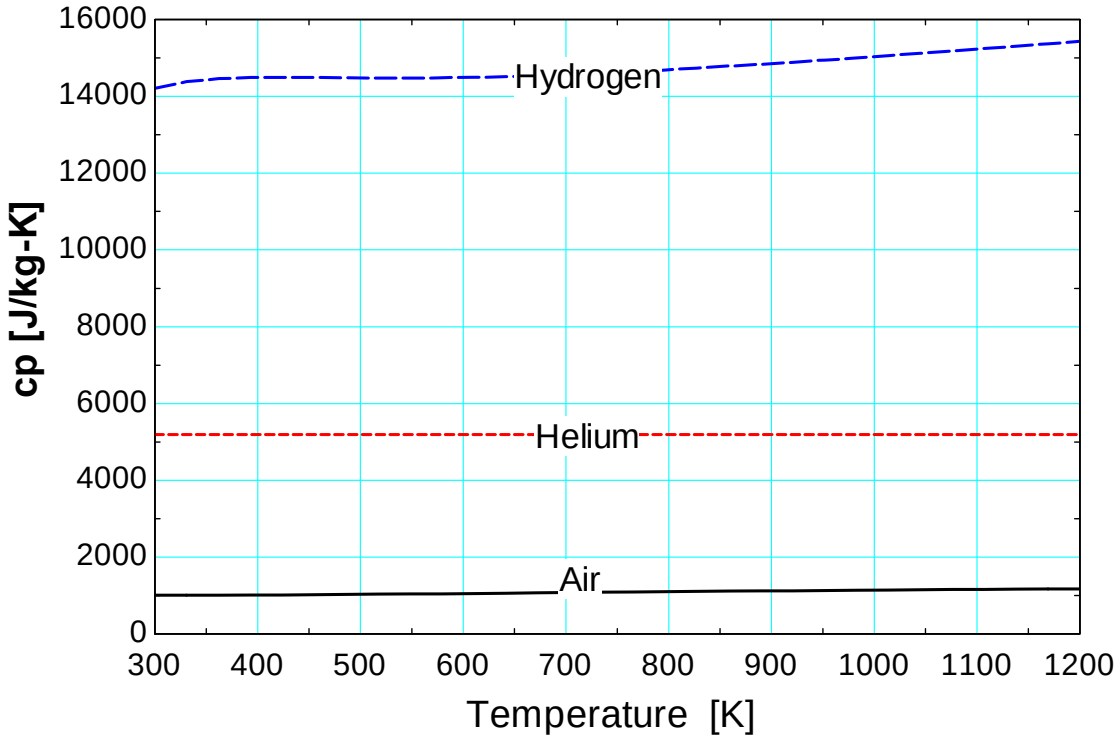

Figure 2-28 Specific heats for working fluids as a function of temperature (Klein, 2007)

The pressure losses in the working spaces and the regenerator are dependent on the viscosity and density of the working fluid. A working fluid with a lower viscosity and density will result in lower pressure drops, which in principle improves thermal efficiency. A comparison of the viscosities and densities for the working fluids is given in Figure 2-29 and Figure 2-30 respectively.

Despite the many benefits of using hydrogen and helium for the working fluids, one disadvantage of helium and hydrogen is that the seal losses will be greater and more difficult to control. Two additional drawbacks of hydrogen are that it may absorb into various materials causing hydrogen embrittlement, and it is combustible when in contact with oxygen. Overall, hydrogen is the primary choice for the working fluid since it has the most effective transport properties to improve the Stirling engine performance.

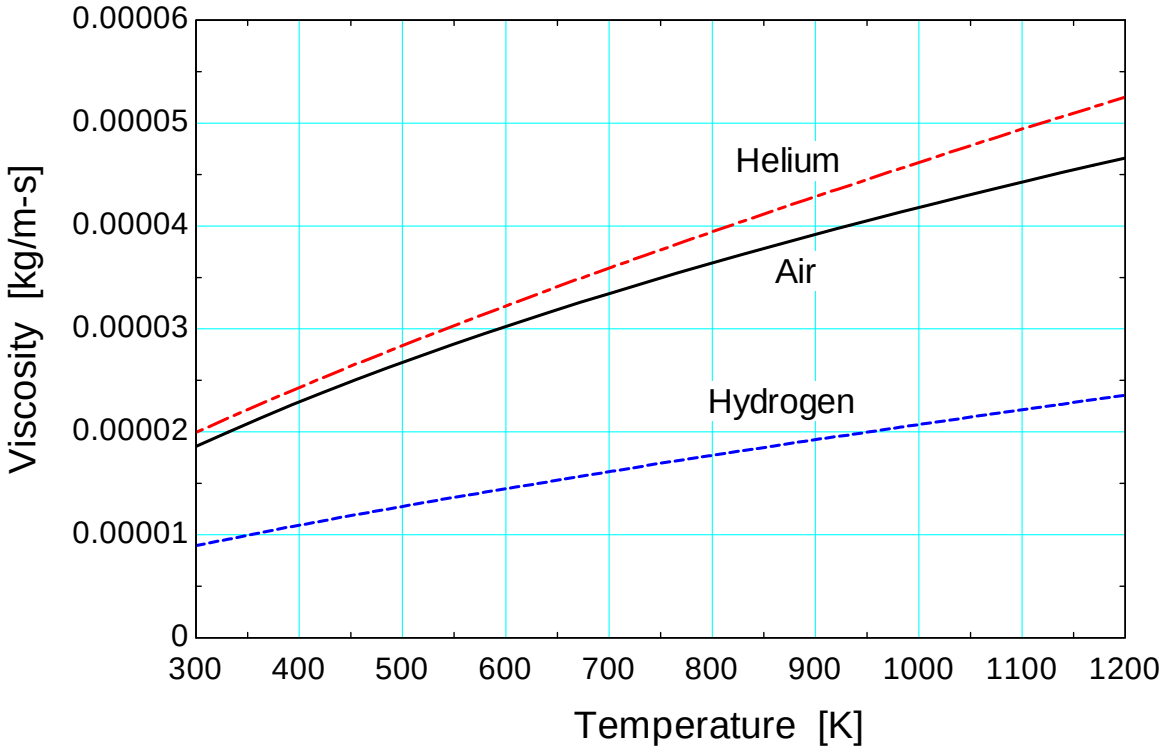

Figure 2-29 Viscosity for working fluids as a function of temperature (Klein, 2007)

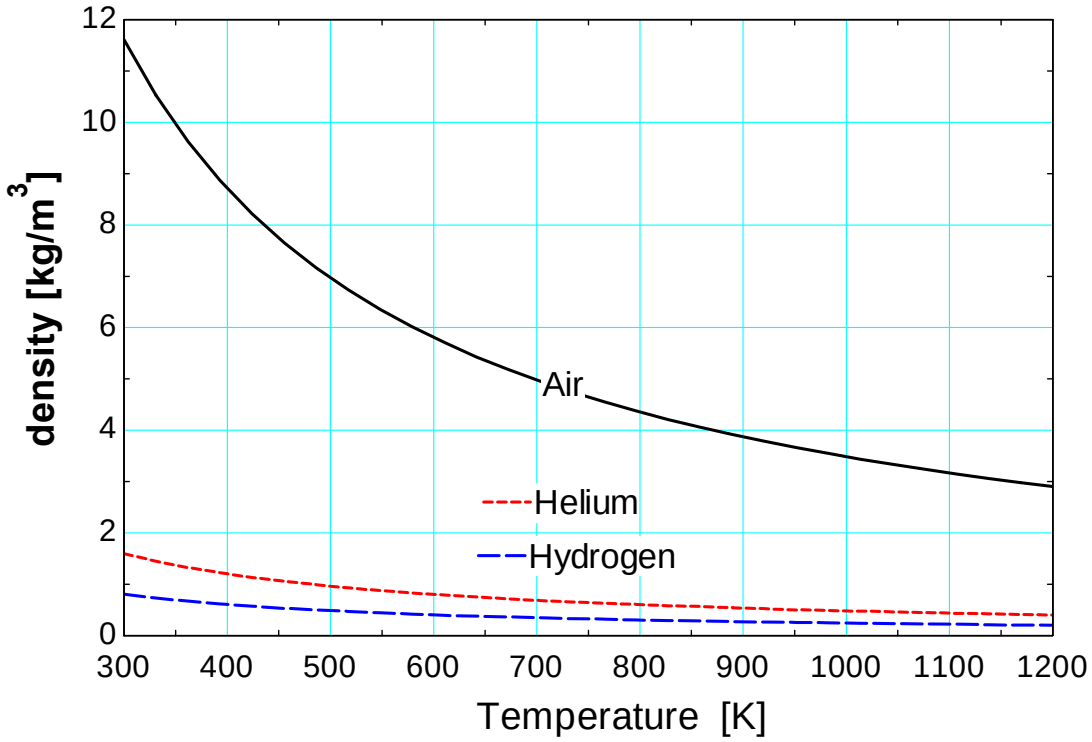

Figure 2-30 Working fluid densities as a function of temperature (Klein, 2007)

2.4 Stirling Engine Analysis Methods

The Stirling engine performance can be analyzed using many different existing methods. These methods range from the most ideal cases such as the Ideal and Adiabatic analyses, to a slightly more realistic model of a Stirling engine using the Quasi-Steady flow method, to the most practical Stirling engine performance prediction models that have been validated against data. The following sections will summarize the theoretical and practical models that exist for predicting Stirling engine performance.

2.4.1 Ideal Stirling Engine Analysis

The ideal Stirling cycle consists of four internally reversible processes as depicted in Figure 2-31 (Moran and Shapiro, 2004).

Process 1-2: Isothermal compression at a temperature T_C while transferring heat from the working fluid to an external sink.

Process 2-3: Constant volume heating of working fluid by the regenerator

Process 3-4: Isothermal expansion at a temperature of T_H. External heat transfer to working fluid

Process 4-1: Constant volume cooling. Heat transfer from working fluid to regenerator

A regenerator with a theoretical 100 % effectiveness stores some of the energy rejected in process 4-1 and uses it in the heat input process 2-3. Heat at temperature T_H is supplied externally in process 3 and 4; energy rejection from the system at temperature T_C occurs in process 1 to 2.

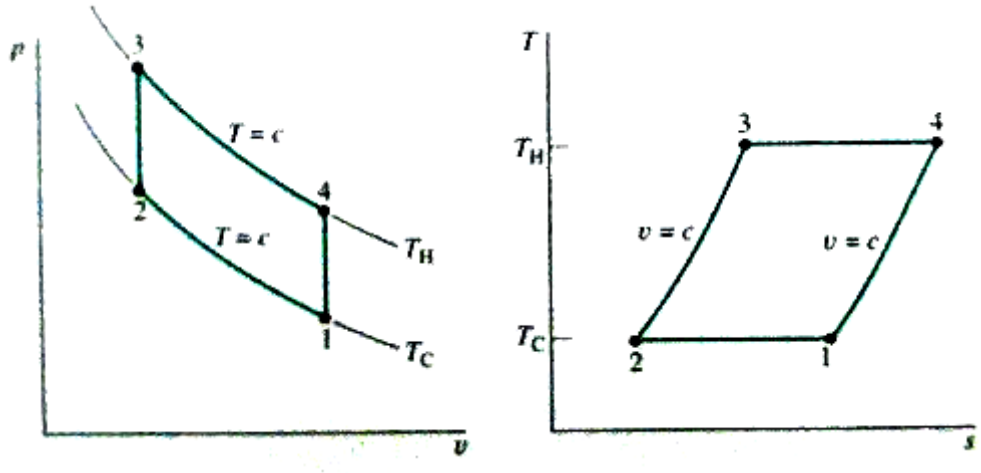

Figure 2-31 Ideal Stirling cycle P-V and T-S diagrams (Moran and Shapiro, 2004)

The Stirling cycle differs from the Carnot cycle in that the two isentropic processes are replaced with two constant volume processes, which significantly increase the area in the P-V diagram and thus the net work per cycle (Walker, 1980). This difference can be observed in Figure 2-32. The efficiency, or fraction of heat supplied to the amount of work, produced in each cycle is comparable between the Stirling and Carnot cycles.

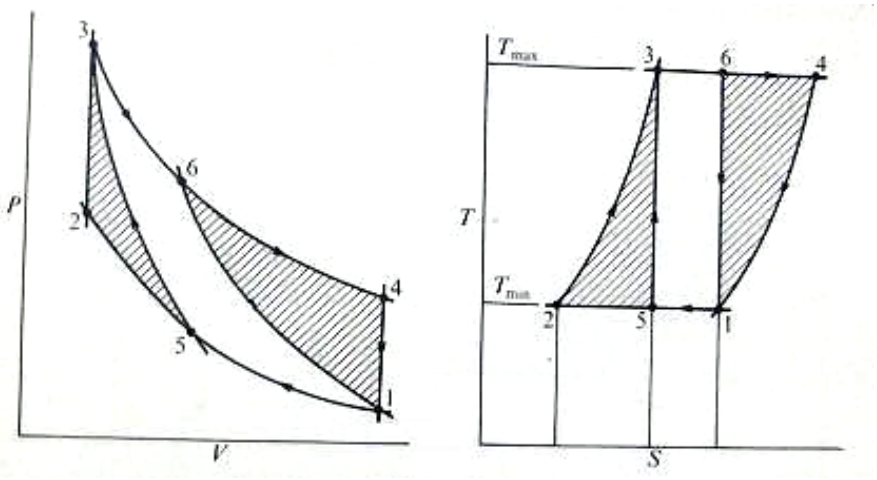

Figure 2-32 Stirling (cross-hatched) and Carnot (1,5,3,6) cycle comparison with similar values for max/min temperatures, pressures, and volumes (Walker, 1980)

Isothermal Ideal Engine Assumptions (Urieli and Berchowitz, 1984)

1. The engine has five components including the compression space, cooler, regenerator, heater, and expansion space as shown in Figure 2-33
2. Each component has a uniform instantaneous temperature, pressure, and mass
3. No pressure drop occurs
4. No working fluid leakage losses occur
5. Ideal gas applies
6. Engine speed is constant
7. Steady-state of the cycle occurs
8. Kinetic and potential energy for the working fluid is neglected

Ideal analysis set of equations (Urieli and Berchowitz, 1984)

For an ideal analysis of the Stirling engine, the mass is uniformly distributed throughout the engine and the ideal gas law is valid, so, using the ideal gas law, the total pressure in the engine is given by Equation (2.37) where m is the mass of the working fluid in the engine, R is the ideal gas constant, V_c is the compression space volume, V_k is the cooler space volume, V_r is the regenerator space volume, V_h is the heater space volume, V_e is the expansion space volume, T_k is the cooler temperature, and T_h is the heater temperature.

$$P = m \cdot R \cdot \left(\frac{V_c}{T_k} + \frac{V_k}{T_k} + \frac{V_r \cdot \ln(T_h / T_k)}{(T_h - T_k)} + \frac{V_h}{T_h} + \frac{V_e}{T_h} \right)^{-1} \tag{2.37}$$

The heat transferred from the compression space and the heat transferred to the expansion space are functions of the engine pressure and the crank angle:

$$Q_c = W_c = \int P \frac{dV_c}{d\theta} d\theta \tag{2.38}$$

$$Q_e = W_e = \int P \frac{dV_e}{d\theta} d\theta \tag{2.39}$$

The total work (W) produced by the engine is the sum of the negative work (W_c) from the compression space and the positive work (W_e) from the expansion space:

$$W = W_c + W_e \tag{2.40}$$

The total Stirling engine efficiency will then be the total work divided by the heat transferred to the expansion space which is equivalent to the Carnot efficiency:

$$\eta_{Carnot} = W / Q_e \tag{2.41}$$

The five components of the Stirling engine are depicted in Figure 2-33 and the corresponding temperature distribution in those components is shown.

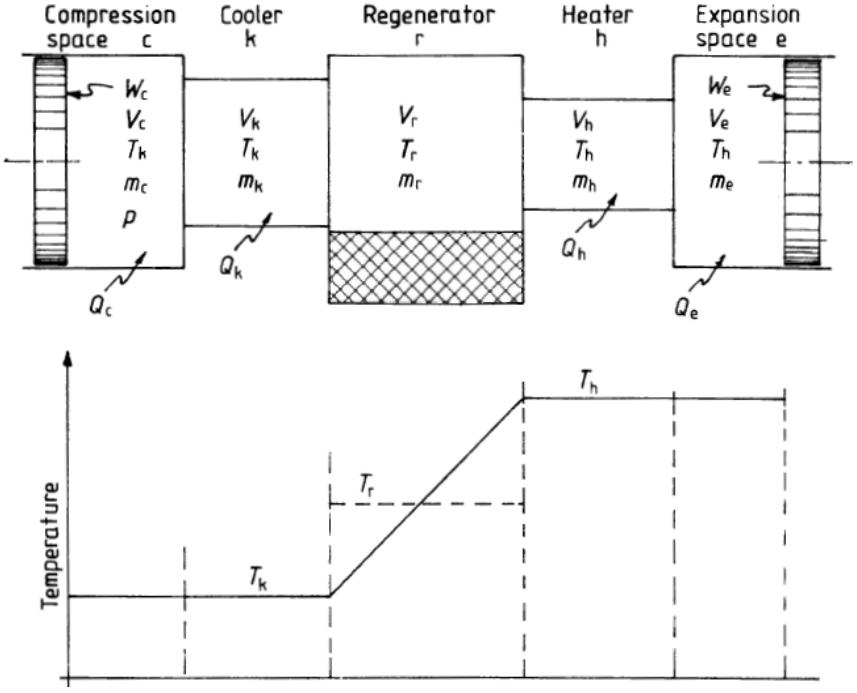

Figure 2-33 Ideal isothermal model (Urieli and Berchowitz, 1984)

2.4.1.1 Schmidt Ideal Analysis

The Schmidt analysis has been the most widely used method for initially sizing Stirling engines. The analysis allows for closed-form solutions to be produced for the engine performance, which designers can easily manipulate (Urieli and Berchowitz, 1984). The Schmidt analysis assumes isothermal expansion and compression spaces, and also ideal heat exchangers. The analysis is capable of generating a P-V diagram for the Stirling cycle, but it is not directly usable for power prediction since the analysis assumes the engine performs at the Carnot efficiency. The

regenerative and pressure losses must be included to get a more accurate prediction of power and the associated efficiency.

Solving the Schmidt analysis for a Stirling engine involves obtaining engine parameters for the swept volume of the expansion and compression spaces, dead volume of the expansion and compression spaces, the regenerator volume, the phase angle between the two pistons, (usually 90 degrees), the mean pressure, engine speed, and the expansion and compression space temperatures. The analysis is outlined by Urieli and Berchowitz (1984).

2.4.2 Finkelstein (Adiabatic) Analyses

Finkelstein's adiabatic analysis assumes that the working spaces are adiabatic rather than isothermal, and accounts for heat transfer in the expansion and compression space through a transfer of enthalpy from the working fluid mass (Urieli and Berchowitz, 1984). This method results in sinusoidally varying temperatures in the working spaces. The predicted engine efficiency using this analysis is more accurate than the Schmidt analysis but still optimistic near the Carnot efficiency since it does not include non-ideal heat exchangers, fluid pressure drops, and incomplete regeneration as shown in Table 2.3.

2.4.3 Quasi Steady Flow Analysis

The "Quasi Steady Flow" model was developed since the flow patterns in Stirling engines are not steady and vary significantly over the cycle, and non-ideal heat exchangers are considered (Urieli and Berchowitz, 1984). The difference between the Quasi Steady Flow and Adiabatic models is the temperature drop between the compression space and cooler, the temperature drop between the heater and the expansion space, the working fluid temperatures are no longer constant over the cycle, and there are pressure losses across the cooler, regenerator, and heater as shown in Figure 2-34 (Urieli and Berchowitz, 1984). It was found in spherical bed regenerators that the friction factors and heat transfer coefficients were 20 percent higher for periodic flow conditions compared to steady flow conditions (Urieli and Berchowitz, 1984).

The Quasi Steady Flow method including pressure drops is more realistic than an Ideal or Adiabatic analysis, but it still does not take several losses into effect. There may be a substantial conduction loss through the walls surrounding the regenerator, shuttle loss from the displacer (for beta/gamma engines), and adiabatic compression loss (Urieli and Berchowitz, 1984). The adiabatic compression loss results from the temperature difference between the cylinder walls and the working spaces causing a transfer of heat at ineffective times during the cycle (Urieli and Berchowitz, 1984). A significant fraction of losses is also predicted to come from pressure losses in the heat exchangers, which are greater than the estimates from steady flow correlations (Urieli and Berchowitz, 1984). The NASA Lewis Research Center reported that the friction factor in the regenerator had to be multiplied by a factor of four to obtain similar values for the measured and predicted output power of Stirling engines (Urieli and Berchowitz, 1984).

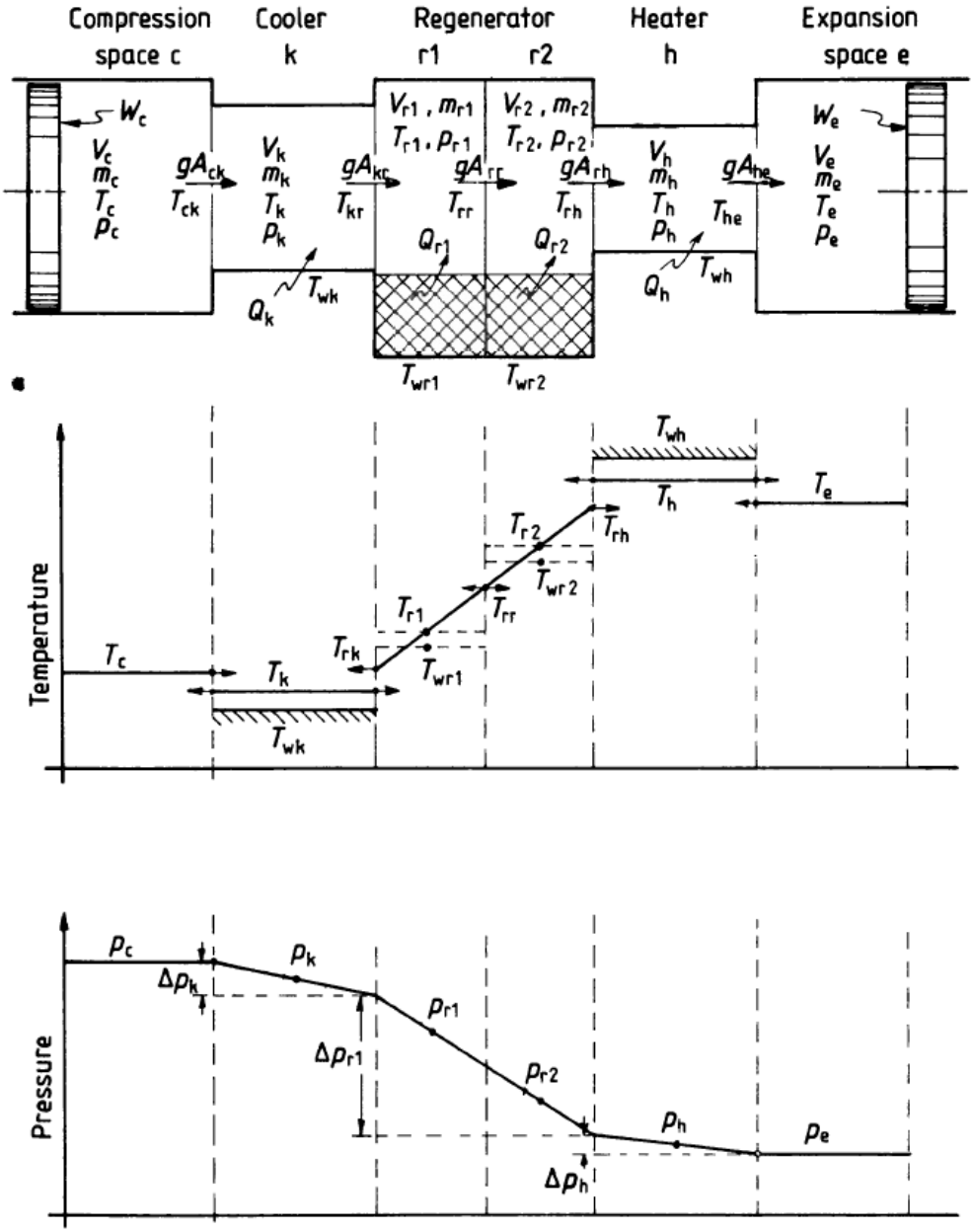

Figure 2-34 Model for Quasi steady flow (Urieli and Berchowitz, 1984)

2.4.4 Summary of Stirling Engine Theoretical Analyses

The Quasi steady flow model gives better predictions of Stirling engine performance than the ideal and adiabatic analysis, but still does not accurately account for all losses in the Stirling engine as shown in Table 2.3. A breakdown of the engine efficiency based on various losses is given in Figure 2-35. The Schmidt analysis operates at the ideal Carnot efficiency and each additional loss including adiabatic working spaces, adiabatic residual loss, flow loss, and thermal

conductivity loss degrades the engine efficiency further (Walker, 1980). The adiabatic residual loss is a result of a phase difference between pressure and volume within the working space. The phase angle α in Figure 2-35 is defined as the angle of the expansion space volume variation leading those in the compression space. Based on the results of the theoretical Stirling engine analyses depicted in Table 2.3, it is clear that a more practical method for predicting the Stirling engine performance is required.

Table 2.3 Theoretical analysis comparison for the GPU-3 engine (7.5 kW, 41.3 bar, Tc = 228K, Te = 977K) (Urieli and Berchowitz, 1984)

Simulation model	Power output (kW)	Efficiency (%)
Ideal Isothermal	7.4	70.5
Ideal Adiabatic	8.3	62.5
Quasi Steady Flow (no pressure drop)	7.4	53.1
Quasi Steady Flow (pressure drop included)	6.7	52.5
Measured	3.96	35

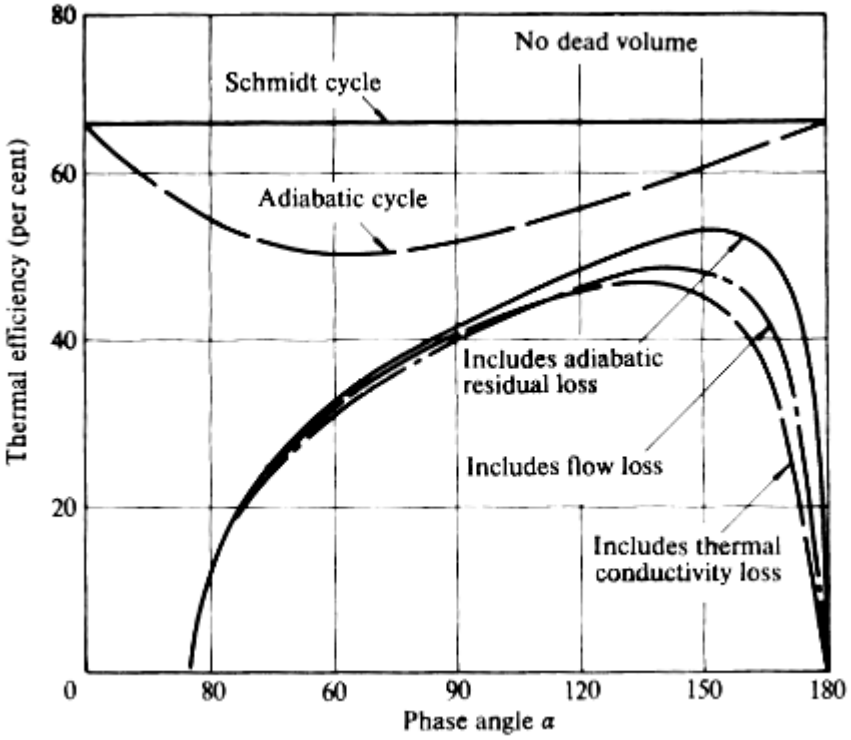

Figure 2-35 Engine efficiencies as a function of phase angle for various losses (Walker, 1980)

2.4.5 Practical Stirling Engine Performance Analyses

The practical Stirling cycle includes many details that the ideal processes neglect. The actual cycle is not reversible, compression and expansion processes are not isothermal, the entire mass of the working fluid is not always in the compression space or expansion space, and there are voids in the regenerator, cylinder clearance space, and connecting piping (Walker, 1980). The practical Stirling cycle also includes pistons that are continuously moving and contributing to friction between the piston and cylinder, and the regenerator is not assumed to have a perfect effectiveness. Flow loss occurs in the regenerator and heat exchangers which can be observed in Figure 2-36 by the variation in pressure between the expansion and compression spaces. The work lost in the regenerator and heat exchangers is represented by the hatched area in Figure 2-37. After including all of these losses, a well designed Stirling engine will have efficiencies between 40 and 70 percent of the theoretical Carnot value (Walker, 1980). The practical analyses cannot account for all of the previous loss mechanisms because of compounding errors, so practical analyses often involve performance correlations that have shown to be accurate or making performance curve fits from data.

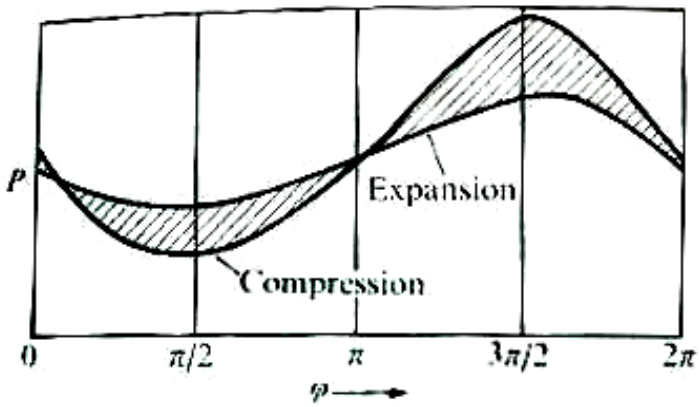

Figure 2-36 Pressure variation between the expansion and compression spaces (Walker, 1980)

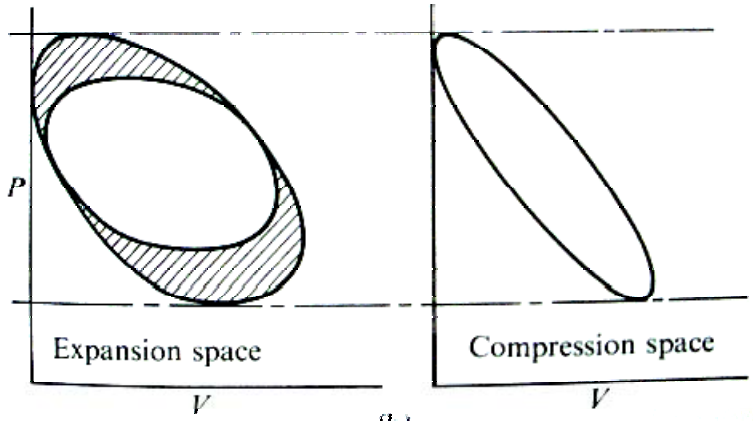

Figure 2-37 P-V diagram for expansion and compression space for a Stirling cycle. The hatched area represents work lost from the regenerator and heat exchangers (Walker, 1980)

2.4.5.1 Beale Number Power Correlation

The Stirling engine theoretical performance analyses listed above were not practical for predicting the efficiency and output power of Stirling engines as shown in Table 2.3. William Beale observed that most engines have similar performance based on the Schmidt optimizations involving the dead volume ratio, temperature ratio, swept volume ratio, and phase angle advance (Urieli, 1984). He observed that most Stirling engines operate with similar internal efficiency losses, so a simple performance prediction could be made. By observing experimental data, he determined the power output of the Stirling engine to be based on the (dimensionless) Beale number:

$$P_{SE} = Beale \cdot P_{mean} \cdot V_{sw} \cdot f \tag{2.42}$$

where P_{SE} is the Stirling engine output power, *Beale* is the Beale number, P_{mean} is the mean engine pressure, V_{sw} is the swept volume of the engine, and f is the engine frequency (Urieli, 1984). A typical value for the Beale number is 0.15. The Beale number power correlation is

more practical than the theoretical analyses and more accurately predicts the performance of a Stirling engine.

2.4.5.2 West Number Power Correlation

The Beale number Stirling engine performance correlation does not include terms for the hot or cold sink temperatures in the engine. The performance of a Stirling engine depends on these temperatures, so the West number correlation was devised to include these temperature terms. The predicted power output of the Stirling engine based on the (dimensionless) West number is given by:

$$P_{SE} = West \cdot P_{mean} \cdot V_{sw} \cdot f \cdot \left(\frac{T_E - T_C}{T_E + T_C} \right) \tag{2.43}$$

where *West* is the West number, T_E is the expansion space temperature, T_C is the compression space temperature (Hirata, 2002). The power estimated using the West number includes consideration of the expansion and compression space temperatures, and should provide more accurate estimates of the engine power if these parameters were varied. A typical value for the West number is between 0.25 and 0.35 (Hirata, 2002).

2.4.5.3 Stirling Engine Efficiency with Regenerative and Pressure Losses

A Stirling engine efficiency correlation was developed by Petrescu et al. (2002) by combining two theoretical thermodynamic techniques The efficiency correlation takes into account the Carnot efficiency, pressure losses, and regenerator losses involving both internal and external irreversibility. Two adjusting coefficients were determined based on experimental data to obtain accurate analytical results for the efficiency correlation. The Stirling engine efficiency is given by Equation (2.44) (Petrescu et al, 2000)

$$\eta_{SE} = \eta_{Carnot} \cdot \eta_{II,irrev} = \eta_{Carnot} \cdot \eta_{II,\Delta T} \cdot \eta_{II,X} \cdot \eta_{II,\Delta P} \tag{2.44}$$

where the Carnot cycle efficiency (η_{Carnot}) is a function of the cooler (T_C) and heater (T_E) temperatures in Equation (2.45)

$$\eta_{Carnot} = \left(1 - \frac{T_C}{T_E} \right) \tag{2.45}$$

The irreversibility factor due to a temperature difference between the heat source and heat sink is given by Equation (2.46)

$$\eta_{II,\Delta T} = 1 / \left(1 + \sqrt{\frac{T_C}{T_E}} \right) \tag{2.46}$$

Incomplete regeneration can contribute to significant losses in Stirling engines. These heat transfer losses are a function of piston speed, cylinder and regenerator dimensions, regenerator and working fluid properties, and operating conditions (Petrescu et al, 2002). The factor for losses due to incomplete regeneration is given by Equation (2.47) where $\eta_{II,X}$ denotes the efficiency factor for the regenerator, C_v is the gas specific heat at constant volume, R is the gas constant, εv is the compression ratio (V_1/V_2), X represents all the losses from incomplete heat transfer in the regenerator.

$$\eta_{II,X} = \frac{1}{1 + \frac{X \cdot C_v}{R \cdot \ln(\varepsilon_v)} \cdot \left(1 - \sqrt{\frac{T_C}{T_E}}\right)} \tag{2.47}$$

The value for X was determined using the first law and heat transfer principles for the regenerator and working fluid and is defined in Equation (2.48) (Petrescu et al, 2000):

$$X = X_1 \cdot y + X_2 \cdot (1 - y) \tag{2.48}$$

Differential equations from this analysis were integrated using a lumped analysis, which gave pessimistic results using X_1 (Petrescu et al, 2000):

$$X_1 = \frac{1 + 2 \cdot M + e^{-B}}{2 \cdot (1 + M)} \tag{2.49}$$

Using a linear distribution of the temperature for the regenerator and working fluid gave optimistic results for X_2 (Petrescu et al, 2000):

$$X_2 = \frac{M + e^{-B}}{(1 + M)} \tag{2.50}$$

Experimental data were used to obtain the adjusting parameter y which was found by Petrescu et al (2000) to be 0.72 or 0.27 in the Reno paper by Petrescu et al (2002). The term M given in Equation (2.51) is the ratio of the mass multiplied by capacitance of the working fluid to that of the regenerator.

$$M = \frac{m_g \cdot c_v}{m_r \cdot c_r} \tag{2.51}$$

The term B in Equation (2.52) is a function of the regenerator heat transfer coefficient h_r, the area of the regenerator A_r involved with heat transfer, the stroke of the piston S, and the speed of the piston w (Petrescu, 2000).

$$B = \left(1+M\right)\cdot\frac{h_r \cdot A_r}{m_g \cdot c_v}\cdot\frac{S}{w} \tag{2.52}$$

The speed of the piston is dependent on the stroke and engine speed (n_r) given by:

$$w = 2\cdot S\cdot n_r / 60 \tag{2.53}$$

The regenerator heat transfer coefficient due to convection is:

$$h_r = \frac{0.395\cdot\left(4\cdot P_m / R\cdot T_C\right)\cdot w^{0.424}\cdot C_p\left(T_m\right)\cdot\upsilon\left(T_m\right)^{0.576}}{\left(1+\tau\right)\cdot\left[1-\frac{\pi}{4\cdot\left[\left(b/d\right)+1\right]}\right]\cdot D_r^{0.576}\cdot P_r^{2/3}} \tag{2.54}$$

where P_m is the mean pressure in the engine, υ and C_p are the viscosity and thermal capacitance of the working fluid evaluated at the mean temperature T_m, D_r is the diameter of the regenerator, d is the diameter of the regenerator wire, b is the distance between wires in the regenerator, and P_r is the Prandtl number.

The equation for the pressure losses factor results from determining the losses of the pistons operating at a finite speed, the working fluid moving through the regenerator, and mechanical friction, and is given by:

$$\eta_{II,\Delta P} = 1-\frac{\frac{w}{w_{S,L}}\cdot\gamma\cdot\left(1+\sqrt{\tau}\right)\ln\left(\varepsilon_v\right)+5\cdot\left(\frac{w}{w_{S,L}}\right)^2\cdot N_S}{\tau\cdot\eta'\cdot\ln\left(\varepsilon_v\right)}-\frac{\frac{3\cdot\left(0.94+0.045\cdot w\right)\cdot 10^5}{4\cdot P_1}}{\tau\cdot\eta'\cdot\ln\left(\varepsilon_v\right)} \tag{2.55}$$

where N_s is the number of screens in the regenerator, τ is temperature ratio, P_1 defined in Equation (2.58) is a function of the mean pressure (Pm), volumetric ratio (ε_v), and temperature ratio (τ), w is the piston speed, $w_{S,L}$ is the speed of sound at the sink temperature (T_C), and η' is the Carnot efficiency multiplied by the regenerator losses factor given in Equation (2.56).

$$\eta' = \eta_{CC}\cdot\eta_{II,X} \tag{2.56}$$

The sound speed at the cooler temperature is defined in Equation (2.57) where γ is the specific heat ratio.

$$w_{S,L} = \sqrt{\gamma\cdot R\cdot T_C} \tag{2.57}$$

The term P_1 is defined:

$$P_1 = \frac{4\cdot P_m}{\left(\varepsilon_v+1\right)\cdot\left(\tau+1\right)} \tag{2.58}$$

The temperature ratio τ is defined:

$$\tau = \frac{T_E}{T_C} \tag{2.59}$$

The analysis for the Stirling engine efficiency and power were compared with twelve Stirling engines over a limited operating range (Petrescu et al, 2000) as shown in Table 2.4. It appears the analysis provides accurate predictions for the efficiency and power of Stirling engines over the limited range. A model was developed (See Appendix F) in Engineering Equation Solver (EES) using the correlation given by Equation (2.44) to duplicate the results of the 4-95 MKII engine in Table 2.4. The results of the Petrescu model did not accurately predict the efficiency of the 4-95 engine as indicated in Figure 2-38. The maximum efficiency of the 4-95 engine is rated to be around 41 % and not 29.4 % as published in Table 2.4 (Stine and Diver, 1994). The peak net SES Stirling dish system efficiency using the 4-95 engine (accounting for collector, receiver, engine, and parasitic losses) is 29.4 % (Mancini et al, 2003). The predicted model results of the 4-95 MKII engine in Table 2.4 indicates that the calculated efficiency (28.9 %) for this model is not close to the operating efficiency of 41 % for unexplained reasons. There was no response from the authors to the email requests for clarification about their method.

Table 2.4 Comparison of the Petrescu et al. results and the actual engine performance (Petrescu et al, 2000)

Stirling Engine	Actual Power [kW]	Calculated Power [kW]	Actual Efficiency	Calculated Efficiency
NS-03M, regime 1 (economy)	2.03	2.182	0.359	0.3392
NS-03M, regime 2 (max.power)	3.81	4.196	0.31	0.3297
NS-03T, regime 1 (economy)	3.08	3.145	0.326	0.3189
NS-03T, regime 2 (max.power)	4.14	4.45	0.303	0.3096
NS-30A, regime 1 (economy)	23.2	29.45	0.375	0.357
NS-30A, regime 2 (max.power)	30.4	33.82	0.33	0.3366
NS-30S, regime 1 (economy)	30.9	33.78	0.372	0.366
NS-30S, regime 2 (max.power)	45.6	45.62	0.352	0.3526
STM4-120	25	26.36	0.4	0.4014
V-160	9	8.825	0.3	0.308
4-95 MKII	25	28.4	0.294	0.289
4 - 275	50	48.61	0.42	0.4119
GPU-3	3.96	4.16	0.127	0.1263
MP1002 CA	200 W	193.9 W	0.156	0.1536
Free Piston Stirling Engine	9	9.165	0.33	0.331
RE-1000	0.939	1.005	0.258	0.2285

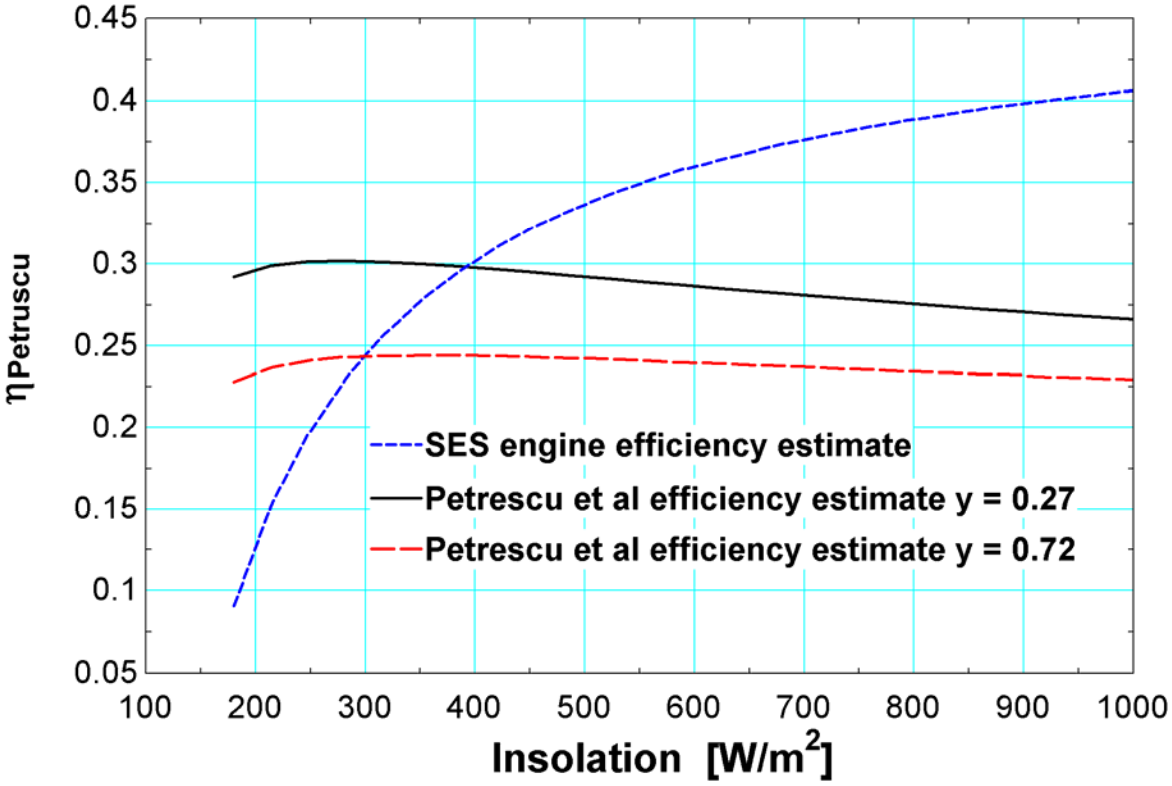

Figure 2-38 Comparison of the Petrescu et al engine efficiency with the predicted engine efficiency of the SES 4-95 engine

2.4.5.4 Stine's Net Power Versus Insolation Model

Stine's long-term energy prediction model does not predict the Stirling engine output power or efficiency, but rather predicts the net power from the entire Stirling dish system. An experimentally validated model has been created by Stine to predict the long-term energy production from Stirling dish systems (Stine, 1995). This model has been validated by testing the Schlaich, Bergermann und Partner (SBP) systems at the Plataforma Solar site in Spain. The model is constructed using a few experimentally derived parameters that are found using data from systems performing over several months. The energy production model developed from these experimental data requires the input solar insolation, the ambient temperature, mirror soiling, and parasitic power to predict the long-term performance of a Stirling dish.

The long-term energy production model uses experimental data to plot the gross output power versus the solar insolation. The performance of these systems can be modeled in a simple linear fashion. The predicted power output is lower in the morning and slightly greater in the evening due to the system thermal capacitance which the model does not include. These system characteristics still result in a very good linear fit for the data to predict system performance. The model uses Equation (2.60) to predict the gross power output for the system where $I_{bm,corr}$ is the corrected beam insolation, m_1 is the slope of the linear fit, and b_1 is the power intercept factor (Stine, 1995).

$$P_{gross} = m_1 \cdot I_{bm,corr} + b_1 \tag{2.60}$$

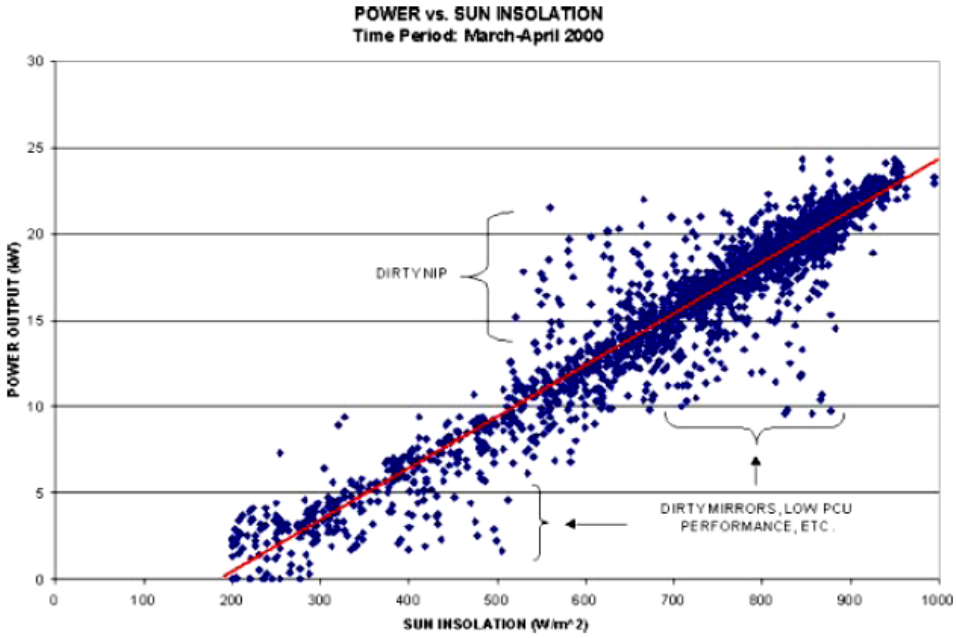

Figure 2-39 SES system power based on solar insolation (Mancini et al, 2003)

Estimates for the values of m_1 and b_1 were obtained by observing measured power output data with a linear fit for each of the four Stirling dish systems (Mancini et al, 2003) as shown in Table 2.5.

Table 2.5 Slope and intercept values for Stirling dish systems using Stine's method

	m_1 (m^2)	b_1 (kW)
SAIC	32.3	-12.3
SES	30.2	-5.7
SBP	14.9	-3.4
WGA (MOD1)	12.6	-2.7

The corrected beam insolation $I_{bm,corr}$ is a function of the mirror soiling and the engine cooling water inlet temperature. The corrected beam insolation is given in Equation (2.61) where I_{bm} is the beam insolation, Φ_R is the normalized mirror reflectance, and $\Theta_{T,cw}$ is the normalized cooling water inlet temperature (Stine, 1995).

$$I_{bm,corr} = I_{bm} \cdot \frac{\Phi_R}{\Theta_{T,cw}} \tag{2.61}$$

The normalized mirror reflectance is the ratio of the measured reflectance R during testing to the reflectance of the mirrors when clean R_{clean}. This ratio is given in Equation (2.62) (Stine, 1995).

$$\Phi_R = R / R_{clean} \tag{2.62}$$

The normalized cooling water inlet temperature given by Equation (2.63) is the ratio of the engine cooling water inlet temperature $T_{cw,in}$ to the standard atmospheric temperature (T_0) of 288˚K (Stine, 1995).

$$\Theta_{T,cw} = T_{cw,in} / T_0 \tag{2.63}$$

A relationship must be derived to obtain the temperature of the cooling water inlet temperature based on the ambient temperature. Obtaining a relationship for the cooling water inlet temperature and not just the ambient temperature is necessary since there is a linear relationship between the gross output power and the engine cooling water temperature (Stine, 1995). Another reason to use the cooling water temperature is when variable speed fans or pumps are used for the cooling system which introduces changes in the engine performance that are not just a function of solar insolation. The performance of an engine cooling system could also be affected by altitude and wind velocity. A correlation to find the cooling water inlet temperature for a fixed speed pump and fan is given by Equation (2.64) where T_{amb} is the ambient temperature, and C is a constant found experimentally (Stine, 1995).

$$T_{amb} / T_{cw,in} = 1 - C \cdot I_b \cdot \Phi_R \tag{2.64}$$

Once the gross power is obtained, the net power can be found by subtracting the parasitic power used to run the tracking, cooling, and control systems from the gross power. The net power from a Stirling dish system is given by Equation (2.65).

$$P_{net} = P_{gross} - \sum P_{parasitics} \tag{2.65}$$

This model was compared with data for two SBP 9 kW systems as shown in Table 2.6 (Stine, 1995). Stine's model appears to provide accurate predictions for the total system performance of Stirling dish systems. The model, however, does not include details for how the system performance will change based on the sun elevation angle, wind velocity, density of air, or a change in the expansion space temperature among others.

Table 2.6 Daily energy production for SBP systems on July 23, 1993 (Stine, 1995)

	North Dish	Center Dish
Measured	41.9 kW-hr	56.1 kW-hr
Predicted	39.2 kW-hr	57.5 kW-hr
deviation	6.4 %	2.5 %

.

2.5 Cooling System

The cooling system for a Stirling dish system rejects the thermal losses from the Stirling engine in order to reduce the compression space temperature and improve the efficiency of the engine. The most common cooling system configuration for a Stirling dish system is a radiator and fan with a pump and cooling fluid loop. This configuration is shown in Figure 2-40 and the labeled temperatures are used in several equations below.

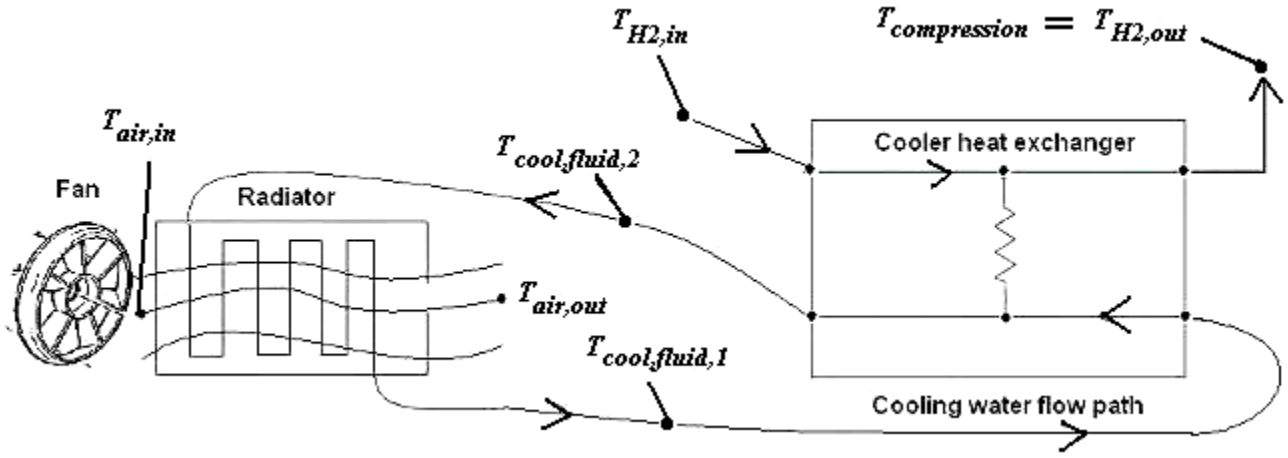

Figure 2-40 Cooling system diagram for a Stirling dish system

2.5.1 Radiator Heat Exchanger

All of the current Stirling dish systems use a fan and plate-finned radiator to reject the thermal load from the cooler into the atmosphere using a cooling fluid loop. The radiator and fan act as a cross-flow heat exchanger with the cooling fluid moving through the radiator, and ambient air passing across the radiator perpendicular to the flow of the cooling fluid. Assuming that the cooler and radiator are operating at steady state, the heat rejection rate ($\dot{Q}_{reject}$) can be expressed by the heat exchanger effectiveness relation given in Equation (2.66) (Incropera and DeWitt, 2002)

$$\dot{Q}_{reject} = \varepsilon_{radiator} \cdot \dot{C}_{\min} \cdot \left(T_{cool,fluid,2} - T_{air,in} \right) \tag{2.66}$$

where $\varepsilon_{radiator}$ is the radiator heat exchanger effectiveness, $\dot{C}_{\min}$ is the minimum capacitance rate of the cooling fluid or ambient air, $T_{cool,fluid,2}$ is the temperature of the cooling fluid entering the radiator (leaving the cooler), and $T_{air,in}$ is the temperature of ambient air entering the radiator. The minimum capacitance rate is given by Equation (2.67)

$$\dot{C}_{\min} = \min\left[\left(\dot{m} \cdot C_p \right)_{cool,fluid}, \left(\dot{m} \cdot C_p \right)_{air} \right] \tag{2.67}$$

where $\dot{m}$ is the mass flow rate, and C_p is the fluid thermal capacitance at constant pressure. The temperature of the cooling fluid into the cooler can then be determined rearranging Equation (2.68) where $\dot{C}_{cool,fluid}$ is the capacitance rate of the radiator loop fluid, and $T_{cool,fluid,1}$ is the temperature of the cooling fluid into the cooler.

$$\varepsilon_{radiator} = \frac{\dot{C}_{cool,fluid} \cdot \left(T_{cool,fluid,2} - T_{cool,fluid,1}\right)}{\dot{C}_{\min} \cdot \left(T_{cool,fluid,2} - T_{air,in}\right)} \tag{2.68}$$

The effectiveness of the radiator will change if a different operating speed is chosen for the fan. The effectiveness-NTU relationship for the radiator would be for a cross-flow heat exchanger with the air unmixed and the cooling fluid mixed which is given in Equations (2.69) and (2.70) where C_r is the capacitance rate ratio, UA is the overall heat transfer coefficient for the radiator heat exchanger. The effectiveness of the radiator and the UA will vary based on the operating speed of the fan or pump. The variation of UA as a function of volumetric flow rate of air (which is likely the fluid having the minimum capacitance rate) can be estimated using Equation (2.73) where $UA_{operating}$ is the overall heat transfer coefficient for operating conditions, UA_{test} is the value determined for the radiator during test conditions, $\dot{V}_{\min,rad,operating}$ is the minimum volumetric flow rate of the air or cooling fluid during operating conditions, $\dot{V}_{\min,rad,test}$ is the minimum volumetric flow rate of the air or cooling fluid during test conditions, and $b_{radiator}$ is the coefficient. The value of $b_{radiator}$ is assumed to be 0.7.

$$\varepsilon_{radiator} = \left(\frac{1}{C_r}\right) \cdot \left(1 - \exp\left(-C_r \cdot \left(1 - \exp\left(-NTU_{radiator}\right)\right)\right)\right) \tag{2.69}$$

$$NTU_{radiator} = -\ln\left(1 + \left(\frac{1}{C_r}\right) \cdot \ln\left(1 - \varepsilon_{radiator} \cdot C_r\right)\right) \tag{2.70}$$

where

$$NTU_{radiator} = \frac{UA_{radiator}}{\dot{C}_{\min}} \tag{2.71}$$

$$C_r = \frac{\dot{C}_{\min}}{\dot{C}_{\max}} \tag{2.72}$$

$$\frac{UA_{operating}}{UA_{test}} = \left[\frac{\dot{V}_{\min,rad,operating}}{\dot{V}_{\min,rad,test}}\right]^{b_{radiator}} \tag{2.73}$$

2.5.2 Stirling Engine Cooler

The Stirling engine utilizes a cooler to reduce the temperature of the compression space and improve the engine performance. Many Stirling engine coolers use a shell-and-tube heat exchanger with the hydrogen working fluid on the tube-side and a secondary fluid on the shell-side (Stine and Diver, 1994). The SES engine, for instance, uses 400 - 3 mm diameter tubes for each of the four coolers in every cylinder with hydrogen passing within the tubes (Stine and

Diver, 1994). The shell-and-tube heat exchanger operates with a counter-flow heat exchange regime when the hydrogen flows from the regenerator into the compression space, and acts as a parallel-flow heat exchanger when hydrogen moves from the compression space back through the regenerator at a rate of thirty times per second. The effectiveness of the cooler and the capacitance rate of hydrogen will dictate the compression space temperature. The temperature of the engine working fluid into the cooler can be estimated by rearranging Equation (2.74)

$$Q_{reject} = \varepsilon_{cooler} \cdot \dot{C}_{\min} \cdot \left(T_{H2,in} - T_{cool,fluid,1} \right) \tag{2.74}$$

where ε_{cooler} is the cooler heat exchanger effectiveness, Q_{reject} is the thermal load rejected from the Stirling engine into the cooler, $\dot{C}_{\min}$ is the minimum capacitance rate of the hydrogen or cooling fluid, $T_{H2,in}$ is the temperature of the hot fluid entering the cooler from the regenerator, and $T_{cool,fluid,in}$ is the temperature of the cold fluid entering the cooler from the radiator loop. The temperature of the compression space can then be determined by rearranging Equation (2.75)

$$\varepsilon_{cooler} = \frac{\dot{C}_{H2} \cdot \left(T_{H2,in} - T_{H2,out} \right)}{\dot{C}_{\min} \cdot \left(T_{H2,in} - T_{cool,fluid,1} \right)} \tag{2.75}$$

where $\dot{C}_{H2}$ is the capacitance rate of the engine working fluid, and $T_{H2,out}$ is the temperature of the compression space.

The effectiveness of the cooler will vary when the capacitance rate of hydrogen or cooling fluid changes. The effectiveness-NTU relationship for a shell-and-tube cooler is given by Equations (2.76) and (2.77). The UA for specific operating conditions can be determined using Equation (2.79) where $\dot{V}_{\min,cooler,operating}$ is the minimum volumetric flow rate of the hydrogen working fluid or cooling fluid during operating conditions, $\dot{V}_{\min,cooler,test}$ is the minimum volumetric flow rate of the hydrogen working fluid or cooling fluid during test conditions, and b_{cooler} is a coefficient that is taken to be 0.7.

$$\varepsilon_{cooler} = 2 \cdot \left[1 + C_r + \left(1 + C_r^2 \right)^{0.5} \cdot \frac{1 + \exp\left(-NTU \cdot \left(1 + C_r^2 \right)^{0.5} \right)}{1 - \exp\left(-NTU \cdot \left(1 + C_r^2 \right)^{0.5} \right)} \right]^{-1} \tag{2.76}$$

$$NTU_{cooler} = -\left(1 + C_r^2 \right)^{-0.5} \cdot \ln\left(\frac{E-1}{E+1} \right) \tag{2.77}$$

$$E = \frac{2/\varepsilon_1 - \left(1 + C_r \right)}{\left(1 + C_r^2 \right)^{0.5}} \tag{2.78}$$

$$\frac{UA_{operating}}{UA_{test}} = \left[\frac{\dot{V}_{\min,cooler,operating}}{\dot{V}_{\min,cooler,test}} \right]^{b_{cooler}} \tag{2.79}$$

2.5.3 Cooling System Pump

A water pump is used in the cooling fluid loop to pump the cooling fluid through the cooler and radiator. The pump must overcome frictional losses in the cooling fluid loop resulting from friction with the pipe walls, and also from form losses resulting due to bends, valves, or locations in the pipe that have a larger or smaller diameter. The power that must be supplied to the pump is proportional to the fluid flow rate and the loop pressure drop as given by Equation (2.80) (White, 2003)

$$P_{pump} = \rho \cdot g \cdot \dot{V} \cdot P_{head} / \eta_{pump} \tag{2.80}$$

where P_{pump} is the pump power, ρ is the density of water, g is the gravitational constant, $\dot{V}$ is the volumetric flow rate of water, η_{pump} is the pump efficiency, and P_{head} is the pressure head given by Equation (2.81) (White, 2003).

$$P_{head} = f_f \cdot \frac{L}{d} \cdot \frac{v^2}{2 \cdot g} + \sum K \cdot \left(\frac{v^2}{2 \cdot g} \right) \tag{2.81}$$

The terms f_f is the friction factor determined using a Moody diagram, L is the length of the pipe, v is the velocity of the fluid, d is the diameter of the pipe, and K is the term for minor losses (bends, reductions, etc).

The parasitic power demands of a pump remain nearly constant for Stirling dish applications since a constant speed pump is used and the density of cooling fluid does not change significantly over the system operating range. A pump performance correlation can be used to determine how the parasitic power of a pump will change as the density of the fluid, the pump speed and the impeller diameter change. This "fan law" relationship is found in Equation (2.82) (White, 2003)

$$\dot{W}_S = C_W \cdot N^3 \cdot d^5 \cdot \rho \tag{2.82}$$

where d is the impeller diameter, N is the speed of the pump, C_W is the power coefficient, and ρ is the density of the radiator working fluid.

There likely would not be an economic benefit for using a variable speed pump since the pump power is small and a reduction in the power resulting from reducing the speed would also result in a reduction of the cooler and radiator effectiveness and therefore a reduction in the radiator and engine performance. The higher initial cost of a variable speed pump to potentially save a minimal amount of energy makes variable speed pumps not an economical solution. Optimizing the cooling system using a variable speed fan, however, may be economical because the fan power is greater than the pump power. The fan power for the WGA system is approximately 400 W and the pump around 75 W (Andraka, 2007).

2.5.4 Radiator Fan

A fan is used on the radiator to dissipate energy from the cooling fluid and therefore reduce the temperature of the engine compression space. The fan and radiator cooling loop is comparable to one on a vehicle with a Stirling engine in place of the gas or diesel engine. The fan typically consumes the greatest fraction of the parasitic power and the operating speed should be optimized to improve the net output power from the system. The fan laws can be used to optimize the system and are given in the following three equations (White, 2003)

$$\dot{V} = C_V \cdot N \cdot d^3 \tag{2.83}$$

$$P_{rise} = C_P \cdot N^2 \cdot d^2 \cdot \rho \tag{2.84}$$

$$P_{fan} = C_W \cdot N^3 \cdot d^5 \cdot \rho \tag{2.85}$$

where $\dot{V}$ is the volumetric flow rate of air, C_V is the capacity coefficient, N is the operating speed of the fan, d is the fan blade diameter, P_{rise} is the fan static pressure rise, Cp is the pressure coefficient, ρ is the density of ambient air, P_{fan} is the parasitic power of the fan, and C_W is the power coefficient. The fan laws were used to determine the power consumption of the Woods 630 mm fan used in the WGA cooling system. The fan power is lower at higher ambient temperatures as depicted in Figure 2-41 due to a lower density of air (and mass flow) at higher operating temperatures. The parasitic fan power consumption as a function of fan speed is shown in Figure 2-42 with power being proportional to the cubic root of the fan speed.

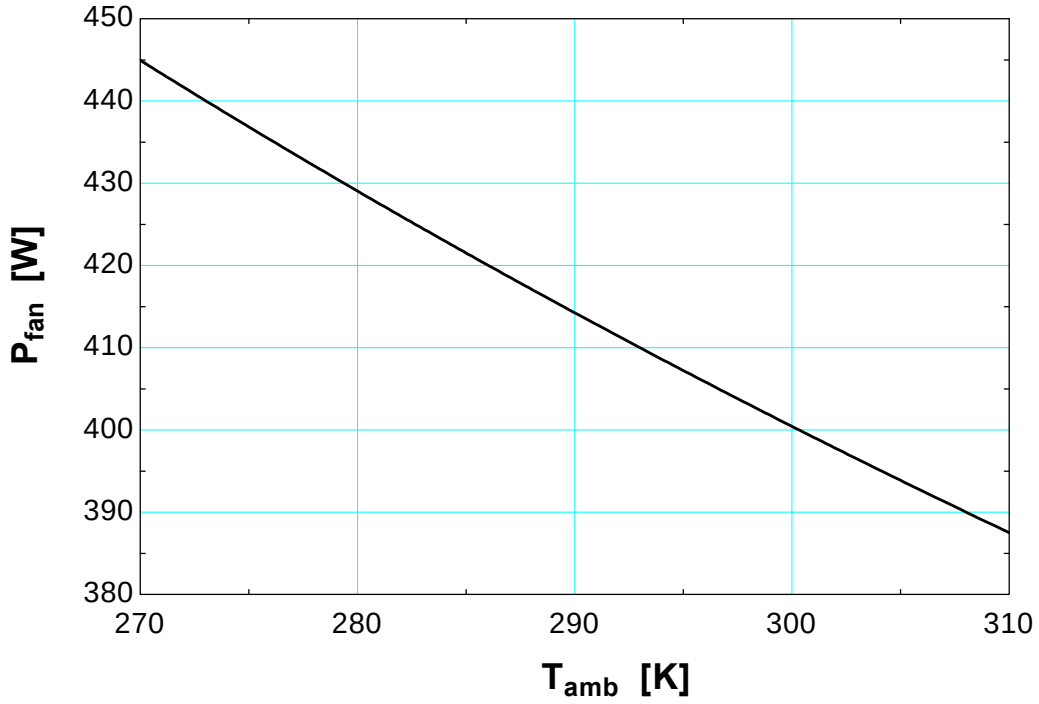

Figure 2-41 Fan power consumption based on ambient temperature operating at 890[rpm] and an atmospheric pressure of 101[kPa]

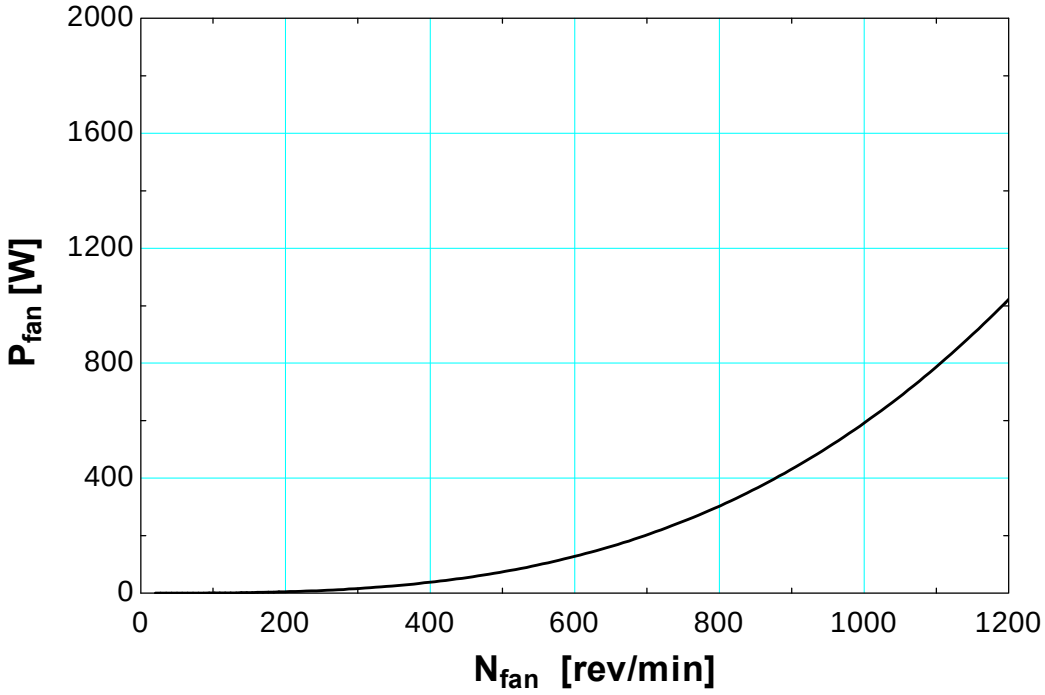

Figure 2-42 Fan power consumption as a function of fan speed operating at an ambient temperature of 288°K and atmospheric pressure of 101[kPa] with a similar cooling system to the WGA system

2.5.5 Cooling Tower

Cooling towers are used in power plants to reduce the temperature of the cooling fluid and improve the performance of the system. Closed-loop cooling towers are often used when environmental concerns prohibit the discharge of warmer water back into a natural body of water or when water quantities are scarce. Cooling towers are categorized as either a wet, dry, or wet-dry type in addition to being classified as either natural draft or mechanical draft depending on whether fans are used to improve the mass flow rate of air into the cooling tower (El-Wakil, 1984).

A wet cooling tower dissipates rejected heat from the power plant to the environment through evaporation of the cooling water, and by transferring energy to the cooling tower air. About 75 % of the rejected heat from the power plant is transferred to the environment through evaporation in hot weather and 60 % in cold weather with the additional heat rejection occurring from heat to the air (El-Wakil, 1984). The additional make-up water that must be added to the system due to evaporation is approximately 1.3 % of the cooling water mass flow rate in hot weather and 1.0 % in cold weather (El-Wakil, 1984).

An energy and mass balance can be used to determine the cooling fluid outlet temperature exiting the cooling tower based on the ambient air conditions, and the mass flow rate of the circulating water and air. A depiction of the energy balance is shown in Figure 2-43, and the energy balance is given in Equation (2.86) (El-Wakil, 1984) where h_a is the enthalpy of dry air, h_v is the enthalpy of water vapor, h_f is the enthalpy of the fluid, ω is the absolute humidity (mass of water vapor per mass of dry air), W is the mass of the circulating water per unit mass of dry

air, *1* refers to the air inlet conditions, *2* refers to the air outlet, *A* represents water inlet conditions, and *B* represents the water outlet. The makeup water is not included in the energy balance in Equation (2.86).

$$h_{a1} + \omega_1 \cdot h_{v1} + W_A \cdot h_{f_A} = h_{a2} + \omega_2 \cdot h_{v2} + W_B \cdot h_{f_B} \tag{2.86}$$

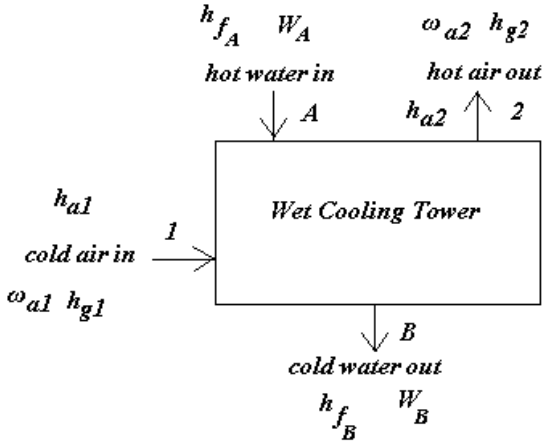

Figure 2-43 Wet cooling tower control volume

A mass balance is given in Equation (2.87) and a simplification can be made for the change in the enthalpy of dry air as shown in Equation (2.88) where $C_{p,air}$ is the thermal capacitance of air, T_2 is the outlet temperature of air, and T_1 is the inlet temperature of ambient air. These equations can be combined with Equation (2.86) to form another expression for the energy balance given in Equation (2.89) (El-Wakil, 1984). Using a cooling tower in place of the radiator and fan would have the potential to drive down the compression space temperature in the engine since the compression space temperature would be limited by the wet bulb temperature and not the ambient dry bulb temperature.

$$\omega_2 - \omega_1 = W_A - W_B \tag{2.87}$$

$$h_{a2} - h_{a1} = C_{p,air} \cdot \left(T_2 - T_1\right) \tag{2.88}$$

$$\omega_1 \cdot h_{v1} + W_A \cdot h_{f_A} = C_{p,air} \cdot \left(T_2 - T_1\right) + \omega_2 \cdot h_{v2} + \left[W_A - \left(\omega_2 - \omega_1\right)\right] \cdot h_{f_B} \tag{2.89}$$

2.6 Additional Stirling Components

The generator on the Stirling engine converts the mechanical shaft power into electricity which is supplied to the grid. Induction generators are often used due to their durability and ability to convert the mechanical power into synchronous single or three phase 230/460 VAC that is grid-tied (Teagan, 2001). Four of the five different Stirling dish systems fabricated thus far have used three phase 480V induction generators (Mancini et al, 2003). Induction generators are a small fraction of the Stirling dish system cost since they are produced in high volume and can be purchased "off-the-shelf." Induction generators can have efficiencies over 94 % (Teagan, 2001).

To make Stirling dish systems functional, a number of ancillary components are required. There are structural components to mount the dish and Stirling engine at the proper focal length, controls for the dual-axis tracking, a fan and pump for the radiator cooling system required to reject from the engine and many more. It is important to note that these additional components can require parasitic energy that is between five and ten percent of the rated power (Teagan, 2001, Mancini et al, 2003).

The control drives for positioning the parabolic mirror are extremely important components in the Stirling dish systems. If the software is not functioning properly, or if the azimuth or the elevation drives are mechanically not functioning accurately, there will be errors in the concentrator tracking resulting in reduced thermal input and lower efficiencies for the engine. The mechanical functionality of these drives has greatly improved by adding ball screws, which have increased the life expectancy to 1,000,000 inches from about 350,000 inches for machine screws (Sharke, 2006).

3 Component Models

One of the primary goals of this research was to develop a location dependent performance prediction model of a Stirling dish system. The Stirling dish system model developed combines individual component models including the collector, receiver, Stirling engine/generator, and ancillary components. The collector model calculates the intercept factor, which is defined as the fraction of energy leaving the surface of the parabolic mirror that enters the receiver aperture. The value of the intercept factor depends on the receiver aperture diameter and errors in the collector. The receiver model includes natural convection losses that vary based on the aperture orientation, air density, speed of the wind, and the ambient temperature, forced convection losses that depend on the wind speed, and receiver radiation losses that vary based on ambient temperature and heater head temperature. The Stirling engine component includes terms for the compression space temperature, which is determined from the ambient temperature, and an expansion space temperature which is dependent on the heater head temperature set point. The ancillary component determines the parasitic power consumption of the fan and pump based on ambient conditions. A schematic of the model components (excluding the collector) is given in Figure 3-1.

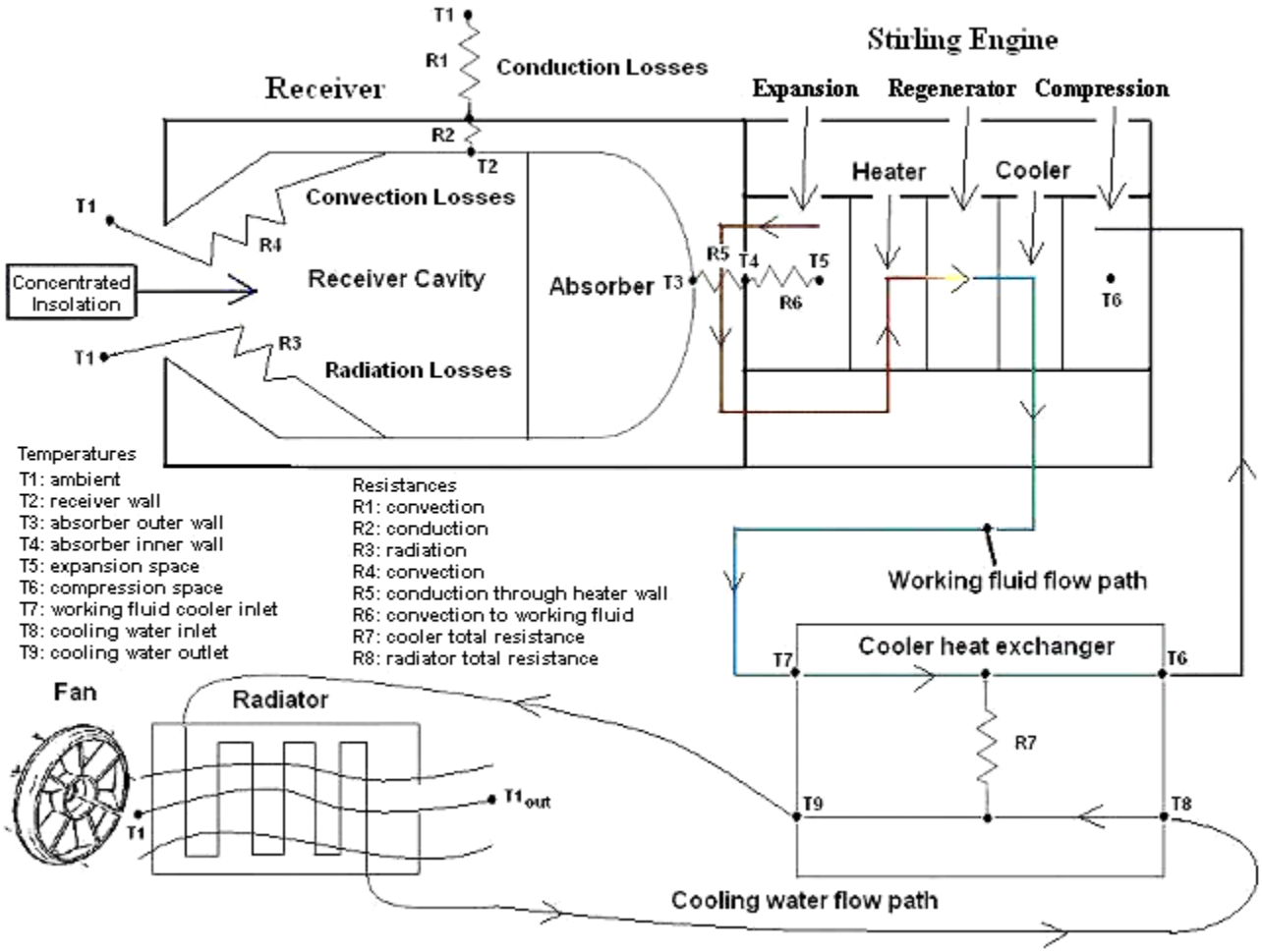

Figure 3-1 Component model components, resistances, and energy flow diagram

3.1 Parabolic Collector Model

The parabolic concentrator model predicts the solar power intercepted by the receiver ($P_{in,rec}$) based on the direct normal insolation (I_{DNI}), projected area of the mirror (A_{proj}), wind cut-out velocity ($wind_{cut,out}$), intercept factor ($\varphi_{\text{int,fac}}$), mirror reflectivity (ρ_{ref}), and the shading factor (φ_{shade}) (see appendix G) as given by Equation (3.1).

$$P_{in,rec} = I_{DNI} \cdot A_{proj} \cdot \rho_{ref} \cdot \varphi_{wind} \cdot \varphi_{\text{int,fac}} \cdot \varphi_{shade} \tag{3.1}$$

$$wind, speed \le wind_{cut,out} \rightarrow \phi_{wind} = 1.0 \tag{3.2}$$

$$wind, speed > wind_{cut,out} \rightarrow \phi_{wind} = 0 \tag{3.3}$$

The wind cut-out velocity is a value indicating the wind speed at which the parabolic concentrator will be sent into a stow position to prevent wind damage. The shading factor (φ_{shade}) is determined using theory from Osborn (1980). The shading factor is a function of the

number of parabolic concentrators, the collector diameter, and the North-South and East-West collector separation distance. The shading factor term is defined in Equation (3.4) where S_{AVG} is given by Equation G-46 and is the average shaded area per dish in a field.

$$\phi_{shade} = \frac{A_{proj} - S_{AVG}}{A_{proj}} \tag{3.4}$$

3.1.1 Intercept Factor

The intercept factor for a Stirling dish system is defined as the fraction of energy reflected from the parabolic mirror that enters the receiver. After a collector system is manufactured and the mirrors have been adjusted for a specified receiver aperture diameter, the intercept factor will remain constant. A collector model was required to optimize the aperture diameter of the receiver considering the energy entering the receiver and the energy leaving the receiver due to radiation and convection. Several models were found that allow for the intercept factor to be determined based on the aperture diameter and imperfections in the design of the collector mirror.

Collector models have been described by Stine and Harrigan (1985), Jaffe (1983), and by Sandia National Laboratory for their CIRCE software (Romero, 1994). The collector models were compared to determine how the predicted performance of the WGA collector is influenced by changing the aperture diameter. The aperture diameter was varied between zero and one fifth of a meter and the resulting fraction of intercepted power predicted by the models were compared in Figure 3-2. The Jaffe model was not consistent with the published intercept factor for the WGA-500 collector system which is over 99 % (Mancini et al, 2003) at an aperture diameter of 0.14 meters, whereas the Stine and Harrigan, and CIRCE models were consistent. The CIRCE model (WGA, 2001) provides more conservative (lower) estimates of the intercept factor at smaller aperture diameters than the Stine and Harrigan model.

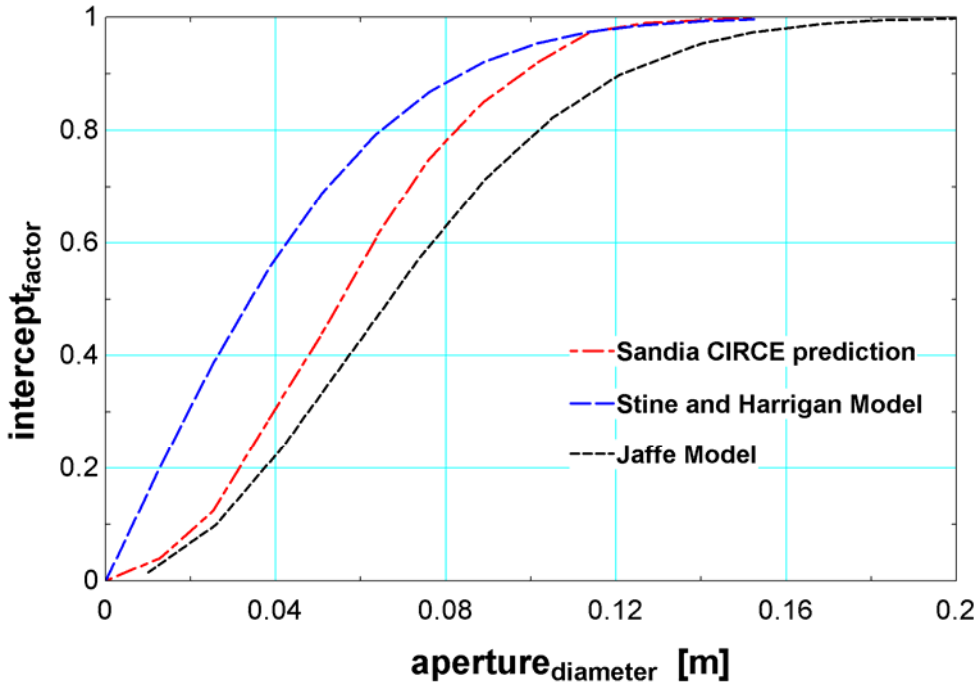

Figure 3-2 Receiver aperture size influence on intercepted power for the WGA-500 Collector

It is unlikely that the net system performance would be optimized with an intercept factor below 95 % since the convection and radiation losses would not be reduced significantly whereas the intercept losses would increase rapidly. A collector model that accurately predicts the intercept factor at values above 95 % for a specified aperture diameter is therefore necessary. Both the Stine and Harrigan, and the CIRCE model have similar predictions for intercept factors above 95 %. The Jaffe model can provide better predictions for the intercept factor compared to the CIRCE prediction by modifying the term σ_{sun} from 2.3 mille-radians to 1.4 mille-radians. The published slope error for the WGA-500 collector is 1.0 mille-radians. The influence of slope error predicted by the Jaffe model is shown in Figure 3-4.

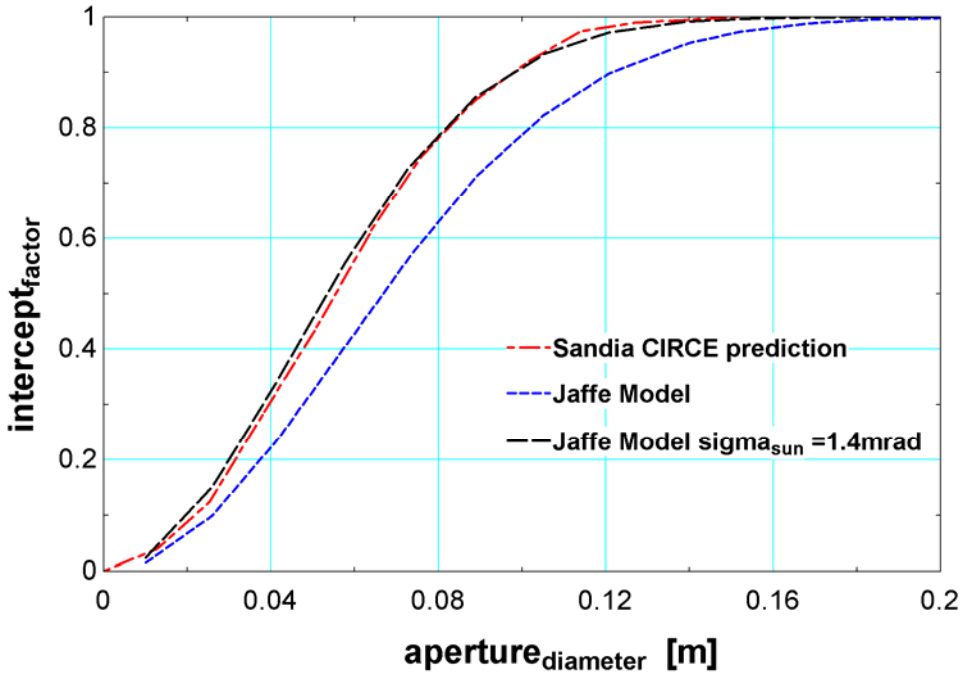

Figure 3-3 Influence of modifying the Jaffe collector model with the 1.0 mille-radian slope error

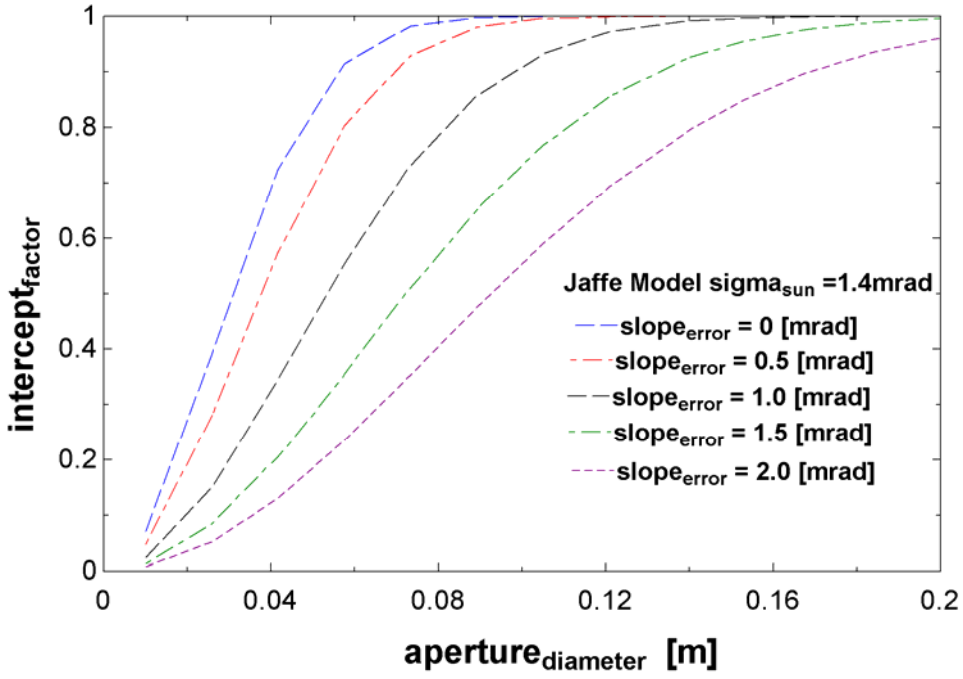

Figure 3-4 Influence of varying the slope error with the modified Jaffe model

The Stine and Harrigan model was also modified to obtain similar results of the CIRCE software. If the flux capture fraction (intercept factor) term is modified in the Stine and Harrigan model, the predicted intercept factor resembles a trend closer to the CIRCE predictions. When the flux capture fraction is modified in the Stine and Harrigan model, the errors in the collector system must also be modified to obtain the correct published value for the intercept factor at a specified diameter. Based on the results of these simulations, it was decided to use the Stine and Harrigan model in the TRNSYS component and allow the user to specify the power that the flux capture fraction is raised to.

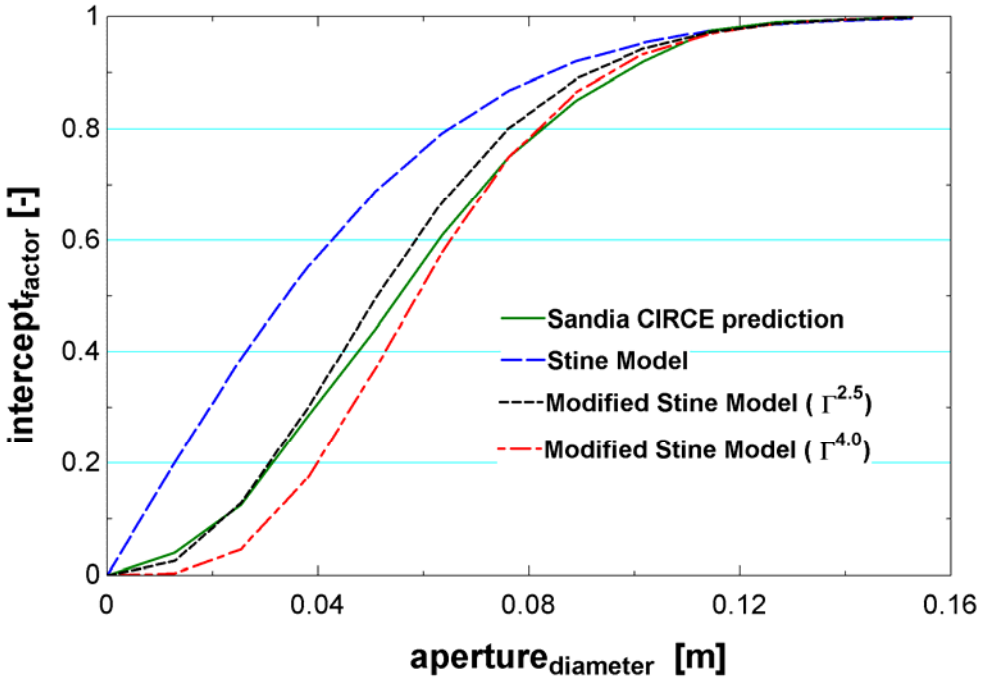

Figure 3-5 Influence of varying the flux capture term with the Stine and Harrigan model

3.2 Receiver Model

The receiver model receives its energy input from the output of the collector model. The input energy is diminished by radiation, convection, and conduction losses from the receiver, which are location and time-of-day dependent. The conduction losses are minimal and are dependent on the receiver temperature, insulation thickness and conductivity, and the ambient temperature. The convection losses represent a large fraction of the receiver losses and depend on the ambient temperature, wind velocity, receiver cavity temperature, and orientation of the receiver aperture. Convection losses will be greater when the elevation angle of the sun is lower during the morning, evening, and winter. The radiation losses include long-wave radiation emission out of the aperture resulting from the high temperature of the cavity walls, and from reflected radiation off of the cavity walls and out of the receiver aperture since the interior cavity is not an effective black body. The power output of the receiver (to the Stirling engine) is given by Equation (3.5) where $P_{in,SE}$ is the thermal input power to the Stirling engine, $P_{in,rec}$ is the input power to the receiver, $\dot{q}_{conv,tot}$, $\dot{q}_{rad,emit}$, and $\dot{q}_{rad,reflect}$ represent the rate of heat loss from the receiver by

convection (natural and forced), emitted radiation out of the receiver aperture, and the reflected radiation out of the aperture, respectively. A consistent set of variables was used in the models as shown in Figure 3-6.

$$P_{in,SE} = P_{in,rec} - \dot{q}_{rad,reflect} - \left(\dot{q}_{cond} + \dot{q}_{conv,tot} + \dot{q}_{rad,emit}\right)_{losses} \quad (3.5)$$

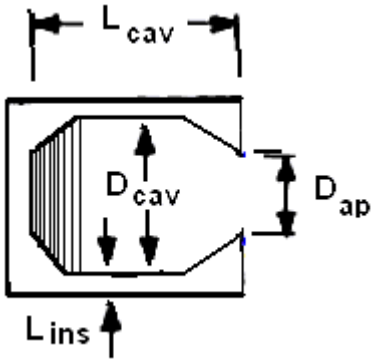

Figure 3-6 Consistent set of variables used for receiver models

3.2.1 Conduction

The conduction model uses a resistance network for conduction through the receiver housing and convection from the exterior receiver housing to the ambient conditions. A model of the SES receiver was used to predict the conduction losses using an approximate steady state interior receiver cavity temperature of 800°C, an insulation thermal conductivity of 0.06 W/m-K, and an area of 0.28 m^2 used for conduction. The total conduction losses estimated with the model was about 200 W with an insulation thickness of 0.075 meters. A plot of the conduction losses with respect to the insulation thickness was generated in Figure 3-7.

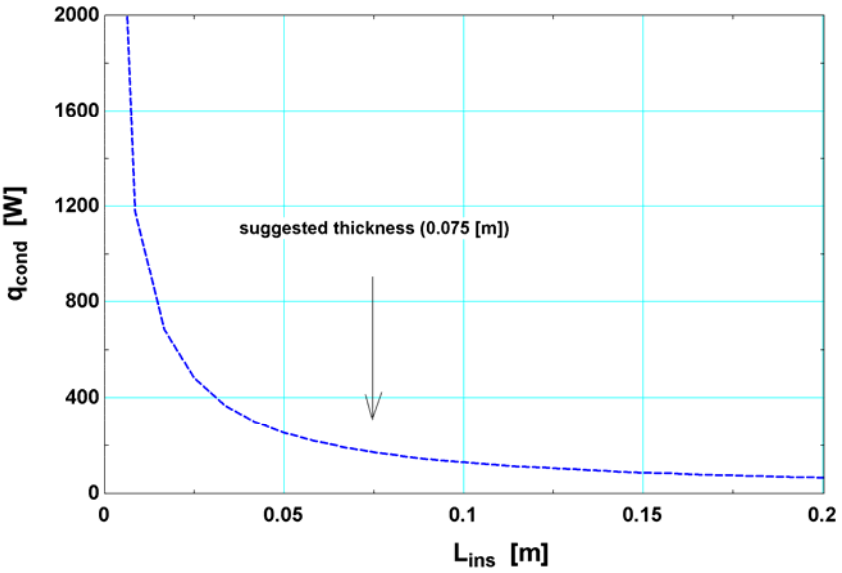

Figure 3-7 Conduction losses as a function of the insulation thickness

3.2.2 Natural Convection

A convection model was generated to compare the various natural convection correlations listed in Chapter 2. The parameters used were held constant for the different natural convection correlations, while the Nusselt number and corresponding convection losses were solved for the Koenig and Marvin (1985), Stine and McDonald (1989), Liebfried (1995) modified Stine, and the Paitoonsurikarn et al. (2004) modified Liebfried correlations. A plot was generated as seen in Figure 3-8 to compare these correlations with consistent inputs. Data were not obtained for a Stirling dish receiver for the work presented in this thesis, so it was difficult to discern which model was the most accurate. The convection correlations also used data from different sized receivers, so there appears to be some dependency on geometry and size. The Stine and McDonald correlation was chosen for the TRNSYS model since the author's analysis was derived using a larger receiver which would correspond closer to the SES or WGA receiver, and the Stine and McDonald correlation was used in the forced convection models developed by Ma (1993).

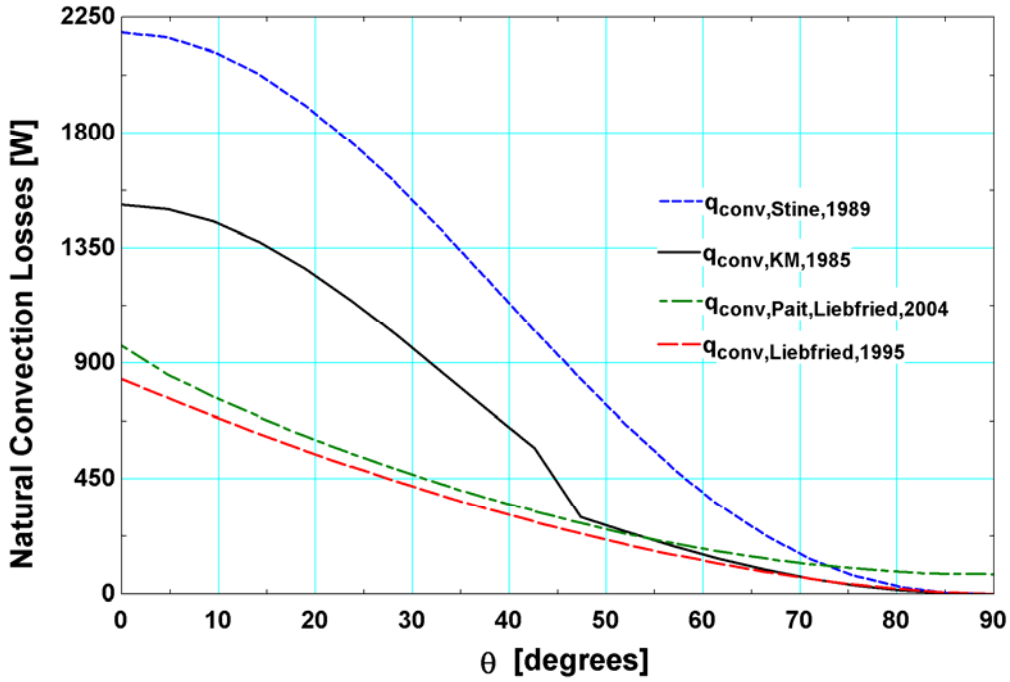

Figure 3-8 Natural convection loss correlation comparison with consistent inputs

3.2.3 Forced Convection

The side-on convection correlation developed by Ma was used to estimate the forced convective losses for the WGA receiver at various wind speeds and aperture orientations (Ma, 1993). The results of the model for the WGA receiver are given in Figure 3-9.

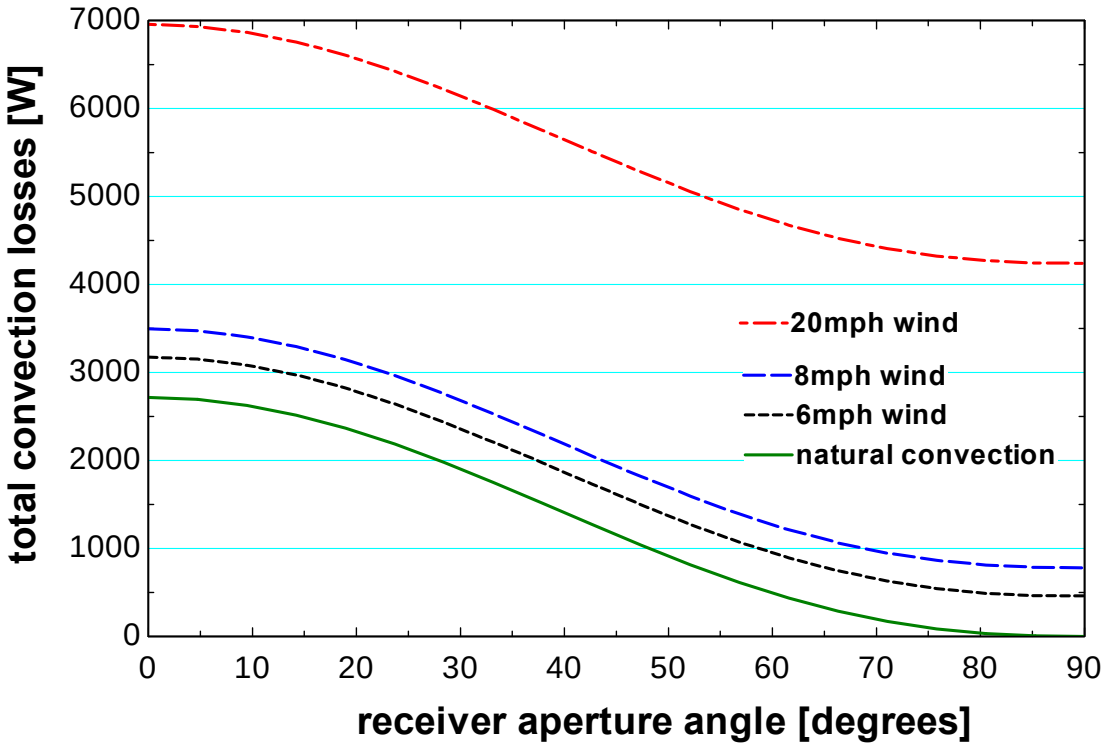

Figure 3-9 Side-on wind predicted losses for the WGA system at various wind speeds and aperture orientations

Similar to the side-on wind condition, a convective loss model created for the WGA receiver for head-on forced convection was prepared and the results are shown in Figure 3-10. The head-on correlation results are shown in Figure 3-9 was chosen for the TRNSYS model since the orientation of the wind may not be known and the head-on correlation gives more conservative energy prediction results

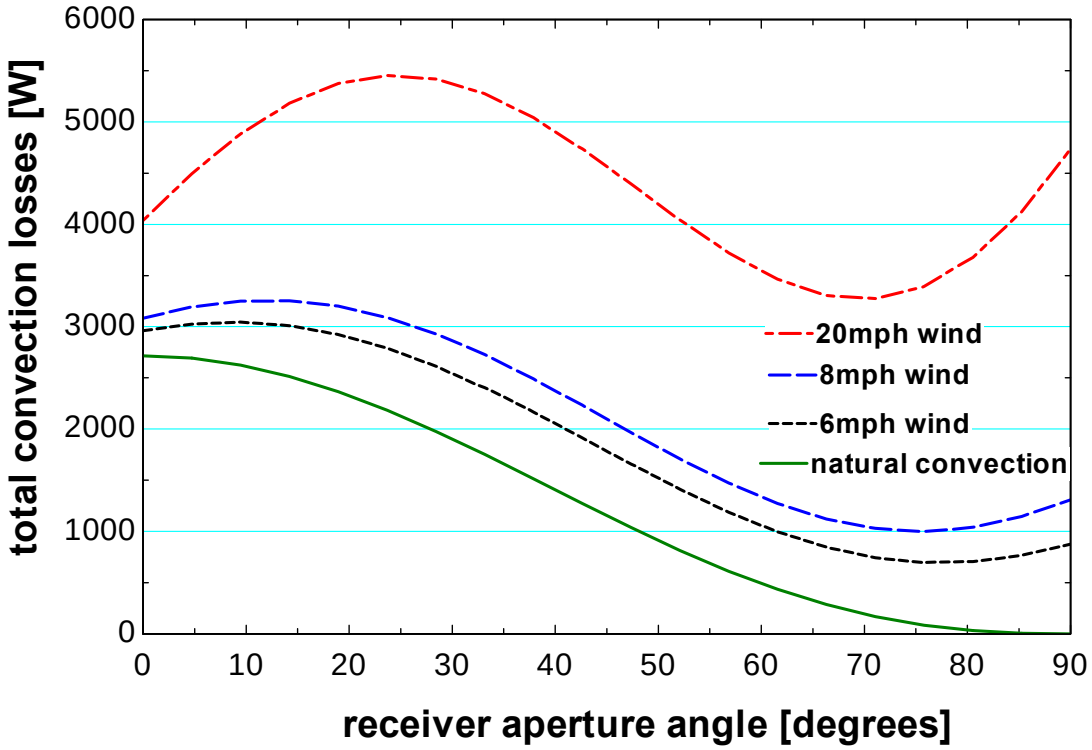

Figure 3-10 Head-on wind predicted losses for the WGA system at various wind speeds and aperture orientations

A plot of the predicted engine efficiency versus input power to the engine was generated from WGA data (Andraka, 2007) to observe the impact of forced convection as shown in Figure 3-11. The wind speeds on 4/27/2004 often surpassed 10 mph and had several peak wind speeds of 20 mph, so the forced convection component should be considerable. The collector and receiver models were used to determine the predicted input power to the engine, and the engine efficiency was predicted using data for the output power and the predicted input power. Including the forced convection term increased the predicted efficiency of the engine by about two percent as observed by the two curve fits in Figure 3-11. Forced convection is included in the TRNSYS component model.

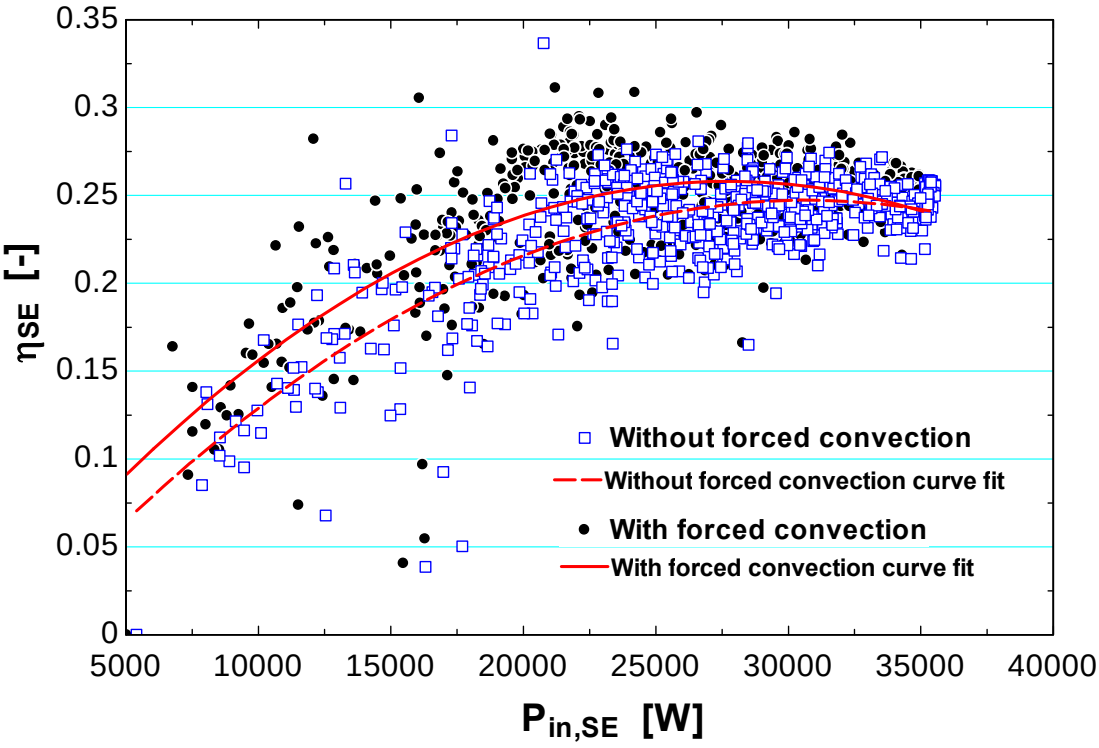

Figure 3-11 Predicted Stirling engine efficiency with and without using a forced convection term for the receiver on 4/27/2004. Data were for the WGA system (Andraka, 2007).

3.2.4 Radiation

The radiation model considered both emitted and reflected radiation from a cylindrical cavity receiver. The general radiation equation given in Equation (3.6) (Incropera and DeWitt, 2002) was compared with the estimated radiation given using view factors (Howell, 2007) as shown in Figure 3-12. The TRNSYS model uses Equation (3.6) since the view factor analysis provides similar results.

$$\dot{q}_{radiation} = \varepsilon \cdot \sigma \cdot A_{ap} \cdot \left(T_{cav}^4 - T_{amb}^4 \right) \tag{3.6}$$

The term ε is the emissivity which was set equal to the effective absorptance of the cavity (it is close to a blackbody), σ is Stephen Boltzmann's constant, A_{ap} is the aperture area, T_{cav} is the cavity temperature, and T_{amb} is the ambient temperature.

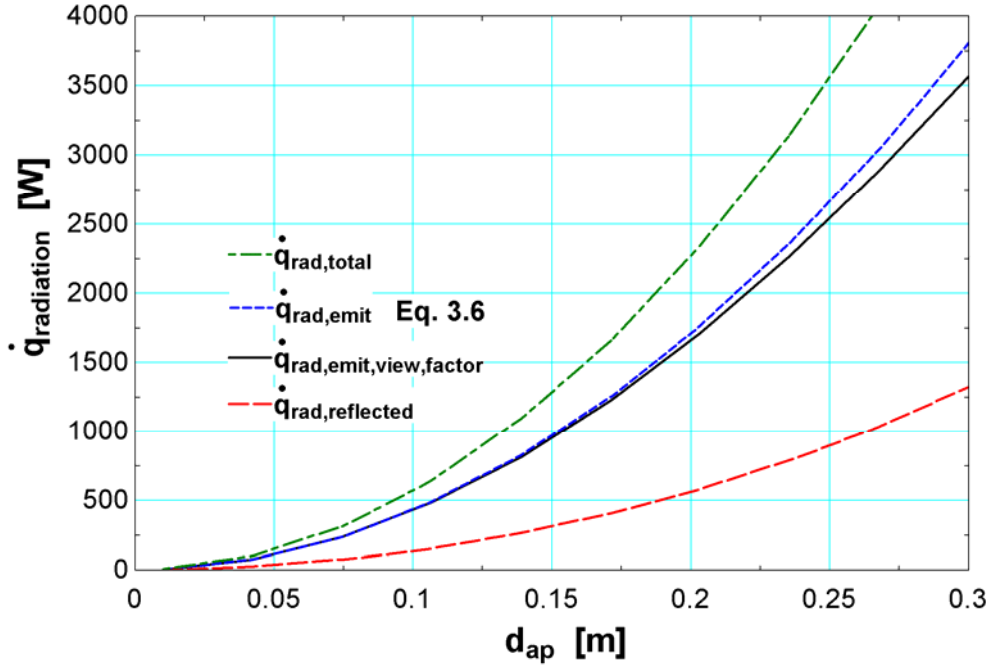

Figure 3-12 Total, emitted, and reflected radiation with a cavity internal diameter of 0.4 meters while varying the aperture diameter. SES has a receiver aperture diameter of 0.2 meters

The reflected radiation was determined using Equation (3.7) with the effective absorptance (α_{eff}) given by Equation (3.8) where (α_{cav}) is the absorptance of the cavity walls. A plot was generated to view the reflected radiation as a function of the aperture diameter as shown in Figure 3-12.

$$\dot{q}_{rad,reflect} = \left(1-\alpha_{eff}\right)\cdot\dot{q}_{in,receiver} \tag{3.7}$$

$$\alpha_{eff} = \frac{\alpha_{cav}}{\alpha_{cav}+\left(1-\alpha_{cav}\right)\cdot\left(A_{ap}/A_{cav}\right)} \tag{3.8}$$

3.2.5 Hybrid Receiver Cover Analysis

A Pyrex or quartz cover can be placed over the receiver aperture when the system is run in a hybrid mode with natural gas or another alternative fuel source other than solar. The cover reduces the performance of the system by reflecting up to ten percent or more of the incoming solar radiation, but also acts as a shield to reduce thermal losses from the receiver cavity. The thermal losses from the cavity with a cover occur from convection and radiation to the inside cover, conduction through the cover material, and finally radiation and convection to the ambient air as shown in Figure 3-13.

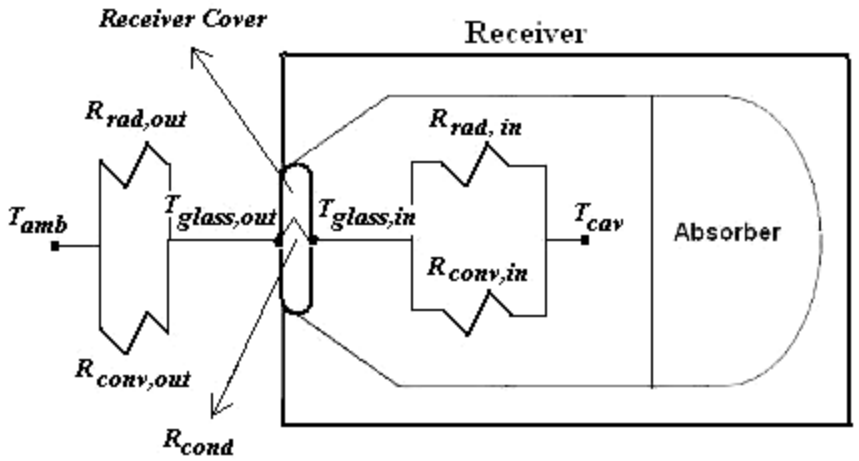

Figure 3-13 Receiver thermal resistance network with a receiver cover

A system of three equations is used to solve for the rate of thermal losses, $\dot{Q}_{losses}$, from the receiver when there is a cover over the aperture. These equations are shown in Equations (3.9), (3.10), and (3.11).

$$\dot{Q}_{losses} = \frac{T_{cav} - T_{amb}}{R_1} \tag{3.9}$$

$$\dot{Q}_{losses} = \frac{T_{cav} - T_{glass,in}}{R_2} \tag{3.10}$$

$$\dot{Q}_{losses} = \frac{T_{glass,in} - T_{glass,out}}{R_{cond}} \tag{3.11}$$

where T_{cav} is the cavity temperature, T_{amb} is the ambient temperature, $T_{glass,in}$ is the internal cover temperature, $T_{glass,out}$ is the external cover temperature, and R_1 and R_2 are given by Equations (3.12) and (3.13) respectively.

$$R_1 = \left[\frac{1}{R_{conv,in}} + \frac{1}{R_{rad,in}}\right]^{-1} + R_{cond,glass} + \left[\frac{1}{R_{conv,out}} + \frac{1}{R_{rad,out}}\right]^{-1} \tag{3.12}$$

$$R_2 = \left[\frac{1}{R_{conv,in}} + \frac{1}{R_{rad,in}}\right]^{-1} \tag{3.13}$$

The conduction, convection, and radiation resistances are given by Equations (3.14), (3.15), and (3.16) respectively

$$R_{cond} = \frac{L}{k \cdot A} \tag{3.14}$$

$$R_{conv} = \frac{1}{h \cdot A} \tag{3.15}$$

$$R_{rad} = \frac{1}{A \cdot \sigma \cdot \varepsilon \cdot \left(T_1^2 + T_2^2\right) \cdot \left(T_1 + T_2\right)} \tag{3.16}$$

where L is the thickness of the aperture cover, A is the surface area of the cover, k is the thermal conductivity of the cover, h is the convective heat transfer coefficient which is different for the internal and external cover surface, σ is Stefan Boltzmann's constant, ε is the emissivity of the material, T_1 is the lower temperature absorbing more radiation ($T_{glass,in}$ for internal radiation to the cover, T_{amb}-cover exterior) , and T_2 is the higher temperature material emitting more radiation(T_{cav} –interior, $T_{glass,out}$ -exterior).

3.2.5.1 Convection in Internal Volumes

The internal convective heat transfer coefficient used is for internal volumes where a convection current is created by the difference in temperature between the cavity walls and the lower temperature aperture cover. The correlation to determine the convection heat transfer coefficient is dependent on the aperture orientation and the Rayleigh number for the internal volume. The internal convection heat transfer coefficient derived from the Nusselt number correlation for characteristics of cavity receivers is recommended by Arnold et al. in Equation (3.17) (Incropera and DeWitt, 2002)

$$\bar{N}u_{\text{internal}} = 1 + \left[\bar{N}u\left(\tau = 90^0\right) - 1\right] \cdot \sin\left(90^0 + \theta\right) \tag{3.17}$$

where $\bar{N}u_{\text{internal}}$ is the Nusselt number, θ is the receiver aperture orientation (0^0 is horizontal, 90^0 is vertically down), and $\bar{N}u\left(\tau = 90^0\right)$ is given by Equation (3.18)

$$\bar{N}u_{\tau=90^0} = 0.18 \cdot \left(\frac{Pr}{0.2 + Pr} \cdot Ra\right)^{0.29} \qquad \begin{pmatrix} 10^3 \le Ra \le 10^{10}; 10^{-3} \le \text{Pr} \le 10^5; \\ 1 < d_{cav}/L_{cav} < 2 \end{pmatrix} \tag{3.18}$$

where d_{cav} is the internal cavity diameter, L_{cav} is the internal depth of the cavity, Pr and Ra are the Prandtl number and Rayleigh number given by Equation (3.19) and Equation (3.20) respectively

$$\text{Pr} = \frac{\upsilon}{\alpha} \tag{3.19}$$

$$Ra = \frac{g \cdot \beta \cdot \left(T_{cav} - T_{glass,in}\right) \cdot d_{ap}^3}{\upsilon \cdot \alpha} \tag{3.20}$$

where υ is the kinematic viscosity of air or the combustion gas mixture, α is the thermal diffusivity, β is the expansion coefficient, and g is the gravitational constant. The interior Nusselt number is plotted as a function of the receiver orientation in Figure 3-14. The plot

indicates that convection to the interior cover surface will be reduced when the colder cover is below the hotter interior cavity walls, which is consistent with buoyant forces of warm air.

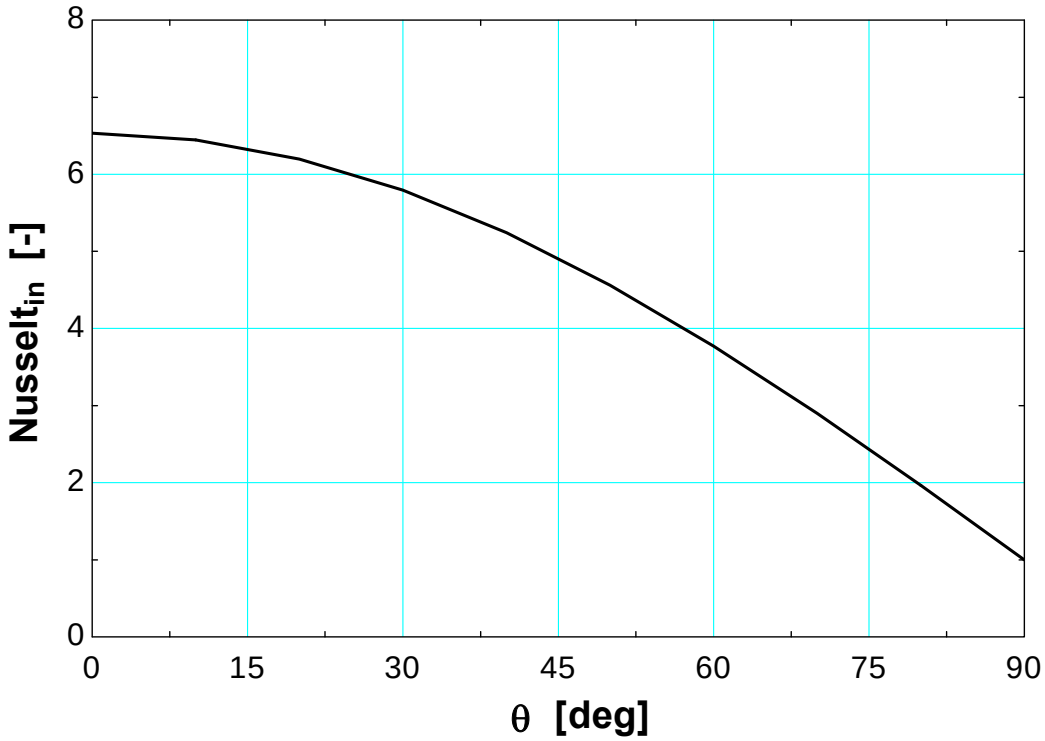

Figure 3-14 Interior cavity Nusselt number as a function of aperture orientation for the WGA receiver cavity with an aperture cover

Heat transfer from the receiver to the aperture cover is dominated by radiation and not convection as shown in Figure 3-15. For some applications with a receiver aperture cover, the interior cavity is pressurized. For this circumstance, heat transfer from convection in the interior cavity will increase due to the ability of higher density air to transfer more energy. A plot of the resistances of radiation and convection for a pressurized cavity is shown in Figure 3-16.

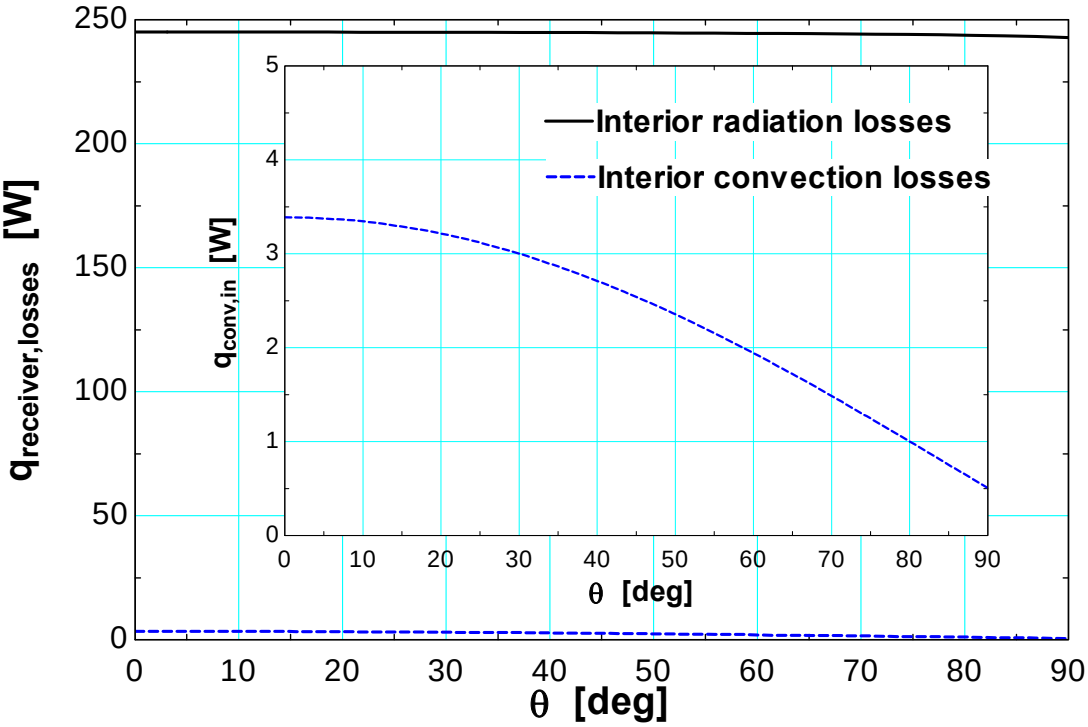

Figure 3-15 Thermal losses of convection and radiation to a WGA receiver cover interior surface with a cavity pressure of 101 kPa

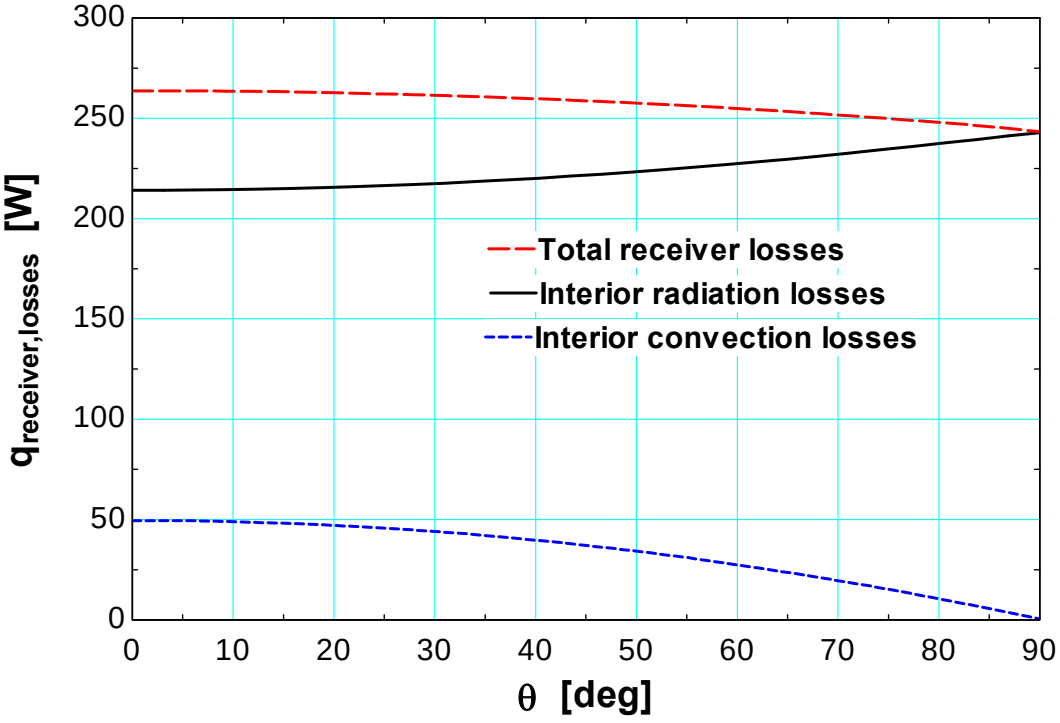

Figure 3-16 Thermal losses of convection and radiation to a WGA receiver cover interior surface with a cavity pressure of 15 MPa

3.2.5.2 Convection for the Exterior Plate Surface

The convection coefficient for the exterior surface of the aperture cover is determined by combined free and forced convection. Forced convection dominates when the ratio of the Grashof number divided by the square of the Reynolds number is much less than one. Forced convection can be neglected when the ratio is much greater than one since free convection will be more significant. Both forced and natural convection should be considered when the ratio is close to one. For Stirling dish applications, both forced and natural convection will be included from the exterior surface of the aperture cover.

Free Convection from a Flat Plate

The Nusselt number correlation used for free convection on the outside of the plate surface is dependent on the aperture orientation. In the morning and evening, the aperture cover will be oriented vertically and the Nusselt number correlation is given by Churchill and Chu (1975) in Equation (3.21) (Incropera and DeWitt, 2002)

$$\bar{N}u_{exterior} = 0.68 + \frac{0.67 \cdot Ra^{1/4}}{\left[1+\left(0.492/\Pr\right)^{9/16}\right]^{4/9}} \qquad \left(Ra \le 10^9; 0^0 \le \theta \le 60^0\right) \tag{3.21}$$

During the day, the aperture plate will be on an incline facing down, and Equation (3.21) should be used with the gravitational constant g in the Rayleigh number computed as $g \cdot \cos(\theta)$ where 0^0 is the aperture facing horizontal (vertical plate) and 90^0 is for the aperture oriented vertically down (horizontal plate) (Incropera and DeWitt, 2002). The Rayleigh number should be corrected by $g \cdot \cos(\theta)$ only when the hot plate is being cooled from the bottom (corresponding to dish receivers), and for angles between zero and sixty degrees. For angles greater than 60 degrees, a horizontal plate Nusselt correlation should be used for the bottom of a hot surface being cooled which is given by McAdams (1954) in Equation (3.22) (Incropera and DeWitt, 2002). The accuracy of McAdams correlation can be improved by defining the characteristic length for the Rayleigh number in Equation (3.22) to be that in Equation (3.23) (Incropera and DeWitt, 2002)

$$\bar{N}u_{exterior,free} = 0.27 \cdot Ra^{1/4} \qquad \left(10^5 \le Ra \le 10^{10}; 60^0 \le \theta \le 90^0\right) \tag{3.22}$$

$$L = {}^{A_s}\!/_{P} = {}^{d_{ap}}\!/_{4} \tag{3.23}$$

where A_s is the surface area of the plate, d_{ap} is the aperture diameter, and P is the perimeter of the plate. Changing the characteristic length to that in Equation (3.23) will reduce the Rayleigh number and therefore reduce the Nusselt number and convective heat transfer coefficient. Conservative estimates of the energy production from Stirling dish systems result from leaving the characteristic length to be the length of the aperture diameter. Figure 3-17 indicates the Nusselt number for forced convection on the outside of the aperture plate as a function of the receiver aperture orientation. To be more conservative, the larger Nusselt number between the vertical plate and horizontal plate correlation is used in the TRNSYS model. The vertical plate

Nusselt number correlation corrected for the angle of the plate will be used when the convection losses from the exterior plate would be greater, and the horizontal plate correlation will be used when the convection losses would be greater than the vertical plate correlation.

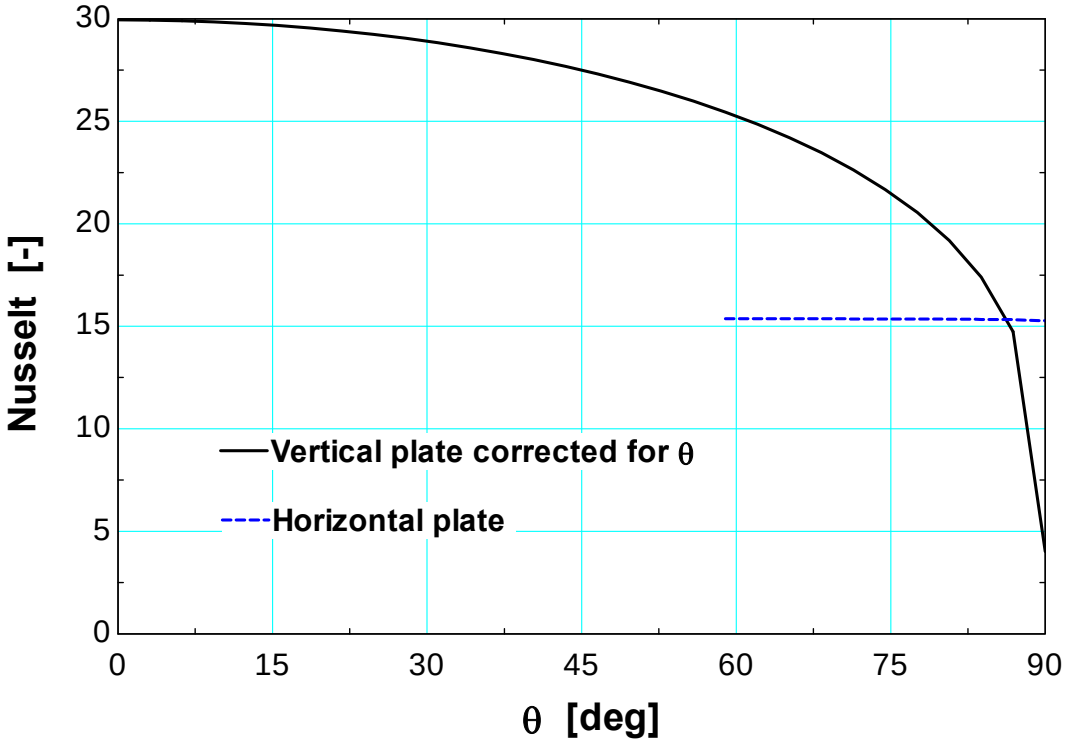

Figure 3-17 Free convection Nusselt numbers for the exterior WGA aperture cover as a function of sun elevation angle

Forced Convection over a Flat Plate

The Nusselt number correlation for forced convection over a flat plate is dependent on whether the flow is laminar or turbulent over the aperture cover. For laminar flow conditions over a plate (Re < 500,000), the Nusselt number can be determined by the Churchill and Ozoe (1973) correlation given by Equation (3.24) (Incropera and DeWitt, 2002). For turbulent flow, the Nusselt number correlation is given by Equation (3.25). For Stirling dish operating wind speeds, the flow over the aperture cover will be laminar and Equation (3.24) is used for Stirling dish systems. A plot of the Nusselt number for forced convection as a function of wind velocity is shown in Figure 3-18.

$$\bar{N}u_{exterior,forced,lam} = 0.664 \cdot \mathrm{Re}^{1/2} \cdot \mathrm{Pr}^{1/3} \tag{3.24}$$

$$\bar{N}u_{exterior,forced,turb} = \left(0.037 \cdot \mathrm{Re}^{4/5} - 871\right) \cdot \mathrm{Pr}^{1/3} \tag{3.25}$$

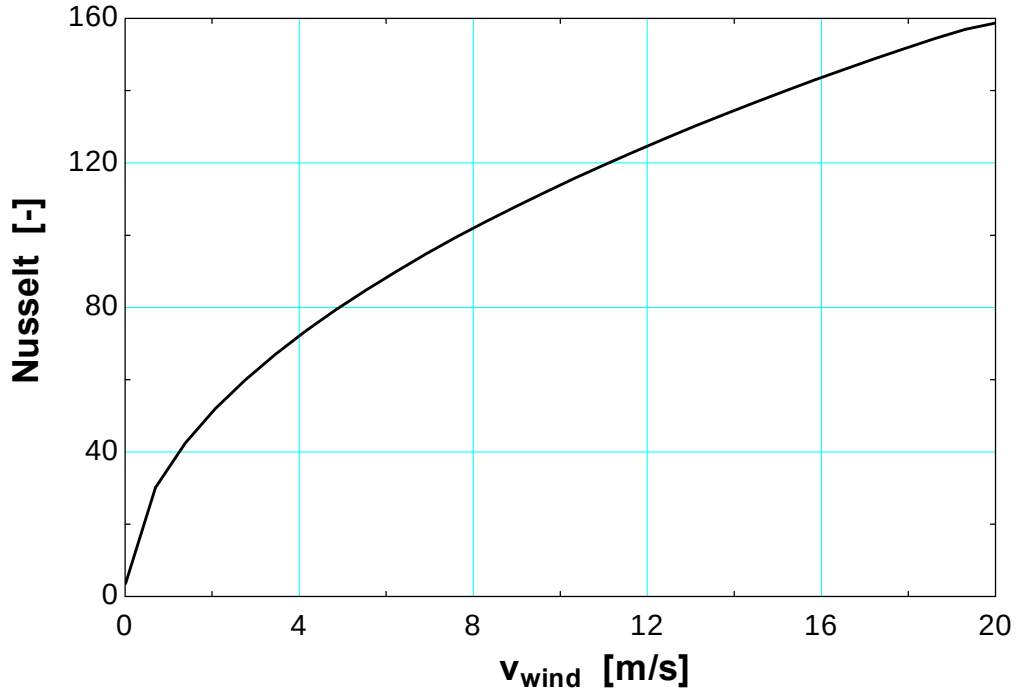

Figure 3-18 Nusselt number for forced convection over a WGA receiver external cover surface as a function of wind velocity

3.2.5.3 Combined Forced and Free Convection

The total convection heat transfer coefficient for the exterior surface of the aperture cover includes both forced and free convection. The combined forced and free convection coefficient can be determined using Equation (3.26) where *n* is chosen to be three (Incropera and Dewitt, 2002).

$$h_{combined,convection} = \left[h_{free}^{n} + h_{forced}^{n} \right]^{1/n} \tag{3.26}$$

3.2.5.4 Total Receiver Thermal Losses with an Aperture Cover

With the appropriate convection correlations determined, Equations (3.9) through (3.11) can be used to compute the total thermal losses from the receiver cavity through the aperture cover. The total thermal receiver losses are shown in Figure 3-19 as a function of the wind velocity and in Figure 3-20 as a function of the aperture orientation for the WGA system. The thermal losses from radiation emission without a receiver cover was approximately 560 W, and the convective losses without a cover were typically between 200 W and 4 kW depending on the receiver orientation and wind velocity. Including a receiver cover significantly reduces radiation and convection losses from the receiver, but also increases reflected radiation. The aperture cover will be more effective in colder climates that have lower sun elevation angles. The greatest benefit of an aperture cover is to enable the Stirling dish system to provide electricity on demand by combusting an alternative fuel. A Brayton cycle engine can also replace the Stirling engine when an aperture cover is used.

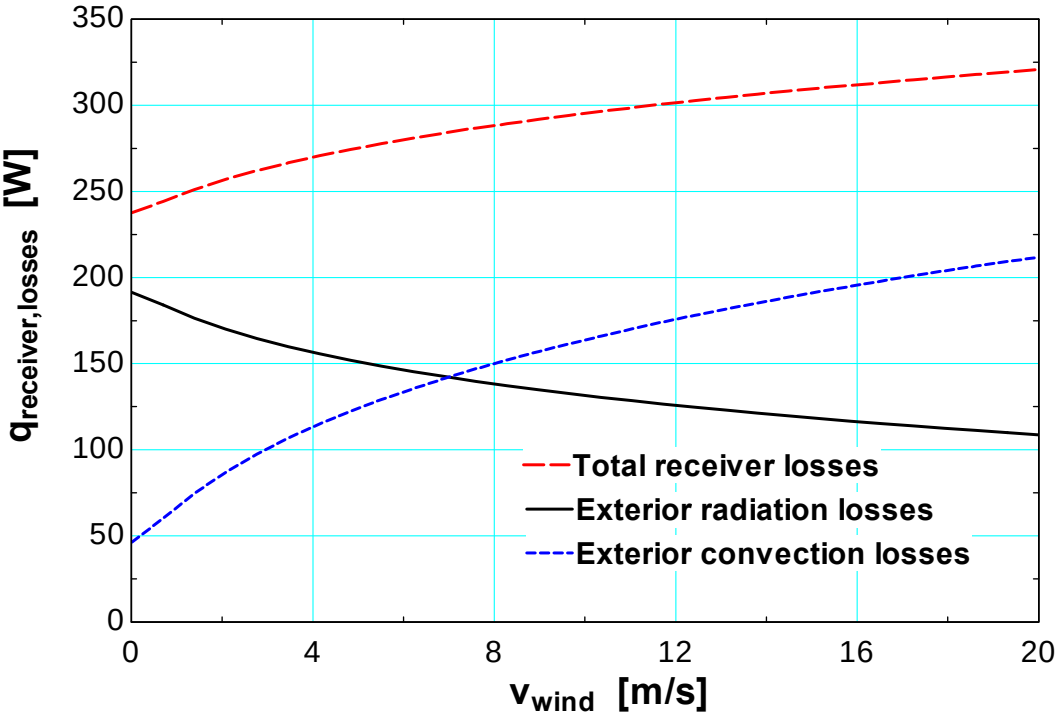

Figure 3-19 Total WGA receiver thermal losses as a function of wind speed for a receiver with a cover and aperture oriented at 45 degrees

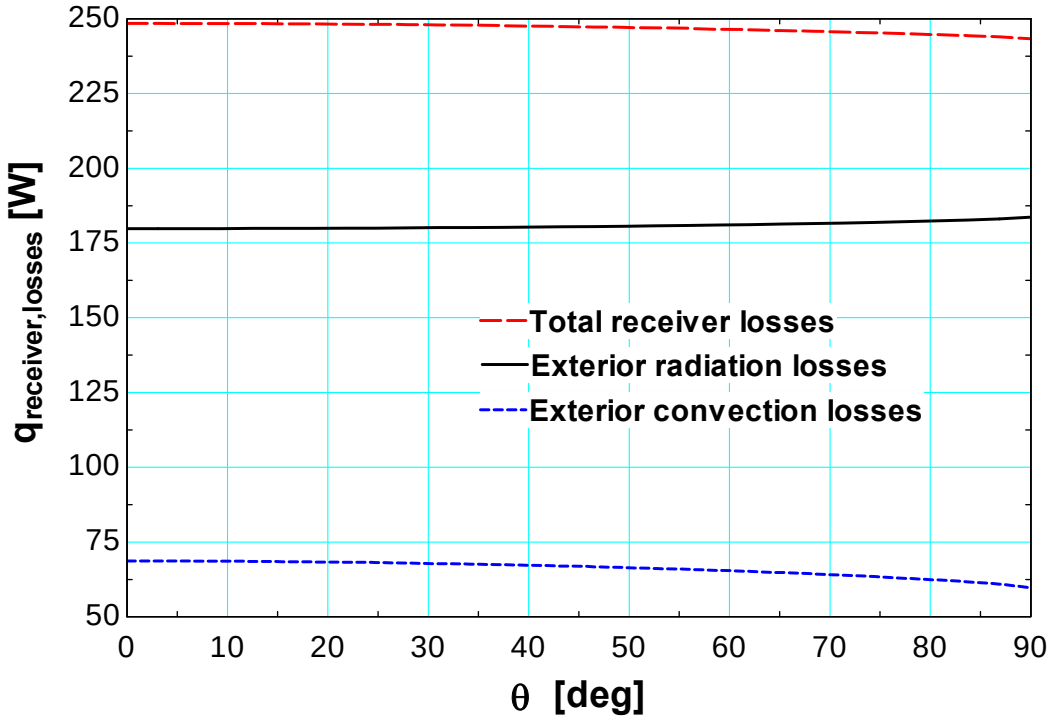

Figure 3-20 Total WGA receiver thermal losses as a function of aperture orientation for a receiver with a cover and wind speed of 1m/s

3.3 Stirling Engine/System Models

The filter criteria from the "Filtering Data for Model Simulations" below were used to generate the curve fits for all of the models. There are two main categories of Stirling dish models that were simulated and compared with WGA data. The first type of model is a system model consisting of detailed models of the collector, receiver, and Stirling engine. The second type of model is the Stine (Stine, 1995) and Sandia (Igo and Andraka, 2007) models that predict the net power as a function of insolation and then correct the power based on the cooling fluid and ambient temperature respectively.

3.3.1 Stirling Engine Component Models

The component-based models consist of models for the collector, receiver, Stirling engine/generator, and the parasitic power to predict the Stirling dish systems performance. These models all use the same collector and receiver model, and the Stirling engine component always consists of a performance curve based on the thermal input power into the engine. The performance curve for a specific engine is generated using data and includes both the Stirling engine and the generator, so the curves are an indication of the efficiency of converting from thermal power to electrical power. Some component-based models include an engine pressure term and/or a term for correcting the engine performance based on the expansion and compression space temperatures. The results section indicates that including a term for predicting the operating pressure, compression space, and expansion space improved the accuracy of the Stirling engine component.

3.3.1.1 Part-load Stirling Engine Component

One Stirling engine component model was created by predicting the Stirling engine efficiency as a function of input power to the Stirling engine as shown in Figure 3-21 using one day of data. The curve fit ($\eta_{SE,curve}$) of the data in Figure 3-21 is then used to predict the engine efficiency using a different set of data. The power input to the engine ($P_{in,SE}$) is predicted using measured data for the collector and receiver models, and the engine efficiency (η_{SE}) in Equation (3.27) is determined by dividing the gross power (P_{gross}) (net power from data subtracted by an estimate for the parasitic power) by the predicted input power to the engine. The mean bias error, average difference in power, and normalized average difference in power are shown in Figure 3-21. These values are determined using the trend line and data for the same day.

$$\eta_{SE} = P_{gross} / P_{in,SE} \tag{3.27}$$

The electrical output power of the Stirling engine in the component model is then predicted using Equation (3.28)

$$P_{out\_SE} = P_{in\_SE} \cdot \eta_{SE,curve} \tag{3.28}$$

where P_{out_SE} is the output electrical power of the Stirling engine which is equivalent to the system gross power, P_{in_SE} is the input thermal power to the Stirling engine determined by the collector and receiver models, and $\eta_{SE,curve}$ is the predicted Stirling engine efficiency from the curve fit given by Equation (3.29).

$$\eta_{SE,curve} = \left[C_1 + C_2 \cdot P_{in\_SE} + C_3 \cdot \left(P_{in\_SE} \right)^2 \right] \tag{3.29}$$

The terms C_1, C_2, and C_3 are the constants obtained from a second order polynomial efficiency curve fit of data such as from Figure 3-21. Any improvements in the Stirling dish system performance with respect to the input power to the engine will require a new engine efficiency curve to be generated to obtain new coefficients. These improvements would include design changes to the engine such as the swept volume, the regenerator, or other components. If a new temperature set point is chosen for the heater head, however, the model predicts the affect it will have on the performance without requiring data to be taken to obtain new coefficients. The collector, receiver, or cooling system can also be modified without requiring a new curve fit for the Stirling engine component.

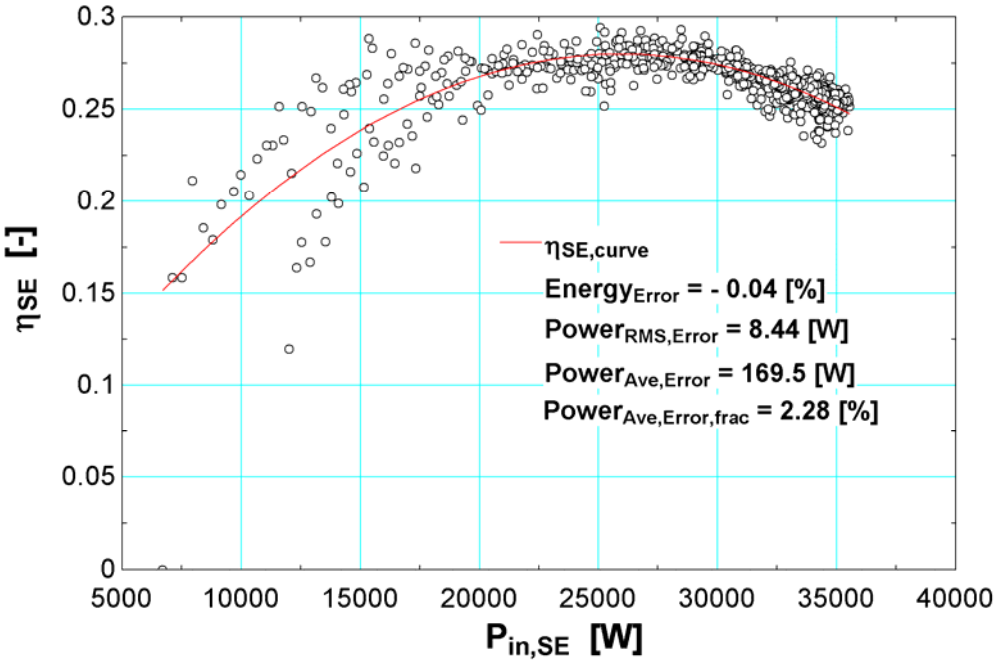

Figure 3-21 Stirling engine efficiency curve for the WGA system on 4/26/2004

Using the data in Figure 3-21, an engine efficiency curve fit was generated using one day (4/26/2004) of data, and then used to predict the net power produced by the WGA system over that same day. The model accurately predicted the engine performance for the same day when using the engine efficiency curve fit as shown in Figure 3-22. The engine efficiency curve fit must also be able to accurately predict the engine performance on different days which can be improved by including terms for pressure and temperature.

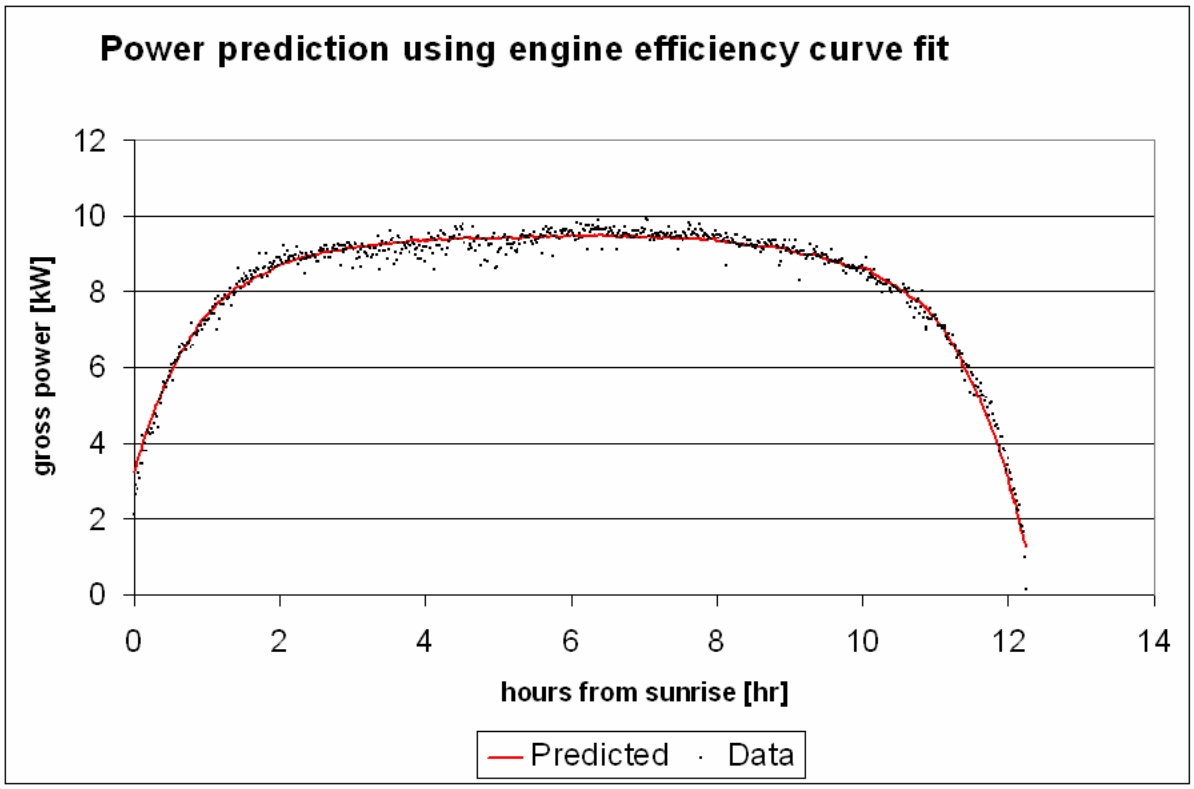

Figure 3-22 Predicted gross power using an engine efficiency curve fit for 4/26/04

3.3.1.2 Part-load Stirling Engine Component including Pressure

Another Stirling engine component was tested using the Beale number equation which includes a term for pressure as shown in Equation (3.30) (Urieli and Berchowitz, 1984)

$$P_{SE,Beale} = Beale \cdot P_{mean} \cdot V_{sw} \cdot f \tag{3.30}$$

where *Beale* is the Beale number, P_{mean} is the mean engine pressure, V_{sw} is the swept volume of the engine, and f is the frequency. Two plots and curve fits are required when using the Beale number Stirling engine component. The first is a plot of the Beale number as function of input power to the Stirling engine as shown in Figure 3-23. The second is a curve fit of the engine pressure versus input power to the engine given by Figure 4-1. These curves are then used in Equation (3.30) to predict what the output power to the Stirling engine when the receiver model predicts the input power to the engine during different ambient conditions. The two curve fits were also generated using the direct normal insolation as opposed to the input power to the engine to see if the collector and receiver models were accurate. Plotting the Beale number and pressure versus input power to the engine resulted in better performance predictions than plotting these versus the direct normal insolation, which indicates the receiver model improves the accuracy of the model.

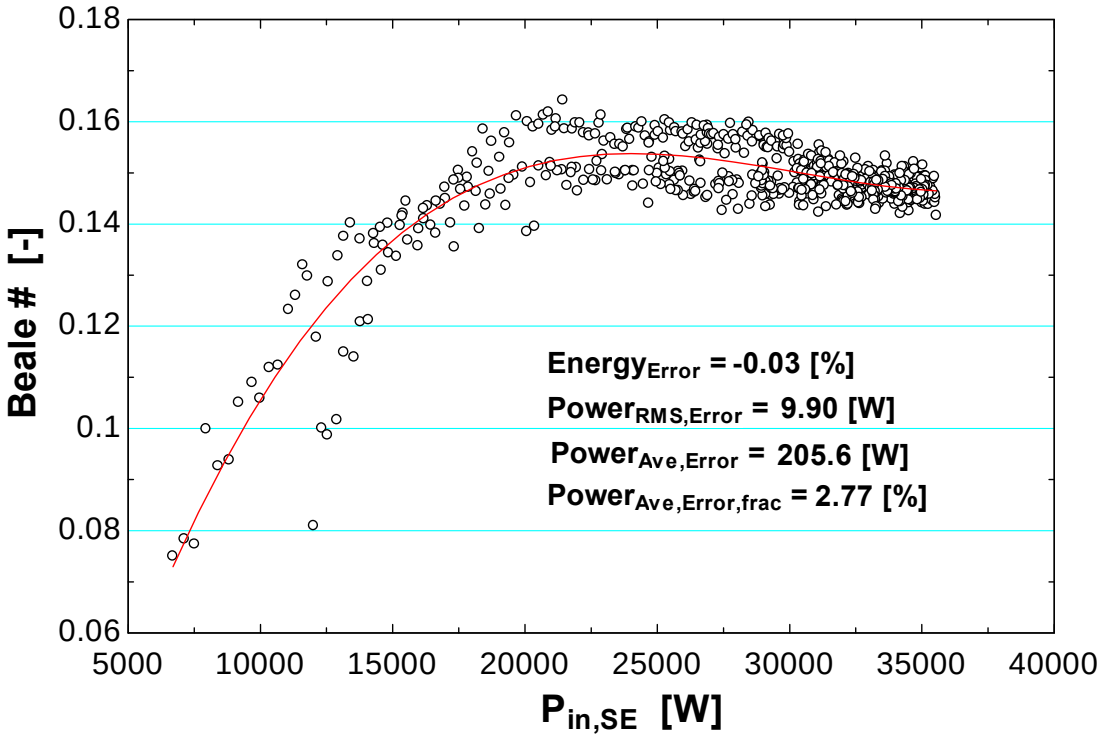

Figure 3-23 Beale number curve fit for 4/26/2004

3.3.1.3 Part-load Stirling Engine Component Corrected for Temperature

The Stirling engine performance is dependent on the hot and cold sink temperatures. The accuracy of a component model can be improved by including terms to correct the Stirling engine performance based on these temperatures. In the experimental data, the expansion space temperature remains mostly constant due to the system being controlled off of the heater head temperature; however, the compression space temperature varies throughout the day and year based on the ambient temperature and insolation.

Three different temperature correlations were used to correct the performance of the Stirling engine. These included the Carnot efficiency in Equation (3.31), the maximum power efficiency given in Equation (3.32) (McMahan, 2007), and the West temperature correlation in Equation (3.33) (Hirata, 2002) where T_E and T_C are the expansion and compression space respectively.

$$1 - T_C / T_E \tag{3.31}$$

$$1 - \sqrt{T_C / T_E} \tag{3.32}$$

$$\left(\frac{T_E - T_C}{T_E + T_C} \right) \tag{3.33}$$

These temperature correlations were used to generate curve fits by dividing the predicted engine efficiency given in Equation (3.27) by these temperature correlations. The resulting curves are shown in Figure 3-24 through Figure 3-26. These curves are then used to predict the engine

efficiency on different days by multiplying the predicted temperature corrected engine efficiency for a specific input power to the engine by the temperature correction terms given by ambient conditions. The results section indicates the maximum power fraction and the West number temperature correlation are the most precise and accurate, followed by the Carnot fraction number. Including a temperature correction term significantly improved the model simulation results and the maximum power fraction temperature correction term using the Beale number has been included in the TRNSYS model.

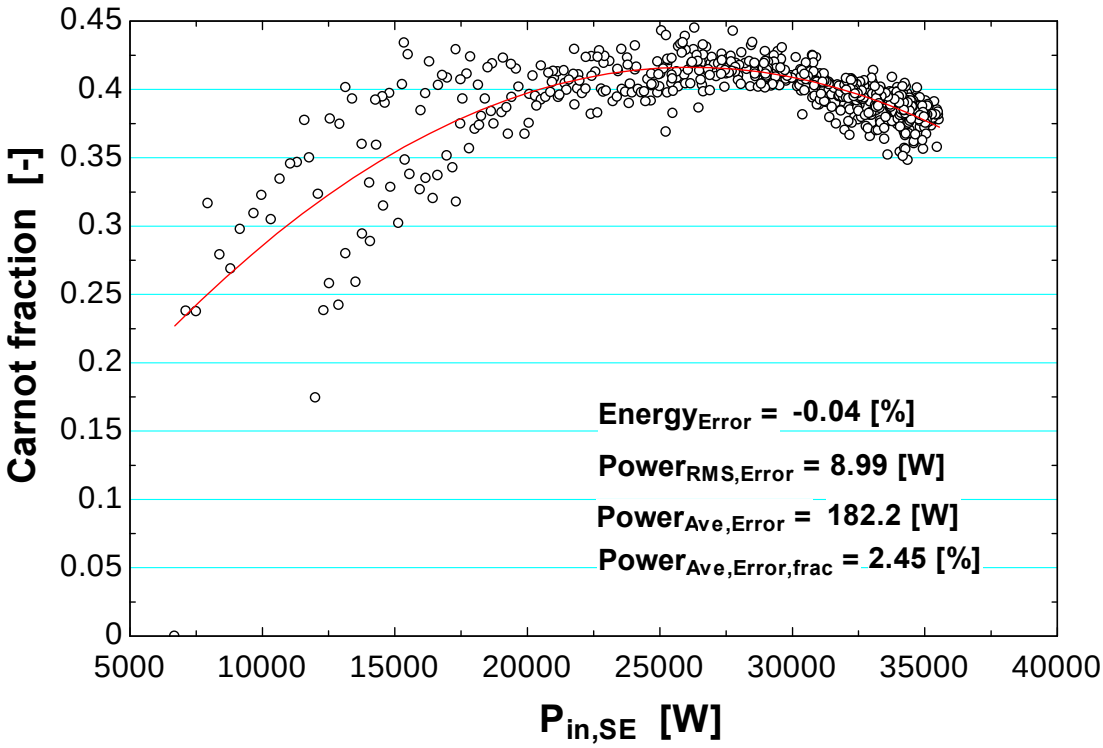

Figure 3-24 Carnot fraction curve generated for 4/26/2004 data

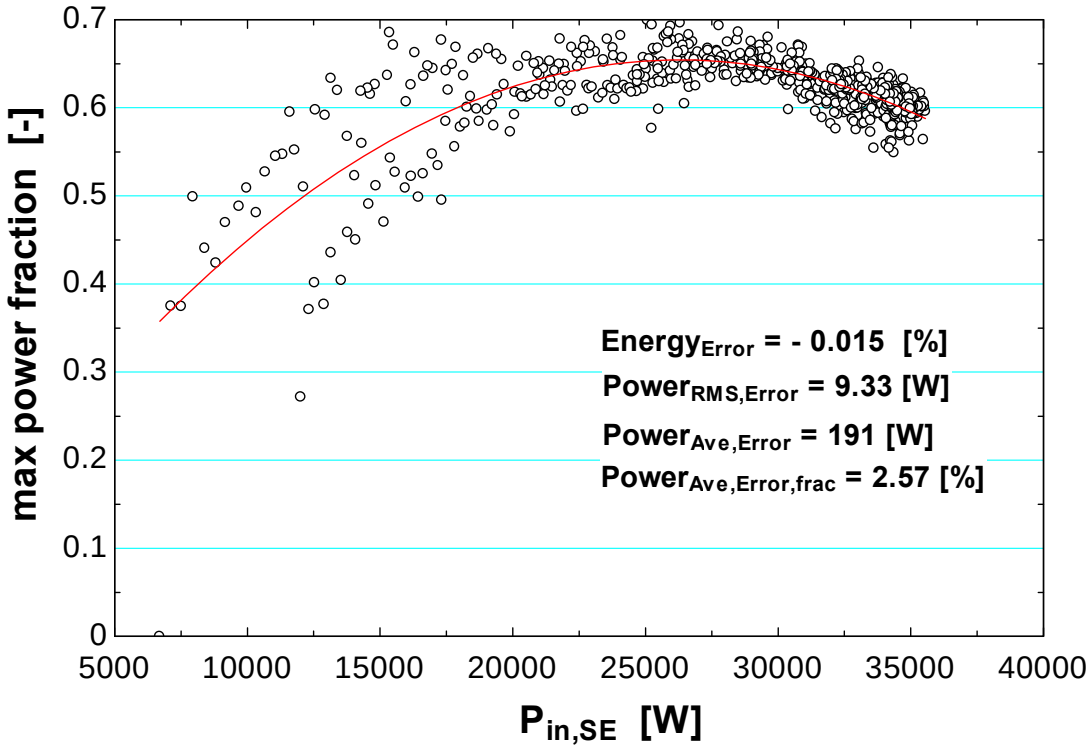

Figure 3-25 Maximum power fraction curve generated for 4/26/2004

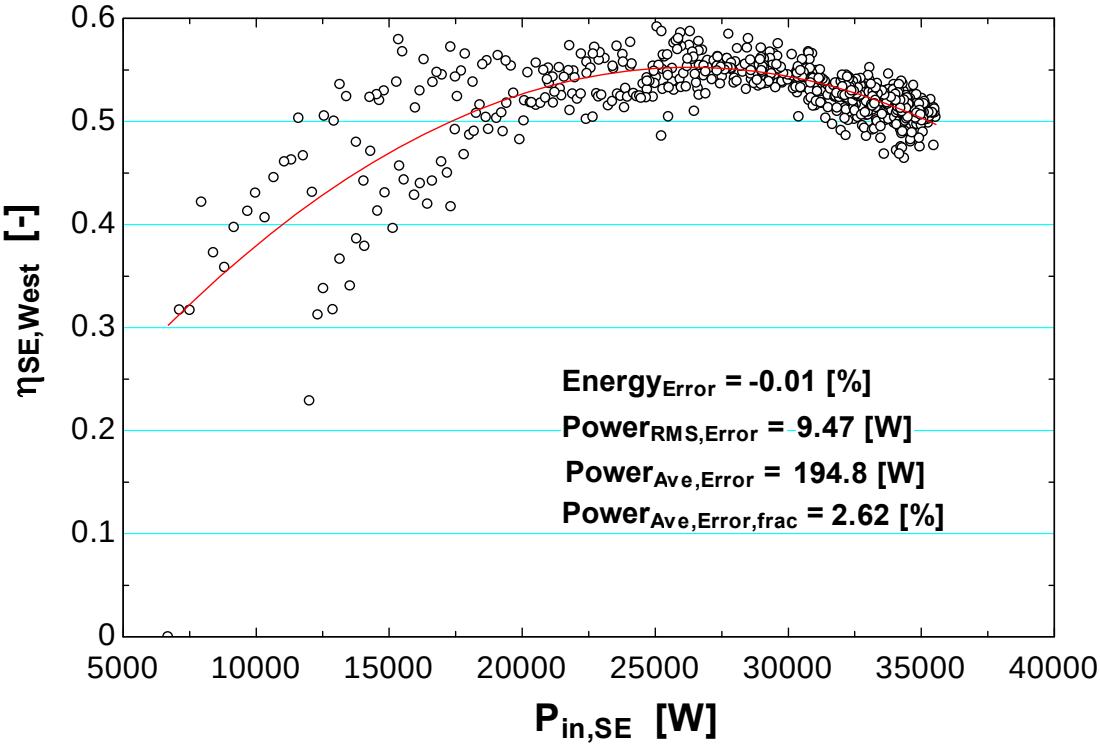

Figure 3-26 West number fraction curve generated for 4/26/2004

3.3.1.4 Stirling Engine Component Corrected for Temperature Including Pressure

The Stirling engine component was corrected for temperature and included a term for pressure using the West correlation in Equation (3.34) (Hirata, 2002)

$$P_{SE,West} = West \cdot P_{mean} \cdot V_{sw} \cdot f \cdot \left(\frac{T_E - T_C}{T_E + T_C} \right) \tag{3.34}$$

where *West* is the West number, T_E is the expansion space temperature, and T_C is the cooling water inlet temperature. The West number correlation is the same as the Beale number correlation except that it has the temperature correction term. The West model Stirling engine component requires a curve fit using the West correlation as shown in Figure 3-27 and also a curve fit of the engine pressure versus input power to the engine similar to the Beale correlation. The Stirling engine component using the West number correlation proved to be tied for the most accurate model when comparing it with WGA data.

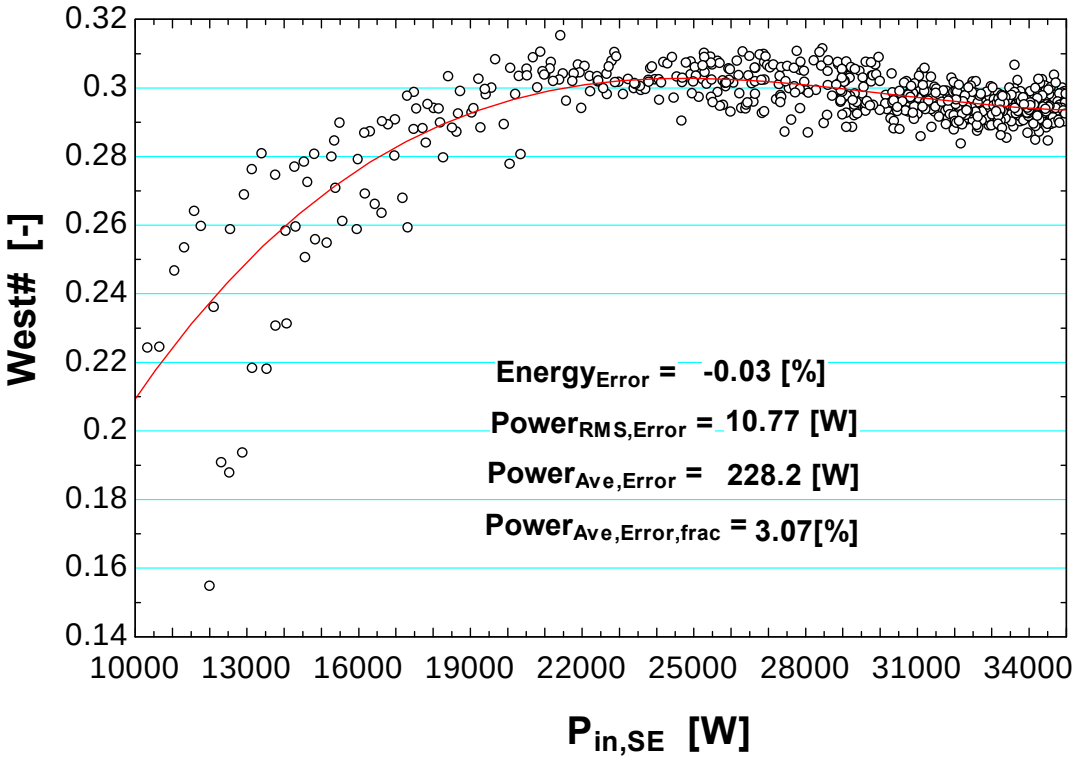

Figure 3-27 West number correlation curve for 4/26/2004

3.3.2 Combined Component Models

Stirling dish system models were created by Stine (1995) and Sandia Labs (Igo and Andraka, 2007) to predict the system performance without using separate models for the collector, receiver, and Stirling engine. These combined models do not include terms for the sun elevation angle, wind speed, or altitude, which vary based on location compared with the component

models that use separate components for the collector, receiver, and Stirling engine. The combined component models are outlined below.

3.3.2.1 Stine Model

Stine created a Stirling dish system model to predict the long term performance of the Stirling dish systems. The model corrects the direct normal insolation by a temperature correction term as shown in Equation (3.35) (Stine, 1995).

$$DNI_{Stine} = I_{bn} \cdot \frac{T_0}{T_{cw,in}} \tag{3.35}$$

where I_{bn} is the direct normal insolation, $T_{cw,in}$ is the engine cooling water inlet temperature, and T_0 is the standard atmospheric temperature of 288˚K. A curve fit of the net power verse corrected direct normal insolation is then plotted as shown in Figure 3-28. The Stine model proved to give less accurate results compared with other models when tested against WGA data.

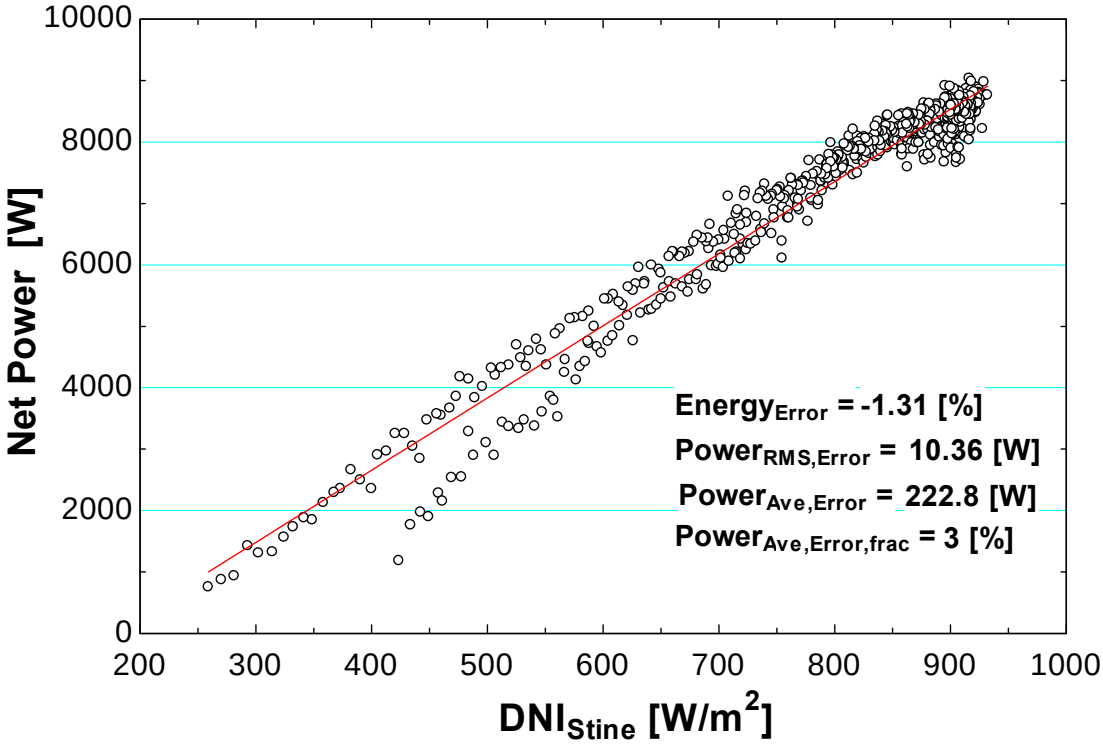

Figure 3-28 Stine model curve fit for 4/26/2004

3.3.2.2 Sandia Model

The Stirling dish system model created at Sandia National Laboratory is similar to Stine's model except for the temperature correction term and how the curve fit is created. The net power of a Stirling dish system is plotted against the direct normal insolation as shown in Figure 3-29, and

then a temperature correction term is introduced as given in Equation (3.36) (Igo and Andraka, 2007).

$$Net_{power} = Net_{power,slope} \cdot T_{amb,ave} / T_{amb} \tag{3.36}$$

The terms Net_{power} is the total Stirling system net power, $Net_{power,slope}$ is the net power predicted by the curve fit in Figure 3-29, and $T_{amb,ave}$ is the nominal ambient temperature for the period of time and location the model is being simulated for. A plot of the predicted output power using the Sandia model is shown in Figure 3-30. The Sandia model proved to be reasonably accurate despite its simplicity and the fact that it is a system (versus a component-based) model.

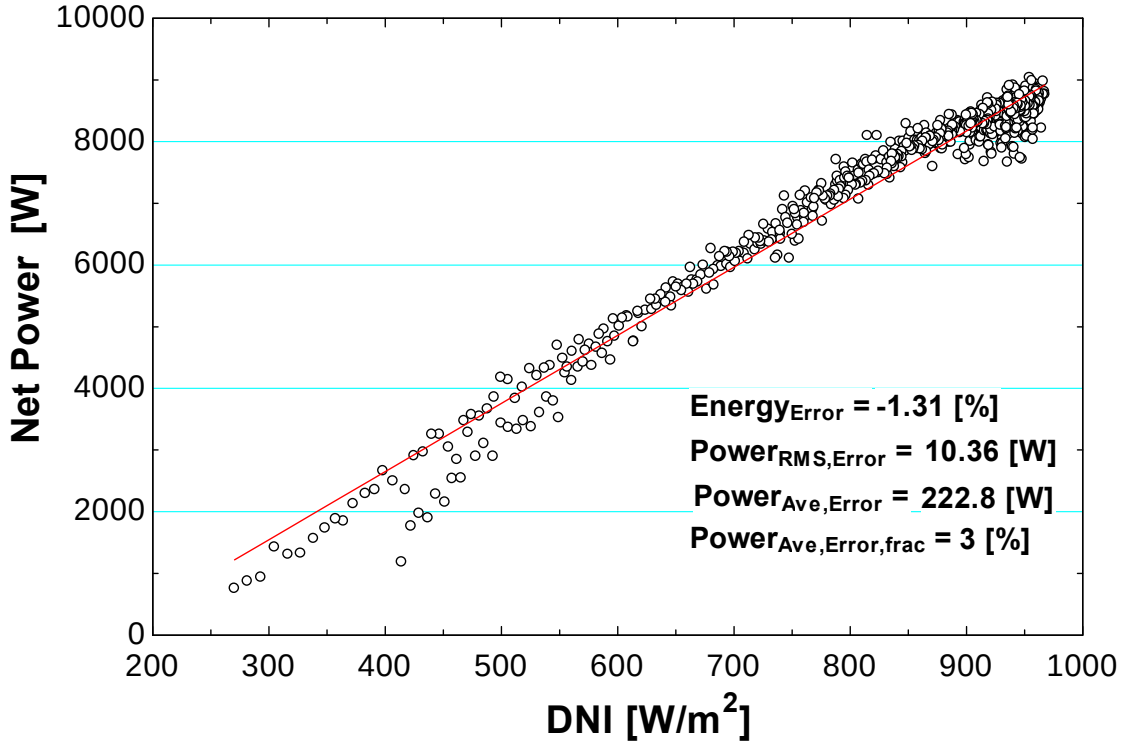

Figure 3-29 Sandia model curve fit for 4/26/2004

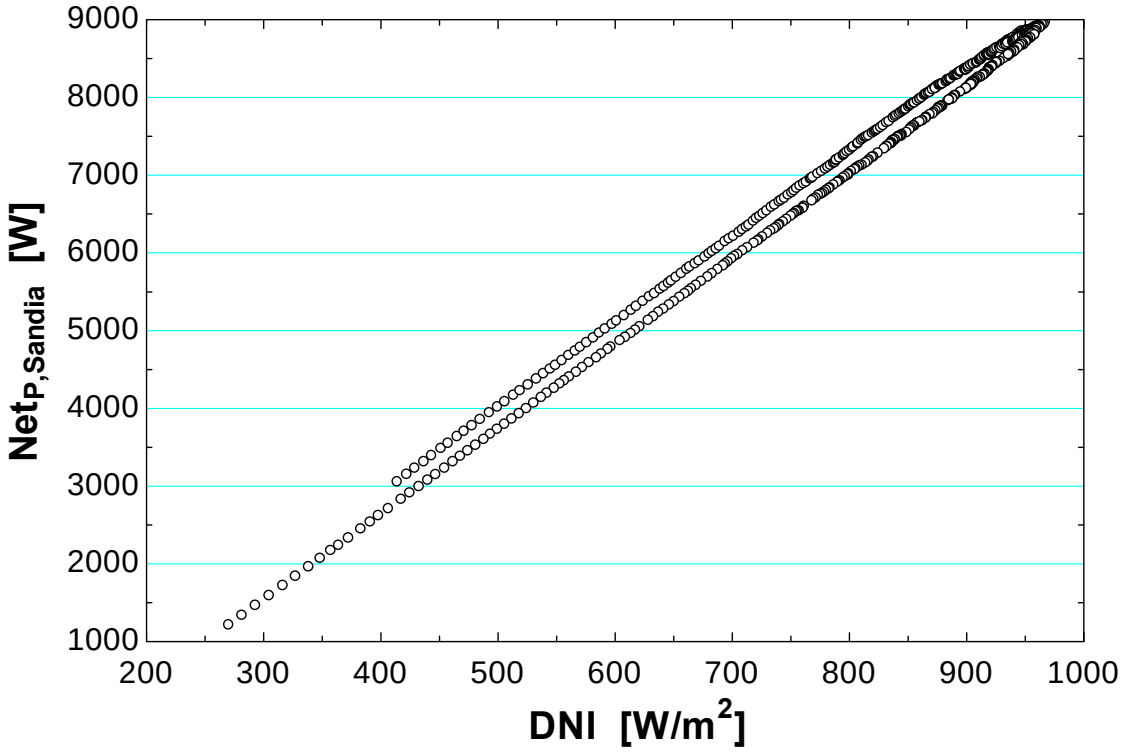

Figure 3-30 Sandia model predicted power using the curve fit for 4/26/2004

3.3.2.3 Net Power versus Engine Input Power

A model was created similar to Stine's and Sandia's models with the net power plotted against the input power to the engine instead of the direct normal insolation. This model was not corrected for temperature, but viewing the results indicates this model may be improved by using Sandia's temperature correlation presented in Equation (1.16). A plot of this model is given in Figure 3-31.

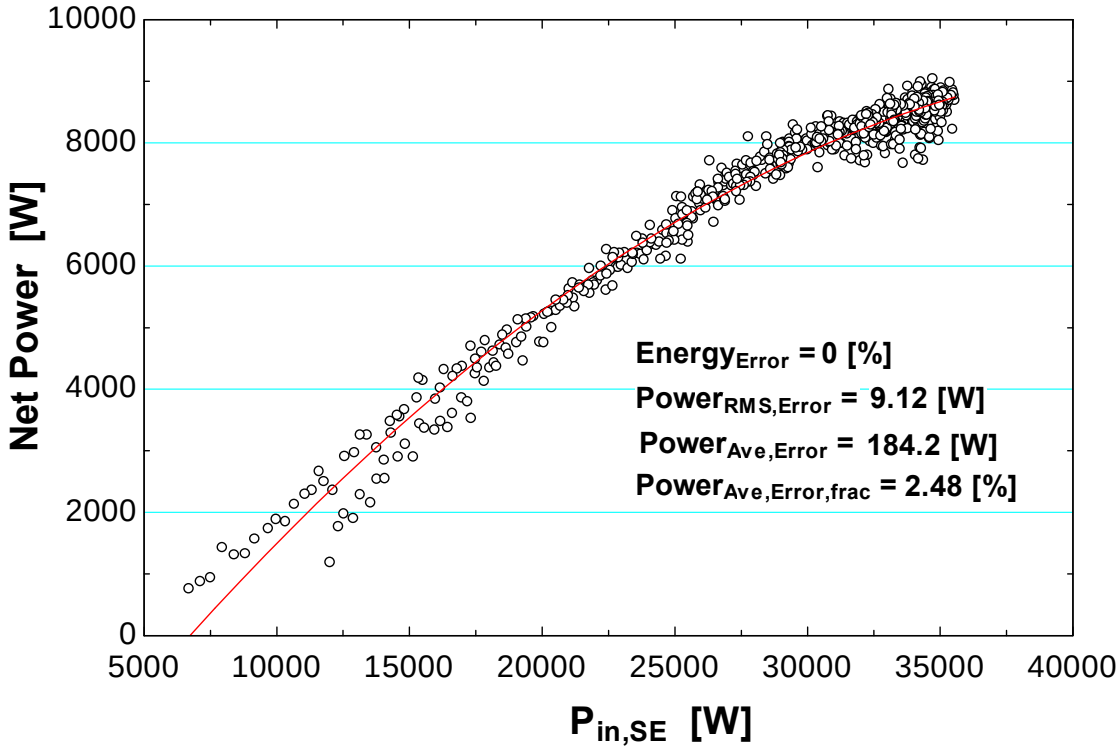

Figure 3-31 Net power versus input power to the engine curve fit

3.4 Cooling System Analysis for Total System Optimization

The power supplied to the radiator fan represents a significant fraction of the Stirling dish system parasitic power and varies significantly based on the density of ambient air and the operating speed of the fan. The power supplied to the cooling fluid pump, tracking system, and system controls are a smaller fraction of the total parasitic power in addition to remaining mostly constant during operation. For these reasons, a program was created to determine the optimal speed of the fan based on various ambient and operating conditions.

A fan curve was obtained for the 630mm Woods fan used in the WGA system (Fläkt-Woods, 2007). A prediction of the pressure drop across the radiator indicated that the volumetric flow rate of the Woods fan would be about 4000 CFM, and the corresponding parasitic power consumption is estimated at 410 W at an ambient temperature of 15°C, fan operating speed of 890 RPM, and normal atmospheric pressure of 101 kPa. These values were then used to predict the fan parasitic power based on varying ambient conditions and fan operating speed.

Inputs of the radiator and cooler effectiveness allowed for the compression space temperature to be determined, and the gross output power from the Stirling engine was obtained using ambient conditions and the compression space temperature. The net power is found by subtracting the parasitic power of the controls, pump, and fan from the gross output power of the engine. A plot of the net output power from the WGA system as a function the fan operating speed for specific ambient conditions is given in Figure 3-32. The optimal fan operating speed to maximize the net

output power depends on the atmospheric pressure and temperature as can be seen in Figure 3-33.

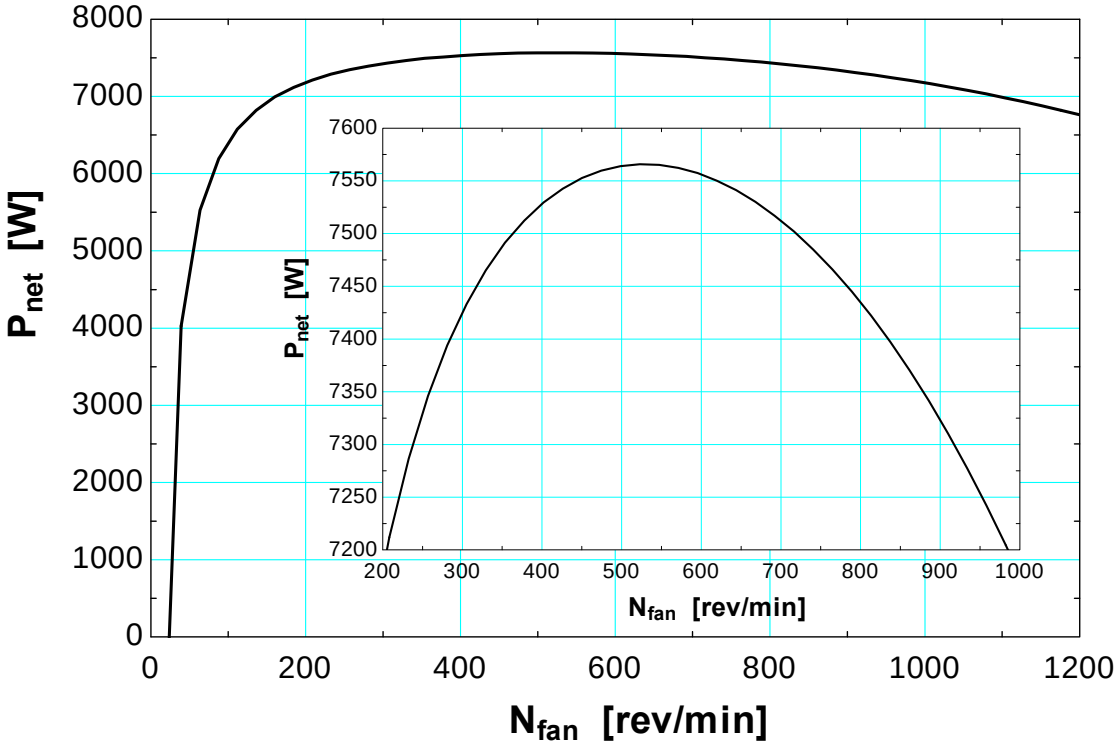

Figure 3-32 Net system power as a function of the fan operating speed for ambient conditions of 288°K, and 101 kPa with an input power of 30 kW

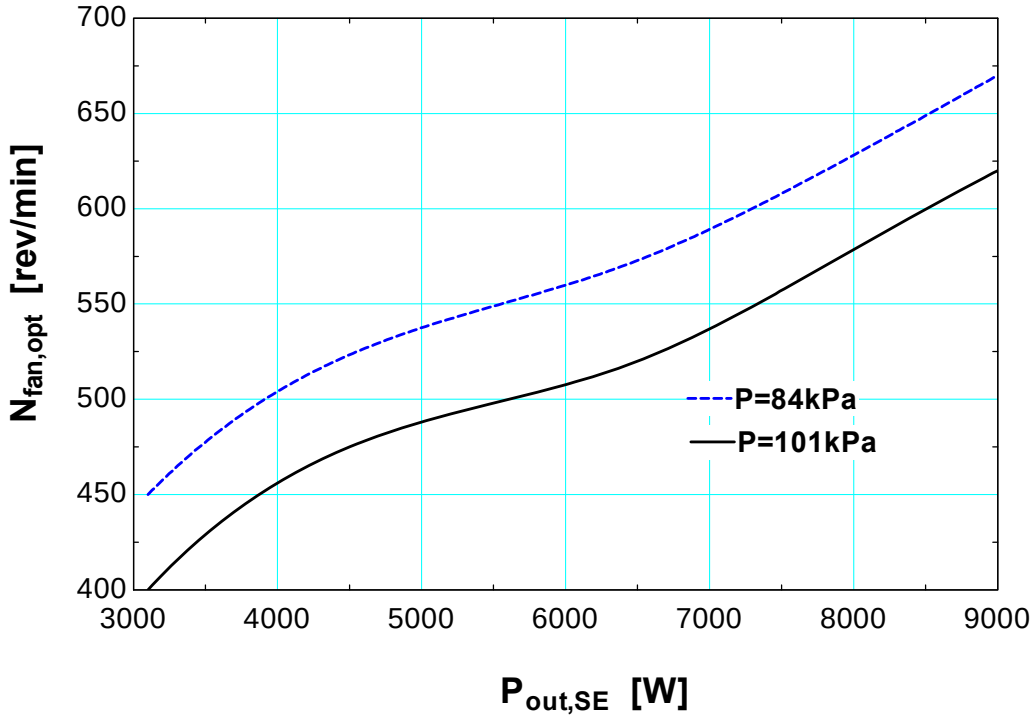

Figure 3-33 Effect of atmospheric pressure on the optimal fan speed to maximize the net power output from Stirling dish systems operating with an ambient temperature of 15°C and a radiator and cooler effectiveness of 0.7

The approach to optimize the output power of the system was to first solve for the cooling fluid temperature into the radiator ($T_{cool,fluid,2}$) by rearranging Equation (3.37) where Q_{reject} is the rejected thermal energy from the engine dissipated into the cooling fluid. The temperature terms are depicted in Figure 3-34.

$$Q_{reject} = \varepsilon_{radiator} \cdot \dot{C}_{\min} \cdot \left(T_{cool,fluid,2} - T_{air,in} \right) \tag{3.37}$$

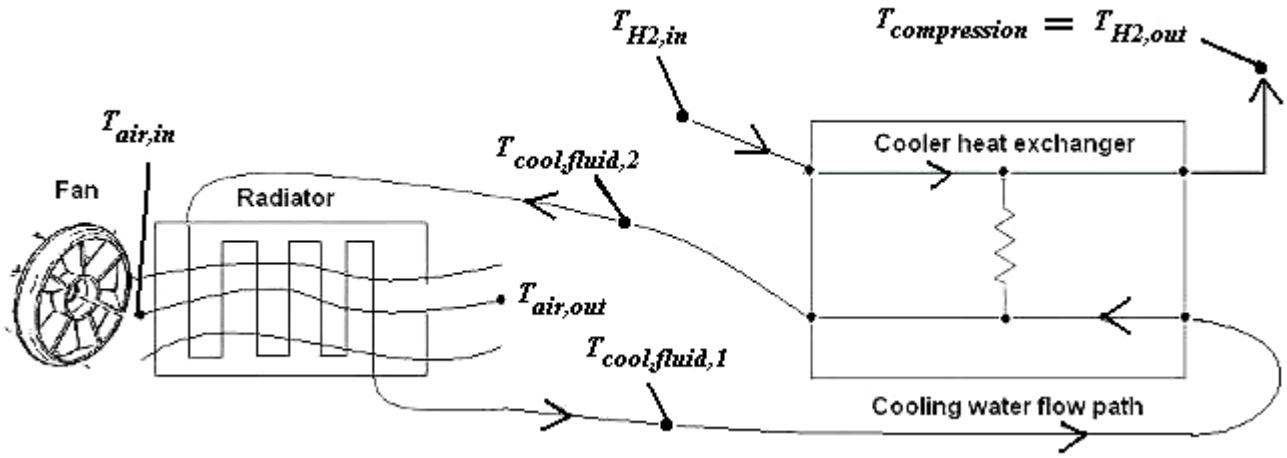

Figure 3-34 Typical cooling system diagram for a Stirling dish system

The cooling fluid temperature out of the radiator ($T_{cool,fluid,1}$) could then be determined using Equation (3.38)

$$\varepsilon_{radiator} = \frac{\dot{C}_{cool,fluid} \cdot \left(T_{cool,fluid,2} - T_{cool,fluid,1}\right)}{\dot{C}_{\min} \cdot \left(T_{cool,fluid,2} - T_{air,in}\right)} \tag{3.38}$$

The temperature of the hydrogen working fluid into the cooler ($T_{H2,in}$) was then found using Equation (3.39)

$$Q_{reject} = \varepsilon_{cooler} \cdot \dot{C}_{\min} \cdot \left(T_{H2,in} - T_{cool,fluid,1}\right) \tag{3.39}$$

Finally, the temperature of the hydrogen working fluid out of the cooler ($T_{H2,out}$) and equivocally the compression space temperature could be obtained by rearranging Equation (3.40) (Incropera and DeWitt 2002)

$$\varepsilon_{cooler} = \frac{\dot{C}_{H2} \cdot \left(T_{H2,in} - T_{H2,out}\right)}{\dot{C}_{\min} \cdot \left(T_{H2,in} - T_{cool,fluid,1}\right)} \tag{3.40}$$

Once the compression space temperature is determined, the engine efficiency is predicted using an engine efficiency curve fit (Figure 3-25) corrected based on the compression and expansion space temperature of the engine. The gross power is found based on the chosen operating conditions, the engine performance, and the effectiveness of the radiator and cooler. The net power is determined by finding the gross power and then subtracting the parasitic power which is a function of the chosen operating speed of the fan and ambient conditions.

To optimize the fan speed to obtain the maximum net system power, a higher operating fan speed should be chosen for a warmer climate with a higher altitude, and a lower operating speed should be chosen for a colder climate with a lower altitude. This situation results from a colder ambient temperature simultaneously reducing the receiver efficiency, improving the engine efficiency, and increasing the fan parasitic power due to denser air, so the net effect is a slightly higher net system output power at a lower fan operating speed. A lower altitude climate will result in a higher air density which will increase the parasitic power consumption of the fan (but also improve the capacitance rate of air), so a lower operating fan speed will improve the system performance.

The cooling system optimization for the WGA system indicated that the optimal fan speed would be approximately 550 RPM depending on the location as seen in Figure 3-33. The optimal fan operating speed is a weaker function of temperature than atmospheric pressure or direct normal insolation (DNI) as shown in Figure 3-35 where the colder temperatures shifts the optimal fan speed lower. The optimal fan operating speed has a greater dependency on the thermal input power to the engine as shown in Figure 3-36 and Figure 3-37 where a lower input power to the engine significantly shifts the optimal fan operating speed lower.

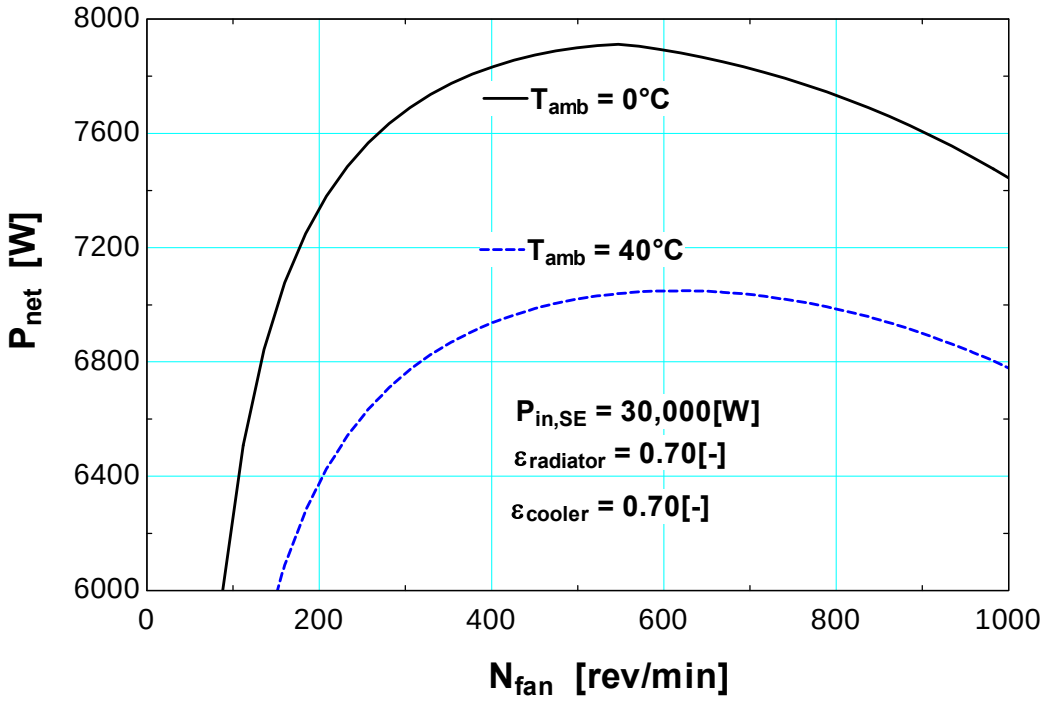

Figure 3-35 Effect of ambient temperature on the optimal fan speed

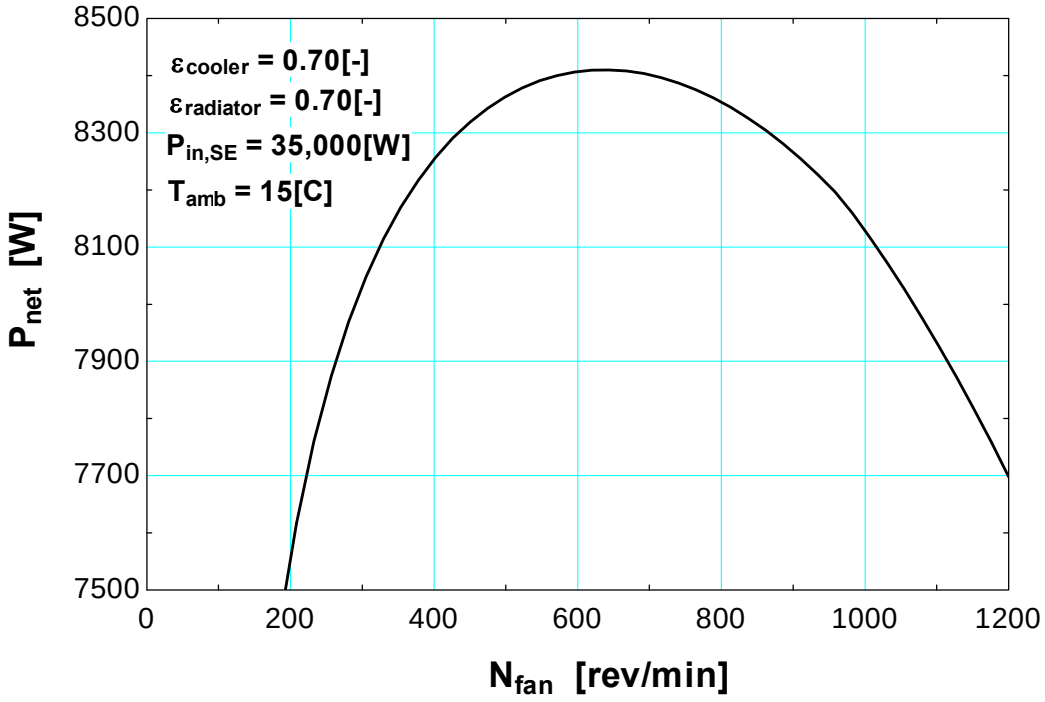

Figure 3-36 Effect of a higher thermal input to the engine producing a higher net electric power at higher fan operating speeds

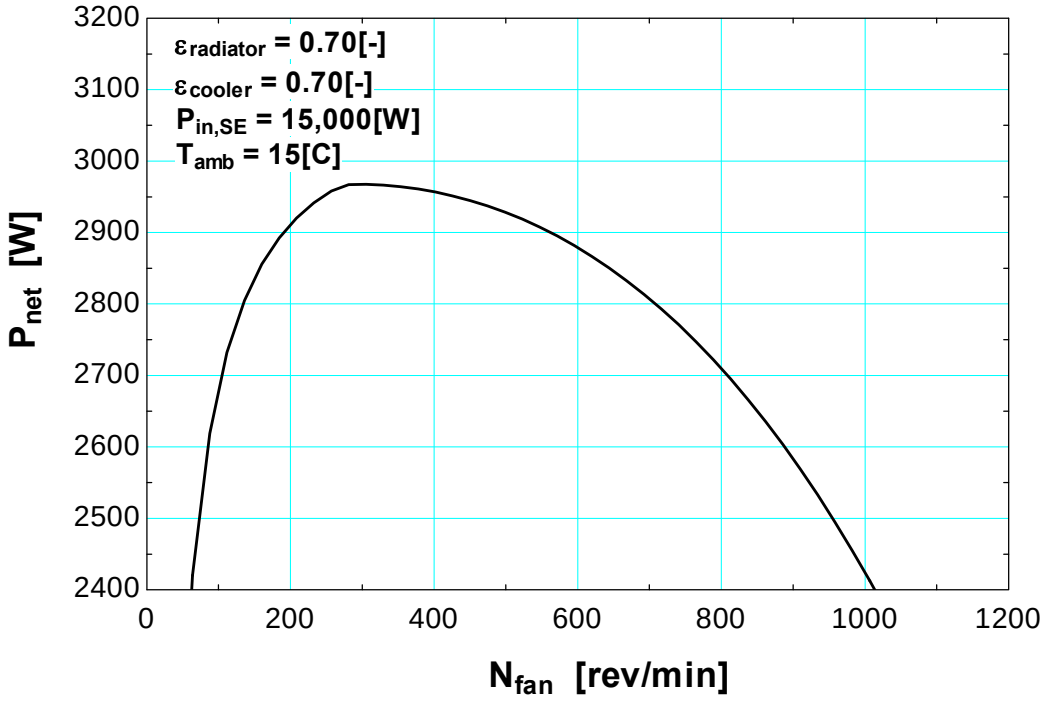

Figure 3-37 Effect of a lower thermal input to the engine producing a higher net electric power at lower fan operating speeds

3.5 Cooling Tower Model

An analysis was performed to quantify the improvement in performance of Stirling dish systems using a central cooling tower instead of a fan and radiator for a 10 kW WGA Stirling dish system. The TRNSYS model of the Stirling dish system described in the appendix was used to analyze the location dependent improvement in performance using a cooling tower in Daggett, California, and Albuquerque, New Mexico. The results of this analysis indicate that cooling towers could improve the yearly net electrical energy production over 3.5 % in Daggett, California with a 1°C approach and over 2.0 % with a 5°C approach. Cooling towers would also have a negative impact on the environment by consuming large quantities of water in arid environments.

The cooling tower model used for this analysis in TRNSYS takes operating inputs of the ambient conditions, cooling fluid inlet temperature and flow rate, and the fraction of the cooling tower fans rated flow rate (TESS, 2005). Some of the design parameters that are user-defined in the TESS cooling tower include the design inlet and outlet fluid temperature, design fluid and air flow rate, and the design ambient air and wet bulb temperature. The cooling fluid outlet temperature is then determined by the TRNSYS cooling tower component based on ambient conditions, the mass flow rate of the cooling fluid and cooling tower air, and the fluid inlet temperature to the cooling tower. The ambient conditions are input using TMY-2 data found in TRNSYS, and the inlet fluid temperature to the tower (T_A) given by Equation (3.41) is determined based on the outlet fluid temperature (T_B), mass flow rate of the cooling fluid

($\dot{m}_{tower}$), capacitance of the fluid ($C_{p,tower}$), and the predicted thermal load rejected ($\dot{Q}_{reject}$) from the Stirling engine component.

$$T_A = T_B + \dot{Q}_{reject} \Big/ \dot{m}_{tower} \cdot C_{p,tower} \tag{3.41}$$

The improvement in system performance using a cooling tower is obtained by reducing the temperature of the compression space in the engine. Without a cooling tower (Figure 3-34), the cooling fluid temperature in ($T_{cool,fluid,2}$) and out ($T_{cool,fluid,2}$) of the radiator is determined by the ambient temperature ($T_{air,in}$), cooling fluid flow rate, air flow rate across the radiator, and the radiator heat exchanger effectiveness. The compression space temperature ($T_{compression}$) is then found with the cooling fluid temperatures, cooling fluid mass flow rate, engine working fluid flow rate, and the cooler heat exchanger effectiveness.

When a cooling tower is included in a Stirling dish system, the compression space temperature is obtained using a similar analysis, but the radiator and fan cross flow heat exchanger is replaced with a counter flow heat exchanger and cooling tower as shown in Figure 3-38. The lowest obtainable temperature using the standard fan and radiator is the ambient dry bulb temperature, whereas the lowest obtainable temperature using a cooling tower is the ambient wet bulb temperature. A counter flow heat exchanger with two liquids used in the cooling tower loop can also be more effective than the cross flow radiator and fan heat exchanger with air as one of the heat transfer fluids.

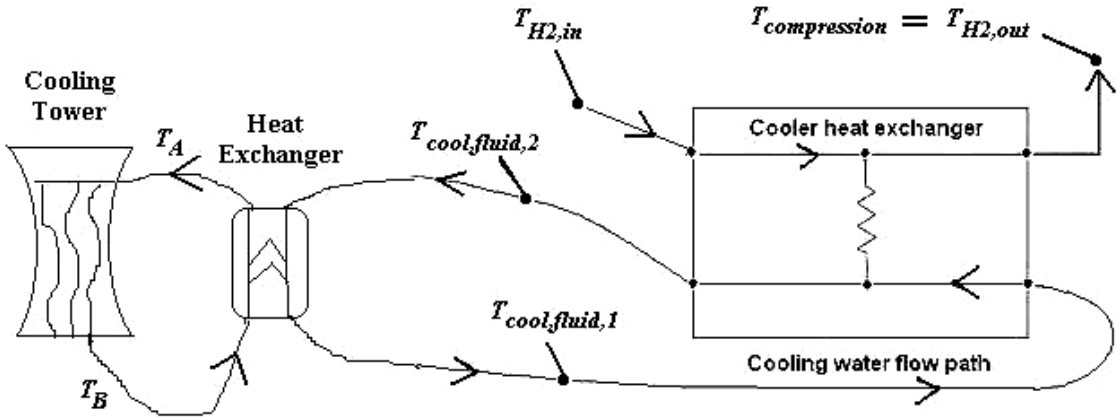

Figure 3-38 Cooling system diagram for a Stirling dish system using a cooling tower

Additional code was required in the TRNSYS model to determine pumping losses in the cooling water distribution pipes. This code determines the total distance of piping by connecting a user-specified number of 10 kW Stirling dish systems in series as shown in Figure 3-39, and summing up the user-defined separation distance between each dish. The friction factor (f_f) within the pipe was determined using Equation (3.42) (White, 2003) where *Re* is the Reynold's number, ε is the roughness value of a material (0.0015mm for plastic), and *d* is the pipe diameter. The water pump power was evaluated using Equation (3.43) where ρ is the density of water, *g* is the

gravitational constant, $\dot{V}$ is the volumetric flow rate of water, and P_{head} is the pressure head defined in Equation (3.44) (White, 2003). The term L is the total length of the cooling fluid pipe, v is the velocity of the cooling fluid, and K is the term for minor losses due to bends in the pipe. The net Stirling dish system power in Equation (3.45) is determined by subtracting the total parasitic power from the gross output power from the Stirling engine. When a series of Stirling dish systems are combined in series as shown in Figure 3-39, the TRNSYS model takes the average between the outlet cooling tower fluid temperature (T_B) and the inlet temperature (T_A) as the lowest temperature in the Stirling dish cooling system into the counter flow heat exchanger.

$$f_f = \left[1 \Big/ \left(-1.8 \cdot \log\left(6.9/\mathrm{Re} + \left[\frac{\varepsilon/d}{3.7} \right]^{1.11} \right) \right) \right]^2 \tag{3.42}$$

$$P_{tower,pump} = \rho \cdot g \cdot \dot{V} \cdot P_{head} / \eta_{pump} \tag{3.43}$$

$$P_{head} = f_f \cdot \frac{L}{d} \cdot \frac{v^2}{2 \cdot g} + \sum K \cdot \left(\frac{v^2}{2 \cdot g} \right) \tag{3.44}$$

$$P_{Net} = P_{Gross} - (P_{controls} + P_{tower,fan} + P_{SE,pump} + P_{tower,pump}) \tag{3.45}$$

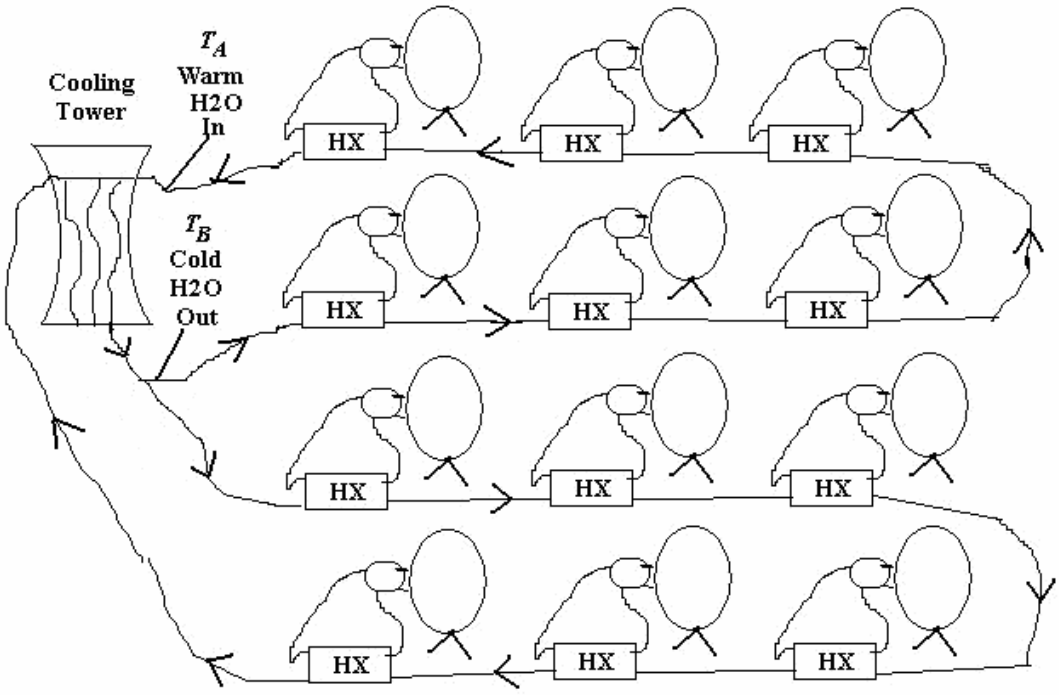

Figure 3-39 Stirling dish system diagram using a central cooling tower

4 WGA 2-2 Stirling Dish System Data Analysis

Data were obtained from Sandia National Laboratory (SNL) for the Stirling dish system, which operated between 2003 and 2006 in Albuquerque, New Mexico. The data used in this model included the sun elevation angle, cooling water inlet/outlet temperatures, engine pressure,

expansion space temperature (heater head temperature), net power, wind speed, ambient temperature, direct normal insolation, and the average receiver temperature. Plots of key measured data were generated for a clear day (4/26/2004) to better understand the factors influencing the Stirling dish system performance. Two days of data from the spring (4/26/04 & 4/27/04), summer (6/2/03 & 7/24/03), and winter (12/9/03 & 1/13/04) were used to obtain the Stirling engine efficiency curves used in the Stirling cycle component model. The component model was then compared with experimental data that were not used to establish the efficiency curves. Results of the comparisons are provided for in the "Results Analysis: Comparison of Component Models to Data" section below.

4.1 Trends in the Data

The data obtained from Sandia National Laboratory (Andraka, 2007) for the WGA systems were analyzed to observe trends. Observations from the data included:

- Engine pressure varies linearly with insolation
- Net output power is nearly linear with insolation
- A transient effect occurs in the morning when the system does not perform as well resulting from heating up the receiver walls and absorber

4.1.1 Pressure Linear with Insolation

The measured data suggest that the mean engine pressure has a linear relationship with the solar insolation as shown in Figure 4-1. This linear relationship exists since the mass (or pressure) within the engine is controlled by keeping the heater head temperature constant. When the insolation increases, the heater head temperature tends to increase, which causes a valve to open and releases working fluid into the engine from an external storage tank. An increase in working fluid mass in the engine increases the pressure and therefore the capacity of the engine. With the engine producing more power, the heater head temperature drops back down to the set point. The linear trend for pressure enabled the Beale number component model, which includes a pressure term, corrected by the maximum power fraction to be the most accurate.

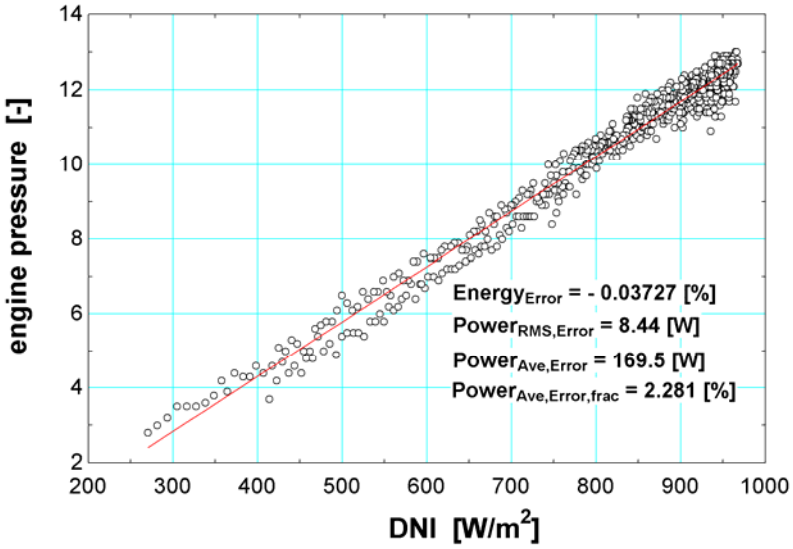

Figure 4-1 Linear relationship between the engine pressure and insolation using 4/26/04 data

4.1.2 Morning Power Transient Effect

A plot of the gross power versus insolation illustrates the transients in performance during the morning and evening as shown in Figure 4-2. The Stirling dish systems tend to perform worse in the morning due to the thermal capacitance of the receiver walls and absorber requiring energy to obtain a steady state heater head temperature. Figure 4-2 also indicates data influenced by shading in the morning resulting from mountains to the east, which eliminates most of the data points at lower insolation values (Andraka, 2007). The effective shading of the mountains results in a curve fit of the data slightly over-predicting the system performance during the morning since the data points recorded at insolation values below approximately 400 W/m^2 all occur in the evening when the performance is greater. The net effect on the data due to the mountains is expected to be minimal.

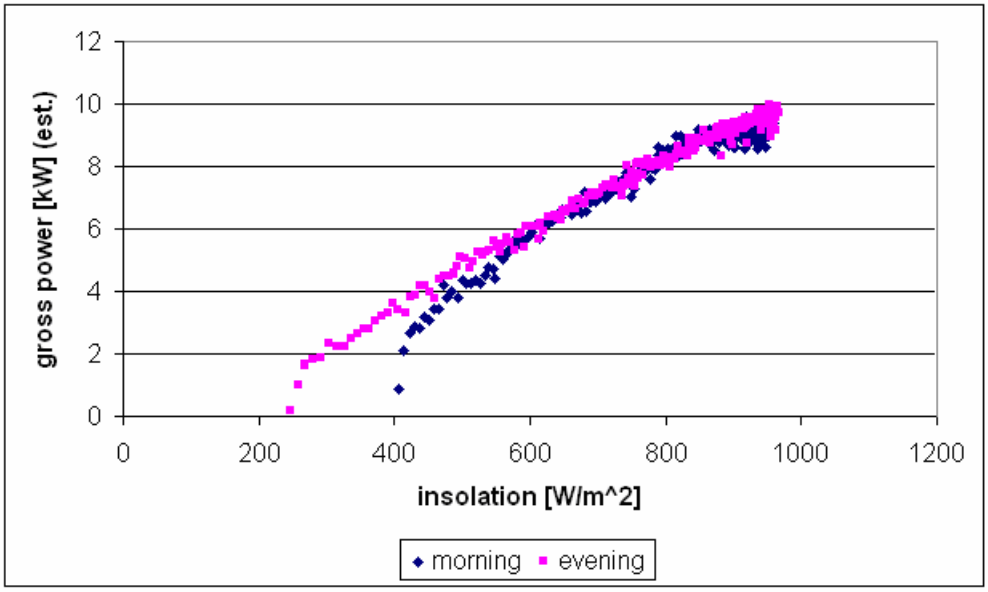

Figure 4-2 Morning and evening transients for the WGA system gross power on 4/26/04. The morning values start around 400 W/m^2 due to mountains to the east.

4.1.3 Cooling Fluid Inlet Temperature

The cooling water inlet temperatures from the WGA data was consistently colder than the ambient air for the first two hours in the morning as shown in Figure 4-3. Although it is possible for the cooling water inlet temperature to be below the ambient temperature for a short period in the morning due to the ambient air warming faster than the cooling water, the period for this difference was expected to be rather short in a closed loop radiator system.

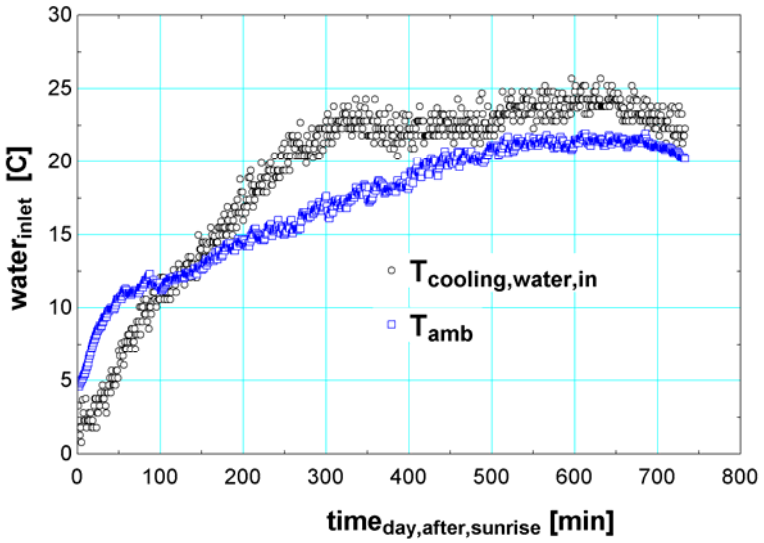

Figure 4-3 Depiction of cooling water inlet and ambient temperatures for 4/26/04

4.1.4 Receiver Temperature Transient Effect

An analysis was performed to determine the variation in the average cavity receiver temperature with insolation. The temperature of the heating head (expansion space) temperature is controlled to a constant temperature to limit material degradation and seal losses, so this temperature is known; the only unknown is the receiver average wall temperature. Sandia measured the receiver temperature at 19 locations to obtain the average receiver temperature for the WGA system. The average of these 19 data points is plotted with respect to the time of day in Figure 4-4 and Figure 4-5.

The difference in temperature between the expansion space and average receiver temperature (delta T) is the greatest in the morning and evening, and the least around noon as shown in Figure 4-5 and Figure 4-6. This behavior is a consequence of the engine pressure being lower in the morning and evening which results in a lower working fluid density, a lower Reynolds number, and therefore a lower convective heat transfer coefficient between the absorber tubes and expansion space working fluid. An average receiver temperature was determined to provide accurate receiver loss predictions, and a model to predict the local receiver temperature was not deemed to be necessary. Using heat transfer correlations such as the Gnielinski convection correlation for the absorber tubes did not provide reasonable predictions of the absorber temperature most likely due to the periodic flow of hydrogen.

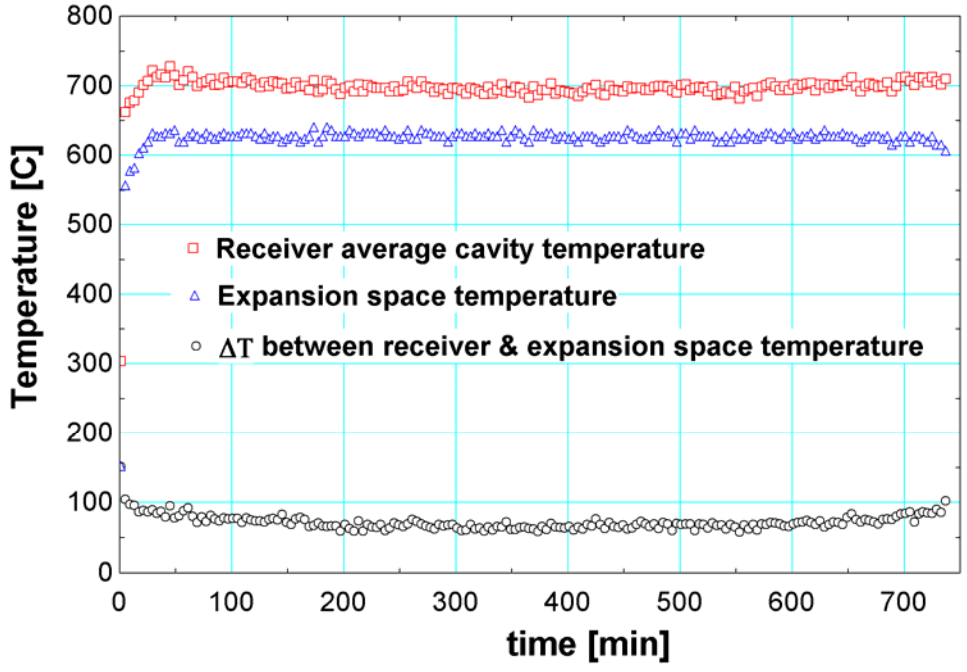

Figure 4-4 Temperature difference between the expansion space and receiver throughout the day for 4/26/04

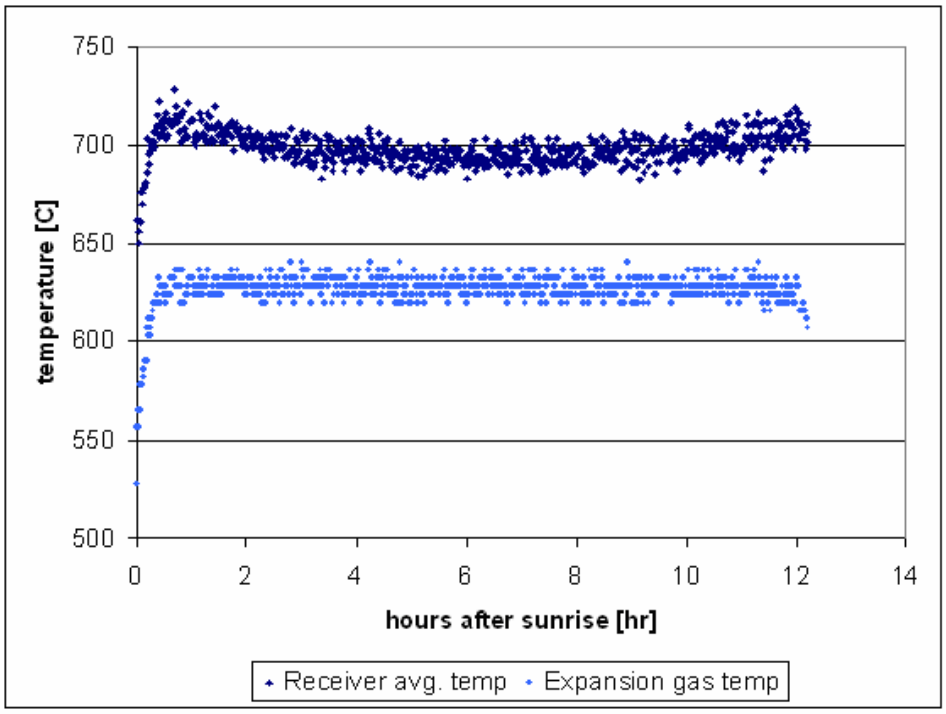

Figure 4-5 Expansion space and receiver temperatures for 4/26/04

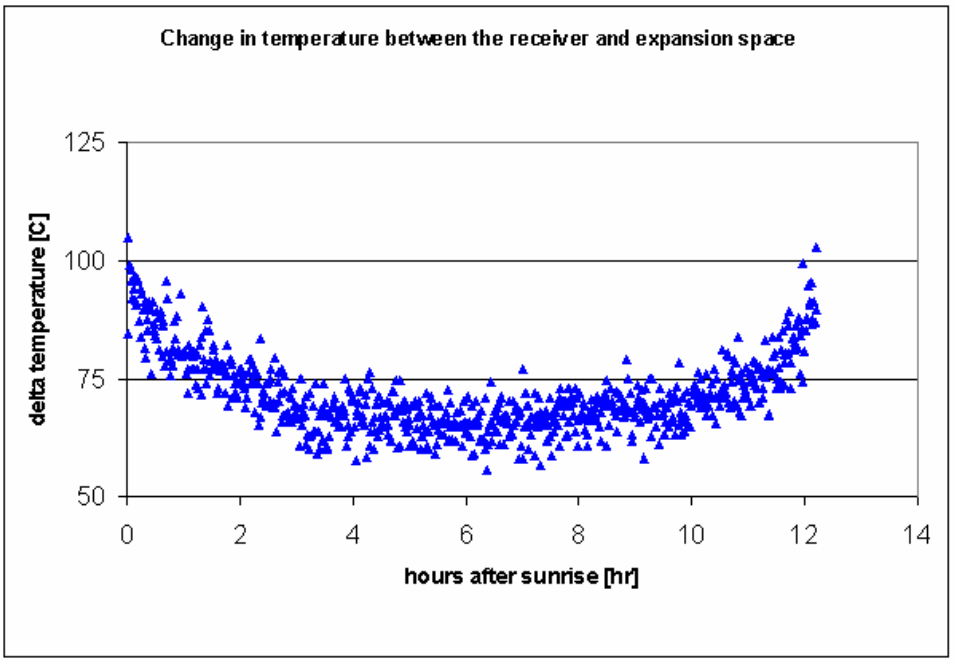

Figure 4-6 Temperature difference between the receiver and expansion space for 4/26/04

4.2 Filtering Data for Model Simulations

Several criteria were used to filter the WGA data to more accurately compare them with the various component models. Many weeks of data were analyzed to determine how to filter data that were recorded during periods when there were collector tracking faults or other system faults. The data were filtered for large tracking error, negative parasitic power, unusually low engine speeds and heater head temperatures, and when there were recorded engine faults.

4.2.1 Tracking Error

The WGA data included minute interval measurements of the sun and receiver elevation and azimuth angles, so determining the tracking error was not difficult. The data for the expected azimuth and elevation angles of the sun, however, were recorded at solar time, whereas the azimuth and elevation angles of the collector system were recorded at standard time. The calculated incidence angle for the data often peaked over 50 mrad as shown in Figure 4-7, which should be well under 10 mrad if the angles had been recorded using the same time in the data. Rather than correct all the data for solar time, an incidence angle above 100 mrad was used to filter significant tracking error. Other filter criteria were used that should also help reduce data with tracking error as explained next.

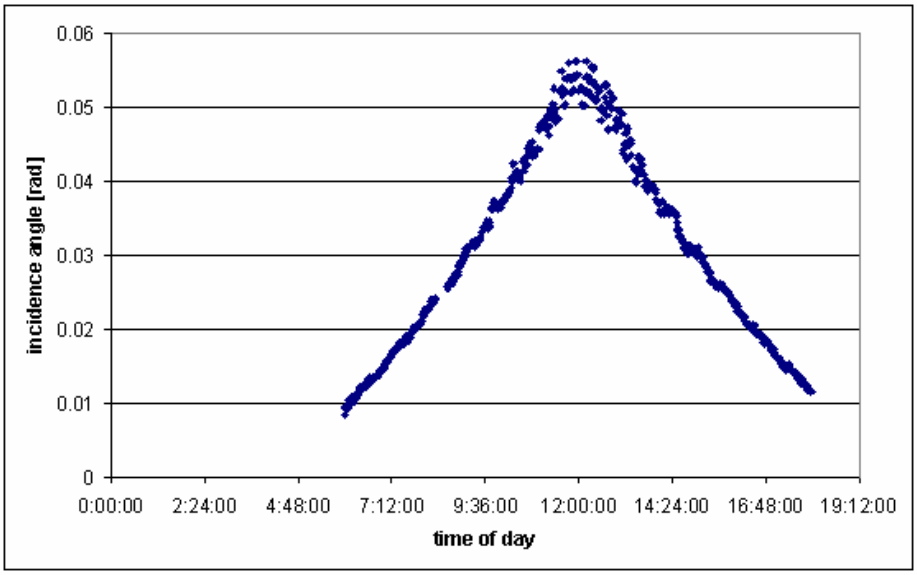

Figure 4-7 Incidence angle as a function of the time of day for 7-24-03

4.2.2 Large Parasitic Power

Large parasitic power loads resulted in large negative values for the net power. The data included the net power, but not the gross power, so data with negative net power values were filtered out in order to obtain better values for the performance prediction simulations. The parasitic power can become greater than 1.0 kW early in the morning or evening due to starting

the engine and the collector leaving or entering the stow position. The additional large parasitic power loads throughout the day most likely resulted from system faults or cloud conditions requiring the engine to shutdown and restart. These data were filtered.

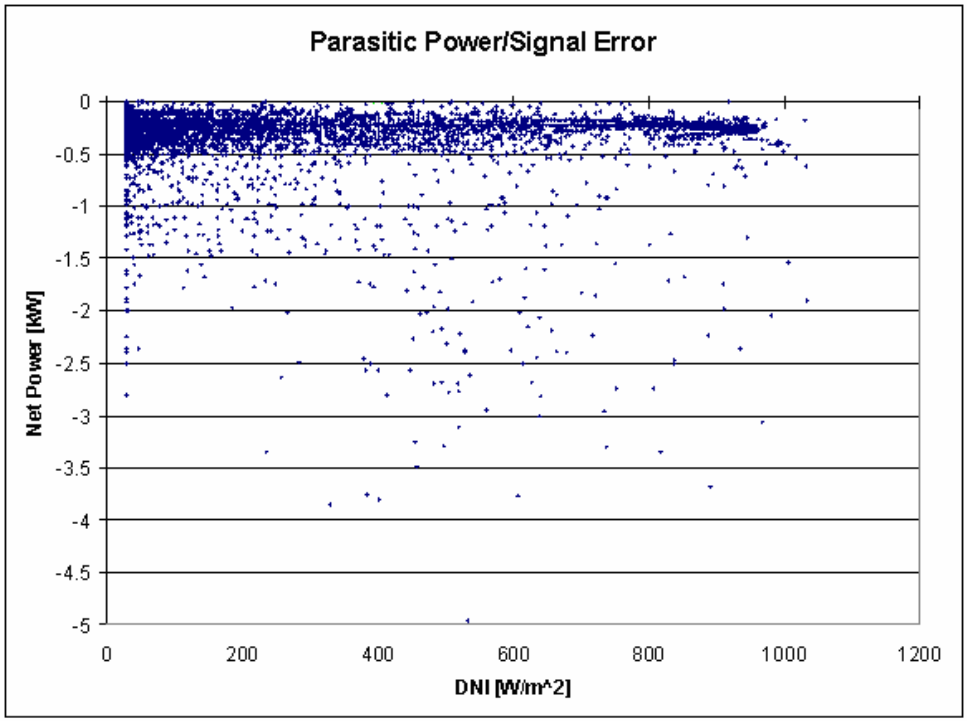

Figure 4-8 Large parasitic power transient losses for the WGA system

4.2.3 Stirling Engine Faults

The data were filtered when the engine or the transmission were not functioning properly. Power conditioning unit (PCU) faults were included in the recorded data, so these data were easy to filter. Data were also filtered when the engine speed was less than 1750 rpm in case the data did not record times when the engine or system was not functioning properly. In addition, data were filtered when the heater head temperature was less than 500ºC, which would occur during tracking errors, engine faults, or system errors. This temperature is sufficiently below the 630ºC heater head temperature set point so many data representing periods of clouds, start up, or shut down transients are not excluded by this filter.

4.2.4 Filtered Data Results

A plot of the unfiltered data from October 2003 until February 2004 is shown in Figure 4-9. The data from this period were then filtered with the criteria listed above and plotted as shown in Figure 4-10. The average difference of the power (Equation (4.3)) went from 1,240 W down to 520 W for the filtered data, so a significant amount of scatter in the data was reduced from filtering. There are still data around 1000 W/m^2 that have lower output powers than expected. The majority of these points occurred on 2/1/2004 when the heater head temperature and engine

pressure were lower than expected. Explanations for the lower output power on this day were not indicated in the data log or easily deduced by viewing data from this day.

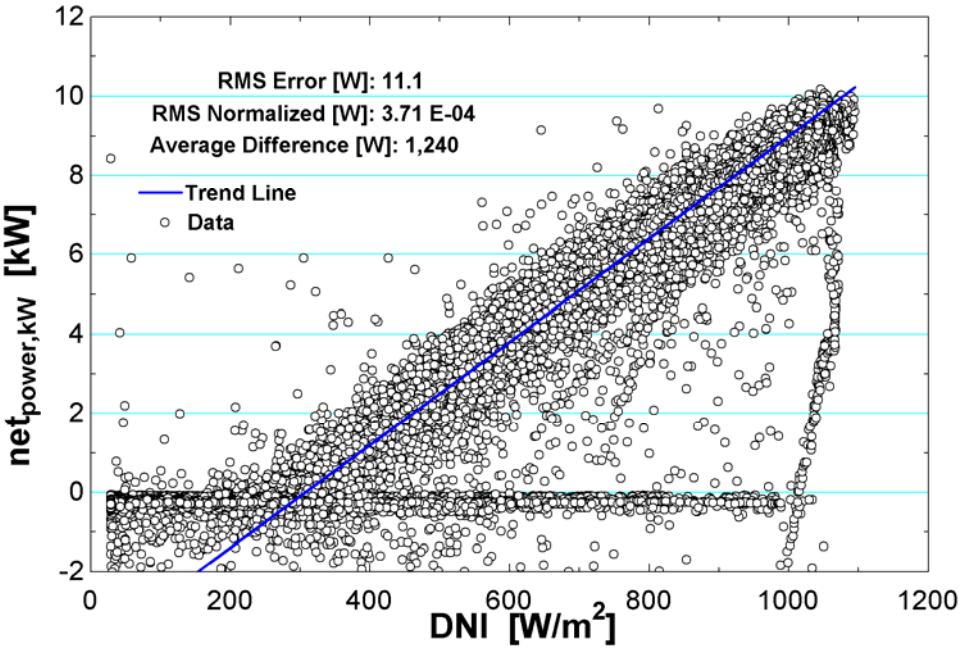

Figure 4-9 Unfiltered data from October 2003 until February 2004

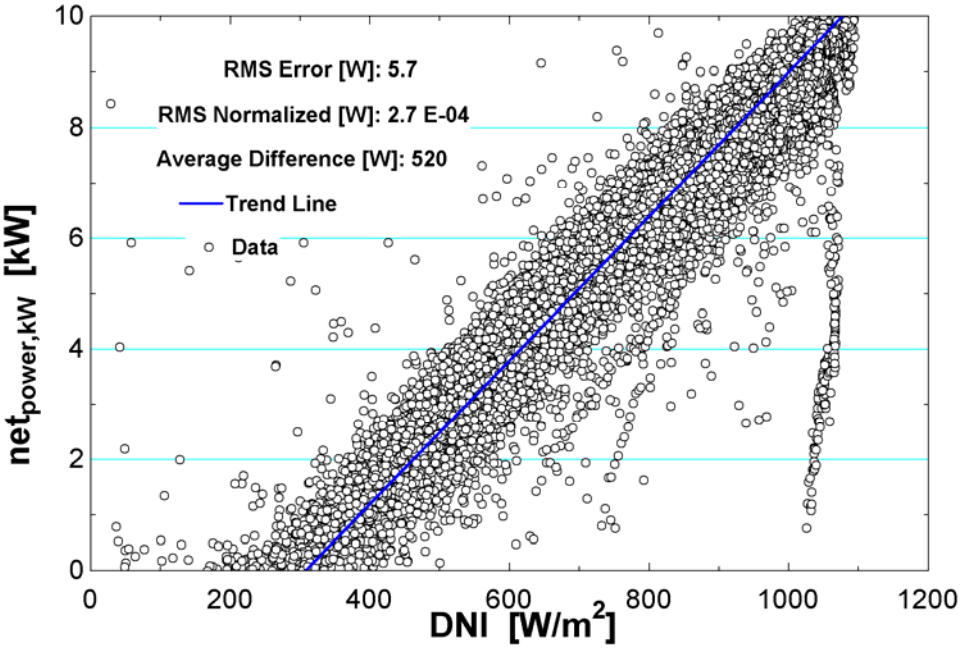

Figure 4-10 Filtered data from October 2003 until February 2004

4.3 Daily Variability in the Data

An analysis was made to determine the reasons for the variability between component model curve fits using different days of data. Six individual days of data were used to generate six separate curve fits for Stirling engine components or system models. Theoretically, if the models were perfect, no measurement error occurred in the data, and there were no system errors, the curve fits should be the same for each day. Curve fits of the engine pressure, engine efficiency, and system net power were analyzed to determine the variability in the curve fits.

The six days of data were taken from the spring, summer, and winter. The ambient temperature and cooling water inlet temperature varied significantly over these days, the cloud cover varied from partly cloudy to very clear, and the maximum engine pressure differed. A summary of some important details from the data for these six days is shown in Table 4.1.

Table 4.1 Important details for determining the variability in the data for various days

Date	T_cool_ave [C]	T_amb max [C]	Clouds	Max Pressure [Mpa]	Insolation@max_Pres [W/m2]	Pwr @ max_Pres [kW]	Pwr @ 900W/m2 [kW]
6/2/2003	26.7	28.2	mostly clear	12	940	9.2	8
7/24/2003	33.9	30.3	clear	10.8	890	7.9	7.3
12/9/2003	4.9	5.3	very clear	13.5	1050	10.2	8
1/13/2004	9.1	12.3	mostly clear	14.3	1030	9.6	8
4/26/2004	19.1	21.9	very clear	13	960	9	8.2
4/27/2004	22.1	23.3	part cloudy	13	960	8.9	8

4.3.1 Pressure Variation

The engine pressure is controlled to maintain a constant heater head temperature, so it will fluctuate constantly throughout the day. During cloud cover, the engine pressure will drop as shown in Figure 4-11 for the day of 4/27/2004. The engine pressure is dependent on the ambient temperature. When the ambient temperature is lower, the engine pressure appears to be lower for a given input power as shown in Figure 4-12, however, after viewing Figure 4-13, this trend appears to be statistically insignificant. At higher input power to the engine, the pressure tends to be higher with colder ambient temperatures as depicted in Figure 4-12 since the Stirling engine operates more efficiently at colder ambient temperatures as depicted in Figure 4-15. This trend does appear to be statistically significant as shown in Figure 4-13, which is realistic since the engine pressure will be higher when the output power is higher.

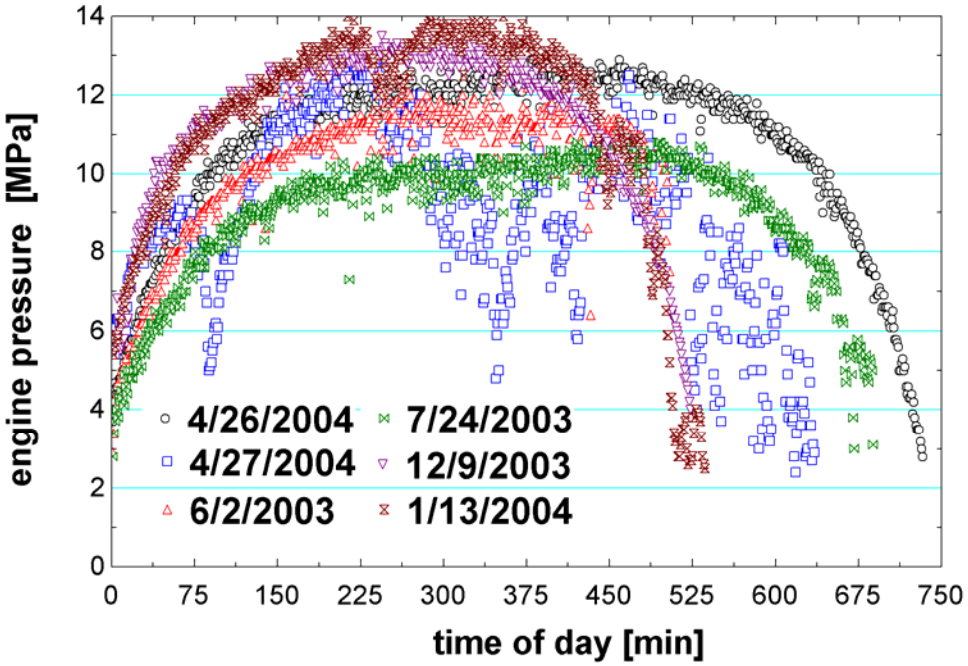

Figure 4-11 Pressure verse time of day for the six days of data

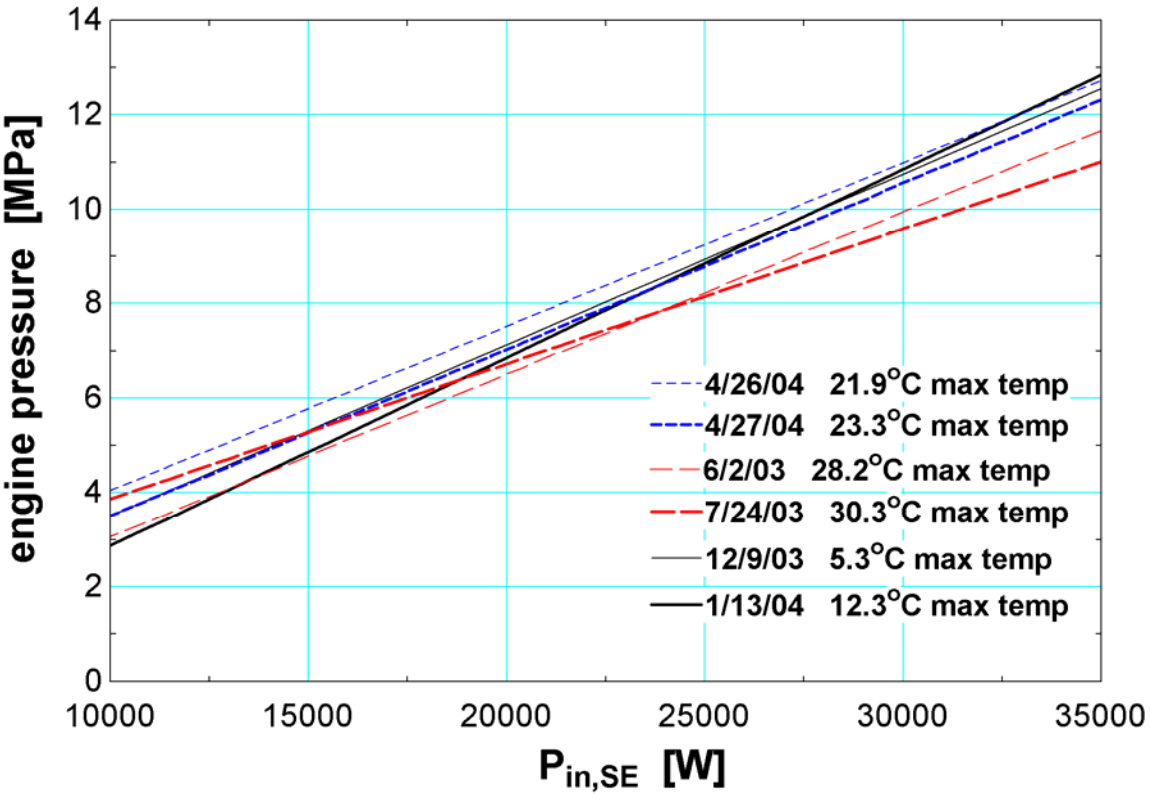

Figure 4-12 Curve fits of the engine pressure versus input power to the engine

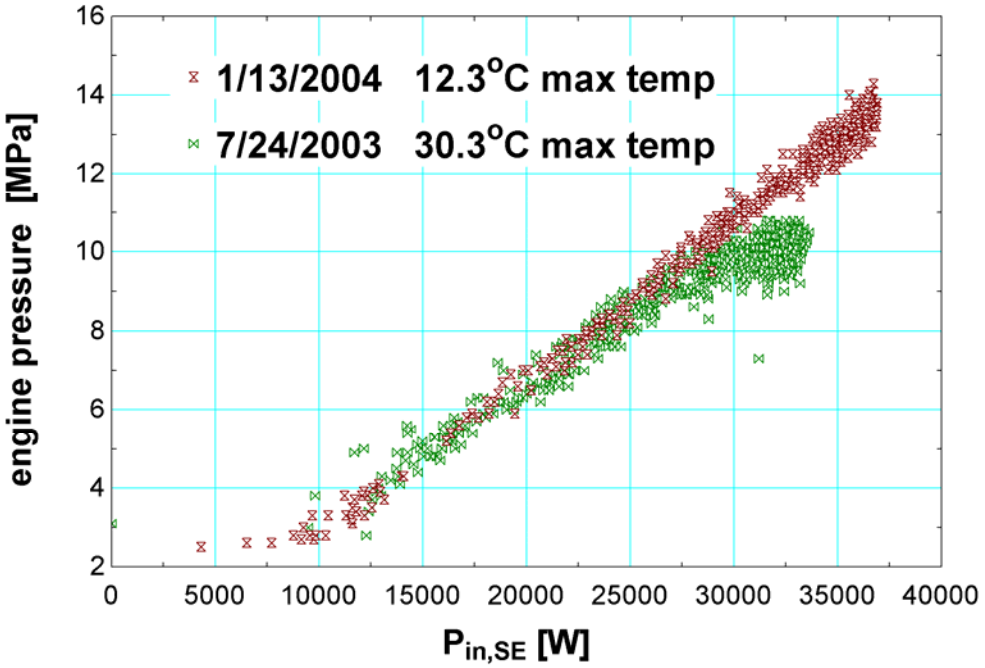

Figure 4-13 WGA data of the engine pressure versus input power to the engine showing ambient temperature influence on engine pressure

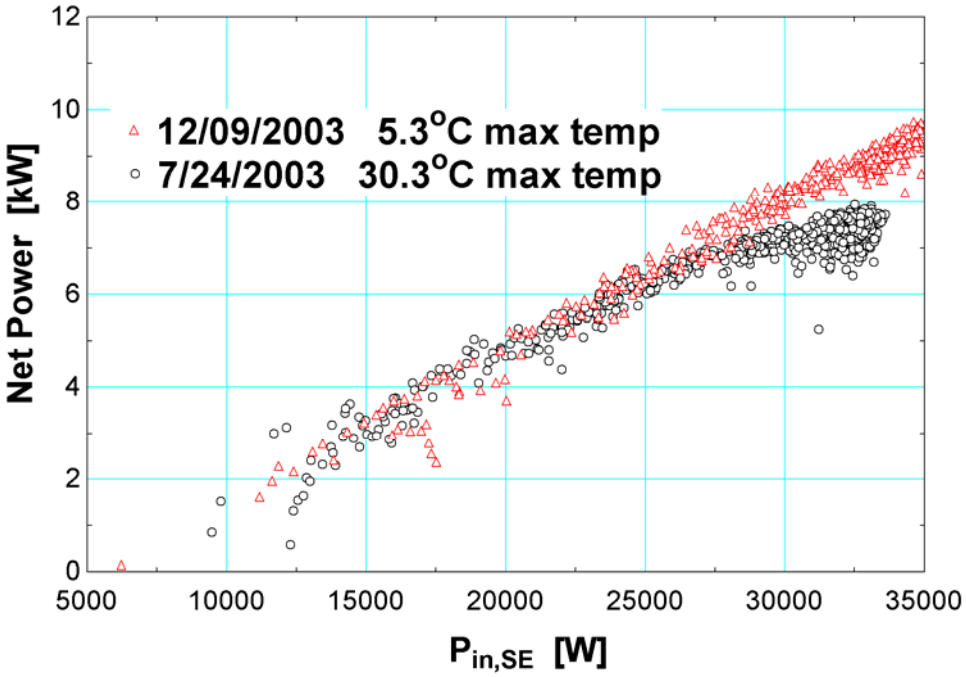

Figure 4-14 Data of the WGA system indicating the engine efficiency and therefore the net power are greater for lower ambient temperatures with the same thermal input power (at higher input powers)

4.3.2 Engine Efficiency Variation

Efficiency curves were also analyzed for the six days of data to observe variation. The six days had similar efficiencies at lower input power to the engine, but the engine efficiency varied significantly at higher input power to the engine. The engine efficiency was greater at higher engine input powers for colder ambient temperatures as shown in Figure 4-15. This behavior should also result from the engine operating more efficiently at colder ambient temperatures as explained by the second law of thermodynamics, and the cooling system may not be able to keep up with the load during these operating conditions.

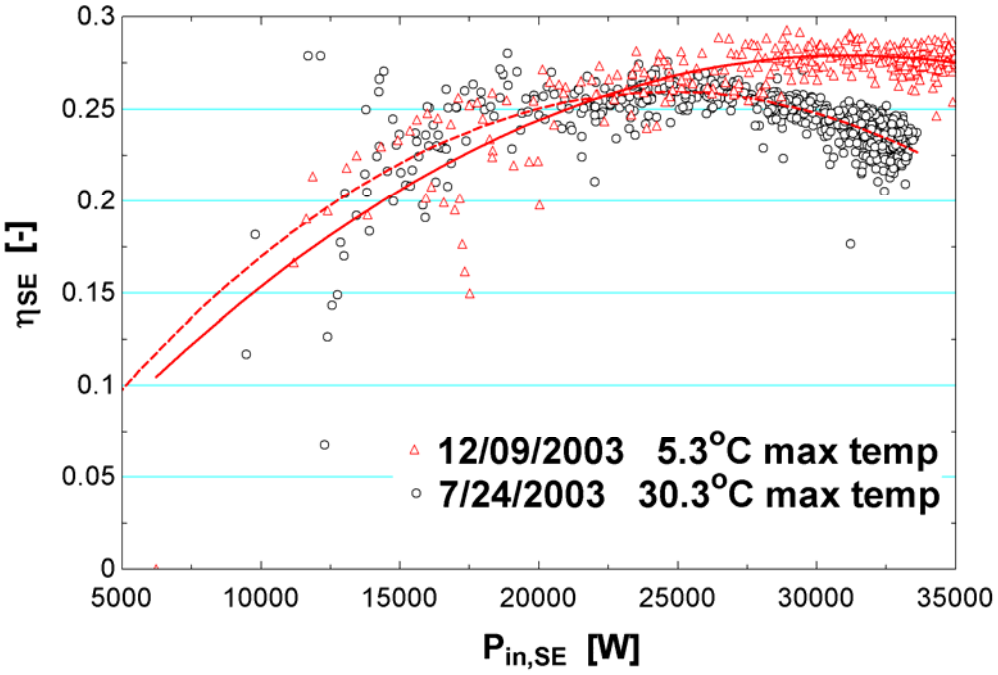

Figure 4-15 WGA data indicating engine efficiency improves with lower ambient temperature at higher thermal input power to the Stirling engine

An analysis was also made to determine if the effectiveness of the Stirling engine temperature correction terms could be observed by viewing the engine performance curves. The Stirling engine component model uses performance curve fits and some of these models include terms that correct the performance for the compression space temperature of the engine. A comparison of the efficiency curve fit (Equation (3.27)), Carnot fraction curve fit (Equation (3.31)), and the maximum fraction curve fit (Equation (3.32)) were analyzed to determine which Stirling engine performance curve fit had the least variability compared with data. The engine efficiency curve for the 6 days indicated in Table 4.1 is shown in Figure 4-16, Figure 4-17 for the Carnot fraction curve, and Figure 4-18 for the maximum power fraction curve. The average difference is defined as the average of all the absolute values of the difference between the curve fit and the value of a data point, divided by the value of the curve fit. There is less variation between curves for the Carnot fraction compared to the engine efficiency, so this indicates the temperature correction term is improving the model. The maximum power fraction appears to be a slightly better correlation than the Carnot fraction. The results section in Chapter 5 indicate that the

Carnot fraction does perform better than the Stirling engine efficiency component model, and the maximum power fraction does predict the system performance a little better than the Carnot fraction model.

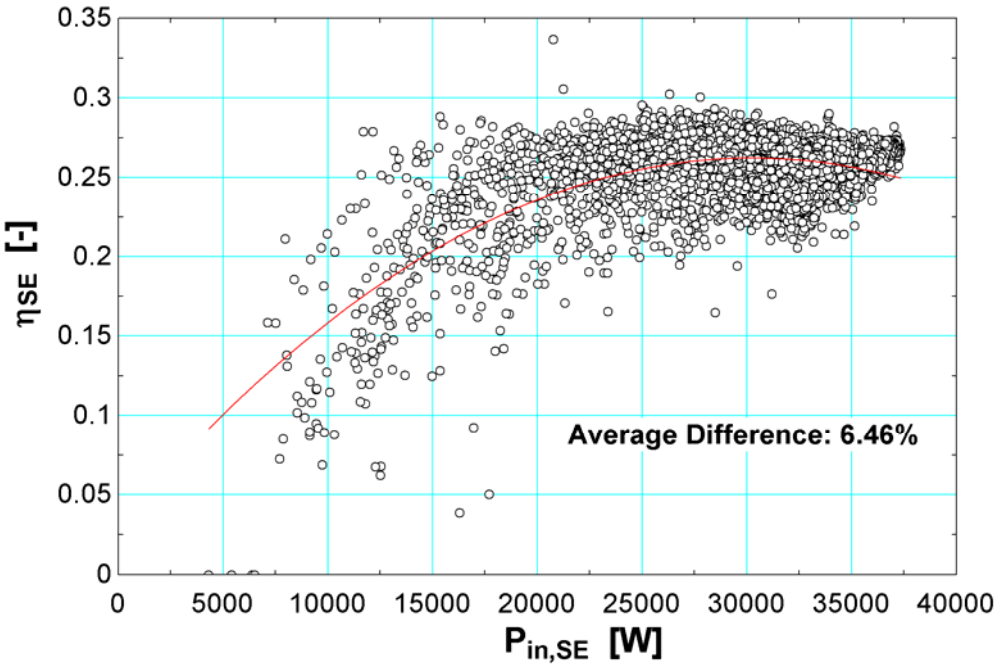

Figure 4-16 Variability in the engine efficiency curve fit for 4/26/2004 for the WGA system

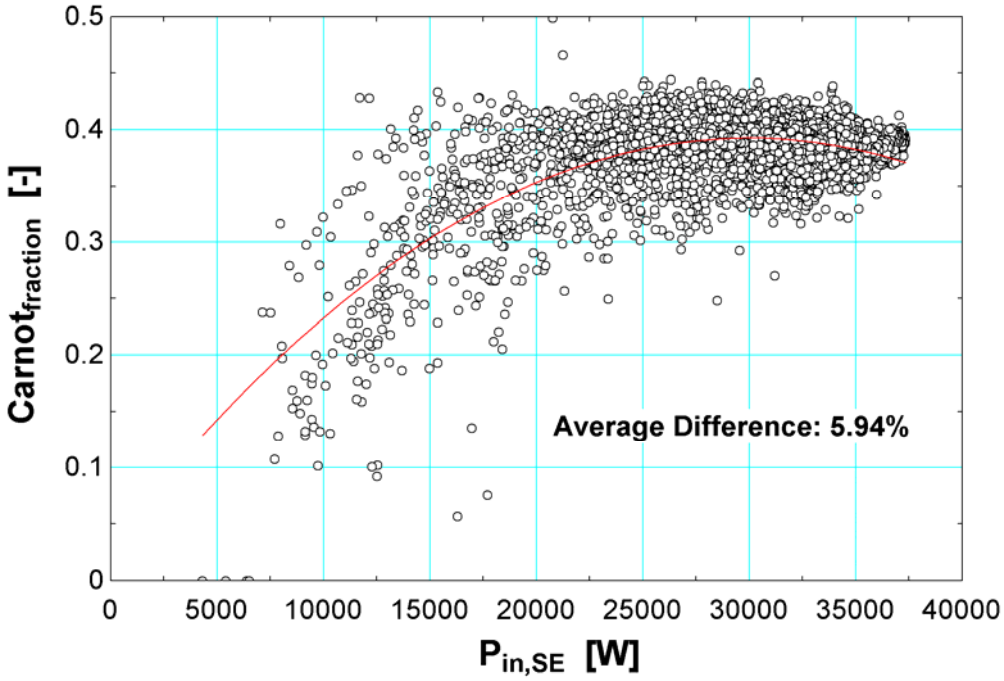

Figure 4-17 Variability in the Carnot fraction curve fit for 4/26/2004 for the WGA system

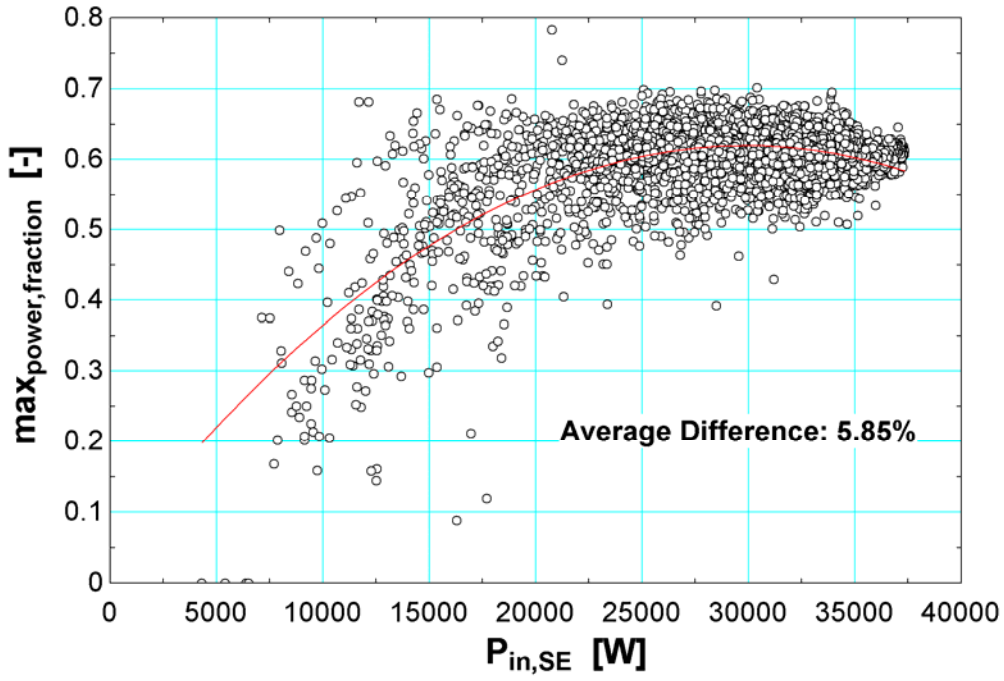

Figure 4-18 Variability in the maximum power fraction curve fit for 4/26/2004 for the WGA system

The Stirling engine efficiency was also analyzed at similar operating conditions to determine if there were any significant differences between the days. Table 4.2 presents results on various days with similar operating conditions. Twenty-five data points were analyzed from 6 days of data from around 11am with similar operating conditions of 900 W/m^2 DNI and a 630˚C expansion space temperature. The average ambient temperature varied for these days, and the effect should be a slightly lower net power and efficiency for higher ambient temperatures.

The WGA data were recorded every minute, so the analyzed 25 data points represented a 25 minute interval. The predicted engine efficiency (including generator losses), and the engine efficiency divided by the maximum power point equation ($1-\sqrt{T_{amb}/T_E}$) were very similar for four of the six days with engine efficiencies around 26 % (including the generator losses) and 60 % for the efficiency divided by the maximum power equation (eta_max_power). The data for 6/2/2003 indicates a larger than expected efficiency for the WGA system, and the data from 7/24/2003 indicates a lower than expected performance when compared with data from the other four days. The data log indicates that the mirror was washed a couple days before 6/2/2003, whereas the mirrors were not washed for a full month before 7/24/2003. The performance is further reduced on 7/24/2003 due to the ambient temperature being the highest.

The net power recorded by the experimental data for these operating conditions should be about 8.0 kW for a direct normal insolation of 900 W/m^2 before noon. The net power data for 6/2/2003 indicates the performance of the WGA system was greater than the norm by approximately 8 %, and the data from 7/24/2003 indicates the system performance was lower than expected by about 10 %. These discrepancies may be a result of the mirror soiling and the ambient temperature.

Table 4.2 Analysis of the Stirling engine component model using days with similar operating conditions by averaging 25 consecutive data points with minute intervals. See Appendix B for sample data.

	average eta_SE	average eta_max_power	average Net Power	average TE	average T_amb	average DNI
	[-]	[-]	[kW]	[C]	[C]	[W/m^2]
4/26/2004	0.265	0.608	8.19	629.7	13.93	899
4/27/2004	0.258	0.597	8.03	628.1	17.66	904
6/2/2003	0.278	0.651	8.64	627.7	22.52	900
7/24/2003	0.227	0.539	7.22	627.9	27.68	900
12/9/2003	0.272	0.606	8.09	627.7	0.10	900
1/13/2004	0.267	0.600	7.96	628.4	4.38	902
ave	0.261	0.600				
std-dev	0.018	0.036				
range	0.050	0.112				
range %	0.193	0.186				
excluding 6/2/03 and 7/24/03						
ave	0.266	0.603				
std-dev	0.006	0.005				
range	0.015	0.011				
range %	0.055	0.019				

4.3.3 Net Power Variation

The net power versus direct normal insolation data were plotted for two days of data in Figure 4-19. The figure shows lower performance during start-up during colder temperatures, but this could also be affected by the location the sun rises over the eastern mountains during different times of the year. The data does indicate higher performance once the system has been running at lower ambient temperatures. The reduction in net power for the system operating near full load with higher ambient temperatures (Figure 4-19) may not be as pronounced as for the engine pressure (Figure 4-13) and efficiency curves (Figure 4-15) since the engine component is not decoupled from the receiver model for the net power versus DNI curve. At lower ambient temperatures, the receiver losses are also greater, so the net power versus direct normal insolation will not be as high at colder temperatures in comparison to the efficiency curves.

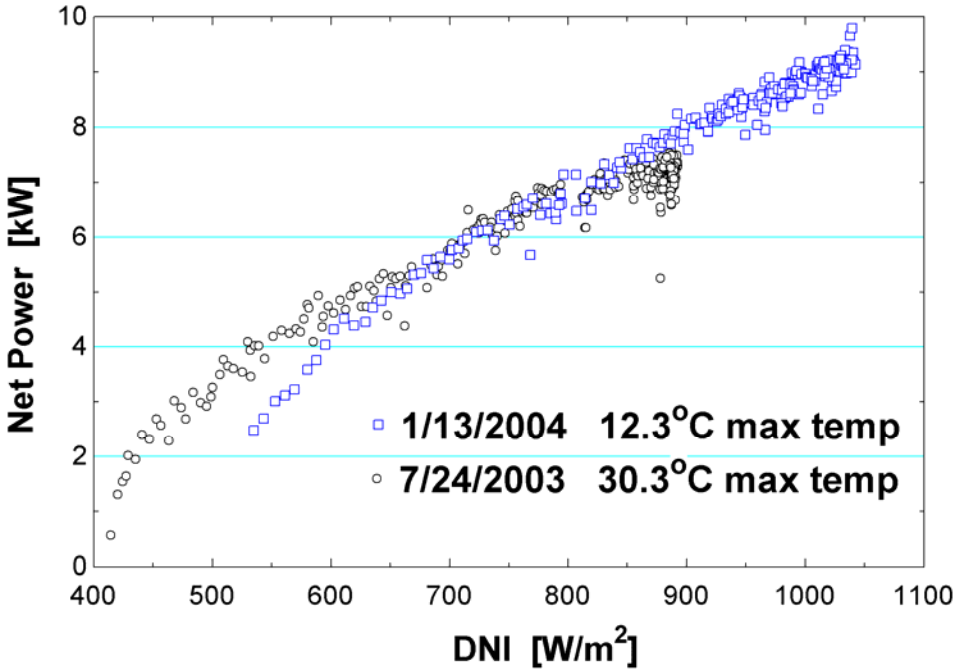

Figure 4-19 Variations in the engine net output power curve fits due to ambient temperature

The net power curves were also analyzed over the six days of data described in Table 4.1 for the Stine (Stine, 1995) and Sandia (Igo and Andraka, 2007) models described in Chapter 3. The Sandia model had a 340 W average difference in power shown in Figure 4-20, whereas the Stine model average difference in power was 440 W as shown in Figure 4-20. The average difference in power is defined in Equation (4.3). The temperature correction correlation used in the Sandia model appears to be more effective than the Stine correlation over the six days of data. The results section in Chapter 5 also indicates the Sandia model to be more accurate than the Stine model.

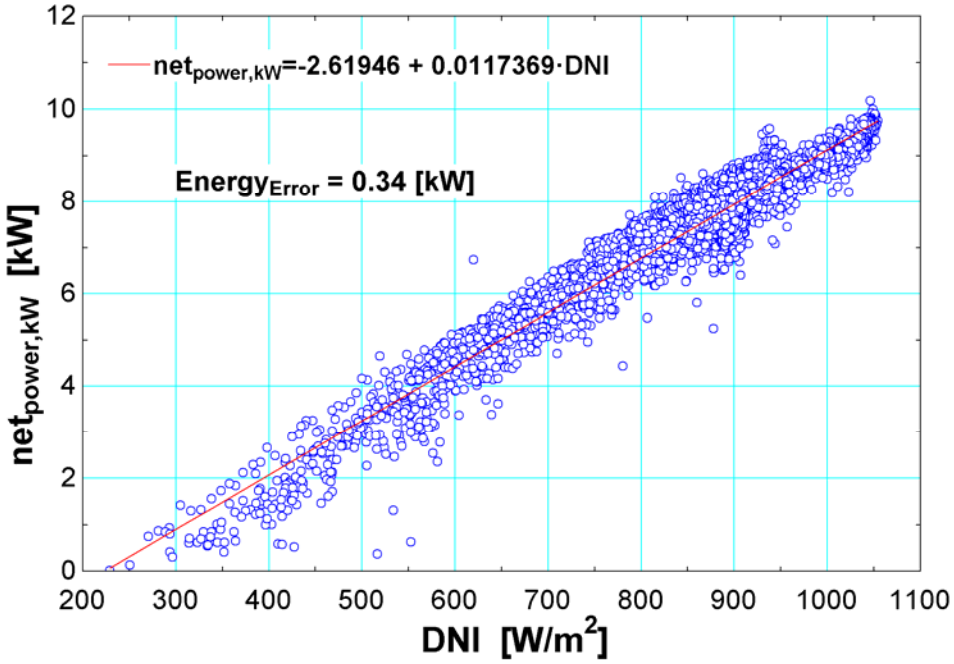

Figure 4-20 Sandia model variability for the curve fits with a 293 °K average ambient temperature chosen for the temperature correction term

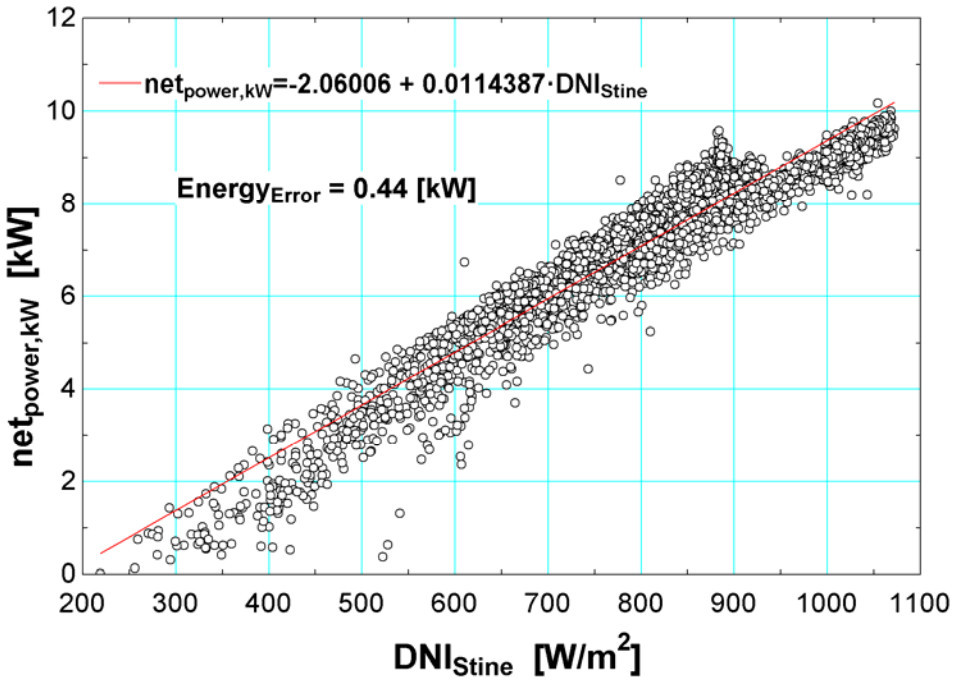

Figure 4-21 Stine model variability for the curve fits on various days

4.3.4 Tracking Error

After observing several days of data, there appeared to be external factors influencing the consistency of the system to produce an expected power output. For example, there were several instances when the WGA system output power dropped to zero even though the insolation was well above 500 W/m^2 such as on 7/24/03. This behavior likely resulted from the tracking of the collector not working properly as evident by the data points that fall significantly below the performance curve fit in Figure 4-22. Five periods of collector de-track occurred on 7/24/2003 with each lasting several minutes. The tracking faults were not a result of high wind speeds since the wind was rarely above ten miles per hour. Each time there was a tracking fault, the data also indicated that there was a PCU fault. Data recorded during PCU faults were filtered as described before. A new curve fit was made for 7/24/03 in Figure 4-23, and this new curve fit was overlaid on the previous curves as shown in Figure 4-24.

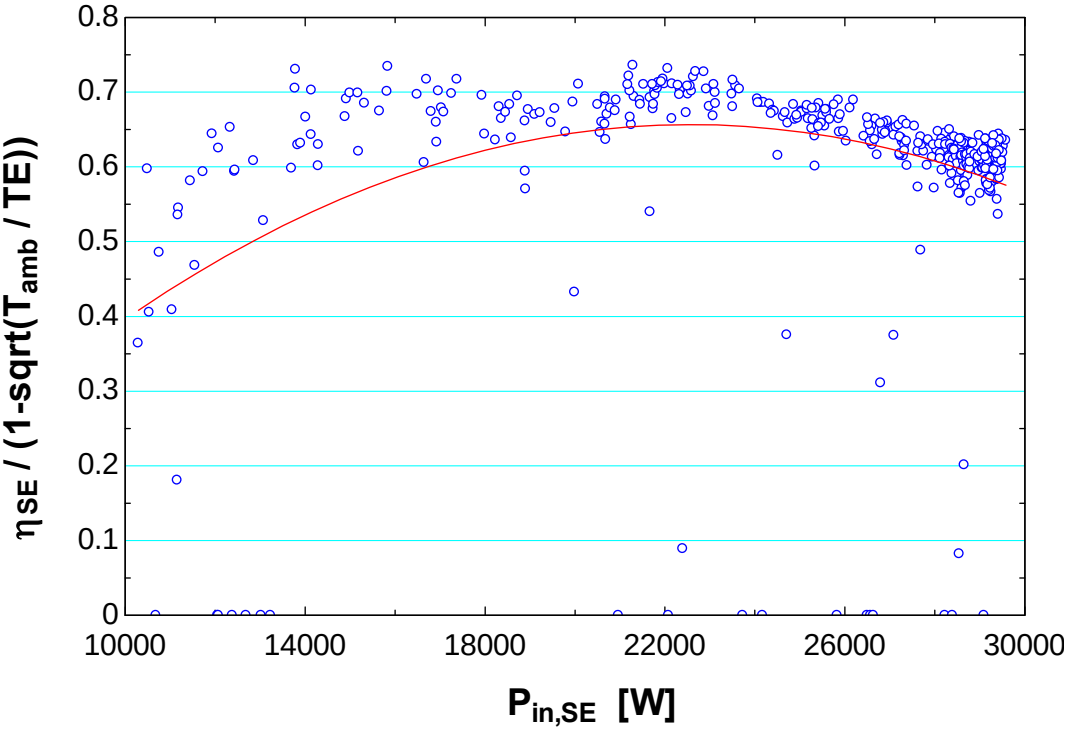

Figure 4-22 Engine efficiency curve fit for 7/24/03 showing tracking errors

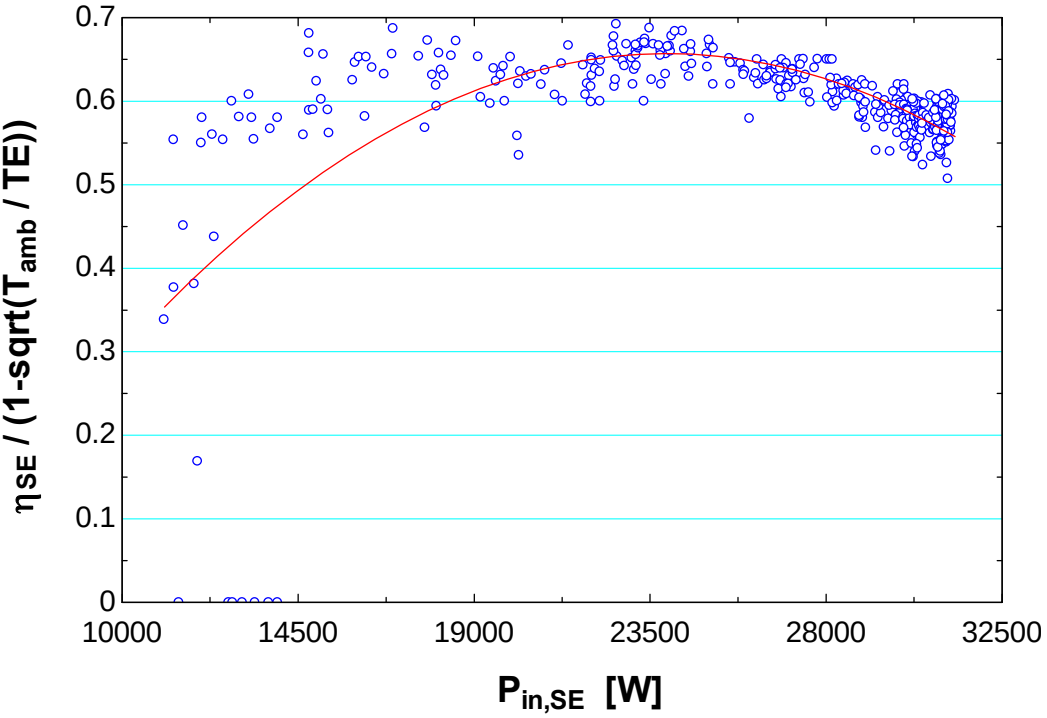

Figure 4-23 Engine efficiency curve fit for 7/24/03 with tracking term errors removed

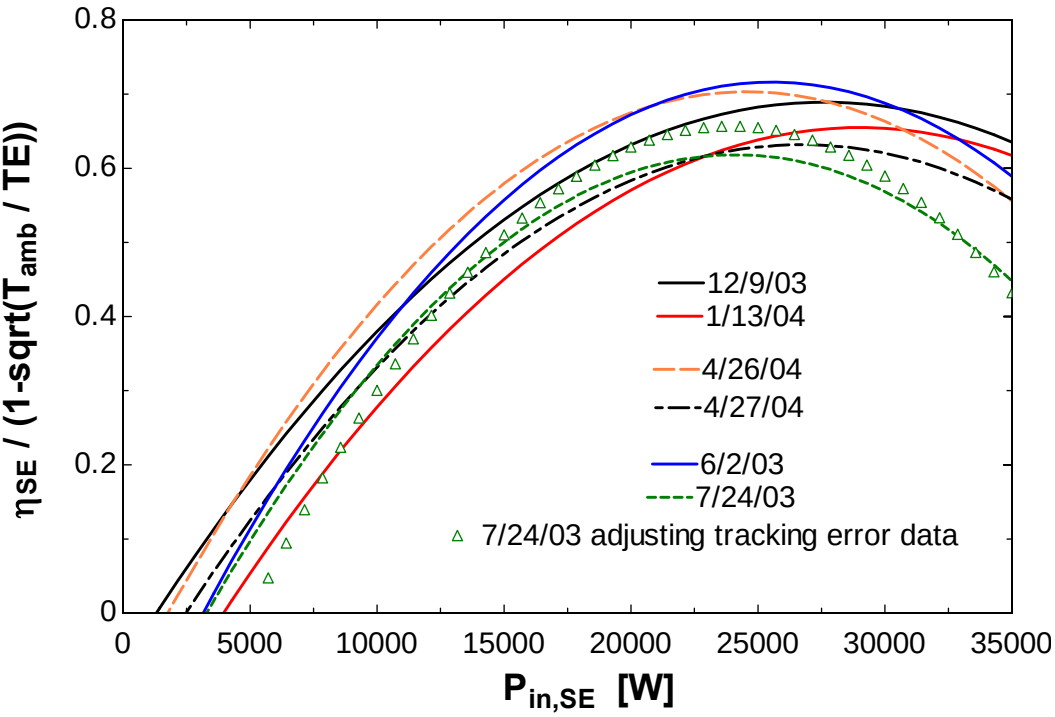

Figure 4-24 Engine efficiency curve fits with 7/24/03 adjusted to remove tracking errors

4.3.5 Mirror Soiling

Mirror soiling can contribute to a significant reduction in the performance of Stirling dish systems. The data log for the WGA system indicated that the mirrors were washed on a regular two week schedule when data were first recorded, but eventually the mirrors were washed irregularly with periods ranging over two months between washings. It is not known if the mirrors continued to be cleaned on a regular basis, or if the recorded mirror washings in the data log represented all of the mirror washings. Table 4.3 lists the days when the collector mirror was washed according to the data log.

Figure 4-25 indicates the performance of the WGA system before and after the mirrors were washed. The performance appears to be improved significantly after washing the mirrors as indicated in Figure 4-25, and this improvement is more prominent since the performance after the mirrors were washed still increased despite the increase in the average ambient temperature. The system performance in the WGA data was influenced by mirror soiling, and the mirrors may not have been washed regularly if all mirror washings were indicated in the data log.

Dates Mirror Washed
5/13/2003
5/29/2003
6/13/2003
6/25/2003
9/17/2003
12/17/2003
1/8/2004
3/30/2004
4/14/2004

Table 4.3 Dates indicated in the data log when the mirrors were washed.

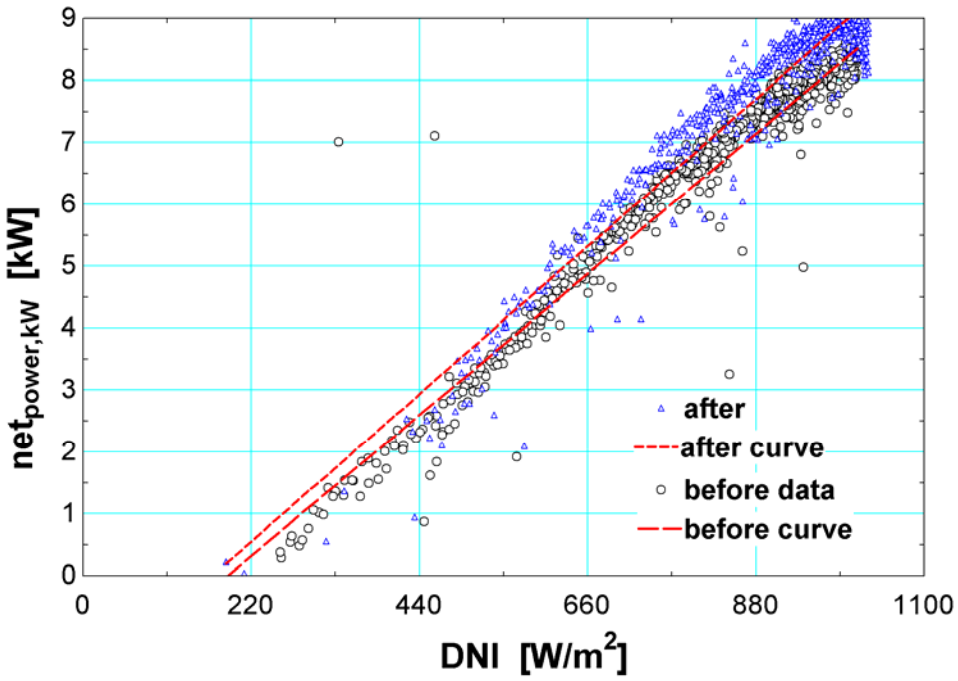

Figure 4-25 Net system performance for the WGA system before (4/12/04-4/13/04 with $T_{amb,ave}$ = 13.7°C) and after (4/15/04-4/16/04 with $T_{amb,ave}$ = 18.7°C) the parabolic mirrors were washed on 4/14/04

5 Results Analysis: Comparison of Component Models to Data

Thirteen different models outlined in Chapter 3.3 were compared with WGA filtered data to determine how accurate they were at predicting the total energy produced and the net power for the WGA Stirling dish system. The Stine ($P_{net,Stine}$) and Sandia ($P_{net,Sandia}$) models were existing models as outlined in Stine (1995) and Igo and Andraka (2007) respectively. The other eleven models were developed during the research for this thesis.

Six randomly chosen individual days of data were used to generate six different performance curve fits for each of the thirteen models. Six performance curve fits were created for each model in order to obtain adjustable coefficients used to determine how accurate each model was using a small sample of one day of data to predict the net system performance for another day of data or for several years of data ranging between 2003 and 2006. Each one of these days generated a different curve fit and consequently a different predicted performance of the engine or system. The data used to generate the curve fits and the three years of data were all filtered according to the methodology described in Chapter 4.2. A list of the abbreviations used in the model simulations are displayed in Table 5.1. The West number correlation (West#) and the Beale number correlation corrected with the maximum power correlation ($Beale\#_{max,pwr}$) were found to best agree with the data.

Table 5.1 Model abbreviations used in the simulation results section

Model	Model Description	Equation
$P_{net,Stine}$	Stine Model	(3.35)

Beale# DNI	Beale number model plotting Beale# vs. DNI and pressure vs. Pin,SE	(3.30)
η	Engine efficiency curve model	(3.27)
$P_{net,Pin,SE}$	Model using the net power versus power into the Stirling engine	Figure 3-31
$P_{net,Sandia}$	Sandia model	(3.36)
η_{Carnot}	Carnot fraction model	(3.31)
Beale# Cor	Beale number correlation corrected using Sandia temp correlation	(3.30)
Beale#	Beale number model plotting Beale# vs. Pin,SE and pressure vs. Pin,SE	(3.30)
$\eta_{max,pwr}$	Maximum power fraction model	(3.32)
η_{West}	Engine efficiency model corrected using the West# temperature correlation	(3.27)(3.33)
West# DNI	West number model plotting West# vs. DNI and pressure vs. Pin,SE	(3.34)
West#	West number model plotting Beale# vs. Pin,SE and pressure vs. Pin,SE	(3.34)
Beale#$_{max,pwr}$	Beale number model corrected using the maximum power temp correlation	(3.30)(3.32)

An 'Energy Error' given by Equation (4.1) is defined as the mean bias error of the percent difference in energy (kW-hrs) predicted by the component model to the energy recorded in the WGA data. The term N is the total number of data points used, P_{calc} is the predicted net power by the component model, P_{data} is the net power given in the data, and Δt is the time interval for each data point which was one minute.

$$Energy\_Error = \left[\sum_{i=1}^{N} \left[P_{calc} - P_{data} \right]_i \cdot \Delta t \right] / \left[\sum_{i=1}^{N} \left[P_{data} \cdot \Delta t \right]_i \right] \cdot 100\% \qquad (4.1)$$

The 'RMS Power' in the results section is given by Equation (4.2) and it is the root mean square deviation.

$$RMS\_Power = \frac{1}{N} \cdot \sqrt{\sum_{i=1}^{N} \left(P_{calc} - P_{data} \right)_i^2} \qquad (4.2)$$

The 'Power Difference' in this section is defined as the average difference in power between the data and the power predicted by the component model. This is shown in Equation (4.3).

$$Power\_Difference = \frac{1}{N} \cdot \sum_{i=1}^{N} \left| P_{calc} - P_{data} \right|_i \qquad (4.3)$$

The 'Normalized Power Difference' is defined as the normalized average difference in power defined in Equation (4.4).

$$Normalized\_Power\_Difference = \frac{1}{N} \cdot \sum_{i=1}^{N} \left[\left| P_{calc} - P_{data} \right| / P_{data} \right] \qquad (4.4)$$

5.1 Different Day Comparison

The thirteen models indicated in Table 5.1 were compared with how well they predicted the energy and power for different individual days of data. One day of data was used to produce the performance curve fits for the models and the predicted system performance of each model was compared with five different days of data to observe how consistent and accurate the models are. A matrix was created (see Appendix C) to obtain the average and standard deviation using 30 simulation results for the total predicted energy error (Figure 5-1), RMS deviation (Figure 5-2), the average difference in the power (Figure 5-3), and the normalized average difference of the power (Figure 5-4). The error bars in Figure 5-1 through Figure 5-4 indicate one standard deviation for the 30 simulations indicated in Appendix C. The Stine model (Stine, 1995) performed the worst, the Sandia model (Igo and Andraka, 2007) performed better than the Stine model, and the West number model and Beale number model corrected using the maximum power fraction performed the best.

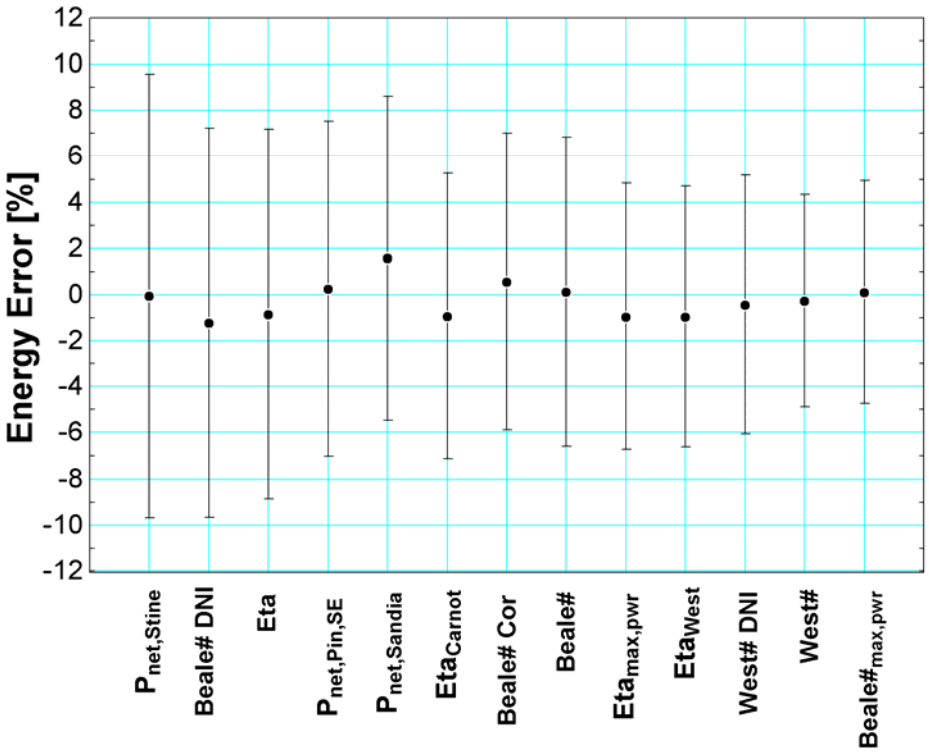

Figure 5-1 Energy error for models compared with different days of data

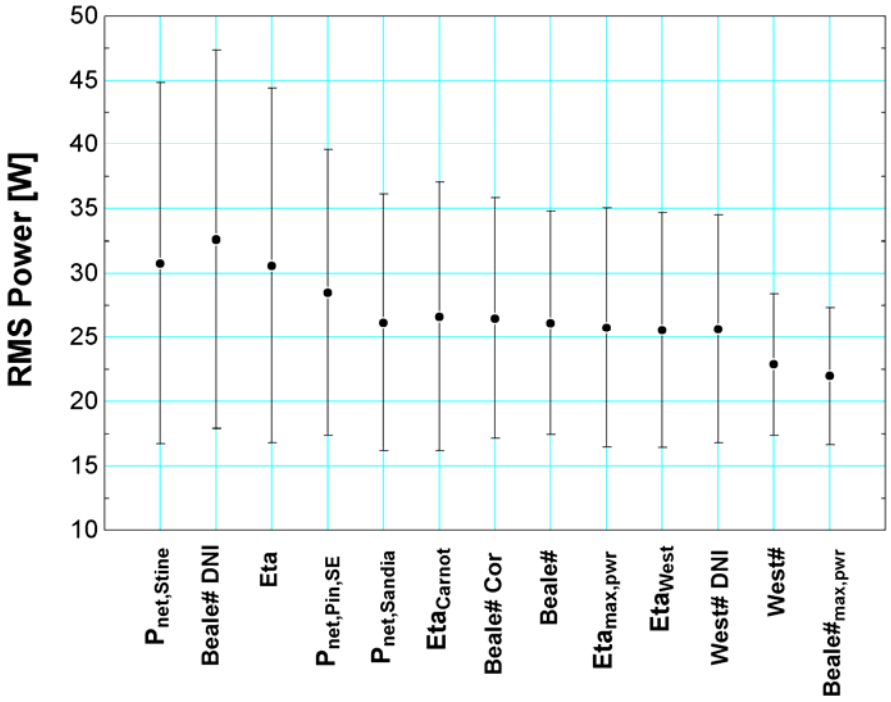

Figure 5-2 RMS deviation in power for models compared with different days of data

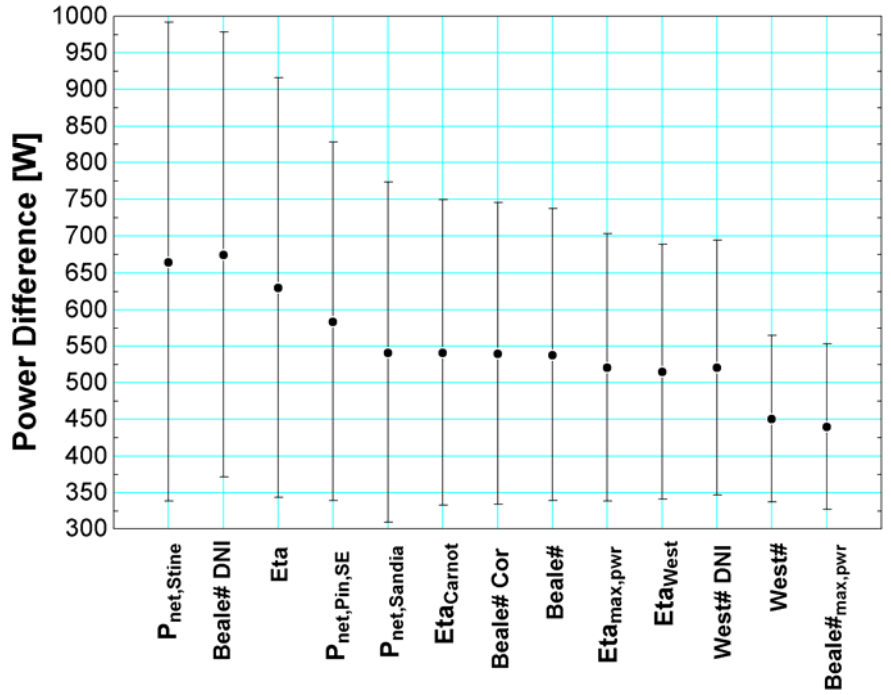

Figure 5-3 Average difference in power for models compared with different days of data

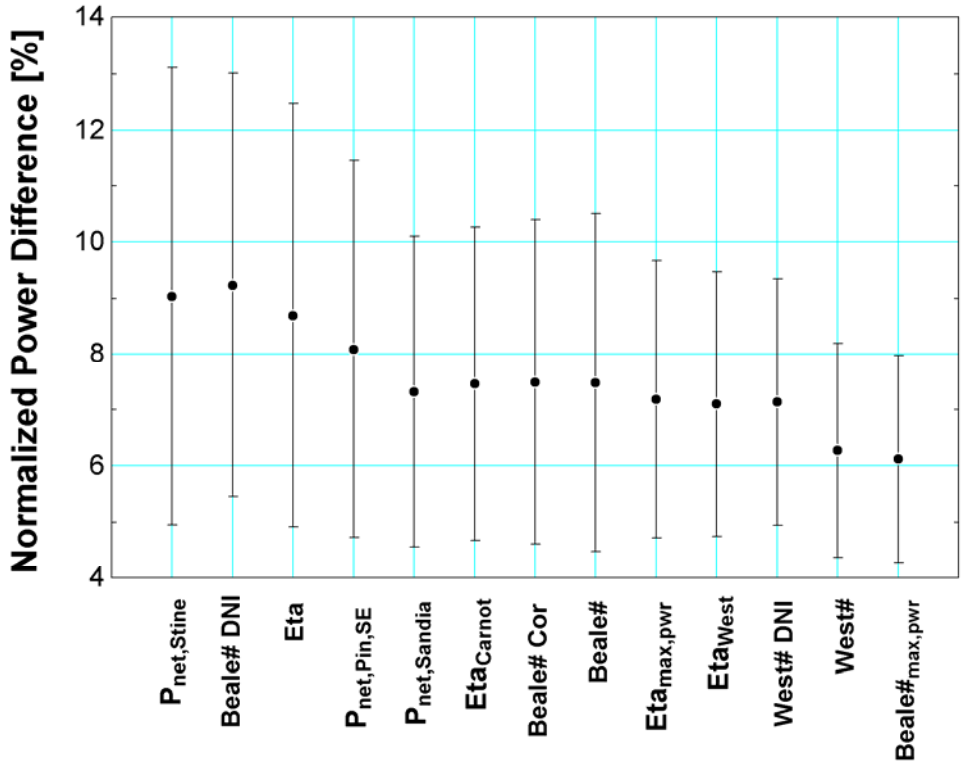

Figure 5-4 Normalized difference in power for models compared with different days of data

5.2 Comparison with All Filtered WGA Data

The fourteen different models were compared with how well they predicted the energy and power for all of the filtered WGA data. The results of the total predicted energy error is given in Figure 5-5, the RMS deviation in Figure 5-6, the average difference in the power in Figure 5-7, and the normalized average difference of the power in Figure 5-8. The error bars indicates one standard deviation of the six simulations for each model. The West number model and the Beale number model corrected with the maximum power fraction performed the best once again.

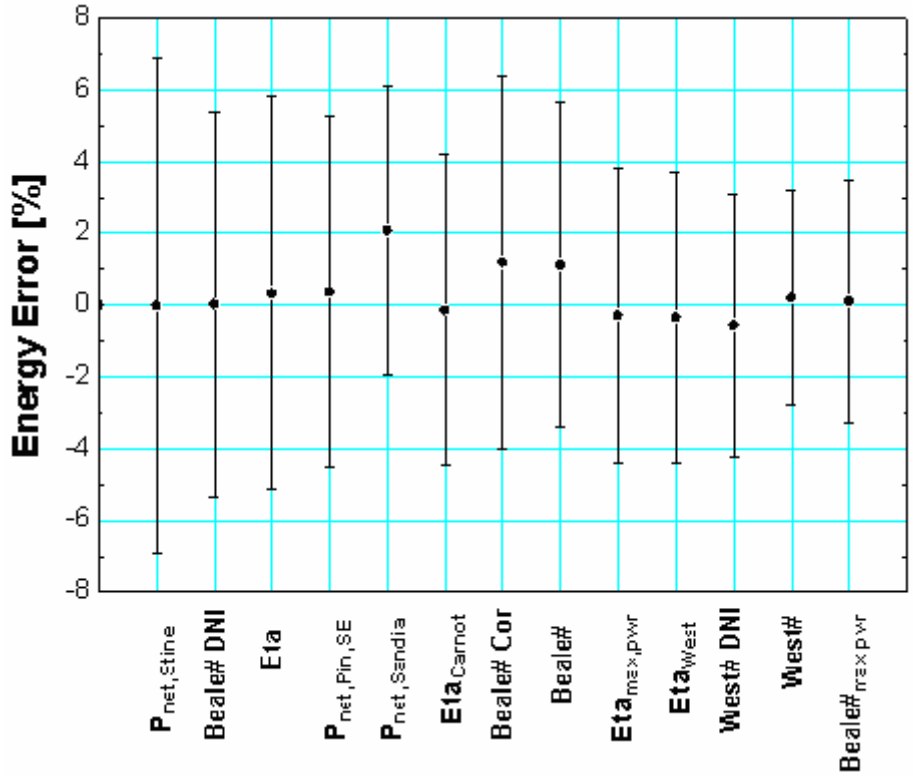

Figure 5-5 Energy error for models compared with all of the filtered data

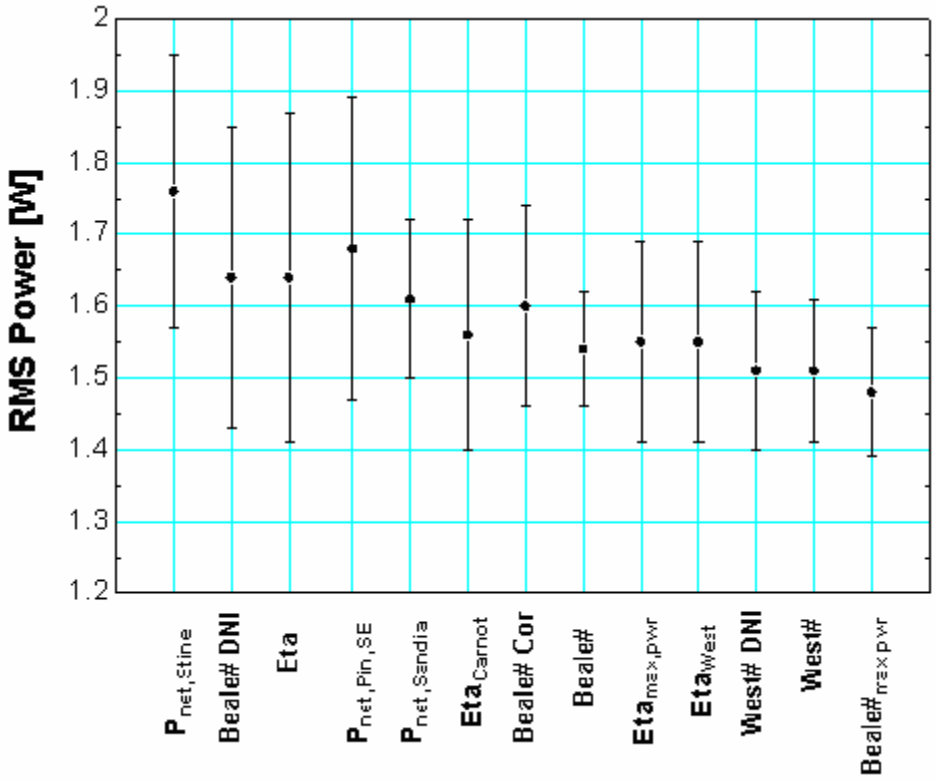

Figure 5-6 RMS deviation in power for models compared with all of the filtered data

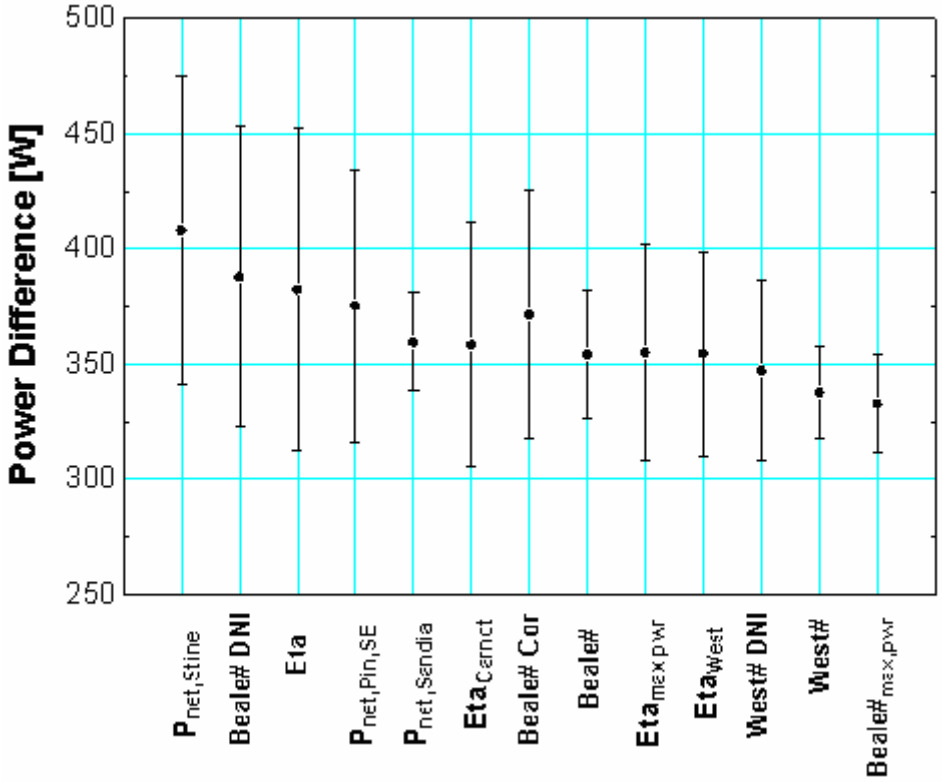

Figure 5-7 Average difference in power for models compared with all of the filtered data

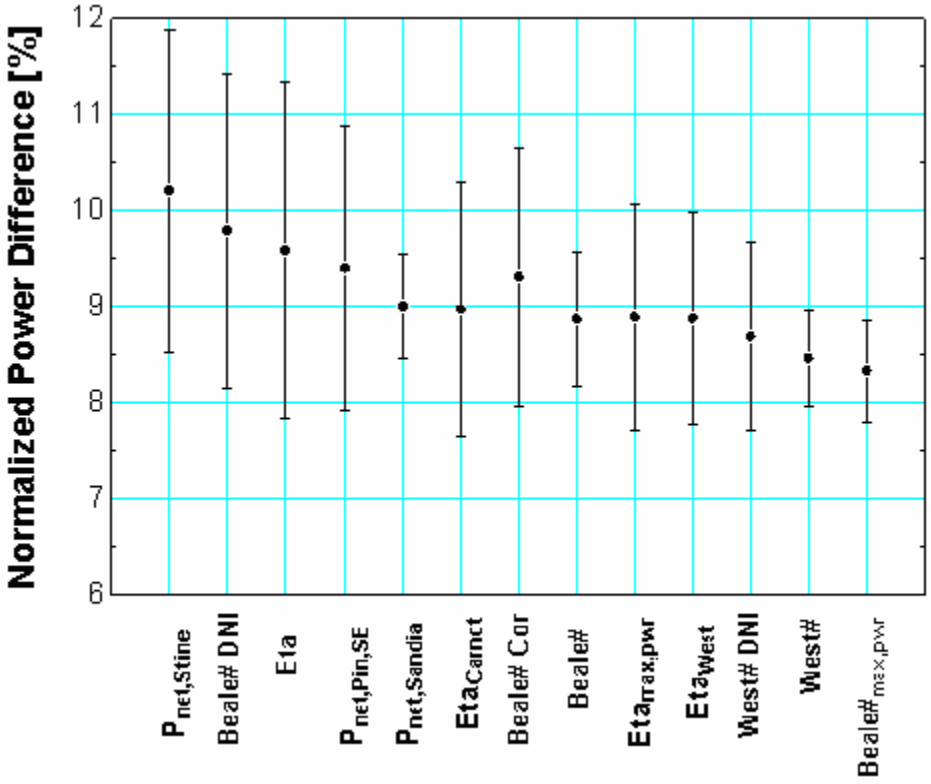

Figure 5-8 Normalized difference in power for models compared with all of the filtered data

5.3 Comparison with All Filtered WGA (10-minute averaged) Data

Six simulations using a different day to generate a curve fit were run to compare the Beale#$_{max,pwr}$ model, the Sandia model (Igo and Andraka, 2007) and the Stine model (Stine, 1995) with three years of filtered 10-minute time-averaged data for the WGA Mod 2-2 system. It was believed that some system transients would be reduced by using 10 minute averages instead of the individual minute data. These three models were chosen because the Stine (Equation (3.35)) and Sandia models (Equation (3.36)) were the two existing published models, and the Beale#$_{max,pwr}$ model (Equations (3.30) and (3.32)) was the best model developed during the research of this thesis.

The results of the mean bias error for the three models compared to the 10 kW WGA system data is given in Table 5.2, and the average difference in power is shown in Table 5.3. The Beale number model corrected with the maximum power correlation as described in section 3.3.1.3, once again had the lowest standard deviation for the mean bias error and the average difference of power. The Stine model indicated the lowest value for the mean bias error as shown in Table 5.2, however, the standard deviation of the mean bias error and the average difference of power are the best indicators of the accuracy and precision of the models. It would be possible for a model to have a mean bias error of positive 100 % using one day of data and negative 100 % using another day of data, and still have an average mean bias error of 0 %. The standard deviation of the mean bias error effectively indicates the range of a models error in total predicted energy compared with data.

Table 5.2 Comparison of the mean bias error for three models using different days to generate performance curve fits. The models are compared with three years of WGA Mod 2-2 data.

	Mean Bias Error [%] (Equation 5.1)		
	Beale#,max,pwr	**Igo & Andraka (2007**	**Stine (1995)**
Day used for performance curve fit	[%]	[%]	[%]
4/26/2004	3.52	5.35	4.30
4/27/2004	-2.59	0.84	0.16
6/2/2003	5.93	9.72	9.15
7/24/2003	-4.14	1.5	3.05
12/9/2003	3.25	-5.96	-6.99
1/13/2004	-1.12	-7.25	-8.83
Average	***0.81***	***0.70***	***0.14***
Standard Deviation	***3.98***	***6.50***	***6.90***

Table 5.3 Comparison of the average difference in power for three models using different days to generate performance curve fits. The models are compared with three years of WGA Mod 2-2 data.

	Average Difference in Power [W] (Equation 5.3)		
Day used for performance curve fit	**Beale#,max,pwr**	**Igo & Andraka (2007**	**Stine (1995)**
4/26/2004	552	564	583
4/27/2004	593	539	574
6/2/2003	581	743	746
7/24/2003	720	545	567
12/9/2003	504	696	760
1/13/2004	514	751	845
Average	***577***	***640***	***679***
Standard Deviation	***78***	***101***	***120***

Scatter in the data is believed to be a large function of mirror soiling and potentially irregular mirror washings in addition to various system components not functioning properly as indicated in the data log. Obtaining a value for the scatter in the data is required to determine how much error is contributed to the models compared to variability in the data. Performance curve fits were generated for the Stine (Figure 5-9), Sandia (Figure 5-10), and Beale#$_{max,pwr}$ (Figure 5-11) models using all the 10 minute averaged WGA data over the three year period to determine the scatter in the data. Scatter in the data contributed to an average difference in power of 490 W for the Beale#$_{max,pwr}$, 505 W for the Sandia model, and 570 W for the Stine model. These curves also indicate that the Beale#$_{max,pwr}$ model produces the least variability when generating curve fits. The maximum obtainable average difference of power for these models if three years of data are known is 490 W, and the Beale#$_{max,pwr}$ model using only one day of data to predict the performance of three years of data averaged 580 W. This indicates the Beale#$_{max,pwr}$ model is capable of using a very small sample of data to predict the long term performance of these systems.

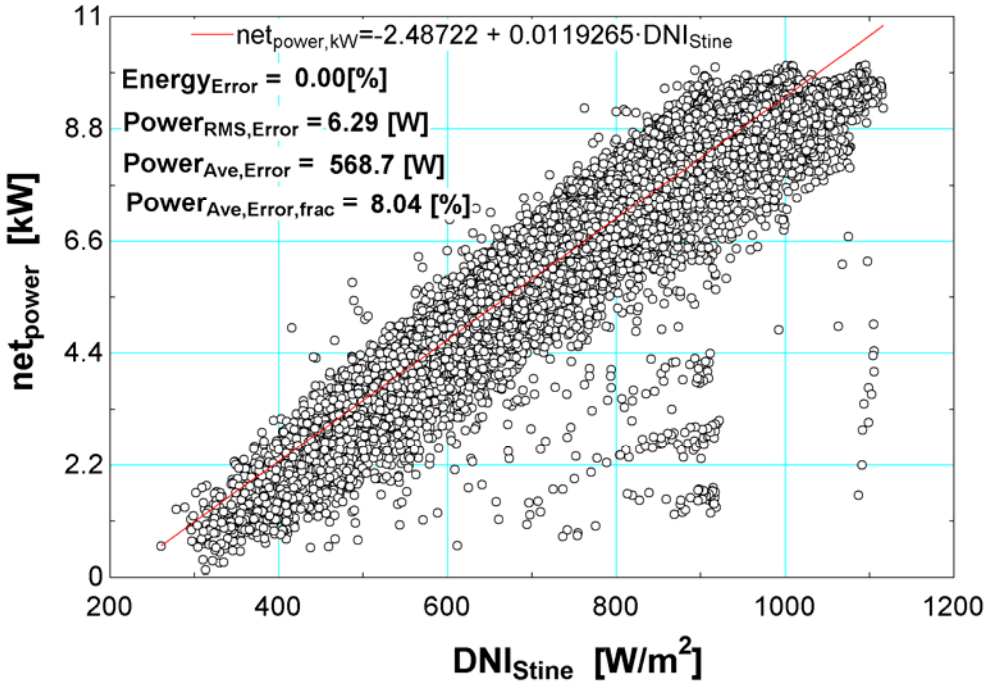

Figure 5-9 Stine model curve fit generated from all of the WGA 10-minute averaged data

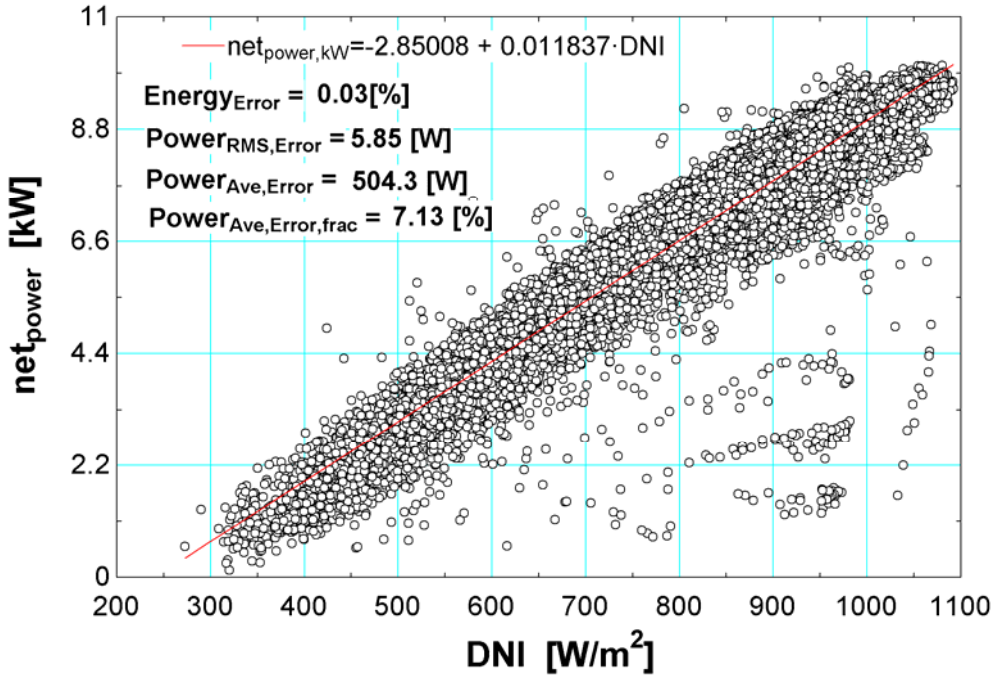

Figure 5-10 Sandia model curve fit generated from all of the WGA 10-minute averaged data

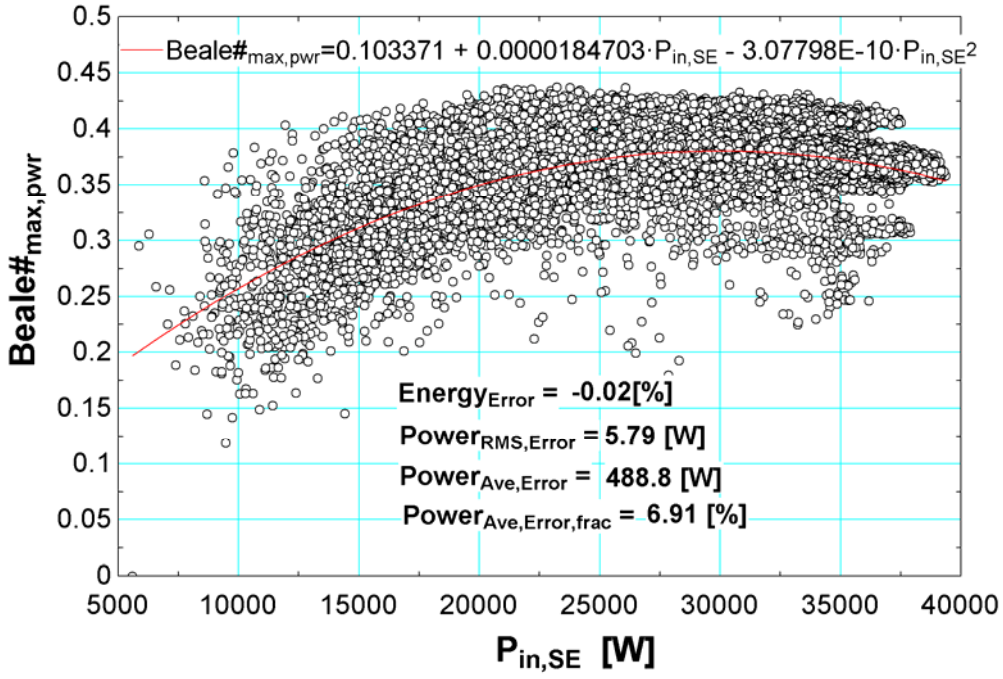

Figure 5-11 Beale#$_{max,pwr}$ model curve fit generated from all of the WGA 10-minute averaged data

5.4 Model Simulation Results Summary

All of these models are capable of taking a small sample of data (1-day) to predict the long term performance of the system. Using three years of data instead of one day of data to predict the system performance did not improve the performance prediction significantly. The results of the model simulations shown in Figure 5-5 and Figure 5-7 indicate that the Sandia system model appears to provide better agreement with experimental data compared to the Stine system model. Several of the (eleven) component based models developed during the research of this thesis agree with the data more closely than the Sandia model.

A plot of three models predicting the system performance for a period of three years are compared to the curve fit of three years of 10-minute time-averaged WGA data in Figure 5-12. For a specific input power to the engine, the net power will only change based on the fan power changing and the engine efficiency changing due to variations in the compression space temperature which is influenced by the ambient temperature. The Stine and Sandia models shown in Figure 5-12 do not appear to provide as reasonable of results since the variation in net power with these models is around +/- 1,000 W due to the temperature correction term for a specified input power to the engine.

Realistically, the fan power for the WGA system only varies about +/- 50 W, and the Stirling engine/generator efficiency would be approximately 27.0 % with a 0°C compression space temperature and 24.1 % with a 50°C compression space temperature assuming the maximum power fraction temperature correction term is accurate. With a 30 kW input power, this temperature difference would result in an approximate gross power of +/- 450 W. For a specific input power to the Stirling engine, the net output power should only vary at most about +/- 500 W due to the parasitic power of the fan changing and the ambient temperature changing. This is also confirmed by Figure 5-11 which indicates that the average difference in power for three years of data was 490 W for a specific input power to the engine due to mirror soiling, tracking error, or other faults. A Stirling dish system model should be less accurate if it predicts a net power of +/- 1,000 W for a specific input power, and the spread of the net power should be less as the input power to the engine is reduced (~+/- 300 W with 15 kW input power). A similar trend occurred when plotting the net power predictions of the three models verse the direct normal insolation as shown in Figure 5-13.

The component based models developed in this research have additional location dependent parameters that are used which predict how the receiver efficiency will change based on the ambient temperature, air density, wind speed and the sun elevation angle. The component models also predict how the engine performance will change based on the ambient temperature, pump speed, fan speed, radiator and cooler effectiveness, and the engine pressure and speed. The component models additionally determine the parasitic pump and fan power based on the operating speed, (radiator) cooling fluid used, and the ambient temperature since the density and viscosity change based on temperature. Overall, the Beale$\#_{max,pwr}$ number correlation appears to be the most accurate and precise model to use for predicting the long term location dependent performance of Stirling dish systems.

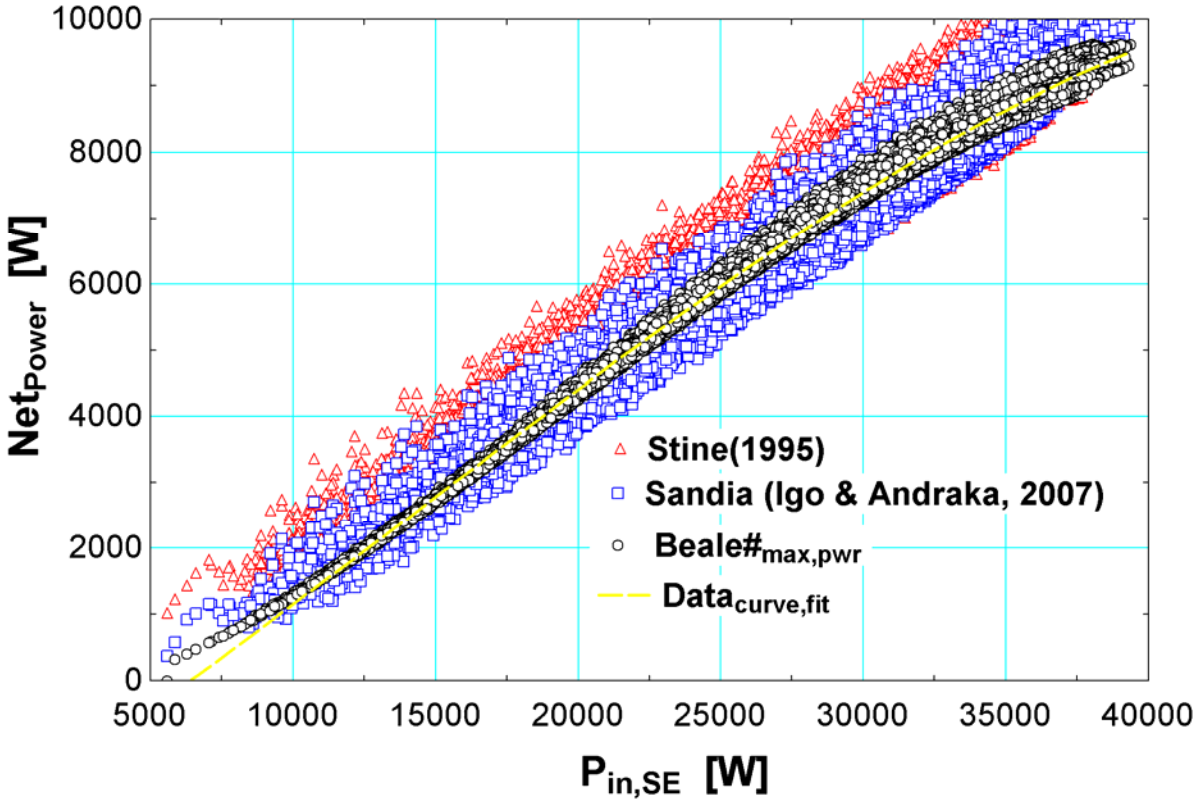

Figure 5-12 Comparison of predicted system performance of various models and the curve fit of 3 years of WGA data as a function of input power to the engine

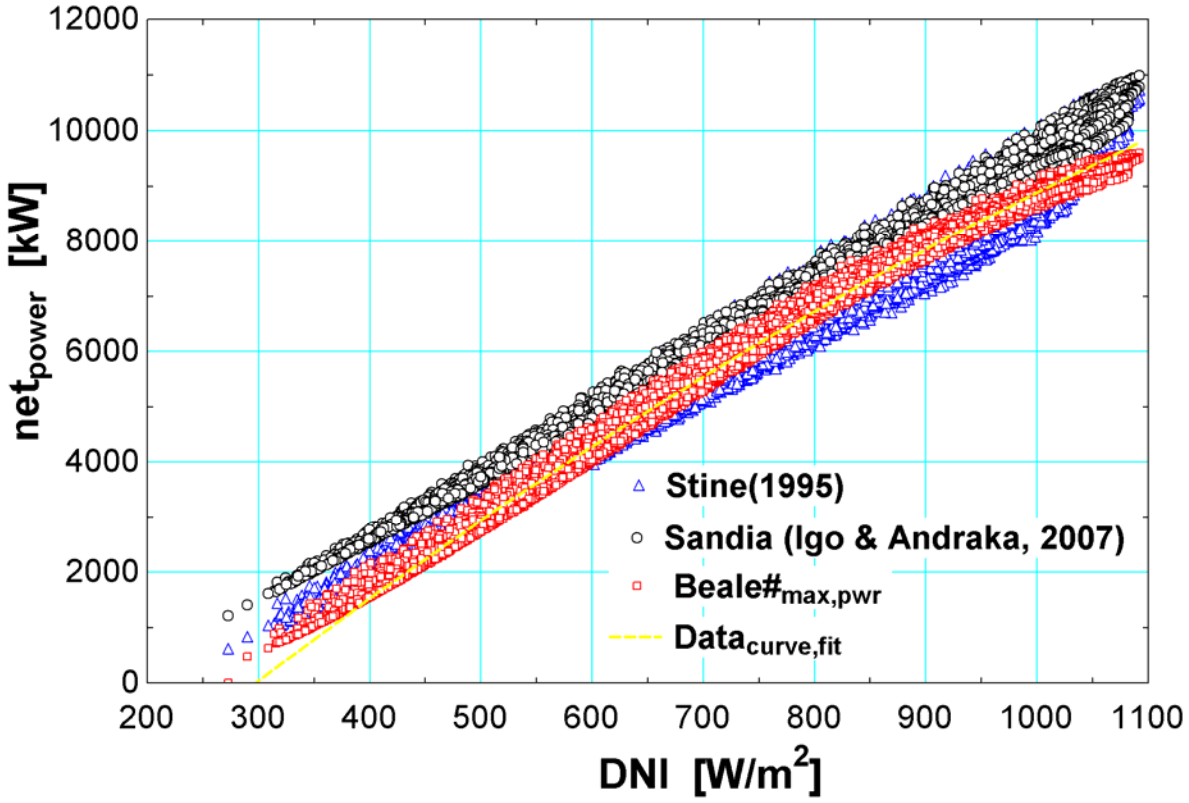

Figure 5-13 Comparison of predicted system performance of various models and the curve fit of 3 years of WGA data as a function of direct normal insolation

6 TRNSYS Model Performance Predictions

Analyses of the Beale#$_{max,pwr}$ component model were run in TRNSYS to observe the predicted yearly energy production of the WGA system in various locations around the U.S. These performance predictions of the WGA Mod 2-2 10 kW system can be viewed in Table 6.1. The annual energy prediction for the WGA system in Albuquerque was similar to a prediction published in a Sandia report (Mancini et al, 2003). Monthly performance predictions were also made for the WGA system in Albuquerque in Table 6.2. The TRNSYS model was also used to predict how the system performance changes based on the aperture diameter, heater head temperature, fan and pump operating speeds, including a transparent receiver aperture cover and other analyses as outlined in this chapter.

Table 6.1 Yearly WGA system energy predictions for Albuquerque using the component model in TRNSYS

Location	**TRNSYS model** Predicted Yearly Energy [kW-hr]	**Sandia model** Predicted Yearly Energy [kW-hr]
Daggett, CA	21293	**x**
Albuquerque, NM	19224	19281*

Boulder, CO	15101	**x**
San Fran, CA	13560	**x**
Madison, WI	9323	**x**
Seattle, WA	7653	**x**
St. Paul Is. AK	2023	**x**
*The Sandia prediction is for the WGA-1 system not the WGA-2 system used in the TRNSYS model The value from the reference was 17,353 kW-hrs in Albuquerque and this included a 90 % availability		

Table 6.2 Monthly predictions for the WGA system in Albuquerque using the component model in TRNSYS

	DNI Weighted Averages----------					
	wind	**sun elevation**	**Tamb**	**T,wet,bulb**	**E_net_tot**	**η_{System}**
Month	**[m/s]**	**degrees**	**[K]**	**[K]**	**[kW-hrs]**	**[-]**
January	4.7	23	278	270	1391	0.192
February	3.7	30	282	272	1297	0.187
March	5.8	34	284	274	1439	0.180
April	4.1	42	289	276	1725	0.183
May	4.6	47	295	279	1931	0.185
June	3.9	48	299	281	1931	0.186
July	4.4	51	302	281	1754	0.187
August	3.7	45	299	281	1614	0.184
September	3.2	39	297	280	1548	0.188
October	3.6	30	289	276	1781	0.192
November	2.8	25	282	272	1470	0.199
December	3.3	22	278	270	1342	0.194
Average	**4.0**	**36.3**	**289.5**	**276.1**	**1602**	**0.188**

6.1 Modifying the Receiver Aperture Diameter

The TRNSYS model was used to investigate the effect of varying the aperture diameter for the WGA system as shown in Table 6.3. A simulation using TMY-2 data for one year in Albuquerque predicted that the WGA system would produce 19,224 kW-hrs with the current 0.14 m aperture diameter design, and 19,336 kW-hrs per year with an optimal aperture diameter of 0.121 m. These values indicate that the system could produce 0.5 % more energy by optimizing the aperture diameter in Albuquerque. A comparison of the power produced using the current 0.14 m aperture diameter design to the power produced if the aperture diameter were optimized for other locations is shown in Table 6.3.

	d_ap=0.14[m]	Optimal		
	Net Power	Net Power	d_ap [m]	
	[kW-hr/yr]	[kW-hr/yr]	optimal	% improve
Daggett, CA	21293	21430	0.122	0.64
Albuquerque, NM	19224	19337	0.121	0.58
Boulder, CO	15101	15221	0.121	0.79
San Fran, CA	13560	13681	0.121	0.89
Madison, WI	9323	9423	0.12	1.07
Seattle, WA	7653	7737	0.121	1.09
St. Paul Is. AK	2023	2058	0.119	1.70

Table 6.3 Yearly predicted net power for optimal WGA system aperture diameters using TMY-2 data.

6.2 Receiver Cover versus no Cover

The TRNSYS model was also used to predict the change in net energy production with a transparent cover over the receiver aperture. Table 6.4 indicates the value for the location specific cover transmittance where the increased losses due to reflection when adding an aperture cover would be offset by the reduction in the receiver thermal losses. A receiver cover with a transmittance of 94 % in Albuquerque is predicted to produce as much power as the system operating without a receiver cover. If the receiver cover has a transmittance lower than 0.94, adding an aperture cover will result in a reduction in net power.

Table 6.4 Predicted cover transmittance values for the WGA system for equivalent energy production with or without a receiver aperture cover

	No Cover	With Cover	With Cover
	Net Power	Transmittance	Net Power
	[kW-hr/yr]	[-]	[kW-hr/yr]
Daggett, CA	21293	0.93	21319
Albuquerque, NM	19224	0.94	19223
Boulder, CO	15101	0.94	15071
San Fran, CA	13560	0.92	13537
Madison, WI	9323	0.92	9210
Seattle, WA	7653	0.94	7652
St. Paul Is. AK	2023	0.87	2028

6.3 Varying the Heater Head Temperature

The TRNSYS model accepts the heater head operating temperature and the temperature difference between the receiver and heater head temperature as inputs. The heater head temperature that results in the maximum net efficiency is a function of the receiver losses and the engine efficiency as shown in Figure 6-1. The current heater head operating temperature for the WGA system is 903 K and increasing this temperature has been prevented due to material limitations. The predicted theoretical optimal receiver heater head temperature for the WGA system with a 70 K temperature difference between the receiver and heater head temperature was 1200 K with a direct normal insolation (DNI) of 806 W/m^2, and 1400 K with a DNI of 1000

W/m^2. These two operating conditions were chosen while observing two separate hourly data points in the Albuquerque TMY-2 data set. The receiver losses are greater earlier in the day due to higher convection losses at lower solar elevation angles. The Stirling engine performance will typically increase with higher heater head temperatures; however, the Stirling engine efficiency drops at higher heater head temperatures for the 'Early-Day' simulation in Figure 6-1 due to the receiver efficiency declining to the point when the thermal input power to the engine is reduced and consequently the engine efficiency is reduced. The engine efficiency declines at lower thermal inputs as shown in Figure 6-1.

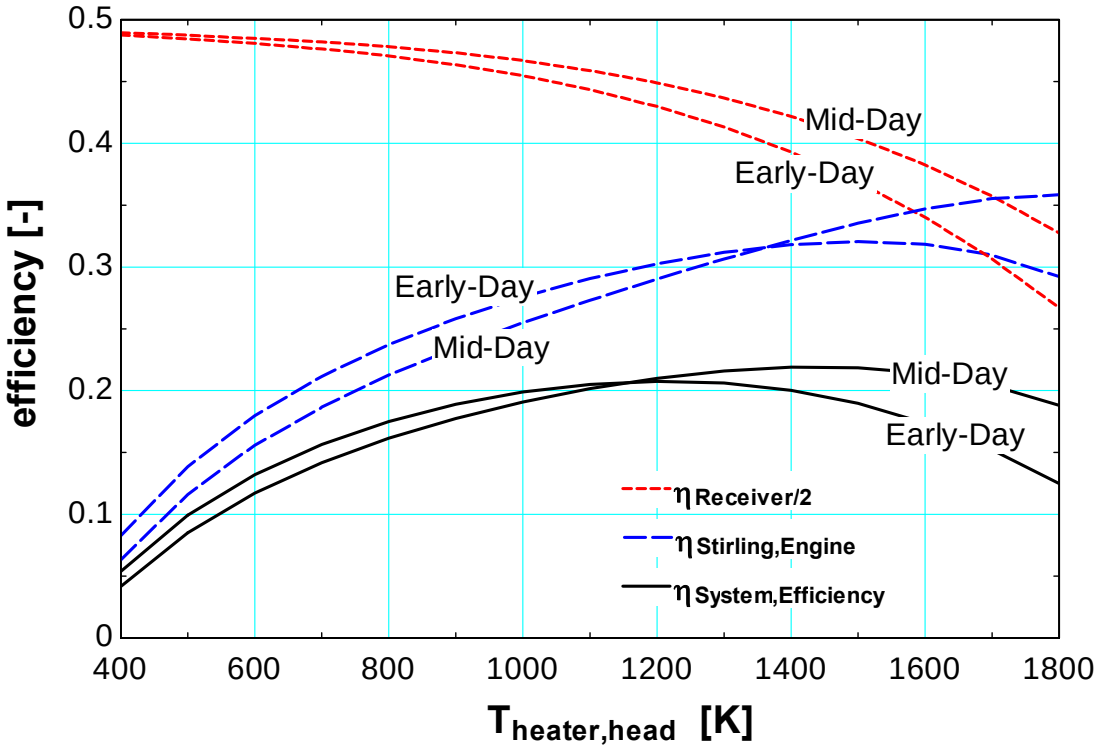

Figure 6-1 Predicted heater head optimal temperature dependent on time-of-day for the WGA system. Early day conditions: T_{amb} = -2.5°C, DNI = 806W/m^2. Late day conditions: T_{amb} = 4.2°C, DNI = 1001W/m^2

6.4 Fan Operating Speed

The power supplied to the radiator fan represents a significant fraction of the Stirling dish system parasitic power and it depends on the density of ambient air and the operating speed of the fan. For these reasons, an analysis was performed to determine the optimal speed of the fan based on various ambient and operating conditions. A fan curve was obtained for the 630 mm Woods fan used in the WGA system (Fläkt Woods). A prediction of the pressure drop across the radiator indicated that the volumetric flow rate of the Woods fan would be about 1.8 m^3/s (4000 CFM), and the corresponding parasitic power consumption was estimated at 410 W at an ambient temperature of 15°C, fan operating speed of 890 RPM, and normal atmospheric pressure (101 kPa). These values were then used to predict the fan parasitic power based on varying ambient conditions and fan operating speeds in the TRNSYS model. The fan operating speed that maximizes the system output power is location dependent as shown in Table 6.5.

Table 6.5 Optimal location dependent fan speeds and improvement over 800 rpm fan speed

	800 [rpm] Net Energy [kW-hr/yr]	Optimal Net Power [kW-hr/yr]	Fan Speed [rpm] optimal	Optimal % improve
Daggett, CA	19164	19641	510	2.49
Albuquerque, NM	17302	17614	550	1.80
Boulder, CO	13591	13909	520	2.34
San Fran, CA	12204	12686	460	3.95
Madison, WI	8391	8766	450	4.47
Seattle, WA	6888	7195	450	4.46
St. Paul Is. AK	1821	1960	440	7.63

6.5 Pump Operating Speed

A similar analysis to the fan was applied towards the optimal operating speed of the pump. An estimate was made for the pump consuming about 75 W of power at the operating speed of 1800 rpm (Andraka, 2007). The pump parasitic power is determined based on the flow rate of the pump and the properties of the cooling fluid used. The TRNSYS model incorporates the dimensionless pump power laws, in addition to determining the compression space temperature based on the capacitance rate and properties of the cooling fluid, so the net effect on system energy production can be found by varying the pump operating speed. The optimal constant speed pump was location dependent and found to be between 1250 and 1600 rpm which is slower than the 1800 rpm currently operated at. A summary of the optimal pump speeds and affect at improving system performance is shown in Table 6.6.

Table 6.6 Optimal location dependent pump speeds and improvement over an 1800 rpm pump speed

	1800 [rpm] Net Energy [kW-hr/yr]	Optimal Net Energy [kW-hr/yr]	Pump Speed [rpm] optimal	% improve
Daggett, CA	19164	19190	1550	0.14
Albuquerque, NM	17302	17323	1600	0.12
Boulder, CO	13591	13622	1500	0.23
San Fran, CA	12204	12240	1450	0.29
Madison, WI	8391	8426	1400	0.42
Seattle, WA	6888	6918	1400	0.44
St. Paul Is. AK	1821	1839	1250	0.99

6.6 Cooling Fluid

An analysis was made to determine how the system performance would be changed by using a different cooling fluid than a 50 % mix of ethylene-glycol and water. The change in cooling fluid affects the capacitance rates and therefore the cooler and radiator effectiveness in the TRNSYS model, which has an impact on altering the compression space temperature and therefore engine performance. The pump parasitic power is also altered by the cooling fluid properties in the TRNSYS model since the pump power is dependent on the density of the fluid

and the viscosity as shown in Figure 6-2. The expression used to correct the pump power based on the viscosity of the fluid is given in Equation (5.1) which was derived from values in White (2003). This expression would only be valid for viscosities of fluids similar to glycol within the range of operating temperatures for these systems. The terms $P_{pump,total}$ is the total pump power including the viscosity multiplier ($visc_{multiplier}$), P_{pump} is the pump power taking into account the density of the fluid, $\mu_{cool,fluid}$ is the viscosity of the cooling fluid, and $\mu_{water,test}$ is the viscosity of water for the pump during test conditions.

$$P_{pump,total} = P_{pump} * visc_{multiplier} \tag{5.1}$$

$$visc_{multiplier} = 1/\left(1.01178 - 0.011778 \cdot \mu_{div}\right) \tag{5.2}$$

$$\mu_{div} = \mu_{cool,fluid} / \mu_{water,test} \tag{5.3}$$

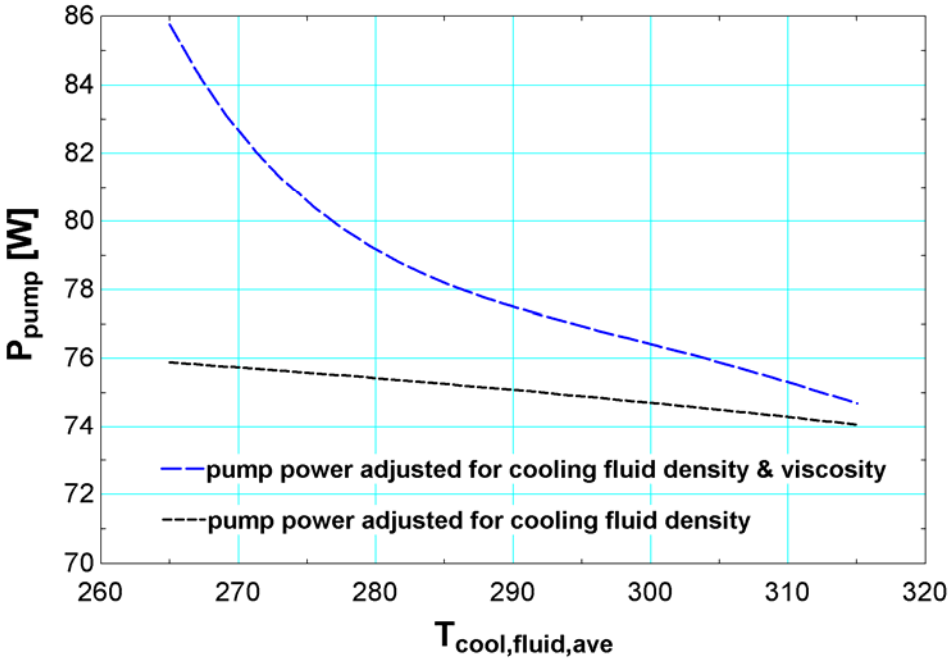

Figure 6-2 Parasitic pump power as the density and viscosity of 50 % ethylene glycol changes

Overall, using water would have about a 0.20 % improvement according to the TRNSYS model even though water would not be a reasonable fluid with a higher freezing point than glycol. A 25 % glycol mixture would still improve the net system performance by about 0.10 % as shown in Table 6.7. If freezing would not be an issue, making a switch from 50 % to 25 % ethylene-glycol would be a simple way to get a small improvement in performance and monetary return.

Table 6.7 Improvement in net WGA system performance based on the radiator cooling loop fluid

			EG 50% baseline	EG 50% baseline
			% improve	% improve
	Daggett	Albuquerque	Daggett	Albuquerque
water	19204	17331	0.21	0.17
EG 50%	19164	17302	0.00	0.00
EG 25%	19190	17320	0.14	0.10
PG 50%	19167	17303	0.02	0.01
PG 25%	19193	17322	0.15	0.12

6.7 Cooling Tower

The TRNSYS model was used to analyze the improvement in system performance when using a cooling tower. A description of the cooling tower model can be found in chapter three. A theoretical analysis without using the TRNSYS component models was first performed to estimate how the Stirling dish system performance would improve based on the difference between the ambient dry bulb and wet bulb temperatures for Albuquerque, New Mexico, and Daggett, California. An average of the ambient dry bulb and wet bulb temperatures weighted for direct normal insolation (*DNI*) using Equation (5.4) and (5.5) was computed for every month in two locations as shown in Table 6.8. The performance of the WGA Stirling engine component in TRNSYS improves by approximately one percent for every four degrees Celsius the compression space temperature is reduced. Using a cooling tower in Daggett could improve the Stirling engine performance by 6 % in the summer, and close to 3 % during the winter. The larger increase in performance during the summer is notable since electric rates are often higher in the summer in locations where solar installations are being considered due to air conditioning loads.

$$T_{amb,ave} = \sum\left(DNI * T_{amb}\right) / \sum\left(DNI\right) \tag{5.4}$$

$$T_{wet,bulb,ave} = \sum\left(DNI * T_{wet,bulb}\right) / \sum\left(DNI\right) \tag{5.5}$$

Table 6.8 Theoretical improvement in WGA Stirling engine performance in two locations

Albuquerque, New Mexico

DNI Weighted Averages----------				theoretical
Month	Tamb	T,wet,bulb	T_diff	% improve
January	278	270	7.9	**2.0**
February	282	272	9.2	**2.3**
March	284	274	10.5	**2.6**
April	289	276	12.8	**3.2**
May	295	279	15.8	**4.0**
June	299	281	18.5	**4.6**
July	302	281	20.1	**5.0**
August	299	281	18.5	**4.6**
September	297	280	17.2	**4.3**
October	289	276	12.9	**3.2**
November	282	272	9.2	**2.3**
December	278	270	7.9	**2.0**

Daggett, California

DNI Weighted Averages----------				theoretical
Month	Tamb	T,wet,bulb	T_diff	% improve
January	285	274	10.7	**2.7**
February	289	276	12.6	**3.2**
March	291	277	13.6	**3.4**
April	294	279	15.5	**3.9**
May	299	281	18.5	**4.6**
June	304	282	21.8	**5.5**
July	307	283	24.3	**6.1**
August	305	283	22.8	**5.7**
September	303	282	21.0	**5.3**
October	296	280	16.9	**4.2**
November	290	277	13.1	**3.3**
December	285	274	10.7	**2.7**

The TRNSYS Stirling dish system components were then used to compare how the predicted net yearly performance improved using a cooling tower in Daggett, California. Three different tower designs were analyzed with an approach of 1°C and a range of 0.5°C, an approach of 3°C and range of 2°C, and an approach of 5°C and range of 4°C. The approach is defined as the temperature difference between the ambient wet bulb temperature and the exit tower cooling fluid, and the range is defined as the difference in temperature between the inlet and outlet cooling fluid to the cooling tower. The design dry bulb and wet bulb temperature used as inputs to the cooling tower model were respectively 37°C and 18°C.

A summary of the results of the cooling tower analysis for the three different tower designs simulated in the model are shown in Figure 6-3. A tower with a one Celsius approach would likely be unrealistic and too expensive, but it provides an indication of the maximum increase in net system efficiency for a Stirling dish system in Daggett, California. The Stirling dish system with a 5°C approach and 4°C range for the cooling tower would potentially be close to the optimal design. The design with a 5°C approach indicated a net system performance improvement of around two percent with a pipe diameter around one third of a meter for a system with a field of 25 10 kW WGA dishes. The parasitic power from the cooling tower fans was not included in the analysis in Figure 6-3, so a natural draft cooling tower was considered. An economic analysis would have to be performed to determine if a central cooling tower would be more cost effective than using a radiator and fan on each system.

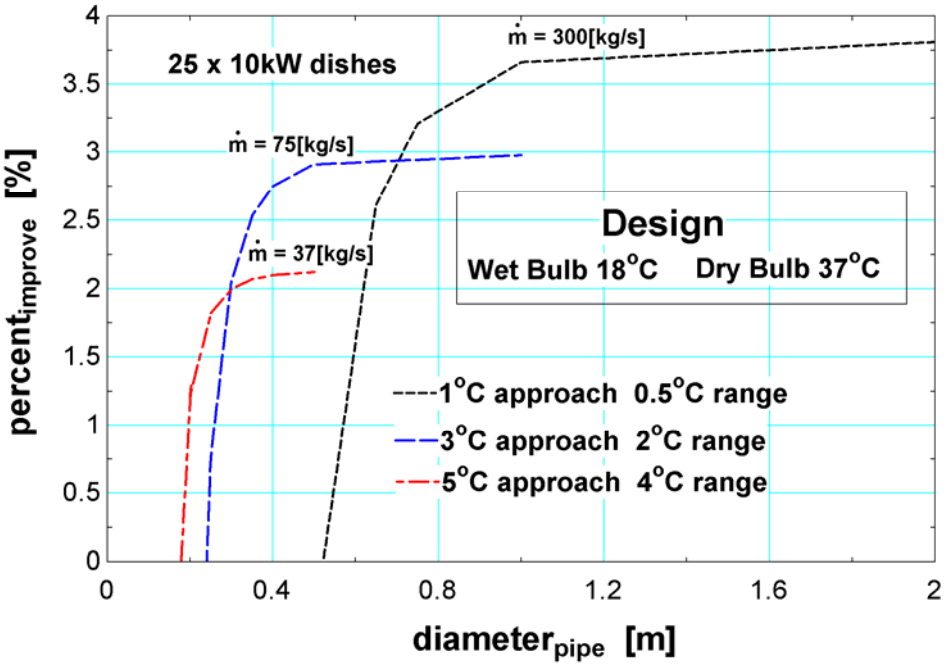

Figure 6-3 Predicted performance improvement using a cooling tower for a specified pipe diameter

6.8 System Efficiency and Optimization

An analysis was performed using the TRNSYS model to determine the system efficiency of the Stirling dish system and the net economical impact of optimizing the WGA system. The maximum location specific system efficiency was predicted to be 18.8 % in Albuquerque, New Mexico, and the lowest system efficiency was predicted to be 14.7 % in Alaska as shown in Table 6.9. The system efficiency could be improved by more than half a percent by optimizing the current design for the operating speeds of the fan and pump, and the aperture diameter. At an electrical rate of $0.10 per kW-hr, optimizing the fan and pump operating speeds in addition to the aperture diameter would increase the electrical earnings by several million dollars in a large Stirling dish field.

Table 6.9 WGA (yearly) system optimization for the fan speed, pump speed, and aperture diameter and the yearly economical impact for electricity at $0.10 per kW-hr

	Location	Current	Optimal	Current	Optimal			500MW
	Net Energy	Net Energy	Net Energy	System Eta	System Eta	Net Energy	per dish	50000 dishes
	[kW-hr]	[kW-hr]	[kW-hr]	[-]	[-]	% improve	$ increase	$ increase
Daggett, CA	115985	21293	22013	0.184	0.190	3.38	$ 72.00	$ 3,600,000
Albuquerque, NM	102391	19224	19723	0.188	0.193	2.60	$ 49.89	$ 2,494,444
Boulder, CO	81513	15101	15631	0.185	0.192	3.51	$ 53.00	$ 2,650,000
San Fran, CA	75224	13560	14281	0.180	0.190	5.32	$ 72.11	$ 3,605,556
Madison, WI	52600	9323	9898	0.177	0.188	6.16	$ 57.44	$ 2,872,222
Seattle, WA	43008	7653	8122	0.178	0.189	6.13	$ 46.89	$ 2,344,444
St. Paul Is. AK	13799	2023	2238	0.147	0.162	10.60	$ 21.44	$ 1,072,222

7 Conclusion and Further Studies

A computational model was created and used to investigate the effects of system design parameters for a Stirling dish system. The model, implemented in TRNSYS, can be used to predict how a system design change influences the net energy production in a specific location using input weather data files. Compared with three years of 10 minute averaged data from the WGA system, the Stirling dish model implemented in TRNSYS predicted the net energy production and power more closely than existing models. The model is expected to have greater accuracy predicting the system performance in different locations due to the additional properties of the wind velocity, sun elevation angle, and altitude. This model ideally will be used by designers to optimize design parameters and by researchers or utilities to obtain a better representation of a Stirling dish systems location specific performance.

Future work could be to research Brayton cycle engines and determine how a performance curve could be made for the gas turbine for a TRNSYS component. The Beale number Stirling engine Stirling engine model corrected with the maximum power temperature fraction could potentially be applied to a Brayton cycle engine. A performance and economic analysis using gas turbines instead of Stirling engines in a closed cycle using hydrogen or helium as the working fluid would be of value. Analyzing a combined cycle using gas turbines in place of the Stirling engines and a centrally located steam turbine in the bottoming cycle may also be a valuable design study. Gas turbines can be purchased off-the-shelf so they likely would be less expensive than Stirling engines on a large scale.

References

Aleksandravieius, Tautvydas Antanas. "Influence of Efficiency of the Regenerator upon Stirling Engine Cycle Performance." Proceedings of the 5th European Stirling Forum 2000. Osnabruck, Germany.

Allen, D. I., and W. A. Tomazic. Hot Piston Ring Tests. Vol. NASA TM-100256, 1987.

Andraka, Charles E., et al. "Solar Heat Pipe Testing of the Stirling Thermal Motors 4-120 Stirling Engine." IEEE.DE-AC04-94AL85000 (1996).

Andraka, Charles E. "Alignment Strategy Optimization Method for Dish Stirling Faceted Concentrators." Energy Sustainability 2007. Long Beach, CA, June 27-30.

--- Solar Heat-Pipe Receiver Wick Modeling. Vol. SAND98-2836C. Sandia National Laboratory, 1998.

Andraka, Charles. Teleconference with the Solar Labs from NREL and Sandia National Laboratory, 5/18/2007.

Bratt, Christer, and Hans-Goran Nelving. "Development and Production of Stirling Engines for Submarine and Solar Application at Kockums." Proceedings of the 5th European Stirling Forum 2000. Osnabruck, Germany.

Clausing, A. M., J. M. Waldvogel, and L. D. Lister. "Natural Convection from Isothermal Cubical Cavities with a Variety of Side Facing Apertures." Journal of Heat Transfer 109 (1987): 407-412.

Clausing, A. M. "Analysis of Convective Losses from Cavity Solar Central Receivers." Solar Energy 27.4 (1981): 295-300.

---. "Convective Losses from Cavity Solar Receivers-Comparisons between Analytical Predictions and Experimental Results." Journal of Solar Energy Engineering 105 (1983): 29-33.

Davenport, Roger L., and Robin W. Taylor. Operation of a Hybrid Solar Dish/Stirling System. Science Applications International Corp. (SAIC), 2005.

"Department of Energy Concentrating Solar Website." <http://www.energylan.sandia.gov/sunlab/overview.htm>.

Diver, Richard B., et al. "The Advanced Dish Development System Project." Washington D.C., April 21-25.

Duffie, John A., and William A. Beckman. Solar Engineering of Thermal Processes. Third ed. New Jersey: John Wiley & Sons, Inc., 2006.

El-Wakil, M. M., ed. Powerplant Technology. New York: McGraw-Hill, Inc., 1984.

Farell, R.A. et al. Automotive Stirling Engine Development Program. Vol. NASA CR-180839, 1988.

Feidt, M., et al. "Optimal Allocation of Heat Exchanger Inventory Associated with Fixed Power Output Or Fixed Heat Transfer Rate Input." International Journal of Applied Thermodynamics 5.1 (March 2002): 25-36.

Finkelstein, Theodor. "Evaluation and Simulation of the Stirling Engine and of its Performance." Proceedings of the 5th European Stirling Forum 2000. Osnabruck, Germany.

--- "Specific Performance of various Stirling Engine Designs." Proceedings of the 4th European Stirling Forum 1998. Osnabruck, Germany.

"Flakt Woods website." 2007. <http://www.flaktwoods.com/169/0/1/6f1fdffd-7f1f-4cad-be50-5da7a62d2dc5>.

Fujii, I., ed. From Solar Energy to Mechanical Power. New York: Harwood Academic Publishers, 1990.

Geng, S. M. Calibration and Comparison of the NASA Lewis Free-Piston Stirling Engine Model Prediction with RE-1000 Test Data. Vol. NASA TM-89853, 1987.

Halford, C., et al. "The UNLV Solar Dish-Stirling Project." Solar 2002. Reno, Nevada.

Harris, James A., and Terry G. Lenz. "Thermal Performance of Solar Concentrator/Cavity Receiver Systems." Solar Energy 34.No. 2 (1985): 133-42.

Hirata, Koichi. "Koichi Hirata Stirling Engine Homepage." 9-5-2002 <http://www.bekkoame.ne.jp/~khirata/>.

Hogan Jr., Roy E. AEETES - A Solar Reflux Receiver Thermal Performance Numerical Model. Vol. SAND91-1280. Sandia National Laboratory, 1991.

Howell, John R. " A Catalog of Radiation Heat Transfer Configuration Factors." University of Texas at Austin. <http://www.me.utexas.edu/~howell/tablecon.html>.

"IEA SolarPACES." 2007. <http://www.solarpaces.org/CSP_Technology/docs/solar_dish.pdf>.

Igo, John, and Charles E. Andraka. "Solar Dish Field System Model for Spacing Optimization." Energy Sustainability 2007. Long Beach, CA, June 27-30.

Incropera, Frank P., and David P. DeWitt, eds. Fundamentals of Heat and Mass Transfer. Fifth ed.John Wiley & Sons, Inc., 2002.

Jaffe, Leonard D. "Optimization of Dish Solar Collectors." Journal of Energy 7.6 (1983): 684-694.

Kalogirou, Soteris, A. "Entroypy Generation Minimization of Imaging Concentrating Solar Collectors." ISES Solar World Congress 2003. Gothenburg, Sweden, June 14-19.

Keveney, Matt. "Animated Engines." 2001. <http://www.keveney.com/Engines.html>.

Klein et al., *TRNSYS, A Transient System Simulation Program, User's Manual,* Version 16, Solar Energy Laboratory, University of Wisconsin-Madison (2006).

Koscak-Kolin, S., et al. "Influence of the Compression Ratio on Stirling and Otto Cycle." Proceedings of the 5th European Stirling Forum 2000. Osnabruck, Germany.

Kuhl, H. D., and S. Schulz. "A Contribution to the Systematic Classification of Regenerative Cycles." Proceedings of the 4th European Stirling Forum 1998. Osnabruck, Germany.

Laing, Doerte, and Michael Reusch. "Hybrid Sodium Heat Pipe Receivers for the SBP Dish/Stirling Systems." Proceedings of the 4th European Stirling Forum 1998. Osnabruck, Germany.

Leitner, Dr Arnold. "SkyFuel website." 2007. <www.skyfuel.com>.

Lewandowski, Edward J., and Timothy F. Regan. Overview of the GRC Stirling Convertor System Dynamic Model. Vol. NASA/CR-2004-213366. Second International Energy Conversion Engineering Conference: November 2004.

Liebfried, U., and J. Ortjohann. "Convective Heat Loss from Upward and Downward-Facing Cavity Solar Receivers: Measurements and Calculations." Journal of Solar Energy Engineering 117 (1995): 75-84.

Lovegrove, K., et al. Paraboloidal Dish Solar Concentrators for Multi-Megawatt Power Generation, 2003.

Ma, Richard Y. Wind Effects on Convective Heat Loss from a Cavity Receiver for a Parabolic Concentrating Solar Collector. Vol. SAND92-7293. U.S.: Sandia National Laboratory, 1993.

Makhkamov, Kh, and D. B. Ingham. "Determination of the Performance of a Stirling Engine as used in a Dish/Stirling System." Proceedings of the 4th European Stirling Forum 1998. Osnabruck, Germany.

---. "Heat Transfer in a Cavity-Type Heat Receiver of a Stirling Engine as used in a Dish/Stirling System." Proceedings of the 4th European Stirling Forum 1998. Osnabruck, Germany.

Mancini, Thomas R. "Solar-Electric Dish Stirling System Development." Proceedings of the 4th European Stirling Forum 1998. Osnabruck, Germany.

Mancini, Thomas, et al. "Dish-Stirling Systems: An Overview of Development and Status." Journal of Solar Energy Engineering 125 (May 2003) <http://scitation.aip.org/getpdf/servlet/GetPDFServlet?filetype=pdf&id=JSEEDO0001250000020 00135000001&idtype=cvips&prog=normal>.

McMahan, Andrew C. "Design & Optimization of Organic Rankine Cycle Solar-Thermal Powerplants." Mechanical Engineering UW-Madison, 2006.

MaMahan, A., Klein, S.A., and Reindl, D.T., “A Finite-Time Thermodynamic Framework for Optimizing Solar-Thermal Power Plants,” ASME J. Solar Energy Engineering, Vol. 129 p. 355, 2007

Mehdizadeh, Seraj N., H. Lemrani and P. Stouffs. "Dynamic Modelling of Stirling Engines using a Simulation Computational Environment." Proceedings of the 3rd European Stirling Forum 1996. Osnabruck, Germany.

"Ministerio De Educación Y Ciencia Website." <http://www.psa.es/webeng/instalaciones/discos.html>.

Moran, Michael J., and Howard N. Shapiro, eds. Fundamentals of Engineering Thermodynamics. 5th ed.John Wiley & Sons, Inc., 2004.

Osborn, D.B., 1980, “Generalized Shading Analysis for Paraboloidal Collector Fields”, Paper Number 80-Pet-33.

Organ, Allan J., Justin N. Jones and Kaare Gether. "Characterization of Stirling Engine Pumping Losses." Proceedings of the 4th European Stirling Forum 1998. Osnabruck, Germany.

Organ, Allan J., and Peter Maeckel. "Connectivity and Regenerator Thermal Shorting." Proceedings of the 3rd European Stirling Forum 1996. Osnabruck, Germany.

---. "Gas Partical Temperature Loci for Exploring Stirling Machine Operation." Proceedings of the 3rd European Stirling Forum 1996. Osnabruck, Germany.

Organ, Allan J. "Classic Regenerator Theory - A Neglected Resource." Proceedings of the 4th European Stirling Forum 1998. Osnabruck, Germany.

---. "The Great Stirling Cycle Simulation Fraud." Proceedings of the 3rd European Stirling Forum 1996. Osnabruck, Germany.

---. "Regenerator Analysis Simplified." Proceedings of the 5th European Stirling Forum 2000. Osnabruck, Germany.

Paitoonsurikarn, S., and K. Lovegrove. "Numerical Investigation of Natural Convection Loss in Cavity-Type Solar Receivers." Solar 2002 Australian and New Zealand Solar Energy Society.

---. "On the Study of Convection Loss from Open Cavity Receivers in Solar Paraboloidal Dish Applications." ANZSES 2003. November 26-29.

Paitoonsurikarn, S., T. Taumoefolau and K. Lovegrove. "Estimation of Convection Loss from Paraboloidal Dish Cavity Receivers." Solar 2004:Life, the Universe and Renewables.

Petrescu, Stoian, et al. "Application of the Direct Method to Irreversible Stirling Cycles with Finite Speed." International Journal of Energy Research 26 (2002): 589-609.

Petrescu, Stoian, et al. "A Method for Calculating the Coefficient for the Regenerative Losses in Stirling Machines." Proceedings of the 5th European Stirling Forum 2000. Osnabruck, Germany.

Petrescu, Stoian, et al. "Analysis and Optimization of Solar-Dish/Stirling Engines." Solar 2002. Reno, Nevada, June 15-20.

Port, Otis. "Another Dawn For Solar Power." Business Week. August 22, 2006 <http://www.businessweek.com/magazine/content/04_36/b3898119_mz018.htm>.

"ReflecTech." 2007. <http://www.reflectechsolar.com/>.

Reuters Health Information Online. New York, 2006. Visited 2007. <http:www.medscape.com/viewarticle/521680>.

Romero, Vicente J. A Software Package for Facilitated Optical Analysis of 3-D Distributed Solar Energy Concentrators. Vol. SAND91-2238. Sandia National Laboratory, 1994.

RSMeans. “Means Building Construction Cost Data,” 65th edition, 2007.

Ryu, S., T. Seo and Y. H. Kang. "Thermal Performance of Receivers for a Multifaceted Parabolic Dish Solar Thermal Collector." ISES 2001 Solar World Congress. Australia.

Seo, Taebeom, Siyoul Ryu and Yongheock Kang. "Thermal Performance of the Receivers for the Dish-Type Solar Energy Collecting System of Korea Institute of Energy Research." Solar 2000. Madison, Wisconsin, June 16-21.

Sharke, Paul. "Sun Rises On Big Solar." January 9, 2006 <http://www.designnews.com/article/CA6294752.html?ref=nbra&text=sun+rises+on+solar>.

Siegel, Andre. "Experimental Investigations on the Heat Transfer Behaviour of Wire Mesh Regenerators in an Oscillating Flow." Proceedings of the 5th European Stirling Forum 2000. Osnabruck, Germany.

"Spectrolab website." <http://www.spectrolab.com/prd/terres/cell-main.htm>.

Stine, W. B., and Richard B. Diver. A Compendium of Solar Dish/Stirling Technology. Vol. SAND93-7026., 1994.

Stine, W. B., and Frank Kreith, eds. Mechanical Engineering Handbook. Boca Raton: CRC Press LLC, 1999.

Stine, William B., and Raymond W. Harrigan, eds. Solar Energy Fundamentals and Design with Computer Applications. New York: Wiley-Interscience, 1985.

Stine, William B., and A. A. Heckes. "Energy and Availability Transport Losses in a Point-Focus Solar Concentrator Field." Journal of Solar Energy Engineering 109 (1987): p. 205-209.

Stine, William B., and C. G. McDonald. "Cavity Receiver Convective Heat Loss." International Solar Energy Society, Solar World Congress 1989. Kobe, Japan, September 4-8.

---. "Cavity Receiver Heat Loss Measurements." 10th Annual ASME Solar Energy Conference. Denver, Colorado, April 10-14.

Stine, William B. "Experimentally Validated Long-Term Energy Production Prediction Model for Solar Dish/Stirling Electric Generating Systems." IECEC'95.

"Stirling Energy Systems (SES)." <http://www.stirlingenergy.com/default.asp>.

"STM Power website." <http://www.stmpower.com/>.

Stone, Kenneth W., et al. "Results of the Boeing/DOE Phase I Stirling Engine Project." Solar Engineering 2000. Madison, June 16-21.

Stone, Kenneth W., et al. "Analysis of Five Years of Field Performance of the Amonix High Concentration PV System." Powergen 2006. Las Vegas, April. <http://www.amonix.com/technical_papers.html>.

Stone, Kenneth, et al. "Four Years of Operation of the Amonix High Concentration Photovoltaic System at Arizona Public Service Utility." Solar Engineering 2004. Portland, Oregon, July 11-14, 2004.

Stone, Kenneth, et al. "SES/Boeing Dish Stirling System Operation Presented at 2001 Solar Forum in." Washington D.C., April 21-25.

Taumoefolau, T., and K. Lovegrove. "An Experimental Study of Natural Convection Heat Loss from a Solar Concentrator Cavity Receiver at Varying Orientation." Solar 2002 Australian and New Zealand Solar Energy Society.

Taumoefolau, T., et al. "Experimental Investigation of Natural Convection Heat Loss from a Model Solar Concentrator Cavity Receiver." Journal of Solar Energy Engineering 126 (2004): p. 801-807.

Teagan, Peter W. Review: Status of Markets for Solar Thermal Power Systems, May 2001. <http://www.energylan.sandia.gov/sunlab/pdfs/adlitt1.pdf>.

Thermal Energy System Specialists (TESS). Type510: Closed Circuit Cooling Tower TRNSYS Component. Last modified: October 2005.

Thomas, Bernd, and Frank Bolleber. "Evaluation of 5 Different Correlations for the Heat Transfer in Stirling Engine Regenerators." Proceedings of the 5th European Stirling Forum 2000. Osnabruck, Germany.

Thomas, Bernd. "Thermodynamische Mitteltemperatur - Eine Methode Zur Vereinfachten Erfassung Des Adiabaten Verlustes in Stirling Maschinen." Proceedings of the 4th European Stirling Forum 1998. Osnabruck, Germany.

Ulmer, Steffen, et al. "Beam Characterization and Improvement with a Flux Mapping System for Dish Concentrators." Solar 2002 Sunrise on the Reliable Energy Economy. Reno, Nevada, June 15-20.

"University of Delaware website." 2007. <http://www.udel.edu/PR/UDaily/2008/jul/solar072307.html>.

Urieli, Israel, and David Berchowitz, eds. Stirling Cycle Engine Analysis. First ed. Bristol: Adam Hilger Ltd, 1984.

Urieli, Israel. "Israel Urieli Course Homepage." 1-1-2007. <http://www.ent.ohiou.edu/~urieli/stirling/me422.html>.

Walker, Graham. Stirling Engines. New York: Oxford University Press, 1980.

WGAssociates. Introduction to WGAssociates and Solar Dish/Stirling Power Systems. <http://www.energylan.sandia.gov/sunlab/PDFs/WGA.pdf>.

White, Frank M., ed. Fluid Mechanics. Fifth ed. Boston: McGraw Hill, 2003.

Wilson, Scott D., et al. Multi-D CFD Modeling of a Free Piston Stirling Convertor at NASA Glenn. NASA/TM-2004-213351 ed. Second International Energy Conversion Engineering Conference, October 2004.

Wright, Richard T. Environmental Science: Towards a Sustainable Future. 9th edition, Pearson/Prentice Hall, 2005.

Yeh, K. C., G. Hughes and K. Lovegrove. "Modelling the Convective Flow in Solar Thermal Receivers." ANZSES 2005.

Appendix A: TRNSYS Model Descriptions

A Stirling dish system model was created in TRNSYS to determine the location dependent performance of the SES, WGA, SBP, and the SAIC systems. Separate components were created for the parabolic collector, receiver, Stirling engine, and the parasitic power. These components can be interchanged to have different manufacturers for every component by choosing which system to use, or the user can input custom variables for every parameter that are not characteristic of a specific system. The model is capable of predicting the system performance if there are changes in the mirror reflectivity, heater head temperature, fan operating speed, cooler or radiator effectiveness, or the receiver aperture diameter. The model also has the capability to predict how the system performance changes if a direct illumination (DIR) or reflux receiver is used, and if a hybrid receiver is used with a cover over the receiver aperture. The TRNSYS model also predicts how the system performance changes based on location dependent variables consisting of the wind velocity, direct normal insolation, ambient temperature, ambient pressure (altitude), and the sun elevation angle.

The parameters listed before the 'Manufacturer' parameter in the TRNSYS model can be modified to observe how the manufacturer specific system performance varies. Changing these parameters allows one to determine optimal parameters based on the location specified for the TMY-2 data. The parameters listed after the 'Manufacturer' parameter should only be modified if a hypothetical or new Stirling dish components are to be simulated. In this case, the 'Manufacturer' parameter should be set to "5-Other." The coefficients for the engine efficiency curve have been specified for each system assuming specific parameters that follow the 'Manufacturer' parameter.

TRNSYS Parabolic Collector Model

The parabolic concentrator model predicts the radiative power intercepted by the receiver ($P_{in,rec}$) based on the direct normal insolation (I_{DNI}), projected area of the mirror (A_{proj}), wind cut-out velocity, intercept factor ($\varphi_{\text{int,fac}}$), mirror reflectivity (ρ_{ref}), and the shading factor (φ_{shade}) as given by Equation (A.1)

$$P_{in,rec} = I_{DNI} \cdot A_{proj} \cdot \rho_{ref} \cdot \varphi_{\text{int,fac}} \cdot \varphi_{shade} \qquad \text{(A.1)}$$

The wind cut-out velocity is a user-specified value indicating the wind speed at which the parabolic concentrator will be sent into a stow position to prevent wind damage. The shading factor (φ_{shade}) is determined using theory from Osborn (1980). The shading factor is a function of the number of parabolic concentrators, the collector diameter, and the North-South and East-West collector separation distance.

The intercept factor ($\varphi_{\text{int,fac}}$) in Equation (A.1) is the fraction of energy reflected from the parabolic concentrator that enters the receiver aperture. The TRNSYS model uses theory from Stine and Harrigan (1985) and requires as an input the intercept factor for a specific receiver aperture diameter, focal length, and collector diameter. The model then determines the total collector error (σ_{tot}) in mille-radians by iterating Eq. (A.2) with a guess value for the total

collector error until the appropriate value for the input of the intercept factor is found. Once the total concentrator error is determined, it can be used to obtain a new intercept factor for a different receiver aperture diameter using the same theory.

The terms $P_{intercept,tot}$ is the total power intercepted by the receiver, $P_{reflect,tot}$ is the total power reflected by the collector, Γ is the intercept factor for a specific differential ring evaluated at the ring-specific rim angle (ψ). The total rim angle at the collector perimeter is given by ψ_{rim}, I_{DNI} is the direct normal insolation, f is the focal length of the mirror, and A_{proj} is the projected area of the mirror. The ring specific intercept factor (Γ) is a function of the total error (σ_{tot}) as shown in Equations (A.3) and (A.4). The terms $Q(n)$ is a function of the number of standard deviations (n) described in Stine and Harrigan (1985), d_{ap} is the receiver aperture diameter, and p is the length between the foci and the specific differential ring on the collector. The concentrator model, combined with the receiver model described below, allows an optimal receiver aperture diameter to provide the greatest solar net energy transfer to the Stirling engine to be found.

$$\varphi_{\text{int,fac}} = \left(P_{intercept,tot}\right) \Big/ \left(P_{reflect,tot}\right) = \left(\sum_{\psi=0^0}^{\psi_{\text{rim}}} \frac{\Gamma \cdot 8\pi \cdot I_{DNI} \cdot f^2 \cdot \sin(\psi) \cdot \Delta\psi}{\left(1+\cos(\psi)\right)^2} \right) \Big/ \left(I_{DNI} \cdot A_{proj}\right) \qquad \text{(A.2)}$$

$$\Gamma = 1 - 2 \cdot Q(n) \qquad \text{(A.3)}$$

$$n = 2/\sigma_{tot} \cdot \tan^{-1}\left(d_{ap} \cdot \cos(\psi)/(2 \cdot p)\right) \qquad \text{(A.4)}$$

The TRNSYS model automatically proceeds through the following steps to find the intercept factor based on the diameter of the receiver aperture for specific collector systems:

1. Solve for the collector rim angle based on the collector focal length and diameter
2. Guess a small value for the total collector error
3. Solve for the number of standard deviations for a specific rim angle (differential ring) based on the guess value for the total collector error
4. Solve for the intercept factor for a specific rim angle in the collector based on the number of standard deviations for the rim angle
5. Solve for the total power reflected from the differential ring
6. Determine the total power intercepted by the receiver for the specific rim angle
7. Sum up the total power reflected over the entire collector (summation of #5)
8. Sum up the total power intercepted by the receiver for the entire collector (sum #6)
9. Divide #8 by #7
10. If #9 is less than the appropriate intercept factor, then guess a larger value for the total collector error in #2 and repeat steps #3 through #10
11. The total collector error is solved to give the correct intercept factor for the one data point measured at a specific aperture diameter
12. Once the total collector error is determined, the previous steps are modified slightly and the total collector error is used to determine what the new intercept factor is for a different aperture diameter

<u>Collector Parameters</u>

1. Receiver (not collector) aperture diameter [-]

2. Mirror reflectivity [-]
3. Number of collectors North-South [-]
4. Number of collectors East-West [-]
5. Dish separation distance North-South [m]
6. Dish separation distance East-West [m]
7. Manufacturer [1-SES, 2-WGA, 3-SBP, 4-SAIC, 5-Other]
8. Wind stow speed [m/s]
9. Projected area of the mirror [m^2]
10. Insolation cut in [W/m^2]
11. Test receiver aperture diameter for the test intercept factor [m]
12. Test intercept factor [-]
13. Test focal length of the mirror [m]
14. Total area of the mirror [m^2]

Collector Inputs

1. Direct normal insolation [$kJ/hr\text{-}m^2$]
2. Ambient temperature [°C]
3. Wind speed [m/s]
4. Sun zenith angle [degrees]
5. Atmospheric pressure [Pa]
6. Solar azimuth angle [degrees]

Collector Outputs

1. Collector output power [kW]
2. Ambient temperature [°K]
3. Atmospheric pressure [Pa]
4. Wind speed [m/s]
5. Sun elevation angle [radians]
6. Collector losses [kW]
7. Efficiency of the collector [-]
8. Number of collectors [-]
9. Direct normal insolation [W/m^2]
10. Insolation cut in [W/m^2]
11. Input power to the receiver [kW]
12. Receiver intercept factor [-]
13. Receiver aperture diameter [m]
14. Input power to the collector [kW]
15. Dish separation distance North-South [m]
16. Dish separation distance East-West [m]
17. Shading factor [-]

TRNSYS Receiver Model

The TRNSYS receiver model computes the thermal input power to the Stirling engine by subtracting the receiver thermal losses due to conduction, convection, and radiation from the total power intercepted by the receiver as shown in Equation (A.5). The conduction losses ($\dot{q}_{cond}$) through the receiver housing are minimal. The natural convection coefficient used for the receiver cavity is location and time-of-day dependent and is determined from the Nusselt number correlation by Stine and McDonald (1989) in Equations (A.6) and (A.7) with the interior cavity diameter parallel to the aperture as the characteristic length. The forced convection heat transfer coefficient for receiver cavity is based on Ma (1993) as shown in Equation (A.8). The total convection heat transfer coefficient according to Ma is given by Equation (A.9) with the natural convection coefficient derived from Equation (A.6). The total receiver heat loss rate due to convection is given by Equation (A.10) where A_{cav} is the total surface area of the cavity interior.

$$P_{in,SE} = P_{in,rec} - q_{rad,reflect} - \left(\dot{q}_{cond} + \dot{q}_{conv,tot} + \dot{q}_{rad,emit}\right)_{losses} \quad \text{(A.5)}$$

$$Nu_{nat,conv} = 0.088 \cdot Gr^{1/3} \cdot \left(T_{cav}/T_{amb}\right)^{0.18} \cdot \left(\cos\theta\right)^{2.47} \cdot \left(d_{ap}/d_{cav}\right)^{S} \quad \text{(A.6)}$$

$$S = -0.982 \cdot \left(d_{ap}/d_{cav}\right) + 1.12 \quad \text{(A.7)}$$

$$h_{forced} = 0.1967 \cdot v^{1.849} \quad \text{(A.8)}$$

$$h_{total,convection} = h_{natural} + h_{forced} \quad \text{(A.9)}$$

$$\dot{q}_{conv,tot} = h_{total,convection} \cdot A_{cav} \cdot \left(T_{cav} - T_{amb}\right) \quad \text{(A.10)}$$

The term $P_{in,SE}$ in Equation (A.5) represents the thermal input power to the Stirling engine while $\dot{q}_{conv,tot}$, $\dot{q}_{rad,emit}$, and $\dot{q}_{rad,reflect}$ represent the rate of heat loss from the receiver by convection (natural and forced), emitted radiation out of the receiver aperture, and the reflected radiation out of the aperture, respectively. The quantity, $Nu_{nat,conv,}$ in Equation (A.6) represents the free convection Nusselt number with the interior cavity diameter as the characteristic length. Gr is the Grashof number using the interior cavity diameter as the characteristic length, T_{cav} is the average temperature of the interior cavity walls, T_{amb} is the ambient temperature, θ is the sun elevation angle, d_{ap} is the aperture diameter, d_{cav} is the cavity diameter parallel to the receiver aperture and v is the wind speed. The emitted radiation from the receiver cavity ($\dot{q}_{rad,emit}$) is estimated as the thermal emission given by the Stefan-Boltzmann law in Equation (A.11) where, ε is the emissivity of the cavity, A_{ap} is the surface area of the receiver aperture opening, and σ is the Stefan-Boltzmann constant. The reflected radiation ($\dot{q}_{rad,reflect}$) from the receiver is given by Duffie and Beckman (2006) shown in Equations (A.12) and (A.13) where α_{eff} is the effective absorptance of the cavity, α_{cav} is the absorptance of the cavity interior surface, and A_{cav} is the interior cavity surface area.

$$\dot{q}_{rad,emit} = \varepsilon \cdot A_{ap} \cdot \sigma \cdot \left(T_{cav}^4 - T_{amb}^4 \right) \tag{A.11}$$

$$\alpha_{eff} = \frac{\alpha_{cav}}{\alpha_{cav} + \left(1 - \alpha_{cav}\right) \cdot \left(A_{ap} / A_{cav} \right)} \tag{A.12}$$

$$\dot{q}_{rad,reflect} = \left(1 - \alpha_{eff}\right) \cdot \dot{q}_{in,receiver} \tag{A.13}$$

An aperture cover can be used for hybrid systems to supplement solar energy with natural gas or for systems that replace the Stirling engine with a gas turbine. A receiver aperture cover can be simulated in the TRNSYS model providing a value for the cover transmittance for radiation at normal incidence (τ_c). An aperture cover will reduce the transmitted energy through the cover to the receiver cavity due to reflection as shown in Equations (A.14) and (A.15) but it will also reduce radiation and convection losses from the receiver cavity. The terms τ_c and τ_d are the transmittance of the cover for incident solar radiation and isotropic diffuse radiation respectively.

$$\tau_c \cdot \alpha_{eff} = \tau_c \cdot \left[\frac{\alpha_{cav}}{\alpha_{cav} + \left(1 - \alpha_{cav}\right) \cdot \tau_d \left(A_{ap} / A_{cav} \right)} \right] \tag{A.14}$$

$$\dot{q}_{rad,reflect} = \left(1 - \tau_c \cdot \alpha_{eff}\right) \cdot \dot{q}_{in,receiver} \tag{A.15}$$

Convection from the cavity to the aperture cover is determined using internal volume convection correlations given by Eqs. (A.16) and (A.17) (Incropera and DeWitt, 2002). Convection from the exterior plate surface to the environment is found by combining free convection with forced convection using Equation (A.21) with the value for n in Eq. (A.21) chosen to be three (Incropera and DeWitt, 2002). Free convection from a flat plate at the appropriate sun elevation angle is given by Equation (A.18) and (A.19) with forced convection given by Equation (A.20). The characteristic length used for these equations is the receiver aperture diameter. The terms *Pr*, *Re*, and *Ra* are the Prandtl, Reynolds, and Rayleigh numbers respectively.

$$\bar{N}u_{\text{internal}} = 1 + \left[\bar{N}u_{x=90^0} - 1 \right] \cdot \sin\left(90^0 + \theta\right) \tag{A.16}$$

$$\bar{N}u_{\tau=90^0} = 0.18 \cdot \left(\frac{\text{Pr}}{0.2 + \text{Pr}} \cdot Ra \right)^{0.29} \tag{A.17}$$

$$\bar{N}u_{exterior,free} = 0.68 + \frac{0.67 \cdot Ra^{1/4}}{\left[1 + \left(0.492 / \text{Pr} \right)^{9/16} \right]^{4/9}} \qquad \left(Ra \le 10^9; 0^0 \le \theta \le 60^0 \right) \tag{A.18}$$

$$\bar{N}u_{exterior,free} = 0.27 \cdot Ra^{1/4} \qquad \left(10^5 \le Ra \le 10^{10}; 60^0 \le \theta \le 90^0 \right) \tag{A.19}$$

$$\bar{N}u_{exterior,forced,lam} = 0.664 \cdot \text{Re}^{1/2} \cdot \text{Pr}^{1/3} \tag{A.20}$$

$$h_{combined,convection} = \left[h_{free}^n + h_{forced}^n \right]^{1/n} \tag{A.21}$$

It is possible to specify in the TRNSYS receiver model whether a direct illumination receiver (DIR), or a reflux receiver are used. Most systems use a DIR receiver even though the reflux receiver improves the system performance. Integration issues for a reflux receiver can be challenging for four-cylinder engines such as the SES Stirling engine, so SES is not planning on using reflux receivers at this point. Specifying a reflux receiver in TRNSYS will automatically increase the heater head temperature by 100°K and reduce the temperature drop between the receiver cavity and heater head, which are characteristic of reflux receivers. It is also possible to specify the heater head temperature and temperature drop in the model if these values are known for a modified system. Other parameters (below 'manufacturer') for the receiver and other models can only be modified if 'Other-5' is chosen for the manufacturer.

Receiver Parameters

1. Receiver type [1-DIR, 2-Reflux]
2. Transmittance of the aperture cover (for hybrid systems…1 is no cover) [-]
3. Manufacturer [1-SES, 2-WGA, 3-SBP, 4-SAIC, 5-Other]
4. Absorptance of the absorber [-]
5. Surface area of the absorber [m^2]
6. Absorptance of the cavity wall [-]
7. Surface area of the cavity wall [m^2]
8. Receiver insulation thickness [m]
9. Insulation thermal conductivity [W/m-K]
10. Internal diameter of the cavity perpendicular to the receiver aperture [m]
11. Internal cavity pressure when a cover is over the aperture [MPa]
12. Internal depth of the cavity perpendicular to the aperture [m]

Receiver Inputs

1. Input power to the receiver [kW]
2. Ambient temperature [°K]
3. Atmospheric pressure [Pa]
4. Wind speed [m/s]
5. Sun elevation angle [radians]
6. Number of collectors [-]
7. Heater head temperature (set point) [°K]
8. Heater head temperature (lowest) [°K]
9. DNI [W/m^2]
10. Insolation cut in [W/m^2]
11. Receiver aperture diameter [m]

Receiver Outputs to the Stirling Engine

1. Receiver output power [kW]
2. Ambient temperature [°K]
3. Receiver losses [kW]
4. Efficiency of the receiver [-]
5. Engine heater head operating temp [°K]
6. Number of Collectors [-]
7. Density of ambient air [kg/m^3]

8. DNI [W/m^2]
9. Insolation cut in [W/m^2]
10. Reflected radiation losses [kW]
11. Radiation losses from long-wave emission [kW]
12. Receiver convection losses [kW]
13. Receiver conduction losses [kW]

TRNSYS Stirling Engine & Generator Model

The Stirling engine model that provided the best agreement with three years of WGA data for the gross output power (P_{Gross}) was based on a Beale number (*Beale*) curve at part- to full-load using a temperature correction term ($T_{correct}$) from finite-time theory (McMahan et al, 2007) as given by Equation (A.23). The temperature correction term includes values for the expansion (T_E) and compression space (T_C) temperatures. The expansion space temperature is the heater head operating temperature, and the compression space temperature is determined by the cooling system model described in Chapter 3. One individual day of data is used to determine the temperature corrected Beale number ($Beale\#_{corrected}$) in Equation (A.23) and generate a curve fit shown in Figure A-1 with the input power to the Stirling engine determined by the collector and receiver models using Equation (A.5). The terms P_{mean}, V_{SW}, and f refer to the mean engine pressure, swept volume, and engine frequency.

$$Beale\#_{corrected} = P_{Gross} / \left[P_{mean} \cdot V_{sw} \cdot f \cdot T_{correct} \right] \quad \text{(A.22)}$$

$$T_{correct} = \left(1 - \left(T_E / T_C \right)^{0.5} \right) \quad \text{(A.23)}$$

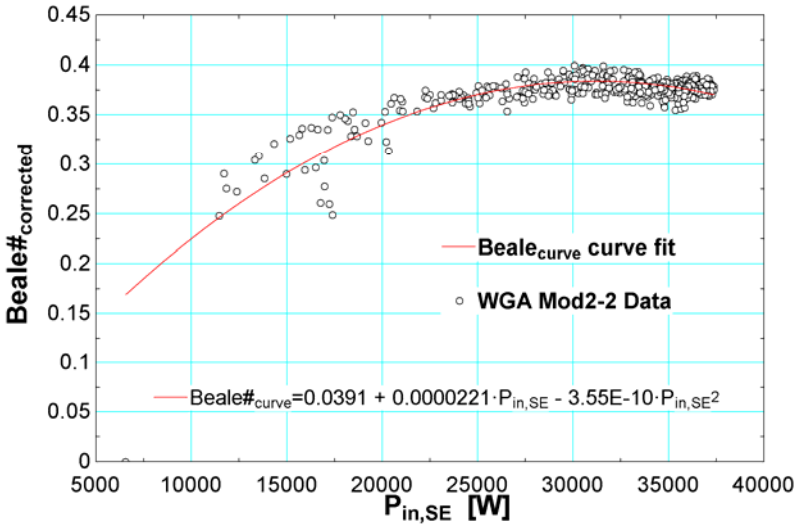

Figure A-1 Temperature-corrected Beale number vs. Stirling engine input power using WGA data on 12-9-03

Once a curve fit is generated using data for a specific engine, the gross output power of the engine is predicted using Equation (A.24) where the Beale number ($Beale_{curve}$) is determined from the curve fit in Figure A-1 and the input power to the engine. The other terms in Equation

(A.24) are determined either using TRNSYS TMY-2 data, or another data set. The temperature-corrected performance of the Stirling engine component allows for system optimization by altering the heater head (expansion space) temperature, fan or pump operating speeds, or replacing the fan and radiator with a central cooling tower.

$$P_{Gross} = Beale_{curve} \cdot \left[P_{mean} \cdot V_{sw} \cdot f \cdot T_{correct} \right] \quad \text{(A.24)}$$

The expansion space temperature can also be modified to determine the effect on system performance. A term can be input for the lowest temperature of the heater head, which would occur in a 4-cylinder engine (SES & SAIC) with varying heater head temperatures. Similar to improving the receiver efficiency by reducing the temperature drop between the receiver and engine heater head, the engine performance will improve by reducing the temperature drop from the highest and lowest heater head in a multiple cylinder engine. This change in performance is simulated in the TRNSYS model by using the lowest heater head temperature in the engine. A Stirling engine from a specific manufacturer can be chosen (SES, WGA/SBP, SAIC), or a new/modified Stirling engine can be chosen (Other).

Stirling Engine Parameters

1. Manufacturer [1-SES, 2-WGA, 3-SBP, 4-SAIC, 5-Other]
2. Heater head set temperature [°K]
3. Heater head lowest temperature [°K]
4. Beale constant coefficient from curve fit [-]
5. Beale first-order coefficient from curve fit [-]
6. Beale second-order coefficient from curve fit [-]
7. Beale third-order coefficient from curve fit [-]
8. Beale fourth-order coefficient from curve fit [-]
9. Pressure constant coefficient from curve fit [-]
10. Pressure first-order coefficient from curve fit [-]
11. Engine operating speed [RPM]
12. Displaced volume of the engine [cm^3]

Stirling Engine Inputs

1. Input power to the Stirling engine [kW]
2. Ambient temperature [°K]
3. Number of Collectors [-]
4. Compression space temperature (Stirling engine cold sink temperature) [°K]
5. Density of air [kg/m^3]
6. DNI [W/m^2]
7. Engine hot-end operating temperature [°K]
8. Insolation cut in [W/m^2]
9. Input power to the collector [kW]

Stirling Engine Outputs

1. Gross output power of the Stirling dish system [kW]
2. Ambient temperature [°K]

3. Stirling engine losses [kW]
4. Stirling engine efficiency [-]
5. Density of ambient air [kg/m^3]
6. DNI [W/m^2]
7. Engine lowest operating heater head temp [°K]
8. Heater head highest temperature (set point) [°K]
9. Displaced volume of engine [m^3]
10. Engine frequency [1/s]
11. Engine pressure [Pa]
12. Number of parabolic collectors [-]
13. Insolation cut in [W/m^2]
14. Gross system operating efficiency [-]

TRNSYS Parasitic Power Model

A cooling system model was generated to predict the compression space temperature of the Stirling engine and the parasitic power consumption of the Stirling dish system. The compression space temperature affects the Stirling engine performance, and the predicted parasitic power is used to obtain the net power from the system. The compression space temperature is determined with inputs of the ambient temperature, pump speed, fan speed, and the effectiveness of the radiator and cooler at test conditions. The appropriate effectiveness-NTU correlations (Incropera and DeWitt, 2002) are used in the TRNSYS model to predict how the radiator or cooler effectiveness will change at different operating speeds. The fan and pump parasitic powers are determined using the "fan laws" and the dimensionless pump performance equations (White, 2003). The net system power (P_{Net}) is found by subtracting the parasitic power of the tracking and controls ($P_{controls}$), pump (P_{pump}), and fan (P_{fan}) from the gross output power ($P_{Gross,op}$) of the engine as shown in Equation (A.25). The pump and controls parasitic power are initiated in the TRNSYS model when the direct normal insolation is positive, whereas the parasitic power from the fan is not included until the DNI is higher than the insolation cut-in value, which corresponds to when the fan is connected to the grid.

$$P_{Net} = P_{Gross,op} - (P_{controls} + P_{fan} + P_{pump}) \quad \text{(A.25)}$$

Parasitic Power Parameters

1. Cooling tower on [0-radiator and fan , 1-cooling tower]
2. Cooling tower mode [1-natural draft (no fans), 2-forced draft]
3. Cooling tower water distribution pipe diameter [m]
4. Mass flow rate of the cooling tower water [kg/hr]
5. Mass flow rate of the cooling tower water during tower test conditions [kg/hr]
6. Material of the cooling tower water distribution piping [1-plastic, 2-cast iron, 3-riveted steel]
7. Efficiency of the cooling tower water distribution pump [-]
8. Fan control signal [-] 0-off, 1-on, values between 0 and 1 are the fraction of the rated volumetric flow rate of the fan

9. Effectiveness of the counter flow heat exchanger between the cooling tower fluid loop and the Stirling dish cooling fluid loop [-]
10. Dish system availability [-]
11. Stirling dish cooling system pump operating speed [rpm]
12. Stirling dish cooling system fan operating speed 1 [RPM]
13. Stirling dish cooling system fan operating speed 2 [RPM]
14. Stirling dish cooling system fan operating speed 3 [RPM]
15. Stirling dish cooling system cooling fluid temperature for fan speed 2 cut-in [°C]
16. Stirling dish cooling system cooling fluid temperature for fan speed 3 cut-in [°C]
17. Cooler effectiveness at test conditions[-]
18. Radiator effectiveness at test conditions[-]
19. Cooling fluid [1 - water, 2 – 50 % EG, 3 – 25 % EG, 4 – 50 % PG, 5 – 25 % PG]
20. Manufacturer [1-SES, 2-WGA, 3-SBP, 4-SAIC, 5-Other]
21. Average control system parasitic power [W]
22. Stirling dish cooling system pump test parasitic power [W]
23. Stirling dish cooling system pump test speed [RPM]
24. Pump test cooling fluid [1 - water, 2 – 50 % EG, 3 – 25 % EG, 4 – 50 % PG, 5 – 25 % PG]
25. Cooling fluid test temperature [°K]
26. Cooling fluid test volumetric flow rate [gal/min]
27. Stirling dish cooling system fan test power [W]
28. Stirling dish cooling system fan test speed [RPM]
29. Stirling dish cooling system fan test air density [kg/m^3]
30. Stirling dish cooling system fan test volumetric flow rate [CFM]

Parasitic Power Inputs

1. Gross output power of the Stirling dish system [kW]
2. Ambient temperature [°K]
3. Number of Collectors [-]
4. Density of air [kg/m^3]
5. DNI [W/m2]
6. Engine lowest heater-head operating temp [°K]
7. Displaced volume [m^3]
8. Engine frequency [1/s]
9. Engine pressure [Pa]
10. Insolation cut in [W/m^2]
11. Engine rejected thermal load [kW]
12. Cooling tower water outlet temperature [°K]
13. Atmospheric pressure [Pa]
14. Dish separation distance north to south [m]
15. Dish separation distance east to west [m]
16. Parasitic power of the cooling tower fan [kJ/hr]
17. Input power to the collector [kW]

Parasitic Power Outputs

1. Net output power of the Stirling dish system (for one collector including system availability [kW]
2. Total parasitic power of the radiator fan, radiator pump, and tracking controls [W]
3. Compression space temperature [°K]
4. Stirling dish system fan parasitic power [W]
5. Stirling dish system pump parasitic power [W]
6. Inlet cooling water temperature to the cooling tower [°C]
7. Mass flow rate of the cooling tower water [kg/hr]
8. Ambient temperature [°C]
9. Fan control signal [-] 0-off, 1-on, values between 0 and 1 are the fraction of the rated volumetric flow rate of the fan
10. Compression space temperature [°C]
11. Parasitic power of the cooling tower [W]
12. Temperature of the Stirling dish system cooling fluid into the radiator [°C]
13. Temperature of the Stirling dish system cooling fluid out of the radiator [°C]
14. Net Stirling dish system efficiency [-]

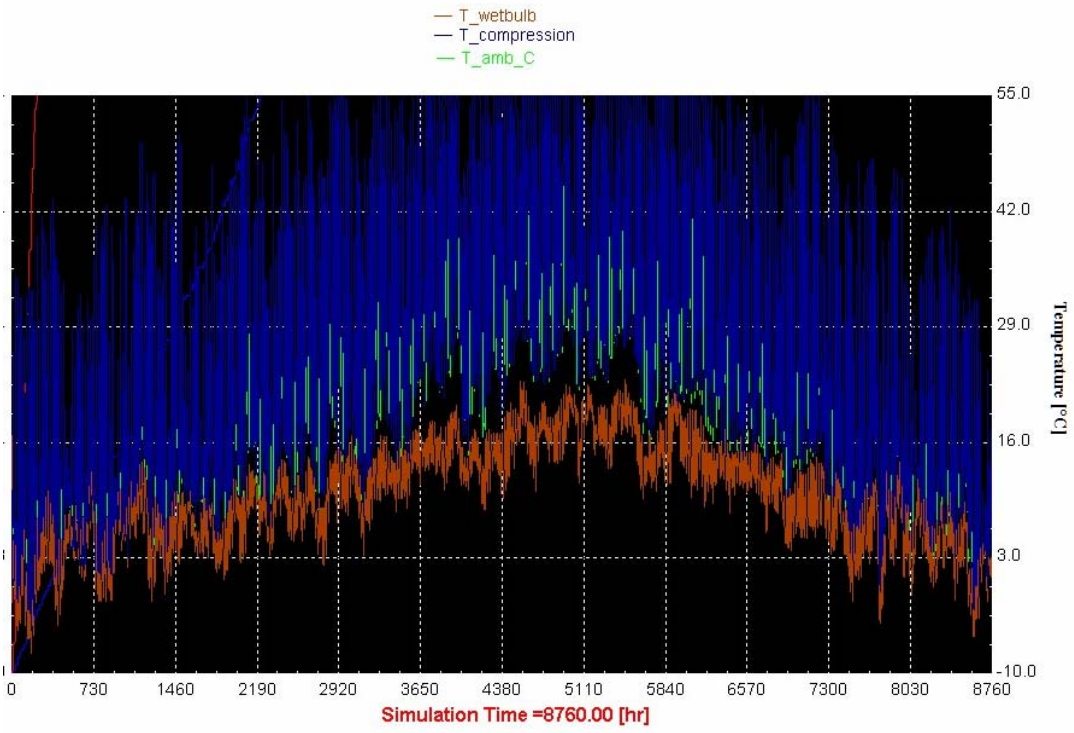

Figure A-2 TRNSYS yearly compression space temperature prediction for a WGA Stirling dish system operating with a radiator and fan.

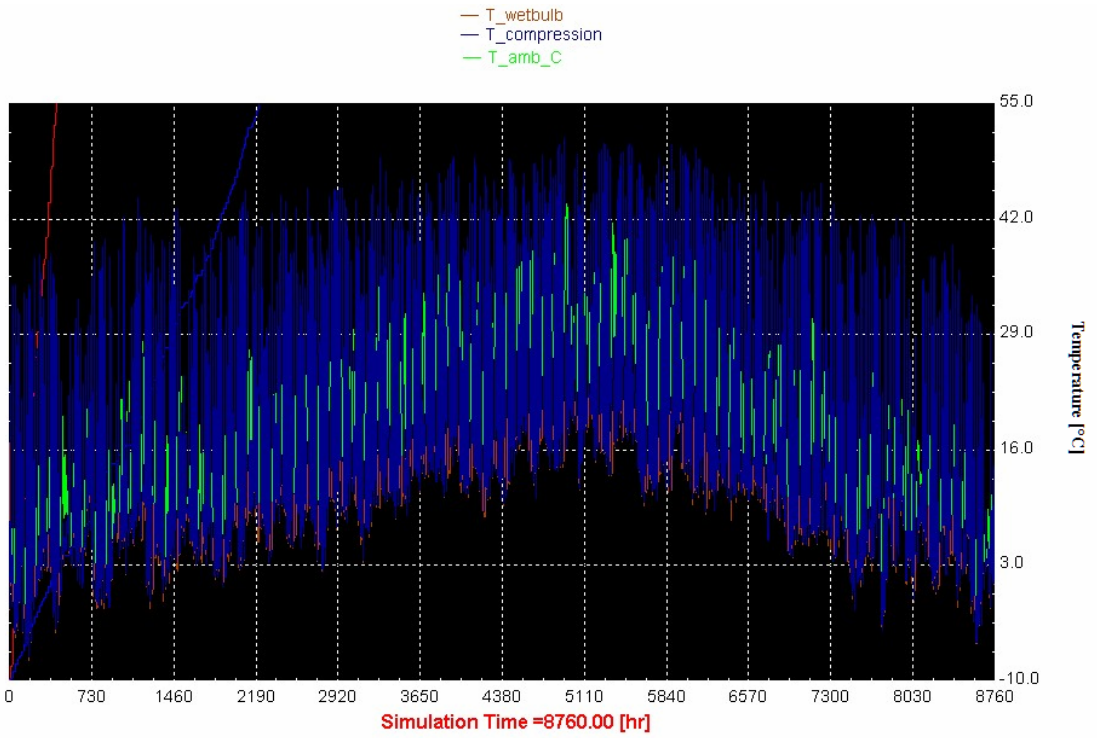

Figure A-3 TRNSYS yearly compression space temperature prediction for a WGA Stirling dish system operating with a cooling tower.

Appendix B Sample engine efficiency data

Table B.1 Comparison of the engine efficiency curve. The predicted values were solved using the collector and receiver models

	predicted eta_SE [-]	predicted eta_SE/(1-sqrt(T_C/T_E)) [-]	data Net Power [kW]	predicted P_in_SE [kW]	predicted eta_rec [-]	data T_rec_ave [C]	data DNI [W/m^2]	data T_amb [C]	data Wind Speed [mph]	data TE [C]	data water inlet [C]
4/26/2004	0.269	0.616	8.2	3.13E+04	0.910	695	892.4	13.8	3	627.9	14.5
	0.269	0.619	8.22	3.13E+04	0.910	696	893.1	13.4	4	623.7	14.5
	0.273	0.625	8.34	3.12E+04	0.908	708	892.5	13.3	5	632.1	14.5
	0.273	0.620	8.32	3.12E+04	0.909	708	892.5	13.8	4	640.4	15.5
	0.255	0.585	7.79	3.13E+04	0.911	696	893	13.9	4	627.9	15
	0.272	0.621	8.32	3.14E+04	0.911	698	894.2	13.5	3	632.1	15.5
	0.266	0.611	8.15	3.14E+04	0.912	690	894.5	13.6	4	623.7	15.9
	0.267	0.616	8.2	3.15E+04	0.912	691	895.3	13.5	2	619.5	15.5
	0.270	0.618	8.32	3.15E+04	0.911	703	898.4	13.6	5	632.1	15
	0.265	0.609	8.19	3.17E+04	0.913	694	900	13.9	2	627.9	15.5
	0.270	0.621	8.37	3.17E+04	0.912	701	901.9	14.1	2	627.9	16.4
	0.271	0.622	8.37	3.16E+04	0.913	695	899.5	13.9	3	627.9	15.5
	0.268	0.617	8.29	3.16E+04	0.913	697	899	14.1	5	627.9	15
	0.268	0.616	8.28	3.16E+04	0.913	697	899.3	14.3	2	627.9	15
	0.250	0.575	7.71	3.17E+04	0.914	691	899.4	14.3	2	623.7	16.9
	0.266	0.606	8.21	3.16E+04	0.912	707	900	14.4	4	640.4	16
	0.270	0.617	8.37	3.17E+04	0.913	705	901.4	14.1	5	636.2	15.5
	0.269	0.616	8.34	3.18E+04	0.915	693	901.7	14.4	4	632.1	15.5
	0.256	0.589	7.95	3.18E+04	0.914	703	903.2	14.1	7	627.9	16.4
	0.261	0.597	8.12	3.18E+04	0.914	703	903.8	14	4	636.2	15.5
	0.258	0.592	8.01	3.19E+04	0.916	693	903.3	14.1	5	627.9	15
	0.249	0.573	7.74	3.18E+04	0.915	696	902.4	14.1	6	627.9	16
	0.265	0.604	8.21	3.18E+04	0.914	706	901.9	13.9	4	636.2	16.9

	0.268	0.615	8.35	3.19E+04	0.916	695	903.5	13.9	3	627.9	16.9
	0.264	0.607	8.26	3.20E+04	0.917	689	905.8	14.2	6	627.9	16.5
ave	0.265	0.608	8.19	31600	0.91	698.00	898.88	13.93	3.92	629.73	15.62
std-dev	0.007	0.015	0.20	221.7	0.00	5.87	4.21	0.31	1.38	5.12	0.74

Appendix C Sample Simulation Results

Table C.1 Stine model simulation results comparing one day of data to generate the performance curve fit for the model with six other individual days of data and with all of the data

Energy Error [%]

	Tested model against these days						
Model Used	*4/26/2004*	*4/27/2004*	*6/2/2003*	*7/24/2003*	*12/9/2003*	*1/13/2004*	*All Data*
4/26/2004	0	6.39	-4.69	1.32	9.21	11.25	4.21
4/27/2004	-3.87	0	-8.15	-4.32	7.72	9	-0.04
6/2/2003	4.73	9.6	0	4.74	16.57	18.16	8.96
7/24/2003	-1.19	4.98	-5.81	0	8.09	10.06	2.95
12/9/2003	-10.73	-7.1	-14.71	-11.12	0	1.19	-7.17
1/13/2004	-12.47	-9.76	-16.28	-13.49	-0.91	0	-9.06

Power RMS Deviation [W]

	Tested model against these days						
Model Used	*4/26/2004*	*4/27/2004*	*6/2/2003*	*7/24/2003*	*12/9/2003*	*1/13/2004*	*All Data*
4/26/2004	11.93	23.95	23.55	14.15	36.68	39.1	1.62
4/27/2004	17.11	17.08	32.52	18.24	32.28	31.95	1.6
6/2/2003	20.09	28.98	14.41	19.85	63.41	62.02	2.03
7/24/2003	12.37	22	26.57	13.76	32.93	35.36	1.57
12/9/2003	31.79	24.76	54.75	31.17	14.03	11.34	1.78
1/13/2004	36.37	29.19	59.93	36.69	14.64	10.23	1.93

Power avg. error [W]

	Tested model against these days						
Model Used	*4/26/2004*	*4/27/2004*	*6/2/2003*	*7/24/2003*	*12/9/2003*	*1/13/2004*	*All Data*
4/26/2004	244.6	456.4	458.4	276.9	764.5	866.5	349.8
4/27/2004	369.1	295.1	676.8	385.4	649.3	697	355.5
6/2/2003	464.7	614.9	216.6	410.2	1376	1400	457.7
7/24/2003	259.1	403.9	531.2	274.7	671.6	775	340.7
12/9/2003	806.8	516.6	1175	745	226.6	194.4	447.6
1/13/2004	929.1	643.5	1294	890.6	247.9	177	495.8

Normalized Power avg. error [%]

	Tested model against these days						
Model Used	*4/26/2004*	*4/27/2004*	*6/2/2003*	*7/24/2003*	*12/9/2003*	*1/13/2004*	*All Data*
4/26/2004	3.29	7.54	5.82	4.24	9.21	11.25	8.76
4/27/2004	4.97	4.88	8.59	5.9	7.82	9.05	8.9
6/2/2003	6.26	10.16	2.75	6.28	16.57	18.18	11.46
7/24/2003	3.49	6.67	6.74	4.21	8.09	10.06	8.53
12/9/2003	10.86	8.53	14.91	11.41	2.73	2.52	11.21
1/13/2004	12.51	10.63	16.42	13.64	2.98	2.3	12.42

Table C.2 Sandia model simulation results comparing one day of data to generate the performance curve fit for the model with six other individual days of data and with all of the data

Energy Error [%]

	Tested model against these days						
Model Used	*4/26/2004*	*4/27/2004*	*6/2/2003*	*7/24/2003*	*12/9/2003*	*1/13/2004*	*All Data*
4/26/2004	1.13	8.14	-3.16	4.69	9.95	11.71	6.1
4/27/2004	-4.25	-0.07	-7.99	-2.45	7.09	7.94	0.32
6/2/2003	2.72	9.13	-1.55	5.89	12.53	14.08	7.72
7/24/2003	-6.47	0	-10.44	-3.18	1.7	3.32	-1.88
12/9/2003	-2.71	1.96	-6.57	-0.61	8.3	9.3	1.96
1/13/2004	-6.23	-2.49	-9.85	-4.69	5.3	6.02	-1.77

Power RMS Deviation [W]

	Tested model against these days						
Model Used	*4/26/2004*	*4/27/2004*	*6/2/2003*	*7/24/2003*	*12/9/2003*	*1/13/2004*	*All Data*
4/26/2004	12.42	27.07	21.36	18.34	38.76	40.66	1.67
4/27/2004	17.88	17.52	32.84	16.77	29.48	28.59	1.55
6/2/2003	14.64	28.2	17.84	20.91	47.82	48.01	1.8
7/24/2003	21.89	21.05	42.28	16.16	16.12	19.07	1.51
12/9/2003	15.25	18.14	28.62	15.48	33.37	32.76	1.56
1/13/2004	21.8	18.51	38.7	19.54	23.84	22.79	1.57

Power avg. error [W]

	Tested model against these days						
Model Used	*4/26/2004*	*4/27/2004*	*6/2/2003*	*7/24/2003*	*12/9/2003*	*1/13/2004*	*All Data*
4/26/2004	253.7	539.9	393.5	358.4	826.5	902	364.4
4/27/2004	399	312.3	674.9	356.5	593.9	614.8	343.4
6/2/2003	309.3	588.2	308	423.7	1040	1085	398.7
7/24/2003	536.9	389.7	878.8	347	216.3	293.8	352.3

12/9/2003	337.8	325.1	578.5	328.7	689.7	718.2	339.4
1/13/2004	502.5	340.4	806.8	417.2	463.7	471.4	358.5

Normalized Power avg. error [%]

	Tested model against these days						
Model Used	*4/26/2004*	*4/27/2004*	*6/2/2003*	*7/24/2003*	*12/9/2003*	*1/13/2004*	*All Data*
4/26/2004	3.41	8.92	4.99	5.49	9.95	11.71	9.13
4/27/2004	5.37	5.16	8.56	5.46	7.15	7.98	8.6
6/2/2003	4.16	9.72	3.91	6.49	12.53	14.08	9.99
7/24/2003	7.23	6.44	11.15	5.31	2.6	3.81	8.82
12/9/2003	4.55	5.37	7.34	5.03	8.3	9.32	8.5
1/13/2004	6.76	5.62	10.24	6.39	5.58	6.12	8.98

Table C.3 West number model simulation results comparing one day of data to generate the performance curve fit for the model with six other individual days of data and with all of the data

Energy Error [%]

	Tested model against these days						
Model Used	*4/26/2004*	*4/27/2004*	*6/2/2003*	*7/24/2003*	*12/9/2003*	*1/13/2004*	*All Data*
4/26/2004	-0.029	6.684	-3.253	5.443	-0.1338	4.571	2.84
4/27/2004	-5.553	-0.1258	-8.229	0.2527	-6.585	-2.624	-3.09
6/2/2003	1.945	6.632	-0.01258	8.002	1.476	4.647	3.93
7/24/2003	-4.372	1.494	-7.315	-0.01137	-2.981	1.78	-1.3
12/9/2003	-0.573	2.726	-2.898	4.141	0.02331	4.493	1.67
1/13/2004	-4.712	-2.369	-6.645	-0.1876	-4.053	0.05209	-2.74

Power RMS Deviation [W]

	Tested model against these days						
Model Used	*4/26/2004*	*4/27/2004*	*6/2/2003*	*7/24/2003*	*12/9/2003*	*1/13/2004*	*All Data*
4/26/2004	10.77	27.51	20.2	18.85	17.54	21.8	1.47
4/27/2004	17.91	22.73	32.82	14.52	31.64	20.87	1.47
6/2/2003	21.5	36.02	14.11	28.18	19.68	27.76	1.7
7/24/2003	17.93	23.53	32.29	13.11	22.2	18.16	1.5
12/9/2003	15.89	24.87	18.91	23.07	12.1	17.59	1.43
1/13/2004	20.69	25.45	28.38	21.62	19.5	9.571	1.46

Power avg. error [W]

	Tested model against these days

Model Used	4/26/2004	4/27/2004	6/2/2003	7/24/2003	12/9/2003	1/13/2004	All Data
4/26/2004	228.2	516.6	375.9	389.2	289.7	370.2	315.8
4/27/2004	433.2	444.9	682.7	289.3	625.5	407.5	347.3
6/2/2003	396.9	689	228.8	604.6	324.7	514	369.8
7/24/2003	404.4	442.5	639.1	266.6	408.5	323.5	341.3
12/9/2003	347.2	493.4	349.9	496	200.9	355.8	318.1
1/13/2004	428.6	512.9	568.6	459.5	385.2	167.2	333.2

Normalized Power avg. error [%]

	Tested model against these days						
Model Used	4/26/2004	4/27/2004	6/2/2003	7/24/2003	12/9/2003	1/13/2004	All Data
4/26/2004	3.072	8.534	4.77	5.962	3.49	4.806	7.91
4/27/2004	5.832	7.35	8.662	4.432	7.532	5.291	8.7
6/2/2003	5.342	11.38	2.903	9.261	3.91	6.674	9.26
7/24/2003	5.444	7.31	8.109	4.084	4.919	4.2	8.55
12/9/2003	4.674	8.15	4.439	7.598	2.42	4.62	7.97
1/13/2004	5.77	8.472	7.215	7.039	4.638	2.171	8.35

Appendix D Natural Convection Correlations

There have been many natural convection correlations derived for Stirling dish systems. Convection losses are much more difficult to predict than conduction or radiation losses due to the non-standard geometry of the receiver and since the convection losses vary continually throughout the day due to the orientation of the aperture. Consequently, many researchers have developed natural convection correlations to predict convection losses from the Stirling dish receiver cavity. The Stine and McDonald (1989) correlation was implemented in the model since it had been validated with data, and it was used for the forced convection analysis by Ma.

Clausing 1981 and 1983 Convection Correlation

Clausing developed an analytical model for cubical central receivers to determine the convective losses from the cavity. The analytical model was validated with experimental data. The convective energy flow out of the aperture is given by Equation (D.1) (Clausing, 1983)

$$q_a = \left(\rho_\infty \cdot v_{ave} \cdot A_{ap}\right) \cdot c_p \cdot \left(T_{air} - T_{amb}\right) \qquad \text{(D.1)}$$

where ρ_∞ is the density of the ambient air, v_{ave} is the average velocity of the air, A_{ap} is the aperture area, c_p is the specific heat of ambient air, T_{air} is the average temperature of air flowing out of the cavity, and T_{amb} is the ambient temperature. This equation indicates how the convection losses will change based on a Stirling dish system operating at different altitudes due

to a change in air density. The Nusselt number relations that Clausing derived from the numerical data for the larger (38 MWt) (Equation (D.2)) and smaller (1 MWt) (Equation (D.3)) central receivers are (Clausing, 1983):

$$Nu = 0.021 \cdot \left(G_r \cdot P_r\right)^{0.4} \tag{D.2}$$

$$Nu = 0.10 \cdot \left(G_r \cdot P_r\right)^{1/3} \tag{D.3}$$

$$G_r = \frac{g \cdot \beta \cdot \left(T_{cav} - T_{amb}\right) \cdot L_c^3}{\upsilon^2} \tag{D.4}$$

$$P_r = \frac{\upsilon}{\alpha} \tag{D.5}$$

where G_r is the Grashof number, P_r is the Prandtl number, g is gravitational acceleration, β is the volumetric thermal expansion coefficient, T_{cav} is the temperature of the cavity surface, T_{amb} is the ambient temperature, υ is the kinematic viscosity, and L_c the characteristic length. The characteristic length (L_c) for the Clausing correlation is the width of the active convective zone within the cavity as shown in Figure D-1 and it is determined with a system of several equations (Clausing, 1983). This distance varies based on the aperture orientation as was indicated in Figure 2-13 above.

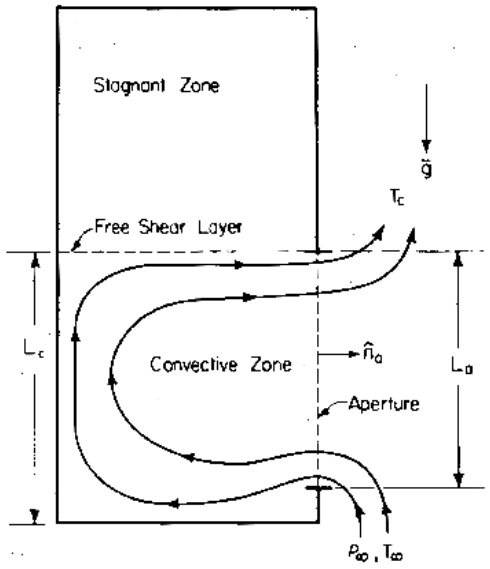

Figure D-1 Convective flow through the aperture and resulting stagnant zone (Clausing, 1983)

Clausing further refined his correlation in 1983 with the following Nusselt number expression (Clausing, 1983):

$$Nu = 0.082 \cdot \left(G_r \cdot P_r\right)^{1/3} \cdot \left(-0.9 + 2.4 \cdot \left(T_w / T_\infty\right) - 0.5 \cdot \left(T_w / T_\infty\right)^2 \cdot z(Z_w)\right) \quad \text{(D.6)}$$

where $z(Z_w) = 1$ when $0 \le Z_w \le 135^o$ (D.7)

$$z\left(Zw\right) = \frac{2}{3}\left[1 + \left(\sin\left(Z_w\right)/\sqrt{2}\right)\right] \quad \text{when } Z_w > 135^o \quad \text{(D.8)}$$

where 180° corresponds to the aperture facing downward, 0° is facing upward, and 90° is horizontal.

Koenig and Marvin 1985 Convection Correlation

A convective loss correlation was developed by Koenig and Marvin from experimental data (Stine and McDonald, 1988). A Nusselt number was derived using a characteristic length that is the square root of two times the mean cavity radius and is given by Equation (D.9) (Stine and McDonald, 1988).

$$Nu = C_1 \cdot P(\theta) \cdot \left(d_{ap} / d_{cav}\right)^{1.75} \cdot \left(Gr \cdot \mathrm{Pr}\right)^{0.25} \quad \text{(D.9)}$$

where $P(\theta)$ is an experimentally determined function of the receiver tilt angle θ given by Equation (D.10) or (D.11), d_{ap} is the cavity aperture diameter, d_{cav} is the mean cavity internal diameter, Pr is the Prandtl number, Gr is the Grashof number, and C_1 is constant determined to be 0.52 by Koenig and Marvin (Stine and McDonald, 1988).

$$P(\theta) = \cos^{3.2}\left(\theta\right) \text{ for } 0^\circ \le \theta \le 45^\circ \quad \text{(D.10)}$$

$$P(\theta) = 0.707\cos^{2.2}\left(\theta\right) \text{ for } 45^\circ \le \theta \le 90^\circ \quad \text{(D.11)}$$

The constant C_1 from Equation (D.9) above is based on the absorber tube surface area as the characteristic area used for the convective heat transfer coefficient (Stine and McDonald, 1988). It is difficult to determine the absorber tube surface area that participates in convection since the insulation may or may not be in contact with the tubes on the outward facing half of the tubes. Stine and McDonald suggest using the cavity interior area with a coefficient C_1 equal to 0.78 which they derived from Koenig and Marvin's data (Stine and McDonald, 1988). Using the interior surface area for the convection correlation also allows for the convection losses from a reflux receiver to be determined since these receivers do not use absorber tubes.

Siebers and Kraabel 1984 Convection Correlation

Siebers and Kraabel developed a convection heat transfer expression using data from cubical cavities used for central receiver systems (Stine and McDonald, 1989). Their correlation is expressed in Equation (D.12)

$$Nu = 0.088 \cdot Gr^{1/3} \cdot \left(T_{wall} / T_{amb}\right)^{0.18} \quad \text{(D.12)}$$

where T_{wall} and T_{amb} are respectively the interior wall and ambient temperatures. This correlation is then modified using area ratios to take into account effects from cavity tilt and closure of the aperture (Stine and McDonald, 1989)

Stine and McDonald 1989 Convection Correlation

A model for predicting convection losses was developed by Stine and McDonald (1989) to predict convective losses in Stirling dish cavity receivers. Most of the previous convection correlations had been developed for central receiver systems that use a cubical receiver, so the Stine and McDonald correlation had the potential to be a better representation of cavity receiver losses. Stine's correlation was refined from Siebers and Kraabel's correlation and developed using experimental data on a cavity receiver, which includes parameters for the receiver tilt angle and the aperture diameter. This correlation is given in Equation (D.13) (Stine and McDonald, 1989)

$$Nu = 0.088 \cdot Gr^{1/3} \cdot \left(T_{wall} / T_{amb}\right)^{0.18} \cdot \left(\cos\theta\right)^{2.47} \cdot \left(d_{ap} / d_{cav}\right)^{S} \quad \text{(D.13)}$$

where

$$S = -0.982 \cdot \left(d_{ap} / d_{cav}\right) + 1.12 \quad \text{(D.14)}$$

d_{ap} is the aperture diameter, Gr is the Grashof number based on the average internal width of the cavity length d_{cav}, Nu is the Nusselt number based on the length d_{cav}, T_{amb} is the ambient temperature, T_{wall} is the average internal wall temperature, and θ is the tilt angle of the cavity ($\theta = 90^{\circ}$ is tilted down such as at noon on the equator, and $\theta = 0^{\circ}$ is facing horizontal as it would during the morning/evening). The surface area to apply the heat transfer coefficient is the full cavity interior area whether it is the absorber surface or the interior side walls. Experimental data were obtained and compared with Stine and McDonald's correlation in Equation (D.13) and Hogan found that the correlation slightly under predicts thermal efficiency at lower elevation angles and over predicts thermal efficiency at higher elevation angles (Hogan, 1991). Ma's experiments, however, indicate the correlation to be very accurate over a range of elevation angles (Ma, 1993). Sandia labs use the Stine and McDonald correlation in their AEETES receiver software (Ma, 1993, Hogan, 1991).

Liebfried and Ortjohann 1995 Convection Correlation

The previous correlations are not applicable to receivers that face upwards, such as those used with a Fresnel lens or a cavity receiver that uses a secondary mirror to reflect radiation down into the cavity. Consequently, Liebfried developed a modified Stine and a modified Clausing correlation to represent receiver orientations between -90° (upward) and +90° (downward). Liebfried determined the modified Stine correlation to provide better results than the modified Clausing model. It was found that 89 percent of deviations from the data did not exceed a 13 percent error for the modified Clausing equation, and 94 percent of deviations were within that

range with the modified Stine equation for temperatures between 573°K and 873°K (Liebfried and Ortjohann, 1995).

In addition to extending Stine's model to behave over a wider range of orientations, Liebfried modified the Stine equation since it overestimated the convective losses at higher cavity temperatures. This result was assumed to occur since Stine's correlation has an increasing Grashof number when there is an increase in wall temperature, whereas the Grashof number should be decreasing (Liebfried and Ortjohann, 1995). A decreasing Grashof number was realized by taking the properties of the Grashof number to be at the film temperature which is given in Equation (D.15).

$$T_{film} = \left(T_{wall} + T_{amb}\right)/2 \tag{D.15}$$

It was also believed that an area ratio between the aperture and interior cavity would give a better correlation than the diameter ratio between these two features. The characteristic length used was the same as in Stine's correlation which is the average cavity diameter (d_{cav}). Liebfried's correlation for the Nusselt number is found in Equation (D.16)

$$Nu = 0.106 \cdot Gr^{1/3} \cdot \left(T_w / T_\infty\right)^{0.18} \cdot \left(4.256 \cdot \frac{A_{ap}}{A_{cav}}\right)^{s} \cdot h\left(\theta, \theta_{\max}, \theta_{stag}\right) \tag{D.16}$$

where θ_{max} is the angle where maximum convection occurs (~ -45°) with

$$\theta_{\max} = -23^o - 260^o \cdot \frac{A_{ap}}{A_{cav}} \tag{D.17}$$

$$s = 0.56 - 1.01 \cdot \left(A_{ap} / A_{cav}\right)^{0.50} \tag{D.18}$$

$$h_0 = 1 - \cos\left[\tilde{\theta}\left(\theta = 0\right)^{0.85} \cdot \pi\right] \tag{D.19}$$

for $\theta \geq \theta_{\max}$

$$h\left(\theta, \theta_{\max}, \theta_{stag}\right) = \frac{1}{h_0} \cdot \left(1 - \cos\left(\tilde{\theta}^{0.85} \cdot \pi\right)\right) \tag{D.20}$$

where

$$\tilde{\theta} = \frac{\theta - \theta_{stag,eff}}{\theta_{\max} - \theta_{stag,eff}} \tag{D.21}$$

$$\theta_{stag,eff} = \theta_{stag} + \left(90^o - \theta_{stag}\right) \cdot \frac{\theta_{stag} - \theta}{\theta_{stag}} \tag{D.22}$$

θ_{stag} is the stagnation angle where the buoyant forces prevent convection from occurring rapidly. This angle is almost always equal to 90° which is when the aperture is facing down.

for $\theta < \theta_{\max}$

$$h\left(\theta, \theta_{\max}, \theta_{stag}\right) = \frac{1}{h_0} \cdot \left(2 - 0.01 \cdot \left(\theta_{\max} + 90^o\right) \cdot \left[1 + \cos\left(\tilde{\theta}^{0.9} \cdot \pi\right)\right]\right) \tag{D.23}$$

where

$$\tilde{\theta} = \frac{\theta + 90^o}{\theta_{\max} + 90^o} \tag{D.24}$$

Paitoonsurikarn et al. 2004 Convection Correlation

Two convection correlations were proposed by Paitoonsurikarn et al. (2004) before refining one of the correlations to be within an accuracy of 20 % over a range of temperatures (Paitoonsurikarn et al, 2004). One drawback of the Paitoonsurikarn et al. correlation is that it fails to accurately predict losses from shallow cavities with aspect ratios below 0.5 (Paitoonsurikarn et al, 2004). Receivers seldom have aspect ratios within this range, however. The Paitoonsurikarn et al. Nusselt number is given by Equation (D.25)

$$Nu = C \cdot Ra^n \tag{D.25}$$

where *Ra* is the Rayleigh number given by Equation (D.26)

$$R_a = \frac{g \cdot \beta \cdot \Delta T \cdot L_c^3}{\upsilon \cdot \alpha} \tag{D.26}$$

$$d_{cav} = \left(4.79 \cdot \cos^{4.43}\left(\theta\right) - 0.37 \cdot \sin^{0.719}\left(\theta\right)\right) \cdot d_{cav} + \left(1.06 \cdot \cos^{3.24}\left(\theta\right) - 0.0462 \cdot \sin^{0.286}\left(\theta\right)\right) \cdot d_{ap}$$
$$+ \left(7.07 \cdot \cos^{5.31}\left(\theta\right) + 0.221 \cdot \sin^{2.43}\left(\theta\right)\right) \cdot L_{cav} \tag{D.27}$$

where L_{cav} is the cavity depth,

$$C = 8.2066 \cdot 10^{-6} \cdot \left(\frac{T_{wall}}{T_{amb}} \right)^{2.5837} \quad \text{(D.28)}$$

$$n = 0.67824 \cdot \left(\frac{T_{wall}}{T_{amb}} \right)^{-0.064548} \quad \text{(D.29)}$$

Paitoonsurikarn et al. also modified the Liebfried (modified Stine) correlation using the same characteristic length (d_{cav}) and Grashof number evaluated at the film temperature. The function h(θ, θ_{max}, θ_{stag}) in Liebfried's correlation was simplified as shown in Equation (D.32). Their data indicated that the convection losses do not go to zero when the aperture is oriented directly towards the ground, but rather approach a value a slightly higher. Their Nusselt number correlation in Equation (D.25) represents a non-zero loss when the aperture is oriented towards the ground. The Nusselt number using Paitoonsurikarn et al. modified Stine correlation is found in Equation (D.30) (Paitoonsurikarn et al, 2004).

$$Nu = 0.106 \cdot Gr^{1/3} \cdot \left(T_{wall} / T_{amb} \right)^{0.18} \cdot \left(4.256 \cdot \frac{A_{ap}}{A_{cav}} \right)^{s} \cdot h(\theta) \quad \text{(D.30)}$$

with

$$s = 0.56 - 1.01 \cdot \left(A_{ap} / A_{cav} \right)^{0.50} \quad \text{(D.31)}$$

$$h(\theta) = 1.1677 - 1.0762 \cdot \sin\left(\theta^{0.8324} \right) \quad \text{(D.32)}$$

where θ is in radians

Appendix E Stirling Engine Configurations

Beta Configuration

The beta configuration incorporates a displacer and power piston in the same cylinder and only has one cylinder for the expansion and compression space as shown in Figure E-1 (Stine, 1999). The beta engine was the original Stirling engine configuration designed by Robert Stirling in 1816 (Urieli and Berchowitz, 1984). The displacer transfers gas between the expansion and compression space through the heater, regenerator, and cooler. The power piston is often at the cold end of the cylinder and compresses the working fluid when most of the gas is in the cold end, and expands the working fluid when the gas has been transferred to the hot end. The

maximum theoretical mechanical efficiency for a beta engine operating at the SBP V-160 engine conditions is 77.1 %, which is slightly greater than the Siemens alpha arrangement at 76.8 %, but much higher than the basic alpha arrangement of 62.2 % (Finkelstein, 1998).

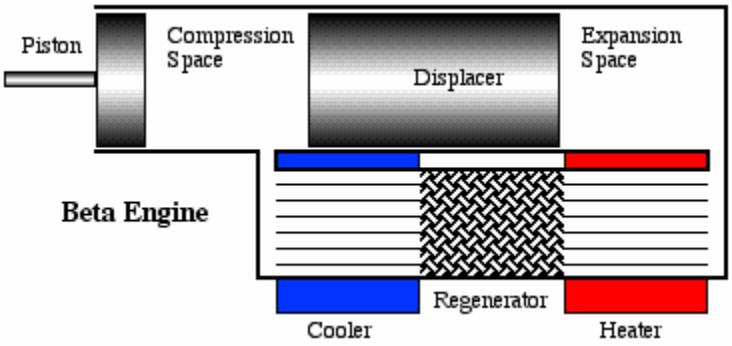

Figure E-1 Beta Stirling engine (Urieli, 2007)

Process 1-2: **Compression**
The majority of the expanded gas is in the compression space and the gas cools as it transfers heat to the external sink. The working fluid contracts as it cools and pulls the power piston inward as shown in Figure E-2.

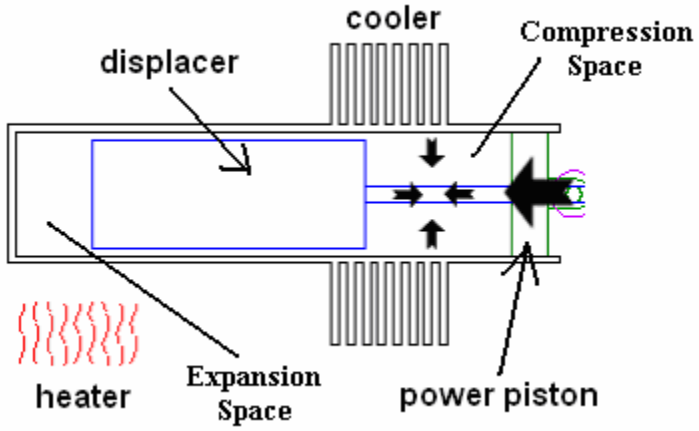

Figure E-2 Beta compression phase (regenerator not shown) (Keveney, 2001)

Process 2-3: **Transfer of heat from the regenerator to the working fluid**
Most of the contracted gas is still in the compression space as shown in Figure E-3. The momentum of the flywheel continues to turn the crankshaft an additional 90 degrees as the working fluid is transferred around the displacer and back into the expansion cylinder. While the gas moves through the regenerator (not shown), it absorbs thermal energy.

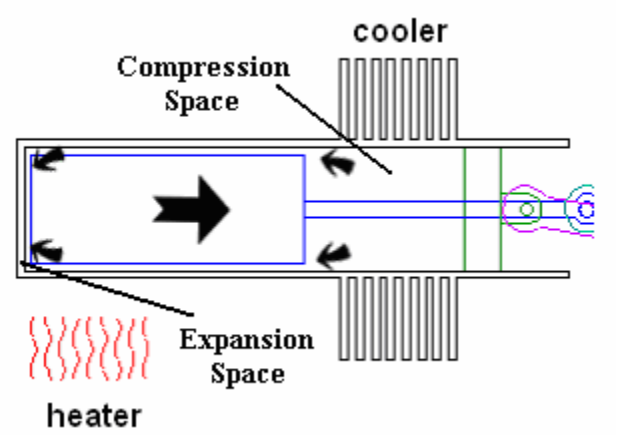

Figure E-3 Beta heat transfer from the regenerator (not shown) to the working fluid (Keveney, 2001)

Process 3-4: Expansion

Most of the working fluid is in the expansion space where it is heated from an external source such as solar energy or biomass. The gas expands in the expansion space and through the regenerator while driving the power piston outward as shown in Figure E-4.

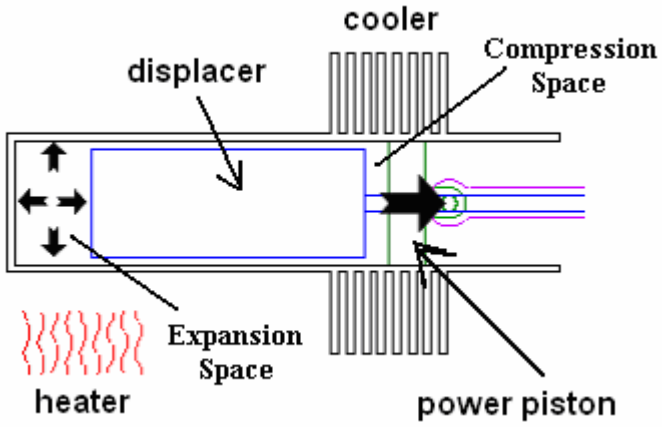

Figure E-4 beta expansion phase (Keveney, 2001)

Process 4-1: **Heat transfer from the working fluid to the regenerator**

Most of the gas is still in the expansion space as the flywheel momentum turns the crankshaft an additional 90 degrees. This causes the remaining gas to be pushed around the displacer into the compression space as shown in Figure E-5. Energy is transferred from the working fluid to the regenerator in this step.

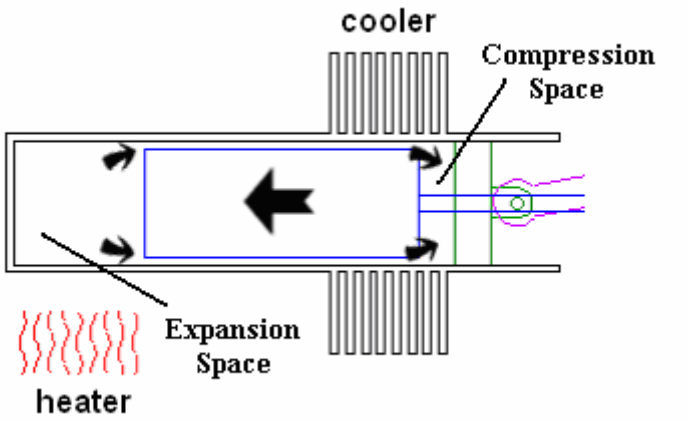

Figure E-5 Beta heat transfer from the working fluid to the regenerator (Keveney, 2001)

Gamma Configuration

The gamma configuration Stirling engine is similar to the beta configuration except that the displacer and power piston is located in different cylinders which are pneumatically connected together as shown in Figure E-6 (Urieli and Berchowitz, 1984). They often have larger dead volumes than the alpha or beta engines, and therefore have lower specific powers. Gamma engines are used when the benefits for using separate cylinders outweighs the disadvantage for power which can be for pumping water.

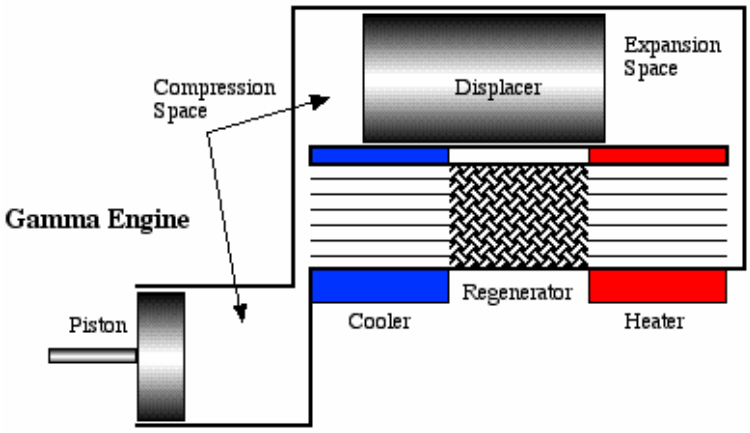

Figure E-6 Gamma configuration Stirling engine (Urieli, 2007)

Appendix F Petrescu et al (2000,2002) method for solving the Stirling engine efficiency

- **Model Implemented in Engineering Equation Solver**

```
"parameters"
{
"values in parametric table"
RPM = 1800[rpm]                                    "engine speed (1/s) "
Volume_displacement = 0.00038[m^3]                 "displaced volume of engine"
TC = 310[K]                                        "compression space temp of engine"
TE = 993[K]                                        "expansion space temp of engine"
Insolation = 180[W/m^2]   "varied in parametric table between 180 and 1000W/m^2"
Pressure_mean = 2[Pa]*10^6   "mean engine pressure varied in parametric table between 2E6 and
2E7Pa"
}
Patm = 101325 [Pa]
P_atm = Patm
TE_max = 995[K]                                    "expansion space operating temperature"
Th = 1083 [K]                                      "heater operating temperature (absorber
temperature)"
TC_max = 310[K]                                    "compression space temperature"
Tk = 293 [K]                                       "cooler temperature....should be just above
ambient"
DNI = Insolation
A_dish = 87.7 [m^2]
intercept_factor = 0.97 [-]
eta_receiver = 0.86 [-]
reflectivity = 0.91 [-]
eta_generator = 0.95[-]
Power_in_SE = Insolation * A_dish * reflectivity *intercept_factor*eta_receiver

"_____engine parameters_____"
k_spec = Cp / Cv
V1 =  540 [cm^3] * convert(cm^3,m^3)               "max volume at state 1"
V2 =  V1 - 380 [cm^3] * convert(cm^3,m^3)          "minimum volume at state 2"
T_S_L = Tk                                         "sink (cooler) temperature"
w_S_L = sqrt(gamma*R*T_S_L)                        "speed of piston for the sound speed at sink
temperature"
Vmax = V1                                          "max volume for P-V diagram"
Vmin = V2                                          "min volume for P-V diagram"
epsilon_v =  (V1 / V2)                             "volumetric compression ratio"
gamma = Cp / Cv                                    "specific heat ratio"
Cv = Cv(H2 , T =AVERAGE(TC,TE))                    "spec heat constant volume"
Cv_g = Cv
Cp = Cp(H2 , T =AVERAGE(TC,TE))                    "spec heat constant pressure"
MM_H2 = MolarMass(H2)
R = R# / MM_H2                                     "working gas constant"
T_H2_ave =   (TE + TC) / 2
m_g = Pressure_mean*V1 / (R*T_H2_ave)              "estimate Urieli p39 & ideal gas law"    "mass
of working gas"
N_cylinders = 4                                    "number of cylinders"
stroke_cyl = 0.04[m]                               "stroke for each cylinder"
S =  (N_cylinders*stroke_cyl)                      "total stroke of the piston [m]"
```

```
T_m = AVERAGE(TC,TE)                                    "mean temperature of gas"
Pr = Prandtl(H2,T=T_m)                                  "Prandtl number"
nu=Viscosity(H2,T=T_m)*Volume(H2,T=T_m,P=Pressure_mean)   "viscosity of working gas [m^2 / s]"
P1 = (4*Pressure_mean) / ((epsilon_v + 1) * (tau + 1))     "initial state inlet pressure"
tau = (TE / TC)                                         "ratio of working gas extreme temperatures"
w = 2*S*RPM/(60 [s/min])                                "speed of piston [m/s]"

"_____regenerator parameters_____"

m_R =  0.2 [kg]      "! guess"                          "mass of regenerator"
TR = (TE - TC) / (ln(TE / TC))                          "mean effective regenerator temp...NASA ref"
c_R = c_('Stainless_AISI316', TR)                       "specific heat of regenerator"
A_R = pi*(D_R /2)^2 * N_S     "! total surface area guessed"     "heat transfer surface area of
regenerator"
D_R = .057[m]                                           "diameter of regenerator"
b2 = 1e-7[m]     "!guess"                               "distance between wires in the regenerator"
d =  4e-5[m]      "!guess....not sensitive"             "regenerator wire diameter"
N_S = 1600     "! 2 x 200 in each of 4 cylinders"       "number of screens in the regenerator"

"_____"

"!Regeneration losses"
y = 0.72                                                "y is an adjusting coefficient"
eta_II_X = 1 / (1 + X *(1-sqrt(Tk / Th))/ ((gamma-1)*ln(epsilon_v)))    "Regeneration losses"

X = X1 * y + X2*(1 - y)                                 " X is coefficient of regenerative
losses"
X1 = (1 + 2*M + EXP(-B)) / (2 * (1 + M))
X2 = (M + EXP(-B)) / (1 + M)
M = (m_g * Cv_g) / (m_R * c_R)
B = (1 + M) * (h*A_R) / (m_g*Cv_g)*(S / w)
h = (0.395*(4*Pressure_mean / (R*TC)) * w^(0.424) * Cp * nu^0.576) / ((1+tau) * (1 - (PI / (4*((b2/d)+1))))*
D_R^0.576 * Pr^(2/3))   "convection heat x-fer coef to regenerator"

"_____"

"!Pressure losses"
eta_II_DELTA_P = 1 - (((w / w_S_L) * gamma*(1 + sqrt(tau))* ln(epsilon_v) + 5 * (w/w_S_L)^2 * N_S) /
(tau * eta_prime * ln(epsilon_v)) + ((3*(0.94[m/s]+0.045*w)*(10^5)[Pa-s/m]) / (4*P1)) /
(tau*eta_prime*ln(epsilon_v)))
eta_prime = eta_CC * eta_II_X

"_____"

"! Stirling cycle efficiency"

eta_CC = 1 - (Tk / Th)     "Carnot efficiency"
eta_2_DELTA_T = 1 / (1+sqrt(Tk/Th))
eta_II_irrev = eta_II_X * eta_II_DELTA_P*eta_2_DELTA_T        "second law efficiency including
irreversibilities"

eta_Petruscu = MAX(0,eta_CC * eta_II_irrev)               "Stirling engine total efficiency"

"_____"
```

Appendix G Shading Analysis by D.B. Osborn (1980)

A shading analysis was described in D.B. Osborn (1980) for parabolic dish systems. The analysis predicts the average shading occurring on each parabolic dish in a field of dish systems. The total shading is summed for North-South, East-West, and diagonal shading. Cross shading is then subtracted from the total shaded area. Cross shading is the area that is shaded by two or three types of shading (N-S, E-W, diagonal) so this area should only be considered once. Figure G-1 indicates the numbers one through four assigned to the specific dishes, the diameter of the dish (D), the dish spacing north to south (l_{NS}), and the dish spacing east to west (l_{EW}).

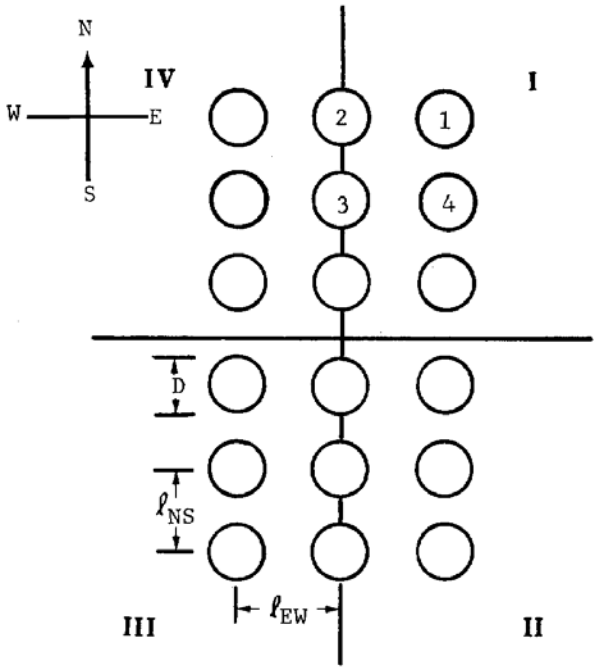

Figure G-1 Spacing of the specific parabolic dish systems and numbers assigned (Osborn, 1980)

North-South Shading

North-South shading occurs when the dish to the south shades the dish to the north. The equations to solve for the North-South shading are given in Equation G-1 through G-9. The term $A_{2\text{-}3}$ is the total shaded surface area for North-South shading, φ_A is the solar azimuth angle referenced from the north, and φ_E is the solar elevation angle referenced from the horizon.

$$x_{2-3} = l_{NS} \cdot \cos(\varphi_A) \qquad \text{G-1}$$

$$y_{2-3} = l_{NS} \cdot \sin(\varphi_A) \qquad \text{G-2}$$

$$L_{NS} = l_{NS} / D \qquad \text{G-3}$$

$$x'_{2-3} = x_{2-3} \cdot \sin(\varphi_E) \quad \text{G-4}$$

$$d_{2-3} = \sqrt{(x'_{2-3})^2 + (y_{2-3})^2} \quad \text{G-5}$$

If $\left(\frac{d_{2-3}}{D}\right) < 1$ then

$$A_{2-3} = \frac{D^2}{4} \cdot (\theta_2 - \sin(\theta_2)) \quad \text{G-6}$$

$$\theta_2 = 2 \cdot \cos^{-1}\left(\frac{d_{2-3}}{D}\right) \quad \text{G-7}$$

If $\left(\frac{d_{2-3}}{D}\right) \geq 1$

$$A_{2-3} = 0 \quad \text{G-8}$$

$$\theta_2 = 0 \quad \text{G-9}$$

East-West Shading

East-West shading occurs when the dish to the east shades the dish to the west in the morning, and when the dish to the west shades the dish to the east in the afternoon. The equations to solve for the East-West shading are given in Equation G-10 through G-14. The term A_{4-3} is the total shaded surface area for East-West shading.

$$d_{4-3} = D \cdot LEW \cdot \sqrt{\sin^2(\varphi_A) \cdot \sin^2(\varphi_E) + \cos^2(\varphi_A)} \quad \text{G-10}$$

If $\left(\frac{d_{4-3}}{D}\right) < 1$ then

$$A_{4-3} = \frac{D^2}{4} \cdot (\theta_1 - \sin(\theta_1)) \quad \text{G-11}$$

$$\theta_1 = 2 \cdot \cos^{-1}\left(\frac{d_{4-3}}{D}\right) \quad \text{G-12}$$

If $\left(\frac{d_{2-3}}{D}\right) \geq 1$

$$A_{4-3} = 0 \quad \text{G-13}$$

$$\theta_1 = 0 \quad \text{G-14}$$

Diagonal Shading

Diagonal shading occurs when dishes 1 or 3 (Figure G-1) shade the other dish, or when dishes 2 or 4 shade the dish. The equations to solve for the diagonal shading are given in Equation G-15 through G-25. The term $A_{1\text{-}3}$ is the total shaded surface area for diagonal shading.

$$L_{EW} = l_{EW} / D \quad \text{G-15}$$

$$l_d = \sqrt{2 \cdot l_{NS}^2} \quad \text{G-16}$$

$$y_{1-3} = l_d \cdot \sin(\beta) \quad \text{G-17}$$

$$\beta = \frac{\pi}{2} - \varphi_A - \alpha \quad \text{G-18}$$

$$\alpha = \tan^{-1}(l_{NS} / l_{EW}) \quad \text{G-19}$$

$$x'_{1-3} = x_{1-3} \cdot \sin(\varphi_E) \quad \text{G-20}$$

$$d_{1-3} = \sqrt{(x'_{1-3})^2 + (y_{1-3})^2} \quad \text{G-21}$$

If $\left(\frac{d_{1-3}}{D}\right) < 1$ then

$$A_{1-3} = \frac{D^2}{4} \cdot (\theta_3 - \sin(\theta_3)) \quad \text{G-22}$$

$$\theta_3 = 2 \cdot \cos^{-1}\left(\frac{d_{1-3}}{D}\right) \quad \text{G-23}$$

If $\left(\frac{d_{1-3}}{D}\right) \geq 1$

$$A_{1-3} = 0 \quad \text{G-24}$$

$$\theta_3 = 0 \quad \text{G-25}$$

Cross Shading

Cross shading occurs when two shadows cast by two or three types of shading (North-South, East-West, diagonal) intersect the same area as shown in Figure G-2. The equations to solve for the cross shading are given in Equation G-26 through G-41. The term $A_{1,2\text{-}3}$ is the total shaded surface area for diagonal shading.

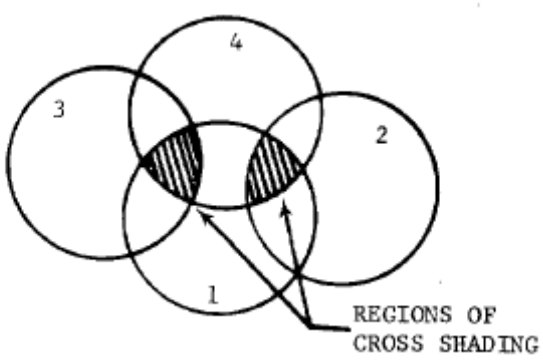

Figure G-2 Cross shading of parabolic dishes (Osborn, 1980)

$$\xi_1 = \cos^{-1}\left(\frac{d_{1-2}^2 + d_{1-3}^2 - d_{2-3}^2}{2 \cdot d_{1-2} \cdot d_{1-3}}\right) \quad \text{G-26}$$

$$\xi_2 = \cos^{-1}\left(\frac{d_{2-3}^2 + d_{1-2}^2 - d_{1-3}^2}{2 \cdot d_{2-3} \cdot d_{1-2}}\right) \quad \text{G-27}$$

$$\xi_3 = \cos^{-1}\left(\frac{d_{1-3}^2 + d_{2-3}^2 - d_{1-2}^2}{2 \cdot d_{1-3} \cdot d_{2-3}}\right) \quad \text{G-28}$$

$$\gamma_1 = 0.5 \cdot (\theta_3 + \theta_1) - \xi_1 \quad \text{G-29}$$

$$\gamma_2 = 0.5 \cdot (\theta_2 + \theta_1) - \xi_2 \quad \text{G-30}$$

$$\gamma_3 = 0.5 \cdot (\theta_2 + \theta_3) - \xi_3 \quad \text{G-31}$$

$$S_1 = \frac{D^2}{8} \cdot (\gamma_1 - \sin(\gamma_1)) \quad \text{G-32}$$

$$S_2 = \frac{D^2}{8} \cdot (\gamma_2 - \sin(\gamma_2)) \quad \text{G-33}$$

$$S_3 = \frac{D^2}{8} \cdot (\gamma_3 - \sin(\gamma_3)) \quad \text{G-34}$$

$$b_1 = D \cdot \sin(0.5 \cdot \gamma_1) \quad \text{G-35}$$

$$b_2 = D \cdot \sin(0.5 \cdot \gamma_2) \quad \text{G-36}$$

$$b_3 = D \cdot \sin(0.5 \cdot \gamma_3) \quad \text{G-37}$$

$$B = 0.5 \cdot (b_1 + b_2 + b_3) \quad \text{G-39}$$

$$A_{tri} = \sqrt{B \cdot (B - b_1) \cdot (B - b_2) \cdot (B - b_3)} \quad \text{G-38}$$

If $\gamma_1 > 0$

$$A_{1,2-3} = S_1 + S_2 + S_3 + A_{tri} \quad \text{G-40}$$

If $\gamma_1 \leq 0$

$$A_{1,2-3} = 0 \quad \text{G-41}$$

An analysis to find cross shading for $A_{1,4-3}$ is the same as $A_{1,2-3}$ besides d_{1-4} and d_{4-3} are used instead of d_{1-2} and d_{2-3} respectively. The total shaded area on all the interior dishes (SA_i) in a field of *NNS* (number of dishes north to south) by *NEW* (number of dishes east to west) dishes is given by Equation G-42. The total shaded area of all exterior dishes is given by Equation G-44 or G-45. The average shaded area per dish (S_{AVG}) is given by Equation G-46.

$$SA_i = (NNS - 1) \cdot (NEW - 1) \cdot SP \quad \text{G-42}$$

$$SP = A_{2-3} + A_{4-3} + A_{1-3} - A_{1,2-3} - A_{1,2-4} \quad \text{G-43}$$

If $0 < \varphi_A < \pi/2$ or $\pi < \varphi_A < 3\pi/2$ (sun in north-east or south-west quadrants)

$$SA_e = (NNS - 1) \cdot A_{2-3} + (NEW - 1) \cdot A_{4-3} \quad \text{G-44}$$

Else (sun in south-east or north-west quadrants)

$$SA_e = (NNS - 1) \cdot A_{4-3} + (NEW - 1) \cdot A_{2-3} \quad \text{G-45}$$

$$S_{AVG} = (SA_i + SA_e) / (NNS \cdot NEW) \quad \text{G-46}$$